

**INTEGRATED MULTI-PHYSICS MODELING OF  
STEELMAKING PROCESS IN ELECTRIC ARC FURNACE**

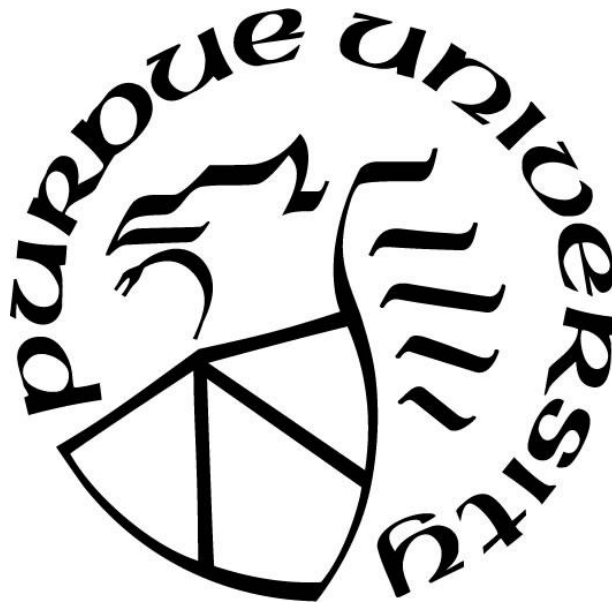
by  
**Yuchao Chen**

**A Dissertation**

*Submitted to the Faculty of Purdue University*

*In Partial Fulfillment of the Requirements for the degree of*

**Doctor of Philosophy**



School of Mechanical Engineering

West Lafayette, Indiana

August 2022

**THE PURDUE UNIVERSITY GRADUATE SCHOOL  
STATEMENT OF COMMITTEE APPROVAL**

**Dr. Chenn Q. Zhou, Chair**

School of Mechanical Engineering

**Dr. Jun Chen**

School of Mechanical Engineering

**Dr. Steven T. Wereley**

School of Mechanical Engineering

**Dr. Tom I-P. Shih**

School of Aeronautics and Astronautics

**Approved by:**

Dr. Nicole L. Key

*To my parents and my girlfriend who made this possible*

## ACKNOWLEDGMENTS

I would like to express my deepest gratitude to my advisor, Prof. Chenn Q. Zhou, whose sincerity and encouragement I will never forget. Prof. Zhou has been an inspiration as I hurdled through the path of this Ph.D. degree. She is the true definition of a leader and the ultimate role model. This thesis would not have been possible without Prof. Zhou, whose guidance and assistance from the initial step of research enabled me to develop an understanding of the project. Her brilliant, skillful supervision enriched my research and vision and helped me to take this project to a new level. I am also thankful for the extraordinary working experiences she arranged for me in the Center for Innovation through Visualization and Simulation (CIVS) and for providing opportunities for me to grow professionally from a master's degree to a Ph.D. degree. I also would like to thank Prof. Jun Chen, Prof. Steven Wereley, and Prof. Tom Shih for serving on my advisory committee and providing great supports to my works.

I would like to thank all my colleagues and friends at CIVS for their kind helps and encouragements, including Dr. Armin Silaen, Dr. Tyamo Okosun, Mr. Nick Walla, Dr. Haibo Ma, Dr. Orlando Ugarte, Mr. John Moreland, Mr. Kyle Toth, Mrs. Melissa Mollett, Mrs. Ana Jovanovich, Mrs. Karen Norman, Mr. Yu Wang, Mr. Qingxuan Luo, Mr. Neel Busa, and many more. I also would like to give my sincere gratitude to all committee members from the Steel Manufacturing Simulation and Visualization Consortium (SMSVC) for the invaluable guidance on the project I worked on. Special thanks go to Steve Ryan (NLMK), Jianghua Li (Cleveland-Cliffs), Yufeng Wang (SSAB), Sunday Abraham (SSAB), Joe Maiolo (Linde), Hamzah Alshawarghi (Linde), Eugene Pretorius (NUCOR), Ian Markon (NUCOR), John Lowry (NUCOR), Bikram Konar (EVRAZ NA), and Mike Lowry (ArcelorMittal).

Further, yet importantly, both my parents and my girlfriend Xintong deserve endless gratitude: your unconditional love and support throughout my entire study in the U.S. helped me pass the bottleneck period of research and kept me motivated and confident. My accomplishments are all because of your selfless giving and companionship.

June 10, 2022 at Purdue

# TABLE OF CONTENTS

LIST OF TABLES .....	10
LIST OF FIGURES .....	11
NOMENCLATURE .....	17
ABSTRACT.....	21
1. INTRODUCTION .....	23
1.1 Electric Arc Furnace .....	23
1.2 Literature Review.....	27
1.2.1 Scrap Heating and Melting .....	29
1.2.2 Electric Arc Plasma .....	33
1.2.3 Injector/Burner System.....	36
1.2.4 Liquid Steel Refining.....	39
1.2.5 Heat Transfer and Post-combustion in Freeboard .....	41
1.3 Motivations for Research.....	43
1.4 Research Objectives.....	44
1.5 Organization.....	44
2. MODELING OF LAB-SCALE DC EAF.....	46
2.1 Problem Description .....	46
2.2 Modeling Methodology .....	48
2.3 Model Description .....	49
2.3.1 Solid Steel Melting Model.....	50
2.3.2 Electric Arc Model (for Lab-scale DC Arc).....	52
2.3.2.1 Interface Tracking .....	54
2.3.2.2 Heat Transfer at Interface.....	54
2.3.2.3 Surface Force at Interface .....	55
2.3.2.4 Electrode Movement .....	56
2.3.3 Simulation Conditions .....	57
2.4 Results and Discussions.....	59
2.4.1 Model Validations .....	59
2.4.1.1 Electric Arc Model (for Lab-scale DC Arc).....	59

2.4.1.2 Solid Steel Melting Model .....	62
2.4.2 Arc Characteristics with Dynamic Electrode Movement .....	64
2.4.3 Steel Ingot Melting with Stationary Electrode .....	68
2.4.4 Steel Ingot Melting with Dynamic Electrode Movement.....	70
2.5 Summary.....	73
3. MODELING OF INDUSTRY-SCALE AC EAF.....	75
3.1 Modeling Methodology .....	76
3.2 Model Description .....	78
3.2.1 Scrap Melting Model .....	78
3.2.1.1 Fluid Phases.....	79
3.2.1.2 Solid Phase .....	81
3.2.1.3 Phase Interactions.....	82
3.2.1.4 Melting/Re-solidification .....	84
3.2.1.5 Scrap Collapse.....	85
3.2.2 Electric Arc Model (for Industry-scale AC Arc).....	89
3.2.2.1 Governing Equations.....	90
3.2.2.2 Arc Heat Dissipation .....	95
3.2.2.3 Arc Impingement on Liquid Bath .....	100
3.2.2.4 Electrode Regulation .....	101
3.2.3 Coherent Jet Model.....	102
3.2.3.1 Shrouding Combustion Flame.....	103
3.2.3.2 Turbulence Viscosity Correction .....	106
3.2.3.3 Gas-solid Heat Transfer .....	107
3.2.3.4 Jet Penetration in Liquid Bath .....	108
3.2.4 Oxidation Model.....	113
3.2.4.1 Reaction Mechanisms .....	114
3.2.4.2 Bath Temperature Rise.....	118
3.2.5 Slag Foaming Model.....	119
3.2.5.1 Slag Foaming Height.....	119
3.2.5.2 Exposed Arc Length.....	121
3.3 Results and Discussions.....	122

3.3.1	Electric Arc Simulator .....	123
3.3.1.1	Simulation Conditions .....	123
3.3.1.2	Validations .....	125
3.3.1.3	AC Arc Power Delivery .....	129
3.3.1.4	AC Arc Performance .....	131
3.3.1.5	Effect of Arc Length .....	132
3.3.1.6	Effect of Arc Operating Current.....	135
3.3.1.7	AC Arc Heat Dissipation Database and Arc Momentum Transfer Database .....	137
3.3.1.8	Summary .....	139
3.3.2	Coherent Jet Simulator .....	140
3.3.2.1	Simulation Conditions .....	140
3.3.2.1	Validations .....	141
3.3.2.3	Effect of Freeboard Ambient Temperature .....	143
3.3.2.4	Effect of Fuel Input .....	145
3.3.2.5	Summary .....	147
3.3.3	Scrap Preheating Simulator .....	147
3.3.3.1	Simulation Conditions.....	147
3.3.3.2	Validations .....	150
3.3.3.2.1	Gas-solid Heat Transfer .....	150
3.3.3.2.2	Non-immersed Burner Preheating .....	152
3.3.3.2.3	Immersed Burner Preheating .....	154
3.3.3.3	Baseline Results .....	156
3.3.3.4	Effects of Single Factors on Scrap Preheating Characteristics .....	158
3.3.3.4.1	Burner Power .....	158
3.3.3.4.2	Initial Scrap Temperature .....	160
3.3.3.4.3	Scrap Porosity .....	162
3.3.3.4.3	Scrap Blockage .....	164
3.3.3.5	Optimization of Scrap Preheating Stage .....	166
3.3.3.6	Summary .....	175
3.3.4	Scrap Melting Simulator.....	176
3.3.4.1	Simulation Conditions.....	176

3.3.4.2	Validations .....	179
3.3.4.3	Scrap Melting Behavior.....	184
3.3.4.4	Electric Arc Performance .....	188
3.3.4.5	Burner Performance .....	190
3.3.4.5	Summary .....	192
3.3.5	In-bath Decarburization Simulator .....	194
3.3.5.1	Simulation Conditions.....	194
3.3.5.1	Validations .....	195
3.3.5.1.1	Jet Penetration Depth .....	195
3.3.5.1.2	Results at Tapping.....	196
3.3.5.2	Stirring Mechanism .....	197
3.3.5.3	Refining Efficiency .....	200
3.3.5.4	In-bath Carbon Distribution .....	203
3.3.5.4	Effect of Coherent Jet Burner #5 on Refining Efficiency.....	205
3.3.5.5	Summary .....	207
3.3.6	Freeboard Post-Combustion Simulator.....	208
3.3.6.1	Simulation Conditions.....	208
3.3.6.2	Validations .....	210
3.3.6.3	Baseline Results .....	212
3.3.6.4	Investigations of Water-cooling Panel Overheating .....	213
3.3.6.4.1	Effect of Burner Operation Mode .....	213
3.3.6.4.2	Effect of Burner Operating Conditions.....	215
3.3.6.4.3	Effect of Bath Level.....	217
3.3.6.4.4	Effect of Arc Power .....	218
3.3.6.4.5	Effect of Lime Input.....	220
3.3.6.5	Web-based Online Calculator .....	221
3.3.6.6	Summary .....	222
4.	CONCLUSIONS AND OUTLOOK .....	224
4.1	Conclusions.....	224
4.1.1	Simulation Methodologies and CFD Models .....	224
4.1.2	Research Findings.....	225

4.2 Outlook .....	229
REFERENCES .....	230
PUBLICATIONS.....	245

## LIST OF TABLES

Table 2.1. Material properties in the model.....	57
Table 2.2. Other parameters in the model.....	58
Table 2.3. Boundary conditions for the simulation domain.....	59
Table 3.1. Oxidation reaction mechanism in the oxidation model. ....	114
Table 3.2. Temperature-dependent slag surface tension and density [144-145]. ....	120
Table 3.3. Coefficient values [146].....	121
Table 3.4. Boundary conditions.....	124
Table 3.5. Material properties.....	125
Table 3.6. Coefficients in the equation. ....	139
Table 3.7. Boundary conditions for lance mode.....	141
Table 3.8. Baseline burner condition (3.2 MW under burner mode).....	149
Table 3.9. Key parameters in scrap melting model. ....	149
Table 3.10. Factor configurations for optimization. ....	167
Table 3.11. $L_9$ ( $3^3$ ) orthogonal design table for CFD simulations. ....	167
Table 3.12. CFD simulation results presented by three evaluation indexes. ....	168
Table 3.13. Range analysis results.....	169
Table 3.14. Three-layer data structure for optimization. ....	171
Table 3.15. CFD results comparison before and after the optimization. ....	173
Table 3.16. Key properties and parameters in the model. ....	179
Table 3.17. Summary of trial information for scrap melting by the electric arc. ....	180
Table 3.18. Key parameters in the model. ....	195
Table 3.19. Comparison of results at tapping (800 seconds).....	196
Table 3.20. Material thermal properties.....	209
Table 3.21. Burner operating conditions under different modes. ....	213

## LIST OF FIGURES

Figure 1.1. Modern steelmaking process [1].	23
Figure 1.2. U.S. EAF steelmaking share [3].	24
Figure 1.3. EAF steelmaking share by country in 2017 [3].	24
Figure 1.4. Typical EAF steelmaking process [6].	26
Figure 1.5. CFD modeling of the scrap preheating [18].	30
Figure 1.6. CFD modeling of the evolution of keyhole melting on the metal plate [23].	31
Figure 1.7. CFD modeling of the melting process of two steel rods in liquid steel [30].	32
Figure 1.8. CFD modeling of the free-burning DC argon arc [44].	34
Figure 1.9. CFD modeling of the 3-phase AC arc discharge behavior [55].	35
Figure 1.10. CFD modeling of the supersonic coherent jet in the open air [69].	38
Figure 1.11. CFD modeling of the supersonic coherent jet penetration in liquid steel [85].	39
Figure 1.12. CFD modeling of the arc radiation in the freeboard under different slag heights [94].	41
Figure 1.13. Dissertation structure outlined under three main terminologies (comprehensive EAF CFD model, model, and simulator).	45
Figure 2.1. Schematic diagram of the lab-scale arc melting furnace.	47
Figure 2.2. Computational domain for steel ingot melting by the electric arc.	47
Figure 2.3. Main physical phenomena of the steelmaking process in lab-scale DC EAF.	48
Figure 2.4. Flow chart within the direct-coupling methodology for models.	49
Figure 2.5. Comparison of simulated isotherms and measurement data [36].	60
Figure 2.6. Comparison of velocity distribution at the domain centerline [43-44].	61
Figure 2.7. Comparison of 2D and 3D simulated isotherms.	62
Figure 2.8. Comparison of 2D and 3D velocity distribution at the domain centerline.	62
Figure 2.9. Schematic diagram of experimental setup [100].	63
Figure 2.10. Melting validation: steel as the workpiece [100].	64
Figure 2.11. Melting validation: aluminum as the workpiece [101].	64
Figure 2.12. Dynamic effect of varying arc length due to electrode movement on the arc characteristics.	65

Figure 2.13. Near-wall gas temperature distribution at the electrode surface during the electrode descent.....	66
Figure 2.14. Distribution of heat flux, pressure, and current density at anode surface during the electrode descent.....	66
Figure 2.15. Steel ingot melting using electric arc under the stationary electrode.....	68
Figure 2.16. Effect of initial arc length on melting efficiency under stationary electrode.....	69
Figure 2.17. Steel ingot melting using electric arc under the dynamic moving electrode.....	70
Figure 2.18. Comparison of steel ingot melting efficiency with and without dynamic moving electrode.....	71
Figure 2.19. Axial temperature and velocity distribution at 0.0005 m above the ingot top surface with the dynamic moving electrode.....	72
Figure 2.20. Axial temperature and velocity distribution at 0.0005 m above the ingot top surface without the dynamic moving electrode.....	72
Figure 3.1. Integration methodology for the industry-scale AC EAF steelmaking process.....	77
Figure 3.2. Connections of scrap melting model with other models.....	79
Figure 3.3. Phase interactions within gas-liquid-solid three-phase system.....	82
Figure 3.4. Sketch diagram of stack approach.....	86
Figure 3.5. Application of stack approach for dynamic scrap collapse simulation.....	87
Figure 3.6. Algorithm of stack approach.....	88
Figure 3.7. Variation of electrode polarity over time.....	94
Figure 3.8. Arc heat dissipation mechanism.....	96
Figure 3.9. Simplified electrical schematic diagram for three-phase AC EAF.....	97
Figure 3.10. Comparison of surface-to-surface radiation, source-to-surface radiation, and source-to-cell radiation.....	98
Figure 3.11. Arc impingement on liquid bath.....	100
Figure 3.12. Constant impedance control for electrode regulation.....	102
Figure 3.13. Comparison of conventional jet and coherent jet used in liquid steel refining stage.....	104
Figure 3.14. Integration of coherent jet model in the in-bath decarburization simulation.....	109
Figure 3.15. Sketch of 3D jet penetration cavity estimation.....	112
Figure 3.16. 3D computational domain with jet penetration cavities for the in-bath decarburization simulator.....	112
Figure 3.17. Exothermic oxidation reactions in liquid bath.....	114

Figure 3.18. Ellingham diagram for determining the reaction orders.....	115
Figure 3.19. Oxygen injection through jet penetration cavities and absorption of oxides. ....	117
Figure 3.20. Oxidation enthalpies for each reaction [141]. ....	118
Figure 3.21. Exposed arc to freeboard.....	122
Figure 3.22. Schematic diagram of computational domain for AC arc modeling.....	123
Figure 3.23. Comparison of simulated arc axial velocity and measurement data [149].....	126
Figure 3.24. Arc temperature field for 1150 A current case.....	126
Figure 3.25. Validation of AC arc in Argon. (a) current = 86 kA; (b) current = 43 kA; (c) current = -79 kA; (d) current = -42 kA. ....	128
Figure 3.26. Instantaneous arc current/voltage variation over time (arc length = 0.4 m and RMS arc current = 60 kA).....	129
Figure 3.27. Instantaneous arc power delivery variation over time (arc length = 0.4 m and RMS arc current = 60 kA).....	130
Figure 3.28. Relationship between the total arc power delivery, arc length, and RMS arc current. ....	131
Figure 3.29. Time-averaged AC arc state variables (arc length = 0.4 m, RMS arc current = 60 kA). (a) Density field; (b) Velocity field; (c) Specific enthalpy field; (d) Temperature field. ....	132
Figure 3.30. Effect of arc length on AC arc performance. ....	133
Figure 3.31. Effect of arc length on AC arc state variables.....	134
Figure 3.32. Effect of arc length on AC arc heat dissipation.....	134
Figure 3.33. Effect of RMS arc current on AC arc performance.....	135
Figure 3.34. Effect of RMS arc current on AC arc state variables. ....	136
Figure 3.35. Effect of RMS arc current on AC arc heat dissipation. ....	136
Figure 3.36. Variations of arc density/velocity with different arc lengths and RMS arc currents. ....	137
Figure 3.37. Variation of the share for different heat dissipation mechanisms with different arc lengths and RMS arc currents. (a) Convection; (b) Electron flow; (c) Radiation. ....	138
Figure 3.38. Computational domain for separate coherent jet simulation.....	140
Figure 3.39. Coherent jet validation – axial velocity distribution. ....	142
Figure 3.40. Coherent jet validation – (a) temperature distribution; (b) velocity distribution; (c) density distribution.....	143
Figure 3.41. Comparison of jet potential core length under different ambient temperatures. ....	144
Figure 3.42. Coherent jet simulation results under different ambient temperatures.....	145

Figure 3.43. Comparison of jet potential core length under different fuel input. ....	146
Figure 3.44. Coherent jet simulation results under different fuel input. ....	146
Figure 3.45. NLMK EAF with scrap charged; .....	148
Figure 3.46. Computational domain with scrap charged. ....	148
Figure 3.47. Gas-solid heat transfer validation – thermocouple temperature reading comparison. ....	150
Figure 3.48. Gas-solid heat transfer validation – (a) melted region at 35 s; (b) melted region at 90 s. ....	151
Figure 3.49. Scrap preheating trial using coherent jet burner – (a) experiment; (b) CFD results. ....	152
Figure 3.50. Scrap melting cavity at 500 s – (a) experiment; (b) CFD results. ....	153
Figure 3.51. Scrap temperature distribution at 500 s – (a) by industrial high-temperature thermal camera FLIR TG297; (b) by CFD simulation. ....	153
Figure 3.52. Experiment observation – (a) thermal image; (b) optical image. ....	155
Figure 3.53. CFD results – (a) thermal image; (b) optical image. ....	156
Figure 3.54. Evolution of melting pits in front of four burners (baseline). ....	157
Figure 3.55. Impact of burner power – (a) scrap temperature rise; (b) melted percentage; (c) burner efficiency. ....	159
Figure 3.56. Comparison of final melting pit at 600 s – (a) 2.4 MW; (b) 3.2 MW; (c) 4.0 MW. ....	160
Figure 3.57. Impact of initial scrap temperature – (a) scrap temperature rise; (b) melted percentage; (c) burner efficiency. ....	161
Figure 3.58. Comparison of final melting pit at 600 s – (a) 300 K; (b) 450 K; (c) 600 K. ....	162
Figure 3.59. Impact of scrap porosity – (a) scrap temperature rise; (b) melted percentage; (c) burner efficiency. ....	163
Figure 3.60. Comparison of final melting pit at 600 s – (a) $\gamma_s = 0.76$ ; (b) $\gamma_s = 0.81$ ; (c) $\gamma_s = 0.86$ . ....	164
Figure 3.61. Impact of scrap blockage – (a) burner efficiency; (b) scrap heating rate; (c) sidewall temperature distribution. ....	165
Figure 3.62. Scrap cavity and sidewall temperature distribution with and without scrap blockage. ....	166
Figure 3.63. Contributions of different factors on impacting – (a) burner efficiency; (b) scrap temperature rise; (c) melted percentage. ....	170
Figure 3.64. Comprehensive contribution rates of each factor on burner preheating results. ....	174

Figure 3.65. Evolution of melting pits in front of four burners (after optimization).....	174
Figure 3.66. Computational domain of industry-scale NLMK AC EAF.....	177
Figure 3.67. Electrical inputs – (a) phase current and phase voltage; (b) arc power and arc length. .....	178
Figure 3.68. Experimental data – (a) trial #1 using shredded scrap; (b) trial #4 using busheling scrap. ....	181
Figure 3.69. Observations of the final electrode pit size. ....	182
Figure 3.70. Comparison of CFD results and observations for final electrode pit size.....	183
Figure 3.71. Comparison of CFD results and experimental data for real-time electrode position. .....	184
Figure 3.72. Simulated scrap melting process. ....	185
Figure 3.73. Variation of scrap mass and electrode position.....	186
Figure 3.74. Observation of scrap melting profile at 900 s. ....	187
Figure 3.75. Simulated scrap collapse during melting.....	187
Figure 3.76. Simulated arc radiation distribution on furnace roof and wall. ....	188
Figure 3.77. (a) variation of share of arc heat dissipation; (b) variation of arc radiation distribution. .....	189
Figure 3.78. Streamlines from burners (colored by gas temperature). ....	191
Figure 3.79. (a) variation of burner efficiency; (b) variation of gas/liquid temperature. ....	192
Figure 3.80. Computational domain for in-bath decarburization simulation.....	194
Figure 3.81. Validation for the estimated jet penetration depth. ....	195
Figure 3.82. Momentum stirring without bubble stirring. ....	198
Figure 3.83. Momentum stirring with bubble stirring. ....	198
Figure 3.84. In-bath tracer mass fraction variation over time (with momentum transfer and bubble stirring).....	199
Figure 3.85. Mixing time of flow field – (a) without bubble stirring; (b) with bubble stirring..	200
Figure 3.86. Variation of volume-averaged bath temperature, carbon content, and manganese content during refining.....	201
Figure 3.87. Variation of simulated in-bath carbon distribution near burner #1. ....	202
Figure 3.88. Variation of simulated bath temperature near burner #1.....	202
Figure 3.89. Variation of simulated in-bath carbon distribution. ....	203
Figure 3.90. In-bath carbon mass fraction (0.5 m from furnace bottom) at tapping. ....	204

Figure 3.91. Coherent jet burner #5 in SDI EAF. ....	205
Figure 3.92. Computational domain with coherent jet burner #5. ....	205
Figure 3.93. Refining efficiency comparison with and without coherent jet burner #5. ....	206
Figure 3.94. In-bath carbon mass fraction (0.5 m from furnace bottom) at tapping with burner #5. ....	207
Figure 3.95. Computational domain for freeboard post-combustion simulation. ....	209
Figure 3.96. Analysis of water-cooling panel temperature. ....	210
Figure 3.97. Simulation results for validations – (a) no-overheating; (b) overheating. ....	211
Figure 3.98. Baseline simulation results – (a) CO mass fraction distribution; (b) CO <sub>2</sub> mass fraction distribution; (c) gas temperature distribution; (d) streamline colored by velocity. ....	212
Figure 3.99. Effect of burner operation mode on sidewall temperature distribution. ....	214
Figure 3.100. Sidewall temperature distribution in four viewing directions. ....	215
Figure 3.101. Effect of burner operating conditions on sidewall temperature distribution. ....	216
Figure 3.102. Coherent jet simulations with and without the primary oxygen. ....	216
Figure 3.103. Effect of bath level on sidewall temperature distribution. ....	217
Figure 3.104. Effect of arc power on - (a) exposed arc length; (b) averaged and maximum sidewall temperature. ....	219
Figure 3.105. Effect of arc power on sidewall temperature distribution. ....	220
Figure 3.106. Effect of lime input on sidewall temperature distribution. ....	221
Figure 3.107. Real-Time online calculator launched in SMSVC official website. ....	222

# NOMENCLATURE

## Subscripts

$q$	Phase subscript
$i$	Specie subscript
$g$	Gas phase
$l$	Liquid phase
$s$	Solid phase

## Letters

$h_t'$	Old electrode position
$C_D'$	Constant in turbulent viscosity calculation
$\vec{F}_{df}$	Drag force
$\bar{Q}_s$	Volumetric energy exchange with fluid phases
$\dot{m}_{mt}$	Phase mass transfer rate
$v'_r$	Stoichiometric coefficient
$h_{fusion}$	Latent heat of fusion
$h_s$	Current scrap surface position
$h_t$	New electrode position
$C_1$	Constant in turbulence viscosity correction
$C_{1\varepsilon}$	Constant in turbulence model
$C_2$	Constant in turbulence viscosity correction
$C_{2\varepsilon}$	Constant in turbulence model
$C_D$	Drag coefficient
$C_T$	Function
$C_p$	Specific heat capacity
$C_s$	Inertial resistance factor of scrap
$D'$	Coefficient function
$D_T$	Thermal (Soret) diffusion coefficient
$D_m$	Mass diffusion coefficient

$\bar{G}$	Gain coefficient
$G_1$	Constant in impedance control
$G_2$	Constant in impedance control
$G_k$	Kinetic energy produced by turbulence
$I_{RMS}$	RMS arc current
$K_{eff}$	Effective thermal conductivity
$M_w$	Molecular weight
$M_\tau$	Turbulent Mach number
$M_{\tau 0}$	Constant in turbulence viscosity correction
$N_i$	Number of radiation beams intercepted by cell
$N_{tot}$	Total number of radiation beam emissions
$P_a$	Total arc power
$P_l$	Momentum transfer to liquid bath
$Q_{ht}$	Phase heat transfer
$Q_{arc,i}$	Arc radiative heat transfer to cell
$Q_{rad,tot}$	Total arc radiative heat dissipation
$R_r$	Net rate of production of each species by chemical reaction
$Sc_t$	Turbulent Schmidt number
$T_g$	Normalized local total gas temperature gradient
$T_{liquidus}$	Liquidus temperature
$T_{solidus}$	Solidus temperature
$V_c$	Cell volume
$a_g$	Gas acoustic velocity
$a_\varepsilon$	Emissivity weighting factor
$b_\varepsilon$	Emissivity gas temperature polynomial coefficients
$\vec{g}$	Acceleration of gravity
$\vec{j}$	Species mass diffusion
$k'$	Absorption coefficient of the fictitious gray gas
$l_a$	Arc length

$n'$	Refractive index
$\vec{r}$	Beam position
$\vec{s}$	Beam direction
$\vec{v}$	Velocity vector
$\Omega'$	Solid angle
$\beta_s$	Scrap permeability
$\gamma_s$	Scrap porosity
$\varepsilon'$	Total emissivity
$\mu_t$	Turbulent viscosity
$\sigma_{SB}$	Stefan–Boltzmann constant
$\sigma_k$	Constant in turbulence model
$\sigma_s$	Scattering coefficient
$\sigma_\varepsilon$	Constant in turbulence model
$\bar{\bar{\tau}}$	Stress-strain tensor
$h$	Cell height
$h$	Heat transfer coefficient
$A$	Interfacial contact area
$E$	Energy
$H(x)$	Heaviside function
$I$	Radiation intensity
$K$	Thermal conductivity
$Pr$	Prandtl number
$R$	Arc resistance
$Re$	Reynolds number
$T$	Temperature
$Y$	Local species mass fraction
$a$	Absorption coefficient
$d$	Characteristic diameter
$i$	Phase current

$k$	Turbulent kinetic energy
$m$	Mass
$p$	Pressure of fluid phases
$s$	Path length
$t$	Flow time
$u$	Phase voltage
$\alpha$	Volume fraction
$\varepsilon$	Turbulent dissipation rate
$\lambda$	Thermal conductivity
$\mu$	Molecular viscosity
$\xi$	Constant in turbulence viscosity correction
$\rho$	Density
$\sigma$	Ionized air's specific conductivity
$\tau$	Arc cooling constant
$\varphi$	Difference between the measured arc voltage and the measured arc current
$\omega$	Constant in Cassie-Mayr arc model
$\phi$	Phase function

## ABSTRACT

The electric arc furnace (EAF) is a critical steelmaking facility that melts the scrap by the heat produced from electrodes and burners. The migration to EAF steelmaking has accelerated in the steel industry over the past decade owing to the consistent growth of the scrap market and the goal of "green" steel production. The EAF production already hit a new high in 2018, contributing to 67% of total short tons of U.S. crude steel produced. The EAF steelmaking process involves dynamic complex multi-physics, in which electric arc plasma and coherent jets coexist resulting in an environment with local high temperature and velocity. Different heat transfer mechanisms are closely coupled and the phase change caused by melting and re-solidification is accompanied by in-bath chemical reactions and freeboard post-combustion, which further creates a complicated gas-liquid-solid three-phase system in the furnace. Therefore, not all conditions and phenomena within the EAF are well-understood. The traditional experimental approach to study the EAF is expensive, dangerous, and labor-intensive. Most of the time, direct measurements and observations are impossible due to the high temperature within the furnace. To this fact, the numerical model has aroused great interest worldwide, which can help to gain fundamental insights and improve product quality and production efficiency, greatly benefiting the steel industry. However, due to the complexity of the entire EAF steelmaking process, the relevant computational fluid dynamics (CFD) modeling and investigations of the whole process have not been reported so far.

The present study was undertaken with the aim of developing the modeling methodologies and the corresponding comprehensive EAF CFD models to simulate the entire EAF steelmaking process. Two state-of-the-art comprehensive EAF CFD models have been established and validated for both the lab-scale direct current (DC) EAF and the industry-scale alternating current (AC) EAF, which were utilized to understand the physical principles, improve the furnace design, optimize the process, and perform the trouble-shootings.

For the lab-scale DC EAF, a direct-coupling methodology was developed for its comprehensive EAF CFD model which includes the solid steel melting model based on the enthalpy-porosity method and the electric arc model (for lab-scale DC arc) based on the Magneto Hydrodynamics (MHD) theory, so that the dynamic simulation of the steel ingot melting by DC arc in the lab-scale

furnace can be achieved, which considered the continuous phase changing of solid steel, the ingot surface deformation, and the phase-to-phase interaction. Both stationary DC arc and the arc-solid steel interface heat transfer and force interaction were validated respectively against the experimental data in published literature. For the given lab-scale furnace, the DC arc behavioral characteristics with varying arc lengths generated by the moving electrode were analyzed, and the effects of both the initial arc length and the dynamic electrode movement on the steel ingot melting efficiency were revealed.

For the industry-scale AC EAF, an innovative integration methodology was proposed for its comprehensive EAF CFD model, which relies on the stage-by-stage approach to simulate the entire steelmaking process. Six simulators were developed for simulating sub-processes in the industry-scale AC EAF, and five models were developed for the above four simulators, including the scrap melting model, the electric arc model (for industry-scale AC arc), the coherent jet model, the oxidation model, and the slag foaming model, which can be partially integrated according to the mass, energy, and momentum balance. Specifically, the dual-cell approach and the stack approach were proposed for the scrap melting model to treat the scrap pile as the porous medium and simulate the scrap melting together with its dynamic collapse process. The statistical sampling method, the CFD-compatible Monte Carlo method, and the electrode regulation algorithm were proposed for the electric arc model to estimate the total AC arc power delivery, the arc radiative heat dissipation, and the instantaneous electrode movement. The energetic approach was proposed to determine the penetration of the top-blown jet in the molten bath based on the results from the coherent jet model. The source term approach was proposed in the oxidation model to simulate the in-bath decarburization process, where the oxidation of carbon, iron, and manganese as well as the effect of those exothermic reactions on bath temperature rising was considered. Moreover, corresponding experiments were performed in the industry-scale EAF to validate the proposed simulators. The quantitative investigations and analyses were conducted afterward to explore and understand the coherent jet performance, the AC arc heat dissipation, the burner preheating characteristics, the scrap melting behavior, the in-bath decarburization efficiency, and the freeboard post-combustion status.

# 1. INTRODUCTION

## 1.1 Electric Arc Furnace

Steel is one of the world's most popular materials for construction due to its unique blend of durability, workability, and affordability. The primary steelmaking in the modern steel industry involves converting raw materials (iron ore and coal) into new liquid steel via the blast furnace (BF) and the basic oxygen furnace (BOF) or melting the recycled scrap in the EAF. The liquid steel is then tapped into the ladle for adding or removing specific elements and manipulating the production environment according to the operating specification. The liquid steel is transported afterward and poured into a cooled mold to produce the casting. The solidified steel strip is cut into steel slabs which are fed into the reheating furnace to reheat to the target temperature for the subsequent manufacturing. The aforementioned line of production is illustrated in **Figure 1.1**.

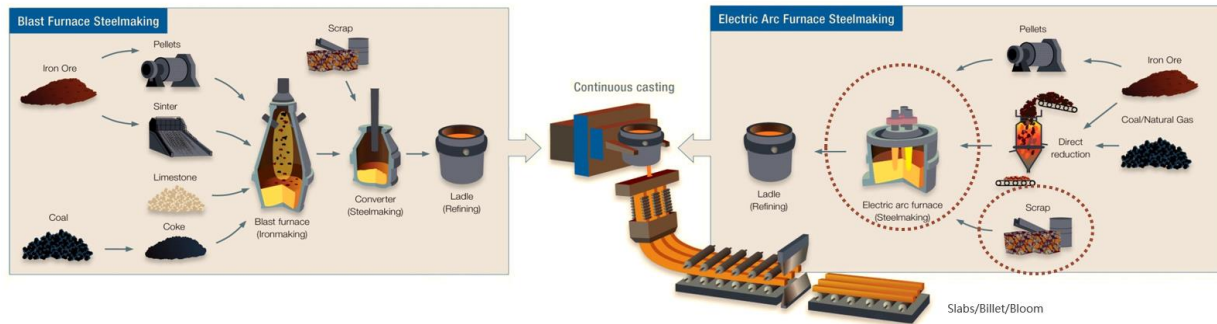


Figure 1.1. Modern steelmaking process [1].

The EAF, as one of the most crucial and extensively used facilities in the primary steelmaking process, utilizes the high temperature produced by the electric arc and fuel combustion to melt the recycled raw material, mainly composed of steel scrap. Although the proportion of electric energy utilization in EAF has declined in recent years, it is still the main energy input for melting scrap. Therefore, it can be acknowledged that the evolution of EAF steelmaking technology is strongly associated with the development of electric energy. After the mid-nineteenth century, the iron and steel metallurgy industry began to focus on the application of electrical energy in melting technology, and various facilities used for achieving electricity-heat conversion have emerged one after another. In 1879, William Siemens invented and patented the world's first AC EAF, which

was only suitable for use in the laboratory. Paul Heroult made it successful for EAF to go into operation in 1906 in France. Since that, the AC EAF has been steadily developed and was dominant in the steelmaking industry until now. In the late 1980s, new techniques such as high-impedance and variable-impedance were developed and further applied to AC EAF steelmaking. After entering the 21st century, the successful utilization of neural network technology in AC EAF systems has greatly improved the accuracy of the identification/control system during the operation of the furnace. Those applications of new technologies largely promoted the EAF steelmaking productivity, and at the same time reduced the interference and impact of EAF operation on the power grid.

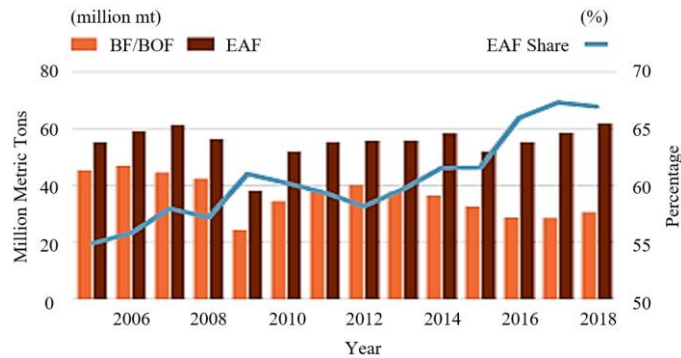


Figure 1.2. U.S. EAF steelmaking share [3].

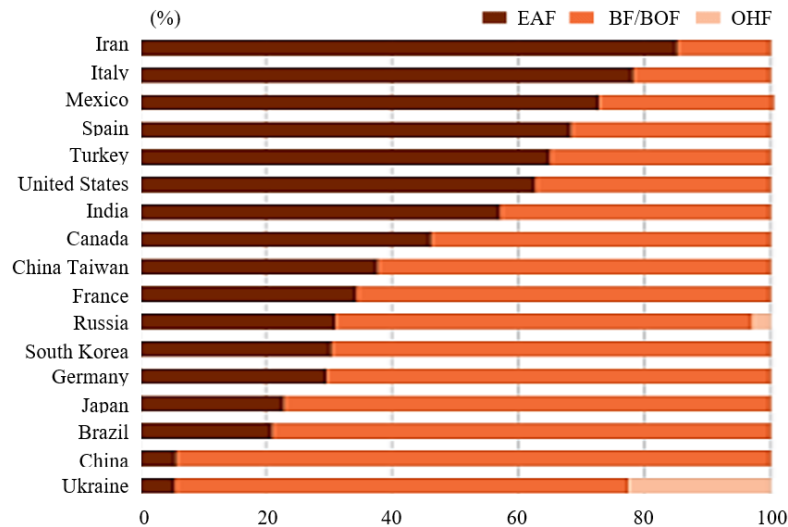


Figure 1.3. EAF steelmaking share by country in 2017 [3].

In the past 70 years, steel scrap consumption has been increasing worldwide [2]. The steel and foundry sectors consumed approximately one-third of the world's steel scraps. As one of the most critical pieces of equipment in the modern steelmaking process, EAF crude steel output accounted for 67% of the overall U.S. production in 2018, and this number is projected to rise to about 70% by 2040 [3] as reflected in **Figure 1.2** and **Figure 1.3**. The EAF steelmaking process is considered to be an energy-intensive process that consumes electrical energy at an average rate of 1.5 MMBtu/short ton. Around 140 EAFs currently operate in the U.S. and altogether consume approximately  $8.6 \times 10^7$  MMBtu/year of electricity [4]. Against this background, the improvement of electrical energy utilization efficiency has become the focus of EAF research recently, including maximizing arc performance and optimizing the furnace operating cost. Additionally, attempts to align and maximize the utilization of electrical and chemical energy will aid in the melting of scrap more efficiently and safely. In addition, the scrap supply stream for EAF is constantly changing and evolving over time, and existing scrap commodities may become scarce and require substitutions with new or alternative materials. Being able to adjust the furnace operations proactively to achieve higher performance based on these new commodities will provide the industry more flexibility and sustainability.

The majority of the EAF operates as a batch process, producing molten steel named "heats". In this process, EAF operating cycle is known as the tap-to-tap cycle and mainly consists of the scrap charging stage, scrap melting stage (including electrode bore-down phase and main melting phase), liquid steel refining stage, and the tapping stage [5], as shown in **Figure 1.4**. A new heat begins with the charging of the raw material through the top of the furnace. The roof and electrodes are raised and swung to the side of the furnace to allow the scrap-charging crane to move a full bucket of scrap into place over the furnace. The bottom of the bucket is designed as a clamshell to permit the scrap to easily fall into the furnace. After the scrap charging stage, the roof is then swung back into place meanwhile electrodes are lowered down to strike an arc on the scrap and start the scrap melting stage. During this stage, the EAF utilizes electricity as the main energy source, together with the chemical energy brought by the coherent jet burners to produce a high temperature up to 2273~3273 K to melt the charged scrap by arc radiation, heat convection, and conduction. The scrap melting stage requires inputting the maximum electric power into the furnace to ensure that the scrap is melted into the liquid steel in the shortest time possible, and the liquid steel will

gradually accumulate at the bottom of the furnace creating the molten bath. Once the solid scrap is almost melted, the liquid steel refining stage starts along with the introduction of supersonic coherent oxygen jets to stir the bath and remove the impure species (C, Si, Mn, and P), so that the thermal homogenization and the metallurgical parameters in the bath can be achieved according to the desired steel grade. When both bath temperature and chemical content meet the requirements, the present heat is ready for tapping. In the modern EAF, there will be an additional stage called the scrap preheating stage after the scrap charging stage but before the scrap melting stage, which utilizes the coherent jet burners to preheat and melt the scrap to improve the overall furnace efficiency and shorten the process.

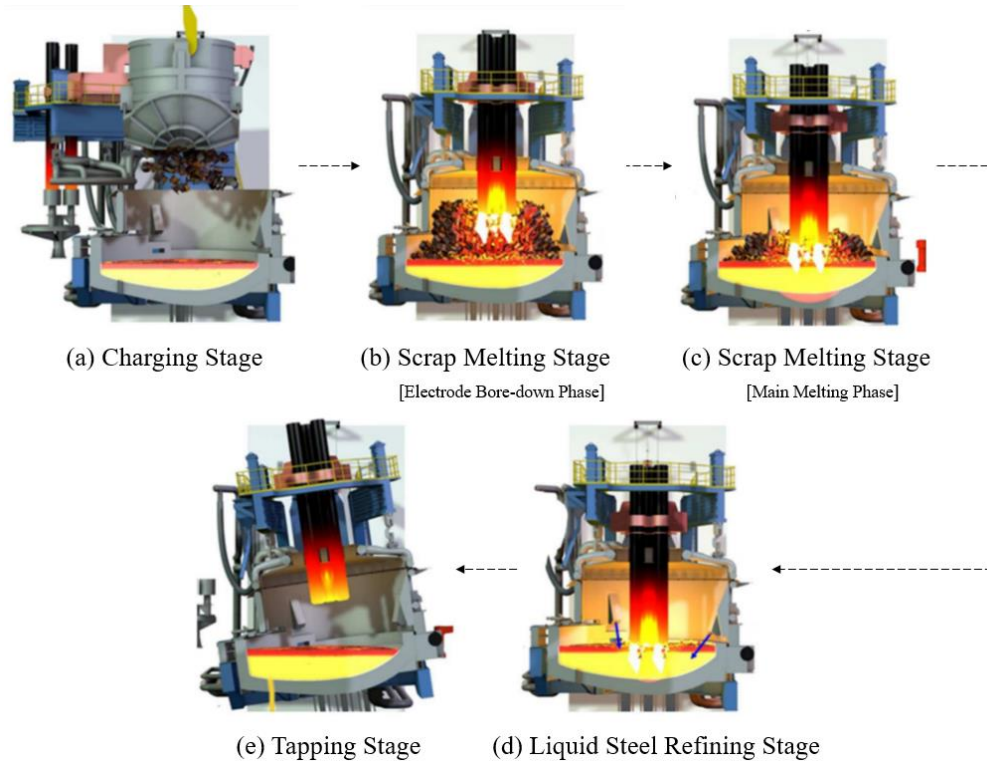


Figure 1.4. Typical EAF steelmaking process [6].

In general, the EAF steelmaking process is a complex, high-temperature physicochemical process in which gas, solid, liquid, and arc plasma coexist, and momentum, mass, and heat transfer are coupled. Considering that the facility is large in scale and high cost during operation, it is difficult for researchers to obtain the necessary data during furnace operation through traditional routine experiments and actual measurement methods, for optimization purposes. Since the end of the

1960s, researchers have attempted to conduct studies by using numerical simulation methods to solve conservation equations, which is known as the CFD model. However, solving the conservation equations was a tough problem subject to the development of computer technology at that time. Since the 1980s, the rapid development of high-performance computing (HPC) has driven the evolution of CFD, which makes solving complex conservation equations not only possible but efficient. Using the CFD models to analyze and study the physical process in the EAF has gradually become an economic and efficient approach, which has prominent advantages in terms of large parameter variation and low cost compared with traditional research methods. The rational CFD model serves as an abstraction of objective process science and provides a way to understand, analyze, and improve complex physical processes inside the EAF. In addition, the CFD model has the ability to predict detailed local phenomena and visualize the different physical quantities in the furnace, which is an advantage that traditional methods do not have. Therefore, the CFD model can be applied to investigations including the scrap cave-in, the liquid permeability/re-solidification, the arc reflection, the impact of the stacking of different scrap layers on melting, the bath temperature and substance distribution, etc., which are of widespread attention in the steel industry nowadays.

In summary, exploring the EAF steelmaking processes using CFD has become one of the research hotspots worldwide. Considering the specificity of EAF in the steel industry, the EAF CFD model is highly valuable in providing insights into the EAF physical processes and improving furnace efficiency.

## **1.2 Literature Review**

Due to the complexity of the entire EAF steelmaking process, the relevant CFD modeling and investigations of the whole process have not been systematically reported so far. Simulations of the entire EAF steelmaking process in the literature mainly relied on the semi-empirical models or the dynamic process models.

The semi-empirical model is based on a statistical analysis of the data from the macroscopic process. The black-box model dependent on the neural network is one of the common semi-empirical models. Although the black-box model cannot reflect the nature of the metallurgical

process, it avoids the obstacle of insufficient understanding of the process and is easy to be implemented, which makes the model be successfully applied in the industry [7-9]. However, the semi-empirical model has poor generality and requires large amounts of production data for parameter correction, thus it is only appropriate for predicting results within a specific operating range.

The dynamic process model predicts the entire EAF steelmaking process based on the overall mass and energy balance of the furnace. Therefore, the dynamic process model can establish general physical relationships between different physical phenomena through their natural mechanisms, which improves its flexibility and adaptability for the application. Researchers including Cameron et al. [10], Bekker et al. [11], Morales et al. [12], have made efforts on developing the dynamic process model based on the heat and mass balance between substances in the system. Their models are intended to predict the process in time but without taking them into account in space (zero-dimensional). The model normally incorporates different equilibrium zones (solid, liquid, off-gas, slag, walls, roof, etc.) to store their corresponding amounts of heat or mass. Any two equilibrium zones have an interface that allows heat or mass exchange in between. More detailed physical phenomena can be added into different zones based on the demands by solving more ordinary differential equations. In the proposed models, the total electrical energy input through electrodes and chemical energy input through burners needs to be predefined. The scrap temperature and its melting rate, which controls the mass/heat transfer from the solid zone to the liquid zone, can be estimated by the energy supply to the solid zone. Based on the prior works, MacRosty et al. [13] and Logar et al. [14] enhanced the model to enable the consideration of the electrode regulation and also provided a more precise approximation for arc radiative transfer of the heat to the furnace roof and walls based on a simplified estimation on view factor. Opitz et al. [15-16] further adopted the spatial discretization for the solid zone (24 volume elements in total) to give a more accurate prediction of the electrode descent through the scrap pile to improve the calculation of the view factor in radiation.

Although the dynamic process model involves some physical relationships, it highly relies on some empirical formulas and is still over-simplified without spatial discretization. Therefore, the model lacks generality and physical details, which may lead to inaccurate predictions of some quantities.

To this fact, the CFD model is the optimal alternative to perform the systematical simulations and investigations of the entire EAF steelmaking process. However, due to the complexity of multi-physics during the process, the bulk of CFD-related research in the literature only stays in the phase of model establishment focusing on one or two specific physical phenomena instead of the whole process [6,17], and some key phenomena are still without appropriate CFD models to simulate. Therefore, the existing CFD models cannot be used to evaluate the overall furnace performance and the entire process efficiency.

The following sections review the reported CFD models/simulations according to different main physical phenomena in the EAF to outline the current state of the art. It is noted that some non-CFD-related numerical methods/models are also included in some topics for better readability and reference if they are widely adopted in the field.

### **1.2.1 Scrap Heating and Melting**

The primary use of EAF is to heat and melt solid scrap, in which the simulation of the scrap melting process is the key as well as the most difficult aspect of establishing a comprehensive EAF CFD model. The scrap melting process in EAF can be categorized into direct melting and indirect melting. Direct melting mainly refers to the melting of direct-contacted objects by heat sources such as electric arc and combustion flame, whereas indirect melting refers to melting the solid scrap using overheated molten steel based on its convective or conductive heat transfer. The latter can be essentially understood as the energy migration between different states within the same substance.

Before the melting happens, the scrap undergoes the heating process first. Mandal et al. [18] developed a CFD model to simulate scrap heating using the propane-oxygen combustion flame and validated the model by comparing the measured temperature from the experiments with their simulation results. The model treated the scrap pile as a porous medium and the gas flow inside the pores of the scrap pile was simulated as the non-Darcian flow. The scrap heating simulation was accomplished by applying the appropriate heat transfer coefficient between the hot gas and the scrap phase. Their work only explored the scrap heating by a laboratory-scale traditional burner and did not include the combustion flame simulation and the melting simulation. Giavani et al. [19]

simulated the scrap heating in the Consteel process, that is the scrap heating process outside the EAF. The scrap pile was considered as a groove-shaped computational domain to physically represent the scrap porosity. The desired porosity can be obtained by adjusting the groove distance. The simulation included the natural gas combustion and its heat transfer to the scrap pile and the melting phenomenon was ignored.

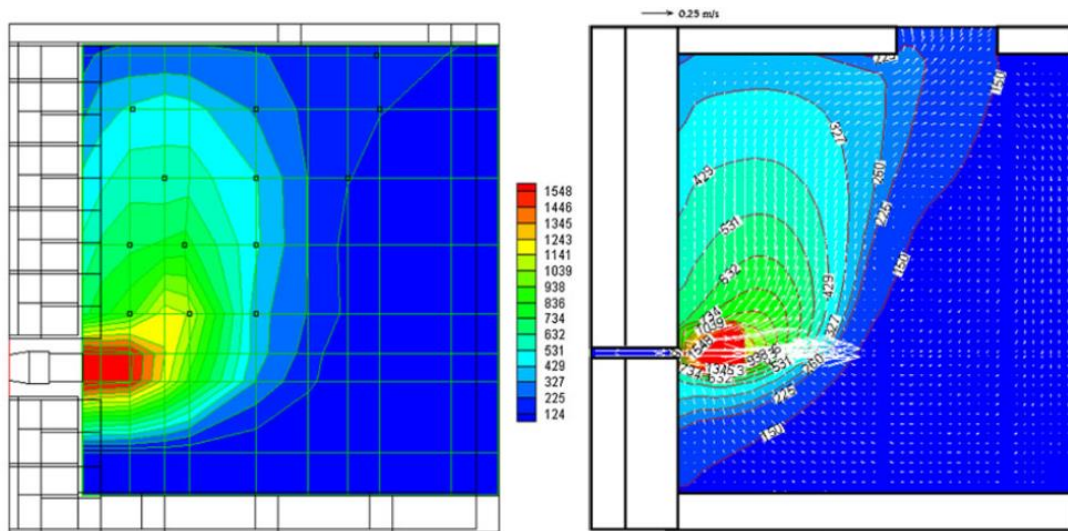


Figure 1.5. CFD modeling of the scrap preheating [18].

Among the melting simulations, the most commonly-used numerical method in CFD is the volume-averaged enthalpy-porosity method. This method was first proposed by Voller et al. [20-21], which treated the solid phase, the liquid phase, and the mushy zone as a unitary phase and adopted the liquid volume fraction to distinguish the state of each other. When the liquid volume fraction in the computational cell equals 0, the cell has the solid phase inside. On the contrary, the computational cell is regarded as containing the liquid phase when its liquid volume fraction is 1. When the liquid volume fraction is between 0 and 1, the computational cell belongs to the mushy zone, which is treated as a porous medium, and its corresponding liquid phase volume fraction is equivalent to the porosity. By adding an appropriate source term to the momentum equation to deal with the additional pressure drop due to the presence of solid materials, the suppression of the solid velocity can be achieved in the method.

The application of the volume-averaged enthalpy-porosity method in the direct melting simulation is commonly found in fields including welding, phase change heat storage, slag re-melting, and others. Among these applications, the solid materials to be melted are usually non-porous or with low porosity. Yan et al. [22] and Li et al. [23] simulated the evolution of the keyhole on the metal plate during the welding process and analyzed the energy diffusion behavior inside. Yadav et al. [24] and Saraswat et al. [25] simulated the transient melting behavior of industrial-grade paraffin as a phase change material, and explored and evaluated its energy storage capacity during the melting process. Karalis et al. [26-27] simulated the slag re-melting process in EAF and further analyzed the electrode shape, immersion depth, and Joule heating effect on its re-melting performance. Carmona et al. [28] simulated the solid aluminum heating process in a crucible by the heat from a plasma torch, and also predicted its total melting time. It should be emphasized that, for the high-porosity material melting like the scrap melting in the EAF, the volume-averaged enthalpy-porosity method cannot characterize the material's porosity through its solid volume fraction, meanwhile, the liquid flow through the porous scrap pile cannot be simulated by this method, thus this method is not suitable for simulating the direct scrap melting by the electric arc or the combustion flame in EAF, and the corresponding CFD method for this phenomenon has not been reported yet.

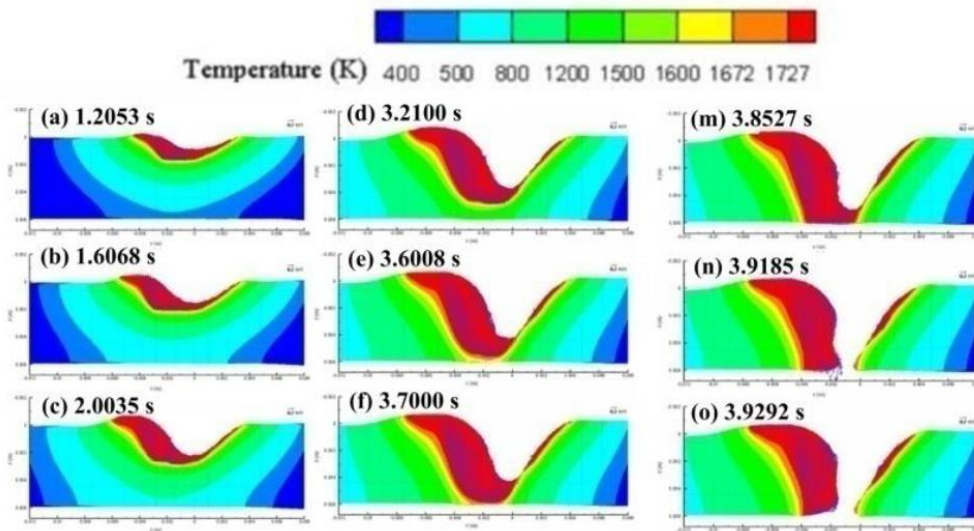


Figure 1.6. CFD modeling of the evolution of keyhole melting on the metal plate [23].

The application of the volume-averaged enthalpy-porosity method in the indirect melting simulation mainly focused on the in-bath solid steel bulk melting simulation, in which the solid steel bulk also refers to the material with zero porosity. Arzpeyma et al. [29] simulated the melting process of a single piece of solid steel bulk immersed in the molten bath under consideration of electromagnetic stirring, and explored the influence of scrap size, preheating temperature, and electromagnetic stirring direction and magnitude on the scrap melting rate. Xi et al. [30-31] used this method to simulate the melting process of both single steel rod and multiple steel rods in liquid steel and explored the influence of porosity on the melting rate by adjusting the distance between rods. It should be noted that, in the non-CFD field, Li et al. [32-35] also developed a numerical model based on the phase field method, which was also applicable to the melting simulation of single steel rod and multiple steel rods in liquid steel.

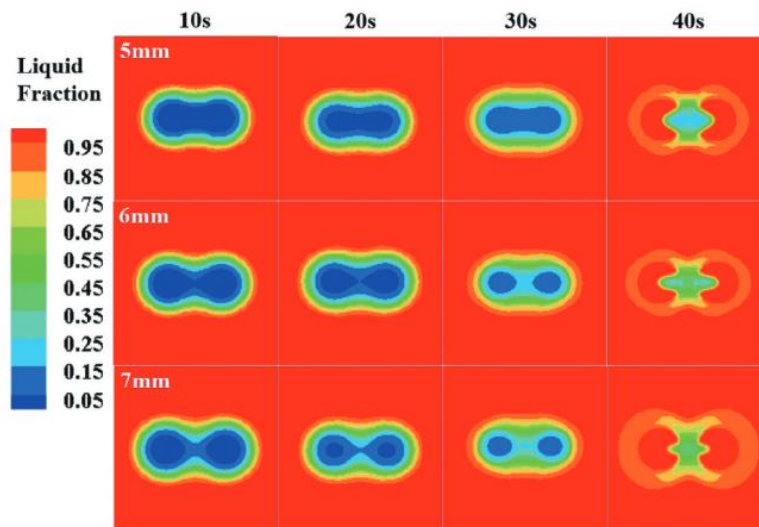


Figure 1.7. CFD modeling of the melting process of two steel rods in liquid steel [30].

In summary, the CFD models regarding the EAF scrap heating and melting process are relatively limited. The scrap heating by the industrial coherent jet burner has not been reported so far. The common-used volume-averaged enthalpy-porosity method for the melting simulation is only suitable for materials with zero or low porosity, and there is no appropriate CFD model available so far for the EAF scrap melting simulation. In reality, the scrap melting process is even more complex: the direct scrap melting and the indirect scrap melting coexist, and the scrap pile collapse always happens together with the scrap melting, which maintains the un-melted scrap settling to

the front of burners and electrode for the consistent heating and melting. Therefore, more efforts are needed in developing a feasible scrap heating and melting model to capture all the above key features.

### **1.2.2 Electric Arc Plasma**

Electric arc plasma, the name-giving part of the EAF and the most important substance in the EAF, is usually extracted separately for detailed research. Physically, thermionic electrons excited by the voltage difference between the graphite electrode tip and the scrap surface repeatedly collide with gas molecules in their travel path and trigger the ionization of the gas, thereby producing a high-temperature electric arc plasma. The intensive electrical arc plasma is considered as the key to transforming the electrical energy into heat, accounting for 65% to 85% of the total energy input in an EAF. The heat from the arc will be dissipated mainly in the form of convection and radiation to serve the purpose of heating and melting the steel scrap mixes. The heat dissipations of each mechanism in this process are usually affected by a combination of several factors, such as operating current, arc length, and etc., and they will further determine the overall arc melting efficiency. The majority of investigations of electric arc plasma were conducted based on the MHD model and the Channel Arc Model (CAM).

The MHD model is most commonly found in studying the DC arc case. This model solves the governing equations of the flow field and Maxwell's equations in every single computational cell to predict the arc in time and space, so that detailed arc status, including density, temperature, velocity, pressure, and etc., can be obtained at all moments in the simulation. Hsu et al. [36-37] firstly modeled a laboratory-scale DC free-burning argon arc proving the feasibility to describe the arc behavior based on the MHD theory. The characteristics of the DC free-burning arc were analyzed and a related experiment was designed to measure the arc temperature distribution in the study. A good agreement was found between the measurement data and the simulation predictions. McKelliget et al. [38] developed a similar model to capture the arc status and anode surface current density distribution under different arc currents. The detailed mechanism of arc heat transfer and fluid flow behavior was also illustrated in the study. Tsai et al. [39] explored the impact of different electrode shapes on the arc electromagnetic field. The simulation results showed that the arc behavior was very sensitive to the current distribution on the electrode tip. When the electrode

cone angle was about  $60^\circ$  or less, the arc took on the bell shape as observed in the experiment. Lowke et al. [40] explored the mechanism of arc cathode region in detail and introduced a feasible way to calculate the cathode current density based on arc current instead of assigning the given current density as the boundary condition, which made the model be more universal. The study further considered and analyzed the anode evaporation phenomenon in the simulation, which was achieved by modifying the thermo-physical properties and electrical conductivity of the arc based on the amount of anode material evaporated into the plasma. Gonzalez et al. [41] used a similar method to further study this phenomenon. The results showed that the metal vapor produced was concentrated near the anode area and the edge of the arc leading to a cooling effect on these areas, while the current density in the cathode area and core area of the arc was almost not affected. Morrow et al. [42] established a unified arc-electrode system based on previous work and developed the one-dimensional theory to describe the non-thermodynamic equilibrium state near the cathode region. Freton et al. [43] and Lago et al. [44-45] both constructed three-dimensional models for the free-burning arc and explored the influence of the external magnetic field on the arc behavior. Alexis et al. [46], Wang et al. [47], and Wang et al. [48] introduced the turbulence model to arc simulations with large current, which made the simulation of DC arc in the industrial-scale EAF to be possible.

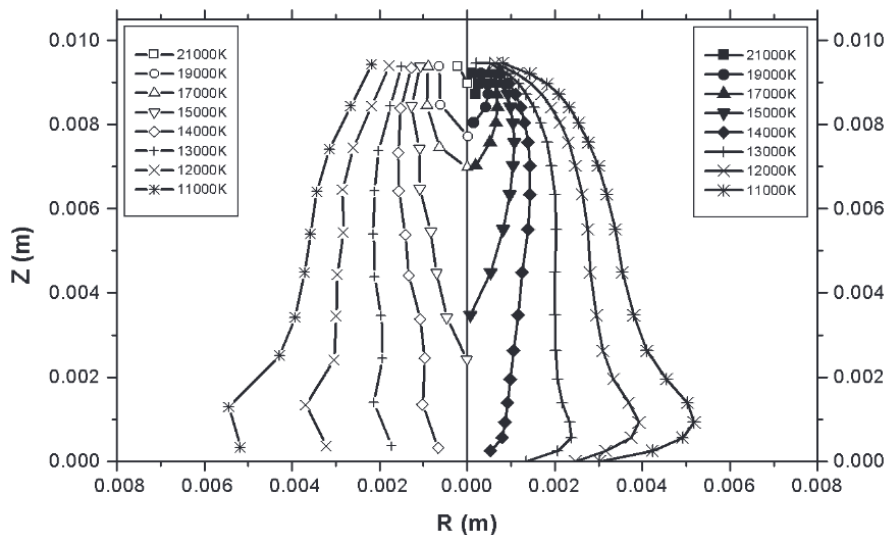


Figure 1.8. CFD modeling of the free-burning DC argon arc [44].

As for the AC arc modeling, there are relatively few reports on the applications of MHD and the start of research in this field was relatively late as well. Larsen et al. [49], Bakken et al. [50], and Saevarsdottir et al. [51] all reported one-phase AC free-burning arc simulations in a silicon metal furnace using a similar model as the DC arc simulations, which proves the feasibility to describe the AC arc behavior based on the MHD theory. The AC arc model was based on the time-dependent N-S equation and Maxwell equation, in which the electromagnetic boundary conditions of the electrode tip and the metal surface can be dynamically adjusted according to the polarity. The influence of different cathode current densities on the simulations was studied, and the results found that  $0.5e7 \text{ A/m}^2$  can make the results consistent with observations. Moghadam et al. [52] developed a similar one-phase AC arc model and introduced the current-dependent parabolic cathode current density distribution based on the industrial-scale DC arc simulation to calculate the required electromagnetic boundary conditions. Different arc currents and different arc lengths were studied to find the optimal arc operation to maximize the heat transfer from the arc to the molten bath. Daszkiewicz et al. [53] and Tarczynski et al. [54] both simulated a three-dimensional AC arc with two electrodes to investigate the discharge channel displacement. The results were compared with the images recorded with a high-speed digital camera, which showed a good agreement. Rehmet et al. [55-58] further simulated 3-phase AC arc discharge behavior in both parallel electrode configuration and coplanar electrode configuration, and also conducted the experimental validations to prove the model accuracy.

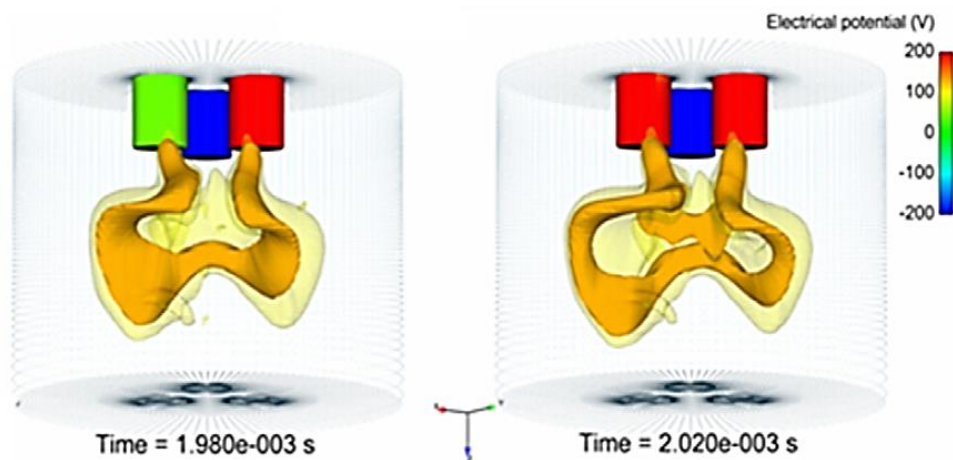


Figure 1.9. CFD modeling of the 3-phase AC arc discharge behavior [55].

In addition to the AC arc modeling based on the MHD, the CAM is another commonly-used numerical model applied in investigating the characteristics of AC arc. Although this model is not related to the CFD simulation that is focused in this section, it is still necessary to have a brief summary here considering its extensive applications in AC arc related modeling. This model approximates the arc as a cylinder fixed in time and space, and derives the AC arc state variables from the steady-state energy-balanced DC arc by introducing the arc mass/energy variation caused by the current change. Both Saevarsdottir et al. [51] and Sanchez et al. [59] adopted this model to obtain the share of different heat dissipation mechanisms, and Sanchez et al. also analyzed the cases at different gas atmospheres and made a comparison. Although CAM can deliver extensive information, the share for radiative heat dissipation of AC arc in the air predicted by this model is about 24% which is much lower than the most values reported in research [13,14,60]. To improve accuracy and reduce the numerical computation in CAM, Fathi el al. [61] further introduced the average arc temperature and average arc pressure obtained from MHD-based simulations to refine the arc state variables in approximating heat dissipation. However, for different arc operating currents and arc lengths, the average arc temperature and pressure were all fixed at 16,136 K and 1,200 kPa respectively in all estimations, which may be unrealistic.

### **1.2.3 Injector/Burner System**

The burner used in the modern EAF is the coherent jet burner, which is a crucial facility in the EAF steelmaking process. The burner system is responsible for heating and melting the solid scrap in the cold spots of the furnace by the combustion flame, meanwhile, it is also responsible for stirring the molten bath and delivering oxygen and fluxes to the molten bath to reduce the carbon content and impurities during the liquid steel refining stage. Therefore, the burner system usually has both a burner mode and a lance mode for the furnace operators to switch between different scenarios.

In contrast to the traditional burner, the coherent jet burner is composed of the primary oxygen nozzle, the fuel nozzle, and the secondary oxygen nozzle. Three types of nozzles are arranged alternately in the radial direction. The primary oxygen nozzle is located in the center of the burner and is surrounded by a circle of fuel nozzles, which is further encircled by a circle of secondary oxygen nozzles. The burner mode is mainly adopted in the scrap preheating and melting stage with

the maximum burner power up to around 5 MW. Under this mode, the flow rate of the primary oxygen nozzle is reduced to around 300 SCFM so that the central oxygen jet is routinely to be in subsonic or sonic status. Instead, the corresponding flow rates through the fuel nozzles and the secondary oxygen nozzles are significantly elevated to be around 300 SCFM, which creates a larger flame and increases the burner power. The lance mode is mostly used in the liquid steel refining. Under the lance mode, the primary oxygen nozzle with a high flow rate (around 1200 SCFM) produces the supersonic oxygen jet, while the corresponding flow rates of the fuel nozzle and the secondary oxygen nozzle are relatively low (around 80 SCFM), only to generate the shrouding combustion flame envelop to protect the central supersonic oxygen jet and slow the momentum decay in its traveling path. This technology was introduced by Praxair in the 1970s [62-64] and can greatly increase the potential core length of the supersonic oxygen jet. Anderson et al. [65] proved through experiments that the jet potential core length under ideal conditions can reach up to 50 De (De is the diameter of Laval nozzle exit), which is 2 to 3 times longer than that of the conventional supersonic jet without the shrouding flame. The longer potential core length ensures that the jet reaching the bath surface has a higher speed to fully stir the molten bath, meanwhile ensures that a sufficient amount of oxygen is delivered to the bath during the liquid steel refining stage to improve the efficiency of decarburization and impurity removal. In addition, the burner can also be installed at a higher position from the bath surface without reducing the burner performance, which can reduce the burner erosion due to the liquid splashing and increase the lifetime of the burner.

At present, the CFD research on the coherent jet burner system mainly focuses on the lance mode, which includes both supersonic compressible flow and combustion flame. This model can also be backward compatible to simulate the burner mode, which is a simpler scenario. Based on previous studies on the supersonic jet [66-67], Jeong et al. [68] firstly proposed a CFD model with the standard k-epsilon turbulent model to simulate the supersonic coherent jet, and observed that the jet potential core length was 1.8 times longer than the conventional supersonic jet. Alam et al. [69-70] further proposed an enhanced CFD model that modified the turbulent viscosity to make it sensitive to the gradient of the total temperature field, thereby achieving the consideration of the impact from the shrouding flame on the central supersonic oxygen jet behavior. The simulated jet potential core length was compared with that measured by Anderson et al. in the experiment, and

a good agreement was found. Wei et al. [71-73] developed a similar model and further refined the combustion reaction mechanism of methane and oxygen to obtain more accurate simulation results. The application of CO<sub>2</sub> and O<sub>2</sub> mixed injection in the supersonic coherent jet was also explored. Liu et al. [74-75] evaluated the supersonic coherent jet performance at different ambient temperatures and different preheated oxygen temperatures. The study showed that the jet potential core length can be extended with higher ambient temperature, thereby improving the jet's ability of oxygen delivery and bath stirring. Tang et al. [76-78] introduced a modified Weighted-Sum-of-Gray Gases Model (WSGGM) on the basis of the above CFD model to refine the consideration of radiative heat transfer in the simulation. The possibility of replacing CH<sub>4</sub> with blast furnace gas (BFG) and coke oven gas (COF) was evaluated, and their corresponding economic benefits were also analyzed.

Although the simulation of the coherent jet itself is well-explored by many researchers, the reports regarding the coupling/integration of the coherent jet simulation into the scrap melting simulation or the liquid steel refining simulation are still very limited, which needs more efforts when developing the comprehensive EAF CFD model.

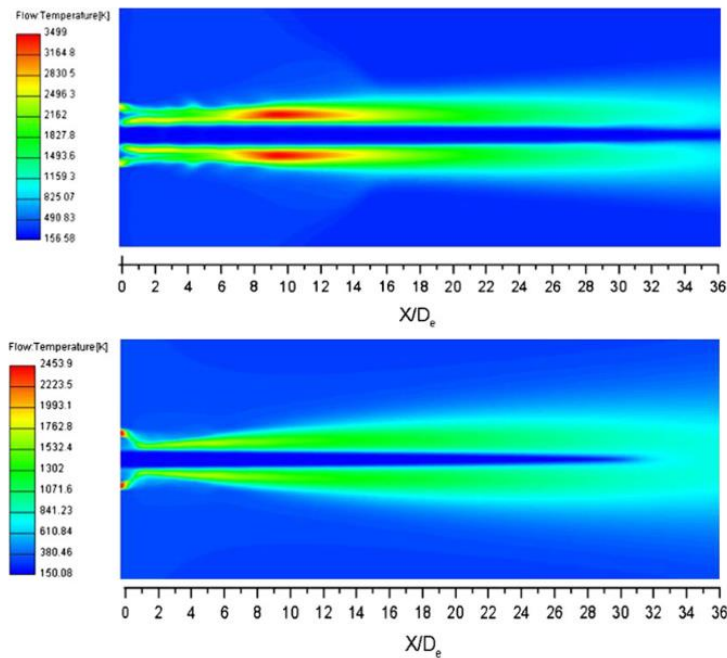


Figure 1.10. CFD modeling of the supersonic coherent jet in the open air [69].

### 1.2.4 Liquid Steel Refining

The liquid steel refining process in EAF is undertaken with the aim to remove phosphorus, sulfur, aluminum, silicon, manganese, and carbon by injecting oxygen and fluxes into the liquid steel after the scrap pile is melted into the flat bath. The oxygen injection is achieved by the supersonic coherent jet generated by the burner system. The supersonic oxygen jet shrouded by the combustion flame can penetrate the slag layer and reach the liquid steel bath at a high initial velocity, which can tear a jet cavity on the bath surface and sufficiently stir the liquid steel. The dissolved oxygen oxidizes with different elements around the region of the jet cavity to produce different oxides. Among them, metal elements including Al, Si, and Mn are easily reacted with oxygen to form metal oxides, which further float to the top surface of the bath to form the slag. These metal elements also react with FeO or C, in which the former reduces Fe yielding it back to the molten bath. It can be seen that the refining process not only involves the impingement, stirring, and oxygen delivery of the supersonic coherent jet to the bath but also involves a variety of bath chemical reactions and exothermic phenomena. At present, no CFD models capable of simulating the above-mentioned complete process have been reported. Therefore, the existing literature will be reviewed from the two perspectives including the interactions between the supersonic coherent jet and bath, and the chemical reactions in the bath.

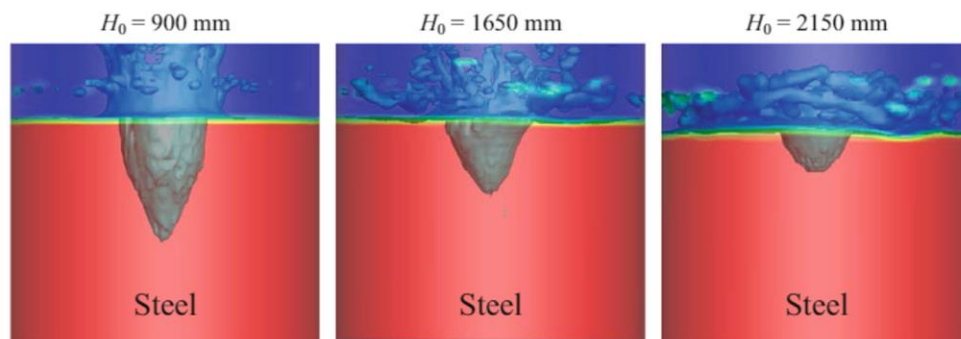


Figure 1.11. CFD modeling of the supersonic coherent jet penetration in liquid steel [85].

Most CFD simulations in the literature focused on using conventional subsonic or supersonic jets to investigate the jet-bath interaction. Research including Nakazono et al. [80], Odenthalet et al. [81], Ersson et al. [82], Muñoz-Esparza et al. [83], Alam et al. [84], and etc. have all made attempts to utilize the VOF model to analyze the deformation of the gas-liquid interface, and evaluate the

diameter of jet cavity and the penetration depth. The corresponding mechanism has been systematically summarized in the above literature. However, there are only a few reported CFD simulations using the supersonic coherent jet to investigate the jet-bath interaction. Wei et al. [85-87] was the only group conducting the relevant research at present. Since the simulation of this process includes but is not limited to combustion flame, supersonic compressible flow, and gas-liquid interaction, a hybrid model was developed which integrates a CFD model and a theoretical model together to evaluate the interaction. The CFD model was to simulate a supersonic coherent jet in an open environment similar to the works stated in section 1.2.3. The user-defined function (UDF) was then adopted to extract four important parameters ( $k_d, v_e, \rho_e, \rho_x$ ) from the simulation results to input into the theoretical model. The theoretical model was a mathematical model based on the conservation of momentum and energy, which can eventually calculate the volume of the jet cavity on the bath and its penetration depth. The hybrid model avoids the direct simulation of the supersonic coherent jet and its interaction with bath providing a feasible methodology in the research field.

There were no reports on the CFD research related to the bath chemical reaction in the EAF liquid steel refining stage. In the non-CFD field, only a few articles introduced different mathematical models to simulate the refining decarburization process. Oltmann et al. [88] established a simple decarburization reaction model, which considered the C-O<sub>2</sub> reaction and the C-FeO reaction. The results can reflect the dynamic changes in the carbon content in the molten bath under different oxygen injection rates, different initial carbon contents, and different carbon injection rates. Matsuura et al. [89] established a decarburization and slag foaming model based on the conservation of mass and further included the Fe-O reaction in the model to refine the reaction mechanism. Memoli et al. [90] estimated the amount of oxygen delivery to the bath based on the developed jet cavity model, and on this basis, the oxidation reaction of C, Si, and Al was considered in their refining model. To sum up, the CFD-related research on liquid steel refining is extremely limited due to many numerical constraints in the simulations of such a complex process. More efforts are still needed to develop an appropriate methodology to achieve the fully coupled or integrated modeling of the process.

### 1.2.5 Heat Transfer and Post-combustion in Freeboard

The freeboard in EAF refers to the gas phase located above the scrap pile or liquid bath surface. The freeboard is usually separated for the individual study to simplify the model since this region only contains the gas phase. The combustion flame created by the burner system is submerged in the scrap pile at the start of the melting phase and is not directly exposed to the freeboard, whereas the arc is only exposed to the freeboard for a very short amount of time after ignition and is likewise submerged in the scrap pile thereafter to melt the scrap. As the scrap pile gradually collapses downwards in the later melting stage, the combustion flames and arcs are exposed to the freeboard again, creating intense convection and radiation heat transfer inside the region. During the refining stage, the slag progressively covers the arc while the top part of the combustion flame shrouding the supersonic oxygen jet remains exposed to the freeboard. Because slag foaming creates a substantial quantity of CO, and the oil, grease, and other combustible materials on the surface of the scrap pieces create H<sub>2</sub> which gets into the freeboard as the melting advances, the primary gas compositions in the freeboard during the refining are CO and H<sub>2</sub>. Post-combustion is to utilize the oxygen to completely burn CO and H<sub>2</sub> to recover heat in the freeboard so that the goals of saving energy and reducing emissions can be achieved. At present, CFD-related research for the freeboard is mainly focused on the liquid steel refining stage.

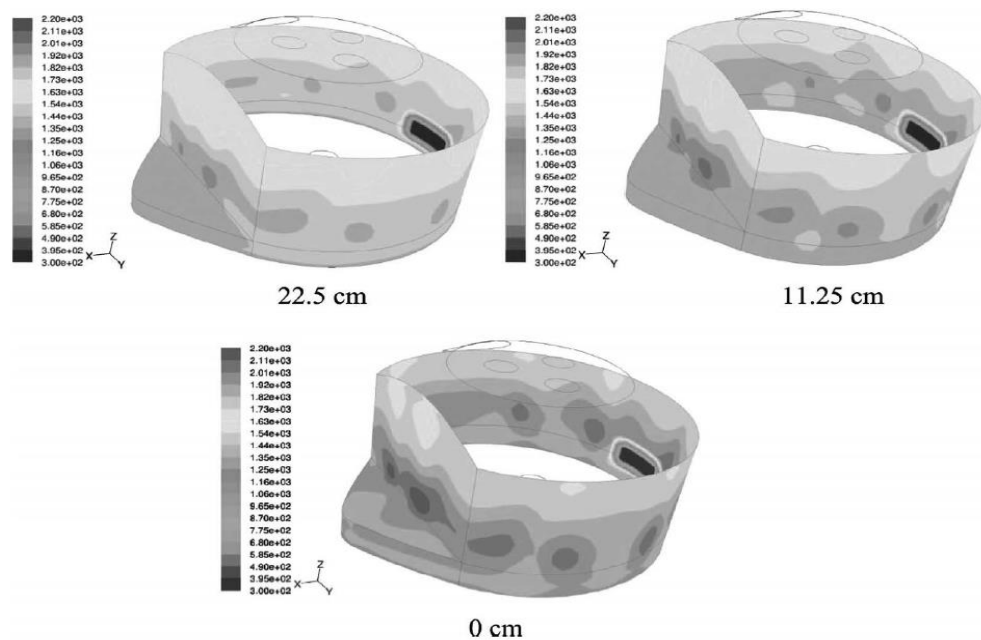


Figure 1.12. CFD modeling of the arc radiation in the freeboard under different slag heights [94].

Guo et al. [79] proposed a CFD model to study the radiative heat transfer in the freeboard. The model did not include the combustion flame and the post-combustion of CO and H<sub>2</sub>, but instead focused on the radiation distribution due to arc exposure. The arc was represented by a cylinder and an appropriate heat flux was applied to the cylinder wall to assign the arc power input. The results showed that the furnace wall temperature can reach up to 1673 K when the arc length was 0.152 m. Li et al. [91] developed a CFD model to study the fluid flow and the post-combustion in the freeboard. Unlike Guo's model, the arc was assumed to be covered by slag, thus the arc region was not included in the computational domain. The CO generated during the refining process was assumed to uniformly enter from the bottom surface of the freeboard region (the top surface of the slag layer) at a fixed mass flow rate to react with oxygen. The injector/burner was simplified as a hole on the wall of the computational domain, and the conventional oxygen injection was considered. Chan et al. [92] had a similar case setup but further adopted both the eddy-dissipation concept and finite reaction rates for combustion kinetics to estimate the post-combustion in the freeboard. Four-step reduced reactions were used to simulate the combustion of CH<sub>4</sub> and CO. The main mechanism of NO<sub>x</sub> formation was studied. Al-Harbi et al. [93]'s freeboard simulation also did not include the arc region but considered the supersonic oxygen jet instead to explore its impact on the refractory lifetime in the Delta zone. The model added a layer of porous medium to represent the slag, and improves the emission distribution of CO to the freeboard based on the position of oxygen injection. Sanchez et al. [94]'s simulation was similar to Guo's. The gas injection and post-combustion were not included in the model. The arc was also represented by a cylinder to study the radiative heat transfer in the freeboard. The influence of different slag heights on the furnace wall temperature was explored. The results showed that the more the arc was exposed, the easier it was to generate hot spots on the furnace wall and damage the water-cooling system. Yigit et al. [95] developed a model that can be used to simulate the coal particle combustion in the freeboard. The model considered the coal particle injection from the burner system and the radiation from the electrode. The bottom surface of the computational domain (top slag surface) was treated as a wall surface. The results analyzed the particle combustion in the freeboard and predicted the temperature distribution on the slag surface. To sum up, different researches above have their own focus but all reported freeboard CFD models were still unable to consider the full phenomena including the arc radiation, the combustion and gas flow generated by supersonic coherent jet, the appropriate CO emission from slag layer, the post-combustion of CO and H<sub>2</sub>, and etc. To

accurately simulate the real operating conditions in the freeboard, the inclusion of the above phenomena in the model is necessary in the author's opinion.

### **1.3 Motivations for Research**

The EAF steelmaking process involves dynamic complex multi-physics, in which electric arc plasma and coherent jets coexist resulting in an environment with local high temperature and velocity. Different heat transfer mechanisms are closely coupled and the phase change caused by melting and re-solidification is accompanied by in-bath chemical reactions and freeboard post-combustion, which further creates a complicated gas-liquid-solid three-phase system in the furnace. Therefore, not all conditions and phenomena within the EAF are well-understood. The traditional experimental approach to study the EAF is expensive, dangerous, and labor-intensive. Most of the time, direct measurements and observations are impossible due to the high temperature within the furnace. Therefore, the EAF CFD modeling is of great significance in the steel industry.

However, the CFD simulation of the entire EAF steelmaking remains at a preliminary stage according to the literature review, that is, the modeling of some specific physics instead of the whole process. Additionally, some appropriate CFD models have yet to be developed for some key phenomena, which significantly restricts the possibility of extending the CFD simulation to the entire steelmaking process to evaluate the overall furnace performance and process efficiency. Moreover, most of the reported modeling in the literature normally relies on different fundamental assumptions or CFD approaches, thus the direct coupling of the existing models for the multi-physics simulation is infeasible or very computational-intensive. Good modeling methodologies are in demand to ensure that the coupled/integrated models can accurately capture local detailed phenomena and have high computational efficiency.

From the perspective of delivered results, the traditional semi-empirical or dynamic process model only reveals the variations of the overall physical quantities over time and lacks the capability of characterizing the inherent mechanisms involving spatial distribution, whereas the CFD model is established based on the physical principles and overcomes the above pain points, which is capable of predicting and visualizing the important phenomena, including but not limited to scrap collapse, arc reflection, bath homogeneity, and etc. Therefore, the development of complete CFD solutions

has attracted considerable interest in the corresponding fields recently due to the accelerated migration to EAF steelmaking in the steel industry. With it, the exploration of more physical quantities in the entire EAF steelmaking process becomes possible, which helps build a fundamental understanding of the process and provides relevant information for subsequent optimization of the process efficiency.

#### 1.4 Research Objectives

The present dissertation follows the path of the development-validation-application to carry out the research work. The main research tasks are as follows:

- 1) To design modeling methodologies to guide the comprehensive EAF CFD model establishments for both lab-scale DC EAF and industry-scale AC EAF.
- 2) To develop corresponding models according to the proposed methodologies for simulating the entire EAF steelmaking process.
- 3) To validate the above models against available data, and design and implement the experiments to collect the desired data if necessary.
- 4) To utilize the comprehensive EAF CFD models to gain insight into the characteristics of the EAF steelmaking process and help the industry to improve furnace design, perform troubleshooting, and optimize process efficiency.

#### 1.5 Organization

The dissertation contains two comprehensive EAF CFD models for simulating the lab-scale DC EAF (illustrated in **Chapter 2**) and the industry-scale AC EAF (illustrated in **Chapter 3**). Each comprehensive EAF CFD model consists of several models. Six simulators are also developed for the comprehensive EAF CFD model for the industry-scale AC EAF to achieve the sub-process simulation, and those simulators partially integrate the specific models above whose details will be demonstrated in the later sections. **Figure 1.13** shows the structure of the dissertation outlined under three main terminologies (comprehensive EAF CFD model, model, and simulator):

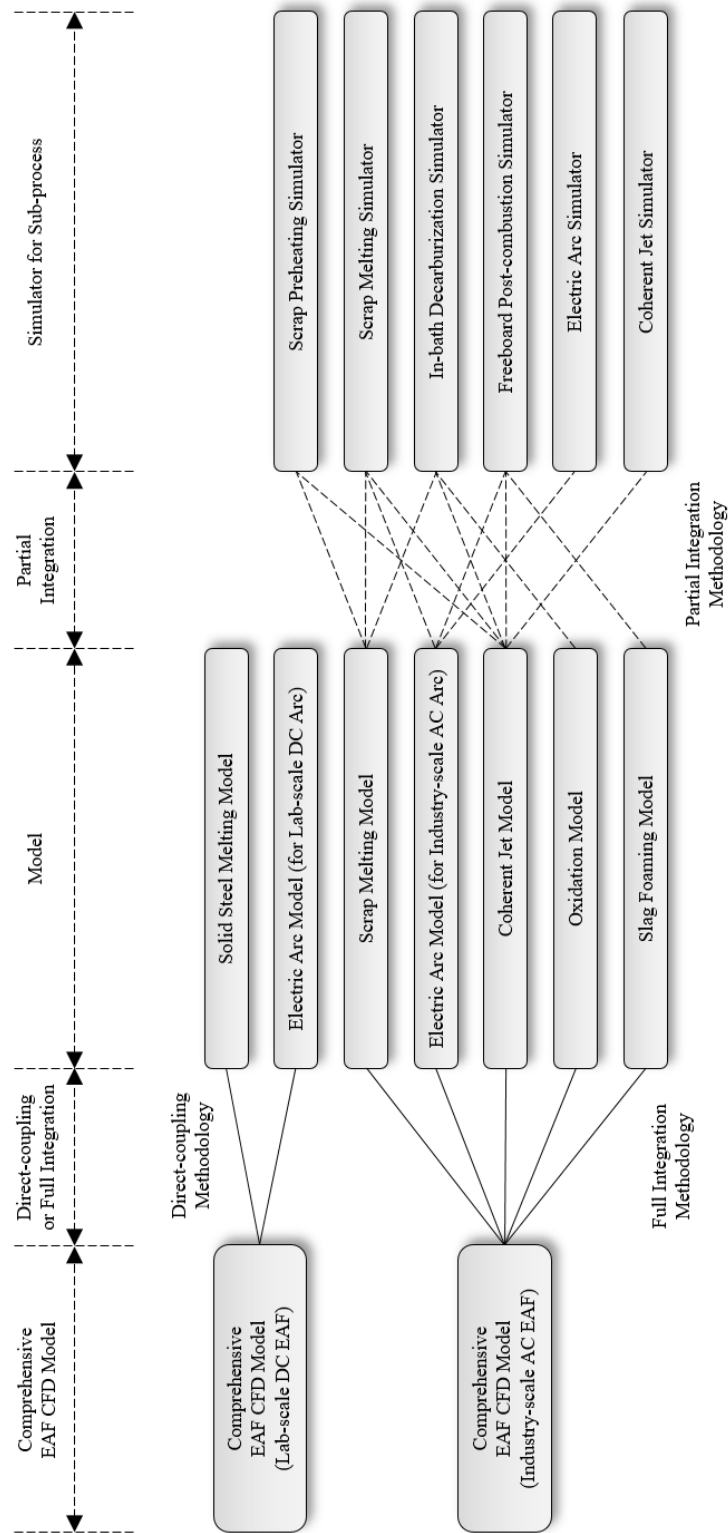


Figure 1.13. Dissertation structure outlined under three main terminologies (comprehensive EAF CFD model, model, and simulator).

## 2. MODELING OF LAB-SCALE DC EAF

The main purpose of this chapter is to establish a self-consistent comprehensive EAF CFD model together with a direct-coupling methodology to simulate the entire steelmaking process in the lab-scale DC EAF, that is, the process of solid steel ingot melting by the lab-scale DC arc. Two models were developed including the solid steel melting model based on the enthalpy-porosity method and the electric arc model (for lab-scale DC arc) based on the MHD theory. The stationary lab-scale DC electric arc and the arc-solid steel interaction modeling were validated respectively against the experimental data in the literature to prove the simulation accuracy. The lab-scale DC electric arc behavioral characteristics were investigated under varying arc lengths generated by the moving electrode. The comprehensive EAF CFD model was utilized to dynamically predict the entire steel ingot melting by arc, which includes the continuous phase changing of solid steel, the surface deformation of steel ingot, and the close interaction between phases. Further attempts were made to evaluate the effects of the initial arc length on the melting efficiency and tried to provide useful guidance for industrial manufacturing. In particular, the comprehensive EAF CFD model was also implemented to simulate the steel ingot melting with the dynamic electrode movement and made the corresponding comparison to the case without the electrode movement. The comprehensive EAF CFD model in this chapter helps to understand the fundamental mechanism of arc melting, greatly benefiting the future investigations for the industry-scale EAF.

### 2.1 Problem Description

The lab-scale DC EAF only involves the solid steel ingot melting by a single electrode, which is shown in **Figure 2.1**. The electrode is inserted from the top of the apparatus to generate a DC electric arc at the electrode tip, melting the steel ingot from top to bottom. The molten liquid steel will flow down the surface of the steel ingot and accumulate at the bottom of the furnace. The apparatus is allowed to connect with the outside atmosphere, and the working gas can be supplemented or escaped through the electrode hole on the top of the apparatus. There is a heat insulation layer around the furnace to prevent heat loss and enhance the melting efficiency. Both the furnace and the steel ingot are cylindrical, and the diameter ( $W$ ) and height ( $H$ ) of the inner furnace are 0.04 m and 0.03 m, respectively, while the diameter ( $w$ ) and height ( $h$ ) of the steel

ingot are 0.02 m and 0.015 m, respectively. The electrode with a diameter ( $d$ ) of 0.00454 m can move up and down on its axis as needed. The arc length ( $l$ ) is originally set to be 0.01 m.

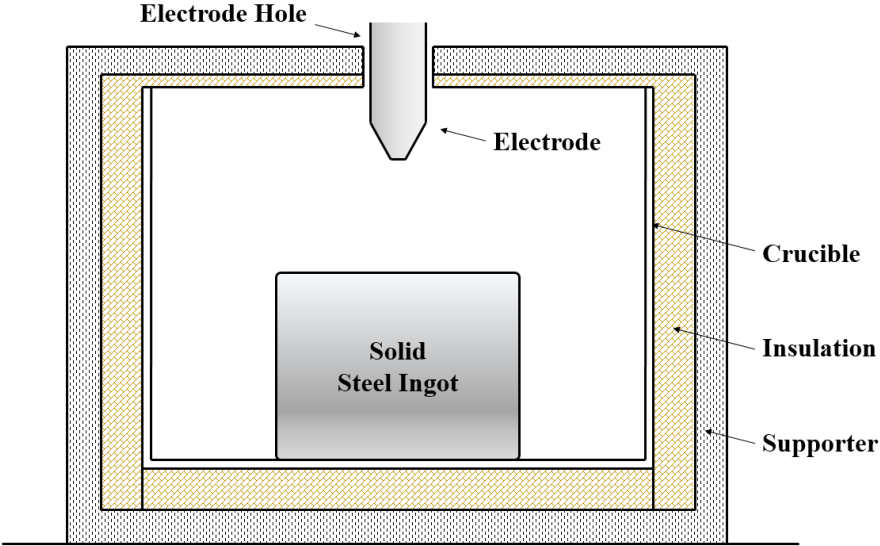


Figure 2.1. Schematic diagram of the lab-scale arc melting furnace.

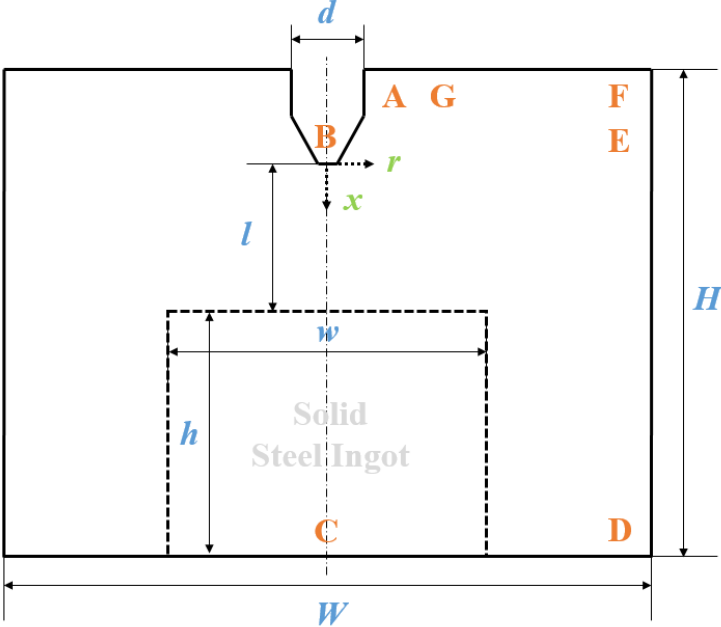


Figure 2.2. Computational domain for steel ingot melting by the electric arc.

**Figure 2.2** shows the simulation domain considered in the present study, which only includes the inner profile of the electrode and the furnace. Due to the axial symmetry of the current physical problem, only half of the geometry in **Figure 2.2** is adopted, and the entire simulation is solved based on the cylindrical coordinate system  $(r, x)$  whose origin is located at the center of the electrode tip. The structured mesh has been applied to the entire simulation domain, whose total cell number is 454,000 determined after the mesh sensitivity study.

## 2.2 Modeling Methodology

The main physical phenomena of the steelmaking process in the lab-scale DC EAF involve the DC electric arc plasma generation and the solid steel ingot melting. Additionally, the interactions including different heat and force exchanges will occur constantly at the interface that the plasma reaches, as shown in **Figure 2.3**. Obviously, the process does not involve the melting of any porous medium material while the electrode polarity remains consistent throughout, which largely reduces the order of physical complexity. Therefore, each of aforementioned phenomena can be captured by one CFD model, namely the solid steel melting model and the electric arc model, and the direct-coupling methodology can be adopted for two models, which relies on the dynamic interface tracking approach and the source term approach to consider the instant heat and momentum exchange at the interface.

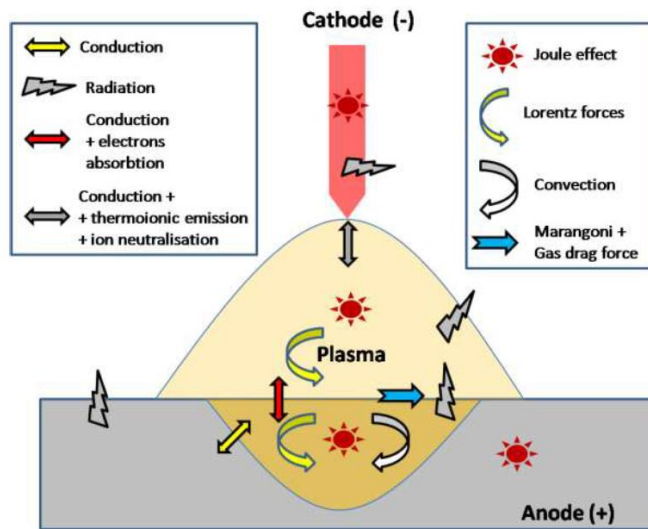


Figure 2.3. Main physical phenomena of the steelmaking process in lab-scale DC EAF.

At the beginning of each time step, the interface will be tracked first to locate the computational cells available for the dynamic heat and momentum exchanges. The electric arc model will then be solved to determine the exchange quantities at the interface, whose amounts will be assigned to the corresponding conservation equations using the source term approach to achieve the melting simulation of solid steel ingot. The detailed direct-coupling methodology is demonstrated as the flow chart in **Figure 2.4**.

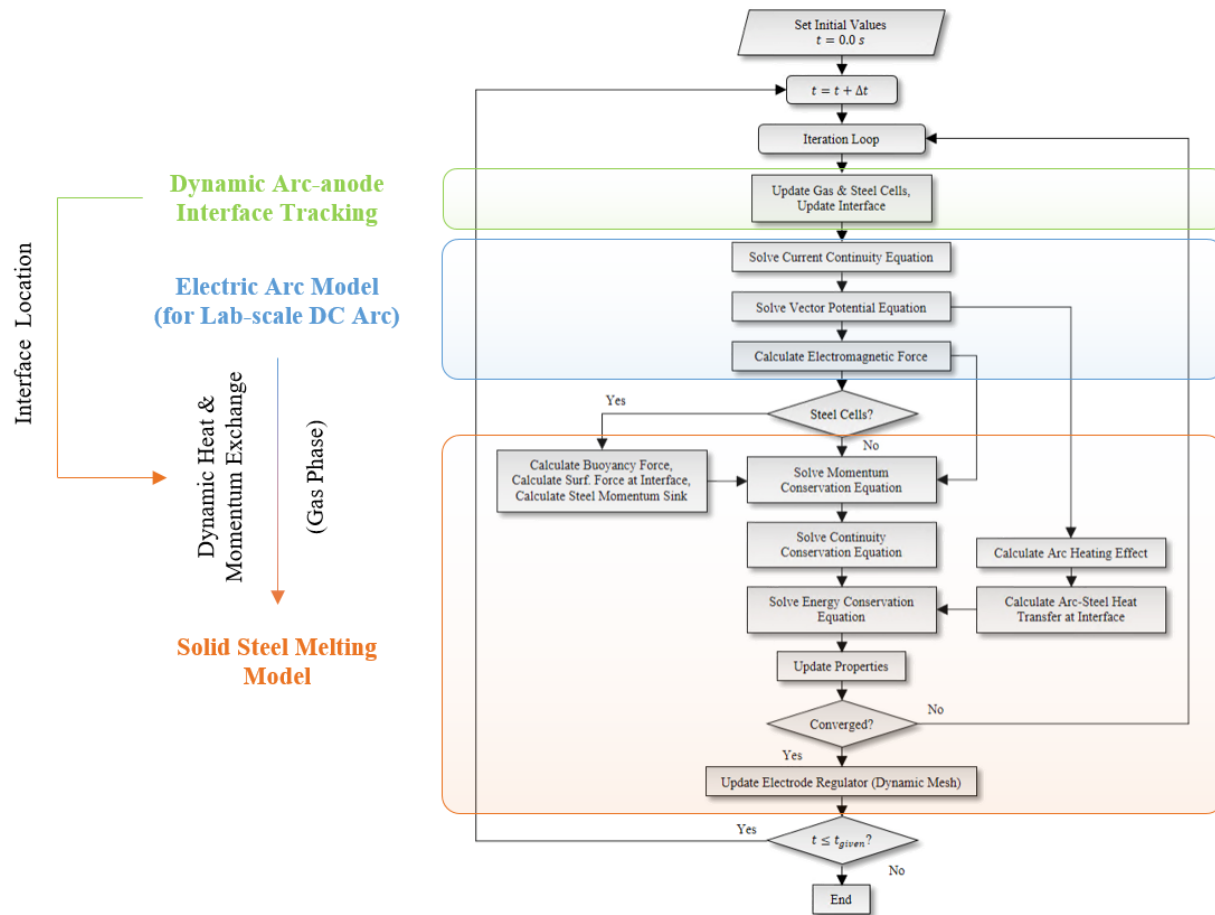


Figure 2.4. Flow chart within the direct-coupling methodology for models.

### 2.3 Model Description

In order to conduct the simulation of the lab-scale DC EAF steelmaking process with the affordable computational time and relatively good accuracy, the following hypotheses are adopted for the comprehensive EAF CFD model in the present study:

- 1) The arc is considered to be the lab-scale DC electric arc and is axisymmetric in the 2D configuration [44,96,97].
- 2) The arc is optically thin and in local thermodynamic equilibrium (LTE) meaning the temperatures of the electron and heavy particles are very close, which has been proven to be true throughout most of the arc region [44,96,98-101].
- 3) The effects of heat dissipation due to the viscosity are neglected in all phases [102].
- 4) The fluids for both the gas phase and the liquid steel phase are treated as an incompressible Newtonian fluid and the corresponding flows are assumed to be the turbulent flow solved by the standard k-epsilon model [101].
- 5) Boussinesq's hypothesis is applied for the buoyancy-driven liquid steel flow.
- 6) The steel vaporization is ignored.

### 2.3.1 Solid Steel Melting Model

The solid steel melting model simulates the gas-liquid-solid three-phase system within the lab-scale EAF. A set of governing equations utilized to describe the system including the gas phase and the steel phase (solid steel and liquid steel) is given as follows. The equation set is based on the volume-of-fluid (VOF) method, which is capable of capturing the gas-steel free surface deformation and the fluid flow during the melting. Different dynamic and thermal coefficients are applied in different phases, the equation set is solved in every computational cell of the simulation domain in order to obtain the continuous flow field variables for all phases.

The volume fraction conservation equation can be expressed as:

$$\frac{\partial(\alpha_q \rho_q)}{\partial t} + \frac{1}{r} \frac{\partial(r \alpha_q \rho_q v_{q,r})}{\partial r} + \frac{\partial(\alpha_q \rho_q v_{q,x})}{\partial x} = 0 \quad (2-1)$$

where  $\alpha_q$ ,  $\rho_q$ , and  $v_q$  are the volume fraction, the density, and the velocity vector component of phase  $q$  (gas or steel), respectively. It should be noted that the sum of the volume fractions in all phases is always unity, i.e.  $\sum_{q=1}^n \alpha_q = 1$ .

The axial and the radial momentum conservation equation are given as:

$$\begin{aligned}
& \frac{\partial(\rho v_x)}{\partial t} + \frac{1}{r} \frac{\partial(r\rho v_r v_x)}{\partial r} + \frac{\partial(\rho v_x^2)}{\partial x} \\
& = -\frac{\partial p}{\partial x} + \frac{\partial}{\partial x} \left( 2\mu \frac{\partial v_x}{\partial x} \right) + \frac{1}{r} \frac{\partial}{\partial r} \left( r\mu \left( \frac{\partial v_x}{\partial r} + \frac{\partial v_r}{\partial x} \right) \right) + \rho g + v_x R^* + S_{m,b} \quad (2-2) \\
& + S_{m,a} + S_{m,sf}
\end{aligned}$$

$$\begin{aligned}
& \frac{\partial(\rho v_r)}{\partial t} + \frac{1}{r} \frac{\partial(r\rho v_r^2)}{\partial r} + \frac{\partial(\rho v_x v_r)}{\partial x} \\
& = -\frac{\partial p}{\partial r} + \frac{1}{r} \frac{\partial}{\partial r} \left( 2r\mu \frac{\partial v_r}{\partial r} \right) + \frac{\partial}{\partial x} \left( \mu \left( \frac{\partial v_r}{\partial x} + \frac{\partial v_x}{\partial r} \right) \right) + v_r R^* + S_{m,a} \quad (2-3) \\
& + S_{m,sf}
\end{aligned}$$

where  $p$  and  $\mu$  are the pressure and the viscosity, respectively;  $S_{m,b}$  is the additional source term equal to  $\rho g \beta (T - T_{ref})$ , which is for the consideration of the buoyancy force of liquid steel in the anode region;  $S_{m,a}$  and  $S_{m,sf}$  are another two additional momentum source terms for the arc modeling and the surface force modeling, respectively, which will be illustrated in the later section;  $R^*$  is the coefficient of the momentum sink, which is used to distinguish the anode region. The expression of  $R^*$  can be defined as:

$$R^* = \begin{cases} 0 & (\text{in arc plasma region}) \\ -\frac{C_{mix}(1-\lambda)^2}{(\lambda^3 + \epsilon)} & (\text{in anode region}) \end{cases} \quad (2-4)$$

and  $C_{mix}$  is the mixture zone constant;  $\epsilon$  is a coefficient with a small value to prevent zero occurring in the denominator;  $\lambda$  is the liquid volume fraction dependent of phase temperature  $T$ , which can be written as:

$$\lambda = \begin{cases} 0 & (T \leq T_{s,steel}) \\ \frac{T - T_{s,steel}}{T_{l,steel} - T_{s,steel}} & (T_{s,steel} < T < T_{l,steel}) \\ 1 & (T \geq T_{l,steel}) \end{cases} \quad (2-5)$$

and  $T_{s,steel}$  and  $T_{l,steel}$  are the solidus temperature and the liquidus temperature of the steel phase.

The energy conservation equation can be expressed as:

$$\begin{aligned} \frac{\partial(\rho T)}{\partial t} + \frac{1}{r} \frac{\partial(r\rho C_p v_r T)}{\partial r} + \frac{\partial(\rho C_p v_x T)}{\partial x} \\ = \frac{1}{r} \frac{\partial}{\partial r} \left( r k_{eff} \frac{\partial T}{\partial r} \right) + \frac{\partial}{\partial x} \left( k_{eff} \frac{\partial T}{\partial x} \right) + S_{e,L} + S_{e,a} + S_{e,ht} \end{aligned} \quad (2-6)$$

where  $T$  is the temperature;  $C_p$  is the specific heat;  $k_{eff}$  is the effective thermal conductivity;  $S_{e,a}$  and  $S_{e,ht}$  are the additional energy source terms, which will be defined in later sections;  $S_{e,L}$  is the explicit latent heat term, which is equal to:

$$S_{e,L} = \begin{cases} 0 & (\text{in arc plasma region}) \\ \frac{L}{C_p} \frac{\partial \lambda}{\partial t} & (\text{in anode region}) \end{cases} \quad (2-7)$$

where  $L$  is the latent heat for the steel ingot melting.

### 2.3.2 Electric Arc Model (for Lab-scale DC Arc)

Electric arc model solves for the electromagnetic field based on the MHD theory, so that the lab-scale DC electric arc plasma can be predicted in the gas region.

In the calculation of electromagnetic field, the electrical current density component takes the following form:

$$\vec{j} = \sigma \vec{E} \quad (2-8)$$

where  $\sigma$  is the electrical conductivity of selected working gas;  $E$  is the electrical field intensity dependent on the gradient of the electrical potential  $V$ , which is given by:

$$\vec{E} = -\nabla V \quad (2-9)$$

The self-induced magnetic field calculation is generally referred to the Biot-Savart formula, however, Ampere's law can also be employed to roughly measure the azimuthal magnetic induction in an axisymmetric model. The corresponding expressions can be written below:

$$\vec{B} = \vec{\nabla} \times \vec{A} \quad (2-10)$$

$$B_\theta = \frac{\partial A_r}{\partial x} - \frac{\partial A_x}{\partial r} \quad (2-11)$$

where  $A_x$  and  $A_r$  are axial and radial vector potential components, respectively. The determinations of the vector potential components are given in **Equation (2-13)** and **Equation (2-14)** listed below.

The current continuity equation is defined as:

$$\frac{1}{r} \frac{\partial}{\partial r} \left( \sigma r \frac{\partial V}{\partial r} \right) + \frac{\partial}{\partial x} \left( \sigma \frac{\partial V}{\partial x} \right) = 0 \quad (2-12)$$

and the axial and the radial vector potential equations can be expressed as:

$$\frac{1}{r} \frac{\partial}{\partial r} \left( r \frac{\partial A_x}{\partial r} \right) + \frac{\partial}{\partial x} \left( \frac{\partial A_x}{\partial x} \right) = -\mu_0 j_x \quad (2-13)$$

$$\frac{1}{r} \frac{\partial}{\partial r} \left( r \frac{\partial A_r}{\partial r} \right) + \frac{\partial}{\partial x} \left( \frac{\partial A_r}{\partial x} \right) = -\mu_0 j_r + \frac{A_r}{r^2} \quad (2-14)$$

where  $\mu_0$  is the magnetic permeability in the medium.

By solving the above set of equations, the Lorentz effect and the arc heating effect can be included by two additional source terms in corresponding governing equations, which are written as follows:

$$S_{m,a} = \vec{j} B_\theta \quad (2-15)$$

$$S_{e,a} = \frac{j_x^2 + j_r^2}{\sigma} + \frac{5}{2} \frac{k_B}{e} \left( j_x \frac{\partial T}{\partial x} + j_r \frac{\partial T}{\partial r} \right) - S_r \quad (2-16)$$

where  $k_B$  is the Boltzmann constant;  $e$  is the elementary electric charge;  $S_r$  is the radiation heat loss. The first term on the right-hand side of **Equation (2-16)** represents the heat generated by the Joule's effect and the second term is referred to the electronic enthalpic flux.

### 2.3.2.1 Interface Tracking

Dynamic interface tracking is critical which impacts the direct-coupling of electric arc model and the solid steel melting model. To define a sharp interface between arc plasma region and anode region, a new variable  $\eta$  is introduced in the present study:

$$\eta = \begin{cases} 1 & (\alpha_s \geq ts) \\ 0 & (\alpha_s < ts) \end{cases} \quad (2-17)$$

where  $ts$  is the threshold used to distinguish the cell belongs to the anode region or arc plasma region, that is,  $\eta$  will be unity if the cell is an anode cell. Therefore, the interface can be represented using the normalized gradient of  $\eta$ , which is written as:

$$\vec{\psi} = \frac{\nabla\eta}{|\nabla\eta| + \epsilon} = \begin{cases} 1 & (interface) \\ 0 & (not\ interface) \end{cases} \quad (2-18)$$

### 2.3.2.2 Heat Transfer at Interface

During the steel ingot melting, there exists a low-temperature sheath on the surface of the arc and steel ingots, where the plasma arc temperature, particle density, and voltage have large gradients, resulting in the plasma not meeting the LTE assumption [96]. The presence of a low-temperature sheath causes the electron temperature to be different from the heavy particle temperature, thus the electron temperature and the heavy particle temperature cannot be defined by a unified temperature value. Meanwhile, such a sheath also has a significant impact on the distribution of the arc current density on the surface of the steel ingot and the heat transfer between the steel ingot and the arc. Therefore, the special treatment of the boundary layer is required in the model. The present study adopted the LTE-diffusion approximation to deal with the above-mentioned low-temperature sheath [100,104], and considers the thermal effect of the arc to the steel ingot surface by adding the additional energy source at the interface for each phase [105]. Generally, the heat transfer

mechanism from the arc to the steel ingot surface is mainly composed of three parts: the electronic heat, the conduction heat, and the surface radiative heat. Among them, the electronic heat is caused by the steel ingot surface receiving the electrons from the electrode tip and releasing a large amount of heat.

The aforementioned heat transfer mechanism at the obtained interface can be mathematically expressed as follows [101]:

$$S_{e,ht} = \begin{cases} q_{eh} + q_{ch} - q_{rh} = |\vec{j}|\varphi + \frac{k_{eff}(T_a - T_s)}{\delta} - \varepsilon k_b T_s^4 & (\text{arc plasma side}) \\ -q_{ch} = \frac{k_{eff}(T_s - T_a)}{\delta} & (\text{anode side}) \end{cases} \quad (2-19)$$

where  $q_{eh}$  is the electronic heat;  $q_{ch}$  is the conduction heat;  $q_{rh}$  is the surface radiative heat;  $\varphi$  is the work function of steel ingot;  $T_a$  and  $T_s$  are the interface temperature for arc and steel, respectively;  $\delta$  is the interface thickness;  $\varepsilon$  is the emissivity of steel ingot.

### 2.3.2.3 Surface Force at Interface

In addition to the gravity, the buoyancy force, and the electromagnetic force, there has extra four surface forces that need to be discussed and further considered about their effect at the interface, which includes the surface tension, the Marangoni shear stress, the arc plasma shear stress and the arc pressure. It should be noted that the last force, i.e. the arc pressure, has already included in the model by solving the corresponding momentum equations described above. Thus only the first three forces need additional treatment.

The surface tension pressure  $p_{st}$  at the interface is mainly due to the surface curvature, and its direction is normal to the local free surface, and its value can be calculated by [106]:

$$p_{st} = -\gamma \left[ \nabla \cdot \left( \frac{\vec{n}}{|\vec{n}|} \right) \right] \quad (2-20)$$

where  $\gamma$  is the surface tension coefficient;  $\vec{n}$  is the normal vector to the local free surface.

The Marangoni shear stress  $\tau_{ms}$  is caused by the existence of the temperature gradient, and its direction is tangential to the local free surface, and its value can be estimated by [107]:

$$\tau_{ms} = \frac{\partial\gamma}{\partial T} \frac{\partial T}{\partial \vec{s}} \quad (2-21)$$

where  $\vec{s}$  is the tangential vector to the local free surface.

While the arc plasma shear stress  $\tau_{as}$  is estimated according to the interface velocity on the arc plasma side and further applied on another side of the interface, i.e. the anode side, and its value can be calculated as follows [108]:

$$\tau_{as} = \mu \frac{\partial \vec{v}}{\partial \vec{n}} \quad (2-22)$$

By adding the above surface forces as a volumetric source term  $S_{m,sf}$  to the momentum conservation equation in the appropriate direction, the force interaction at the interface can be predicted as desired.

#### 2.3.2.4 Electrode Movement

Except for using the stationary electrode position, the present study also includes the moving electrode to generate the electric arc with varying arc length for the steel ingot melting, which is one of the common operations in the arc melting manufacturing. In order to achieve electrode movement in the model, a layering dynamic mesh was used, and the integral form of all conservation equations mentioned above in the dynamic mesh needs to be rewritten as follows for a general scalar  $\phi$  on an arbitrary control volume  $V$  whose boundary is moving [109]:

$$\frac{d}{dt} \int_V \rho \phi dV + \int_{\partial V} \rho \phi (\vec{u} - \vec{u}_g) \cdot d\vec{A} = \int_{\partial V} \Gamma \nabla \phi \cdot d\vec{A} + \int_V S_\phi dV \quad (2-23)$$

where  $\vec{u}$  is the flow velocity,  $\vec{u}_g$  is the mesh moving velocity,  $\Gamma$  is the diffusion coefficient regarding different conservation equations, and  $S_\phi$  is the source term of a general scalar  $\phi$ .

By adopting the layering dynamic mesh, the electrode can move up and down on its axis at the assigned proper mesh moving velocity.

### 2.3.3 Simulation Conditions

The material properties adopted in the present study are listed in **Table 2.1** and they are all referred to the published literature. The properties given in the form of references in the table are temperature-dependent values, which were added to the solver by interpolation for the simulation. In addition, some properties of the steel ingot, such as viscosity, specific heat, thermal conductivity, are also temperature-dependent, which were added in the same way to the solver. Other parameters utilized in the model are all given in **Table 2.2**.

Table 2.1. Material properties in the model.

Parameters	Symbol	Values for Arc Plasma (Argon)	Values for Steel Ingot
<i>Density</i>	$\rho$		7200 kg/m <sup>3</sup>
<i>Viscosity</i>	$\mu$	<i>Reference [103]</i>	<i>Reference [100]</i>
<i>Specific heat</i>	$C_p$		
<i>Thermal conductivity</i>	$k$		
<i>Radiation heat loss</i>	$S_r$	<i>Reference [110]</i>	-
<i>Solidus temperature</i>	$T_{s,steel}$	-	1670 K
<i>Liquidus temperature</i>	$T_{l,steel}$	-	1723 K
<i>Latent heat</i>	$L$	-	245000 J/kg
<i>Electrical conductivity</i>	$\sigma$	<i>Reference [103]</i>	770000 S/m
<i>Work function</i>	$\varphi$	-	4.65 V
<i>Surface tension coef.</i>	$\gamma$	-	1.2 N/m
<i>Initial Temperature</i>	$T$	1000 K	1000 K

Table 2.2. Other parameters in the model.

Parameters	Symbol	Values
<i>Mixture zone constant</i>	$C_{mix}$	$10^8$
<i>Constant coefficient</i>	$\epsilon$	$0.001$
<i>Magnetic permeability</i>	$\mu_0$	$1.26*10^{-6} \text{ H/m}$
<i>Boltzmann constant</i>	$k_B$	$1.38*10^{-23} \text{ J/K}$
<i>Elementary electric charge</i>	$e$	$1.6*10^{-19} \text{ C}$
<i>Interface threshold</i>	$ts$	$0.95$
<i>Interface thickness</i>	$\delta$	$0.00015 \text{ m}$

The detailed boundary conditions for the simulation domain are indexed in **Table 2.3**. It should be noted that a commonly-used free-burning DC arc configuration was adopted in the present study to melt the steel ingot. The operating current is 200 A and the working gas is argon and assumed to be at atmospheric pressure. The corresponding current density distribution expression for this type of arc can be written as follows [36]:

$$j(r) = J_{max} \exp(-br) \quad (2-24)$$

where  $J_{max}$  is the maximum current density, which can be approximated based on the experimental measurement of the radius of the hottest part (the “white-hot”), and use the following equation to calculate:

$$J_{max} = \frac{I}{2\pi r_h^2} \quad (2-25)$$

where  $r_h$  is aforementioned “white hot” radius, and normally takes 0.00051 m for the 200 A arc. And  $b$  is a constant, which can be calculated by integrating the current density in radial direction using the expression given below:

$$I = 2\pi \int_0^{R_c} j(r) r dr \quad (2-26)$$

where  $R_c$  is the arc conduction radius (cut-off radius), and normally takes 0.003 m for the evaluation.

Table 2.3. Boundary conditions for the simulation domain.

Variables	BC	CD	DF	AF	AB	BE
$T (K)$	$\frac{\partial T}{\partial r} = 0$	$\frac{\partial T}{\partial x} = 0$	$\frac{\partial T}{\partial r} = 0$	$\frac{\partial T}{\partial x} = 0$	$\frac{\partial T}{\partial r} \frac{\partial T}{\partial x} = 0$	3500 (at the tip)
$V (voltage)$	$\frac{\partial V}{\partial r} = 0$	0	$\frac{\partial V}{\partial r} = 0$	$\frac{\partial V}{\partial x} = 0$	$\frac{\partial V}{\partial r} \frac{\partial V}{\partial x} = 0$	<b>Equation (2-24)</b>
$v (m/s)$	$\frac{\partial u}{\partial r} = 0$	-	-	-	-	-

## 2.4 Results and Discussions

### 2.4.1 Model Validations

#### 2.4.1.1 Electric Arc Model (for Lab-scale DC Arc)

As the arc is the main heat source for the steel ingot melting, the accuracy of the arc simulation needs to be proven first. Otherwise, the subsequent melting results will be meaningless.

The stationary DC electric arc modeling is validated against the temperature measurement of the arc column published in reference. The current validation simulation only includes the electric arc plasma region, i.e. the steel ingot is not considered for the simplification purpose. **Figure 2.5** presents the temperature distribution of the free-burning plasma arc using argon as a working gas. For a 200A-current arc, the highest temperature located just below the electrode tip can reach up to 22000 K, while the middle of the arc column maintains a high temperature around 10000 K. A typical bell shape of the arc plasma can be observed, which is mainly due to the strong

impingement and dispersing of the arc plasma jet on the anode surface. Thus, the high temperature gradually spreads along the centerline of the plasma jet and the strong diffusion of the temperature also occurs in the radial direction. The simulation results were compared with the isotherms measured by Hsu et al. [36]. The isotherms range from 11000 K to 21000 K and the temperature distribution is in a fairly good agreement with the experimental data, whose percentage error is estimated to be less than 5%.

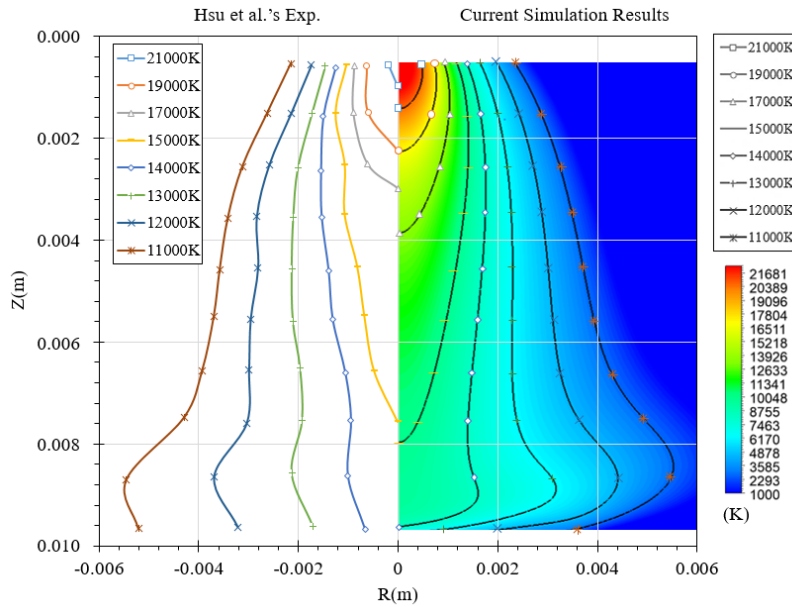


Figure 2.5. Comparison of simulated isotherms and measurement data [36].

In addition to the isotherms of the arc plasma, the axial velocity distribution and the velocity contour are also plotted in **Figure 2.6** to compare with other research works [43-44]. The velocity contour indicates that the velocity of the arc plasma jet maintains concentrated and has a slight diffusion in the radial direction. In the plotted axial velocity distribution, it can be seen that the arc plasma accelerates dramatically just below the electrode tip and reach extremely fast to the maximum velocity at 0.0008 m. Then the arc plasma velocity decays smoothly from 0.0008 m to 0.0088 m until it touches the anode surface. The current simulation results have a good agreement with the published simulation results by other research groups, which further demonstrates the model accuracy in the present study.

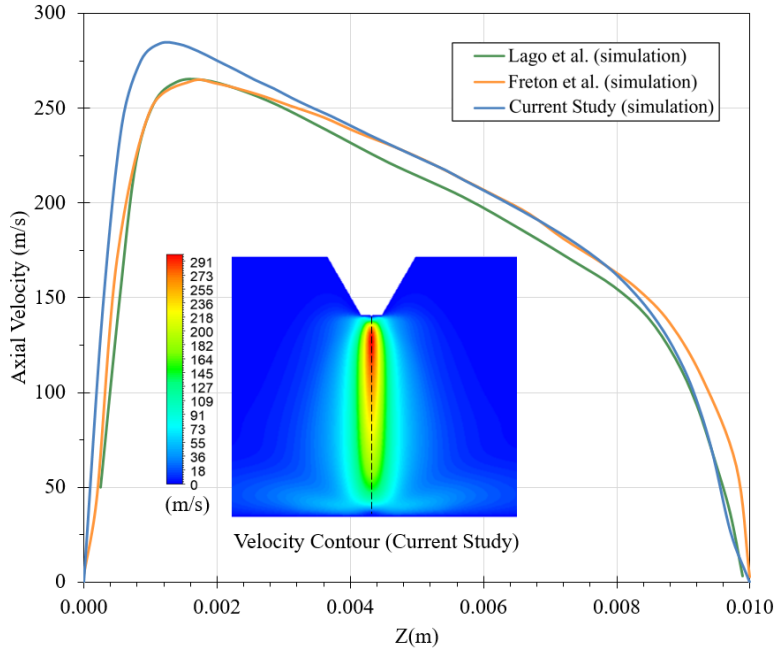


Figure 2.6. Comparison of velocity distribution at the domain centerline [43-44].

Since the current physical problem is axisymmetric, only half of the geometry in **Figure 2.2** is adopted and the entire set of equations is solved in 2D based on the cylindrical coordinate system  $(r, x)$ . For the consideration of the potential future application, the current 2D electric arc modeling was further enhanced to the 3D and corresponding validations were also conducted. The only difference is 3D electric arc modeling is based on the Cartesian coordinate system  $(x, y, z)$ . **Figure 2.7** compares the isotherms of 2D and 3D configuration showing fairly good consistency. With the validated 2D electric arc modeling as illustrated above, the 3D electric arc modeling was indirectly validated. The minor mismatching of the temperature distribution at the domain centerline may be due to the slight difference of the mesh in two simulations. **Figure 2.8** also compares the 2D and 3D axial velocity of the electric arc, whose overall distributions are in line with each other. In summary, 2D modeling based on the cylindrical coordinate has the same prediction of the electric arc as that for 3D modeling based on the Cartesian coordinate. Both 2D and 3D model has been validated in the present study.

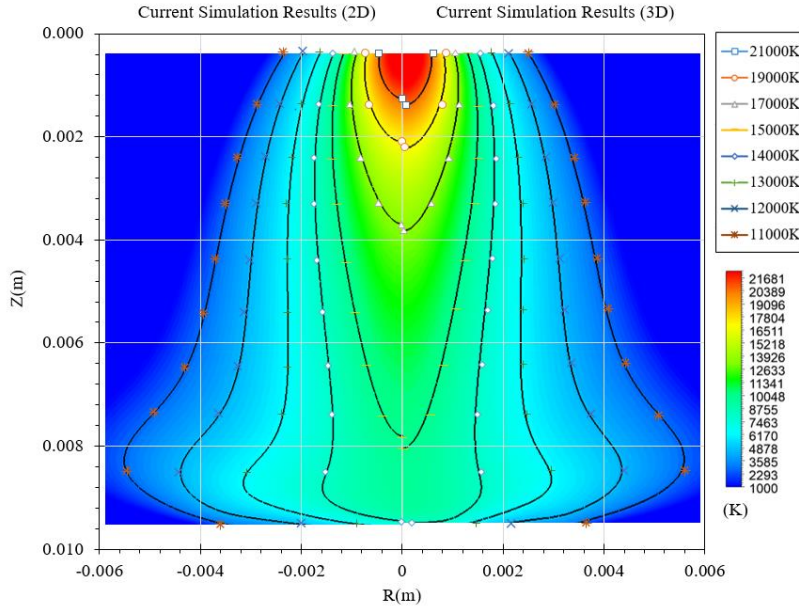


Figure 2.7. Comparison of 2D and 3D simulated isotherms.

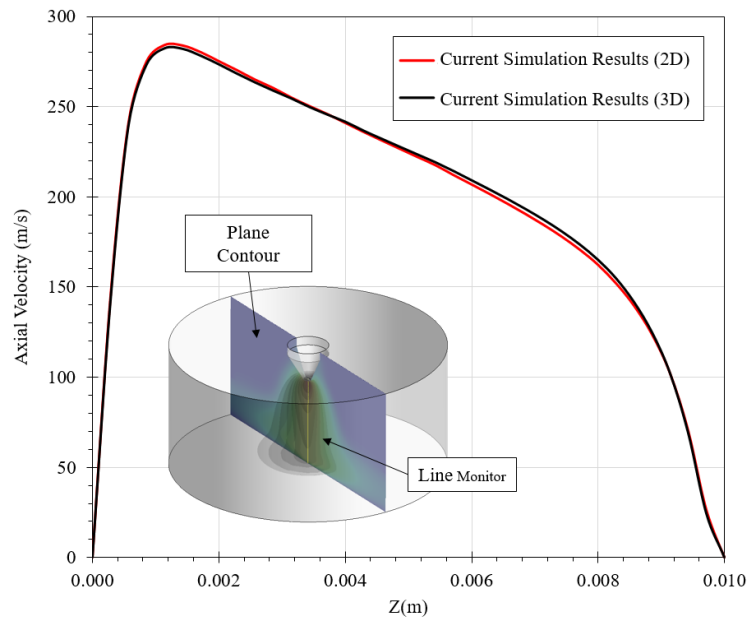


Figure 2.8. Comparison of 2D and 3D velocity distribution at the domain centerline.

### 2.4.1.2 Solid Steel Melting Model

With the validated electric arc modeling, the subsequent validation for solid steel melting model can be conducted. The published experimental and simulation data of the keyhole PAW process [100] was employed to validate the accuracy of the local arc-steel heat transfer and force

interaction prediction during the steel workpiece melting so that those mechanisms can be further applied on the arc melting simulation of the entire steel ingot. The simulation domain and operating conditions were all modified accordingly based on the reported experimental setup, while the heat transfer and force interaction mechanism in the model were kept the same.

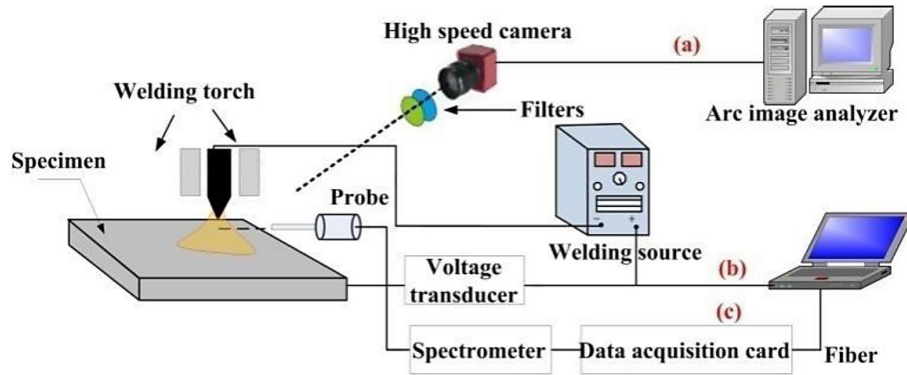


Figure 2.9. Schematic diagram of experimental setup [100].

During the melting process, the heat transfer continuously happens at the arc-solid interface, so that the solid workpiece can be efficiently melted beneath the electric arc. Meanwhile, the force interaction between the arc and the liquid steel results in the liquid steel to be pushed away immediately by the high-velocity and high-pressure plasma jet, thus the keyhole solid surface is exposed again. The exposed solid surface can further absorb the heat from the electric arc triggering the melting again. This phenomenon occurs repeatedly throughout the entire process leading to a keyhole created inside the workpiece until it penetrates the entire workpiece. Locally, the steel ingot melting using the electric arc has a similar mechanism. **Figure 2.10** compares the simulated steel workpiece melting with both experimental measurement and simulation data reported by Jian and Wu [100]. The dashed line represents the measurement position of the keyhole solid surface profile, and the solid line is the corresponding simulation results obtained by the group, and the temperature contour of the steel workpiece is the result predicted by the present model. From the comparison with the reported data, the present model gives a good prediction of the keyhole solid surface profile, which matches the measurement data and simulation results given by Jian and Wu [100]. The overall error is less than 10%, which further proves the accurate prediction of the heat transfer and force interaction in the model.

Moreover, by modifying the corresponding material properties, the model also has the ability to predict the melting process of other types of metal using electric arc since the overall heat transfer and force interaction mechanism stays the same between the arc and the metal. **Figure 2.11** shows another validation simulation using aluminum as the workpiece based on the experiment reported in the reference [101]. The validation was still conducted by comparing the keyhole solid surface profile in the workpiece to prove the melting prediction to be correct. From the figure, the current simulation results and the reported experimental data given in the figure can well match with each other.

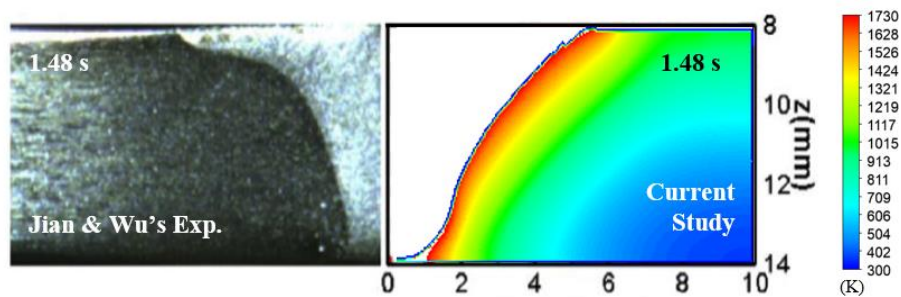


Figure 2.10. Melting validation: steel as the workpiece [100].

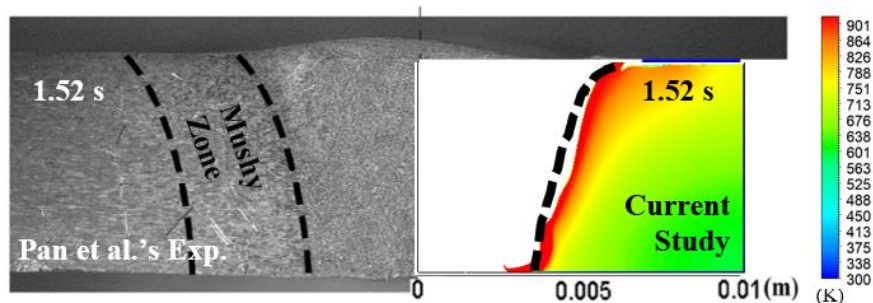


Figure 2.11. Melting validation: aluminum as the workpiece [101].

## 2.4.2 Arc Characteristics with Dynamic Electrode Movement

The investigation of the electric arc with varying arc length due to the electrode movement is of great significance for the industrial applications. Maintaining the arc length within a certain range by moving the electrode will help to stabilize the arc, thereby obtaining better arc performance and achieving higher arc melting efficiency. Generally, the sensor calculates the current arc length by detecting the variance of the impedance in the solid material and returns the signal to the controller

for consequent action if the arc length changed. For example, if the solid surface collapses due to melting, the arc length will be elongated accordingly and the impedance value will change as well. In this case, the controller will move the electrode downward to shorten the arc length and ensure the arc length return to the preset value to meet the requirement of the production. This process is a continuous regulation process, meaning the arc length is changing dynamically. Thus, it is necessary to have a better understanding of the detailed arc characteristic during this period for better controlling. The present study aims to conduct a quantitative analysis of the effect of dynamic variation of arc length on the arc itself and the melting of the anode surface to provide practical guidance for the operation.

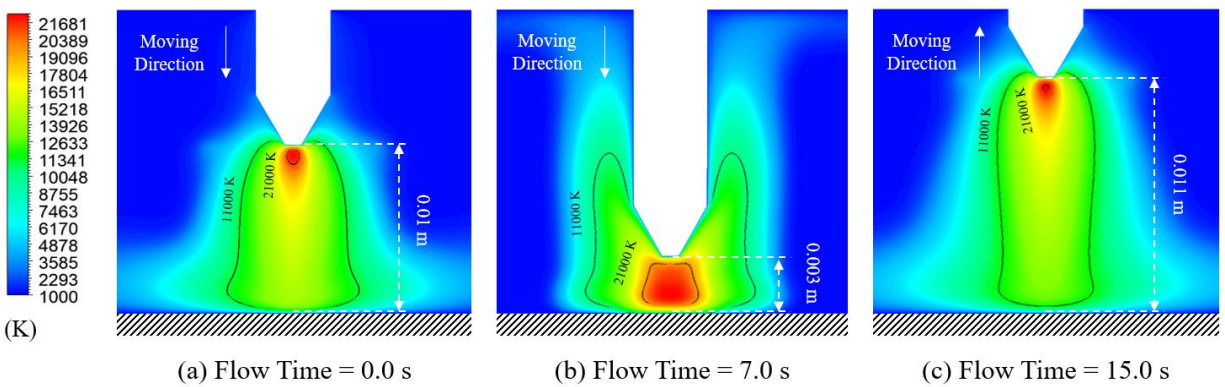


Figure 2.12. Dynamic effect of varying arc length due to electrode movement on the arc characteristics.

For the simplification purpose, the simulation domain adopted in this section includes the electric arc plasma and the top surface of the solid steel ingot (the anode surface). In order to observe the characteristics of the arc, it is only after the electric arc plasma is generated and stabilized that the electrode begins to move up and down along its axis at a constant velocity. The electrode descends continuously at 0.001 m/s between 0 to 7 seconds, then changes the direction of movement and lifts up with the same velocity until the end of the simulation. **Figure 2.12** shows the dynamic effect of varying arc length due to electrode movement on the arc characteristics. From **Figure 2.12 (a)** and **Figure 2.12 (b)**, as the electrode tip gets closer to the anode surface, the reducing arc length makes the entire arc column be greatly compressed. As a result, the arc loses its original bell shape and the high-temperature area beneath the electrode tip expands. Such conclusions can be observed from the 11000 K isotherm and the 21000 K isotherm in the temperature contours.

Under the premise of the same arc operating conditions, the energy released due to the ionization of the gas between the electrode tip and the anode surface needs to diffuse outward in the radial direction based on the conservation of energy if the vertical space is reduced, thus the surrounding gas is rapidly heated up and the high temperature region becomes an M-shaped distribution.

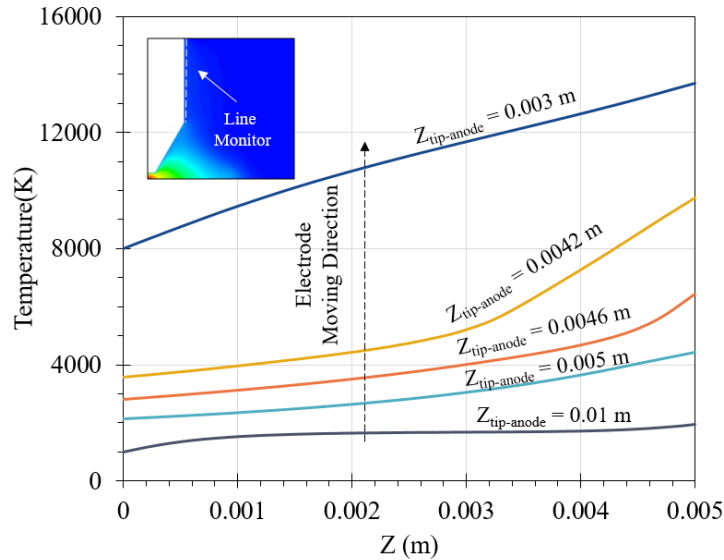


Figure 2.13. Near-wall gas temperature distribution at the electrode surface during the electrode descent.

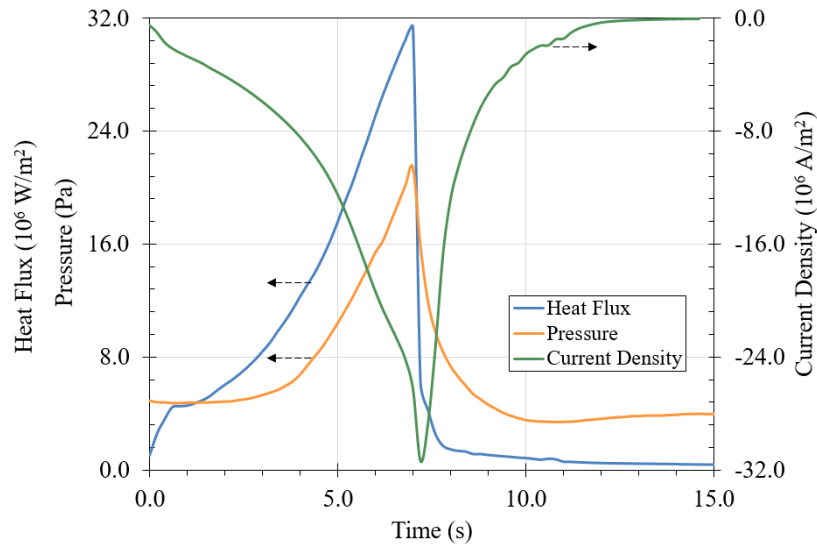


Figure 2.14. Distribution of heat flux, pressure, and current density at anode surface during the electrode descent.

**Figure 2.13** shows the near-wall gas temperature at the electrode surface during the dynamic descent of the electrode. It can be seen that when the tip-anode vertical distance reduces from 0.01 m to 0.003 m, the average temperature increases along the line monitor to reach up to 10000 K, which may result in great consumption of electrode itself in the practical production. As the electrode turns to move upwards from 7 to 15 seconds, the arc gradually returns to the bell shape. At the last moment of the simulation (14 to 15 seconds), the electrode is lifted up over the original arc length leading the entire arc to be stretched. In reality, such an operation increases the resistance of the arc and cools down the arc, which can be reflected from the shrinking of the 11000 K isotherm and the 21000 K isotherm in **Figure 2.12 (c)**.

Furthermore, the dynamic effect of the arc on the anode surface under varying arc length is further studied. The arc performance is evaluated by analyzing the area-averaged heat flux, pressure, and current density on the anode surface. The changes in these variables over time are shown in **Figure 2.14**. From the figure, the electrode descends to the lowest point in about 7 seconds. During this time, the area-averaged heat flux, pressure, and current density on the anode surface all show an exponential increase or decrease, and values of those variables reach the peak at around 7 seconds. The extremely high heat flux and current density significantly enhance the heat conduction between the arc and the anode surface and the generation of a large amount of electronic heat on the anode surface, causing the solid material to have the intensive melting. Meanwhile, the arc also applies a high pressure on the anode surface resulting in the liquid steel being blown away, thereby exposing a new molten solid surface to participate in a new round of melting. Although the short arc length will greatly increase the melting efficiency of the arc based on the previous discussion, the ambient gas surrounding the electrode is more easily heated to the high temperature due to the compression of the arc column. Thus, the electrode consumption rate also increases at the same time. For a long arc, the arc resistance value and the active power consumption are greater, which in turn leads to the reduction of the arc melting efficiency and the poor stability of the arc. Therefore, maintaining a relatively reasonable and stable arc length will balance the electrode consumption rate and melting efficiency to achieve the highest economic benefit.

### 2.4.3 Steel Ingot Melting with Stationary Electrode

This section first analyzes the melting of a steel ingot using the electric arc under the condition of a fixed electrode position. An initial arc length of 0.01 m is used for the arc ignition. The simulation results of the entire steel ingot melting are shown in **Figure 2.15**.

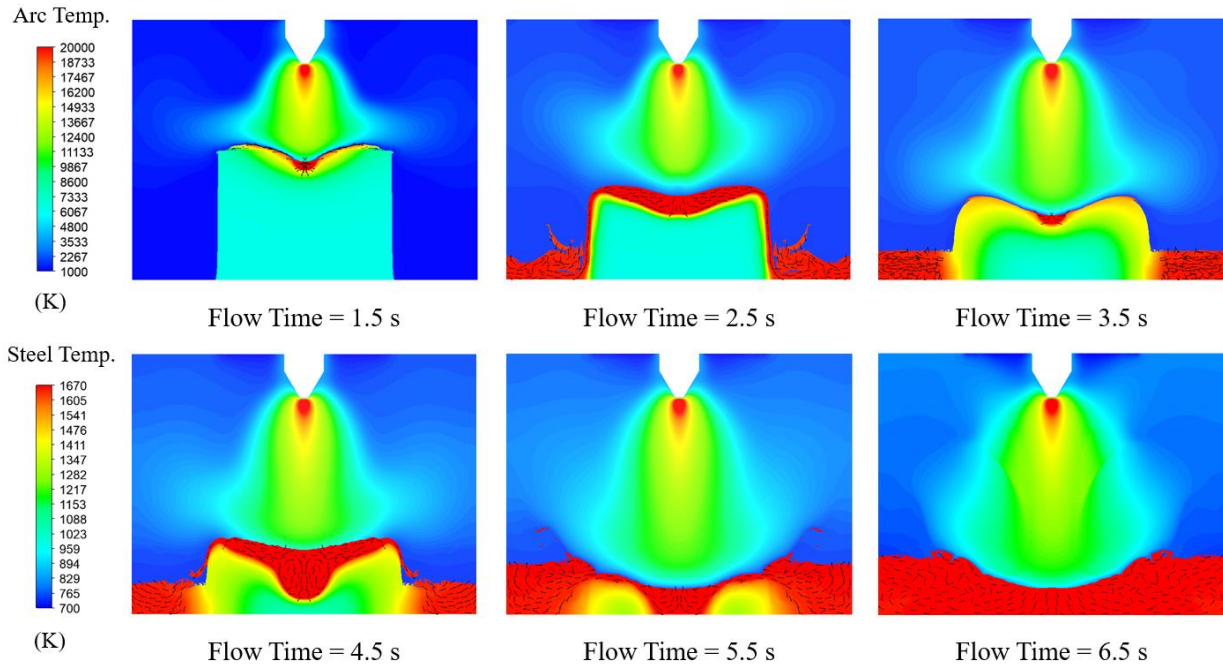


Figure 2.15. Steel ingot melting using electric arc under the stationary electrode.

At the beginning of the melting stage, the electric arc contacts the ingot top surface in the form of a bell shape and transfers a large amount of heat to it. The heat is Gaussian-distributed from the surface center outwards, thus the entire steel ingot follows the melting sequence from the center to the outside and from the top to the bottom. The red area in the contours represents molten liquid steel. From the first three contours, the high-velocity and high-pressure plasma jet hits the liquid steel that just melted and accumulated in the surface depression, causing it to splash or flow to the edge of the ingot and further drip from its side surface. Since the side surface of the steel ingot is not directly heated by the arc, it still maintains a relatively cold condition. The high-temperature liquid steel dripping along the surface or gathering at the bottom of the crucible transfers its heat to the cold side surface and cools down and solidifies again. Furthermore, as the steel ingot melts, the arc melting efficiency gradually decreases with the arc length increasing. The above two main

factors directly cause the solid volume of the steel ingot to decline in a fluctuating manner during the melting process. On the other hand, as the liquid steel is pushed away by the plasma jet, the solid ingot top surface is exposed allowing it to be further melted. The rest of the surface that is still covered by the high-temperature liquid steel melts due to the heat conduction between the solid and the liquid. The above process will be repeated at the beginning and middle melting stages until the remaining solid part is fully immersed in the liquid steel. The last two contours show that the remaining steel ingot is having the in-bath melting. During this period, the main method for the in-bath melting is through the forced convection, that is, the high-temperature liquid steel in the bath is stirred by the strong impact of the electric arc and keeps transferring heat to the immersed solid. The electric arc only heats the liquid steel on the surface of the liquid steel bath.

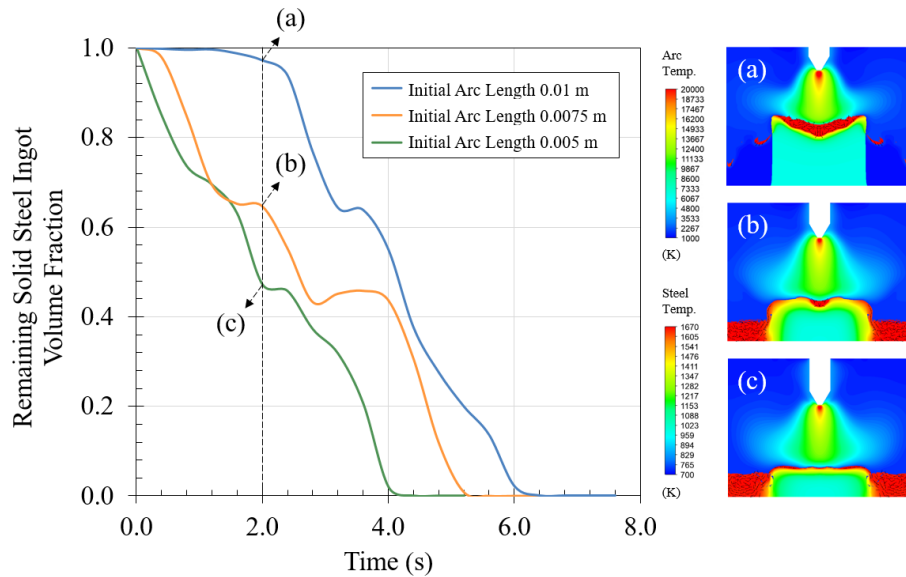


Figure 2.16. Effect of initial arc length on melting efficiency under stationary electrode.

Based on the above discussion, the effect of the initial arc length on the steel ingot melting rate can be further explored. The positions of the fixed electrode are adjusted downward by 0.0025 m and 0.005 m, respectively, so that the initial arc lengths can be set to 0.0075 m and 0.005 m, respectively. The melting rate is analyzed by comparing the remaining volume of the solid steel ingot, whose results are shown in **Figure 2.16**. All three melting curves show a fluctuating decline due to the repeated melting and solidification of steel. The initial arc lengths of 0.01 m, 0.0075 m, and 0.005 m correspond to the melting times of 4.4 s, 5.6 s, and 6.4 s, respectively. Two identical

descending heights of the electrode position reduce the melting times by 12.5% and 21.4%, respectively. Therefore, the initial arc length has a great impact on the steel ingot melting rate. The three temperature contours given at 2 seconds illustrate that the smaller initial arc length can provide higher instantaneous heat flux and current density, and effectively avoid the accumulation of liquid steel in the surface depression (red area), thus more surface can be directly contacted with the arc to achieve the layer-by-layer melting. Such melting behavior greatly accelerates the overall melting efficiency of the steel ingot, which is consistent with the conclusions discussed before. Therefore, in an actual production, it is recommended to shorten the initial arc length to effectively reduce the arc dissipation and to enhance the arc performance acting on the solid surface, thereby improving the melting efficiency of the steel ingot.

#### 2.4.4 Steel Ingot Melting with Dynamic Electrode Movement

This section further considers the steel ingot melting using the electric arc under the dynamic moving electrode. In the cases of using the fixed electrode position, the arc length increases as the height of the steel ingot decreases. According to the previous discussion, longer arc length largely elevates the arc resistance and is not conducive to the stability of the arc, which may easily cause the arc extinction and have a certain impact on the stability of the entire electronic system.

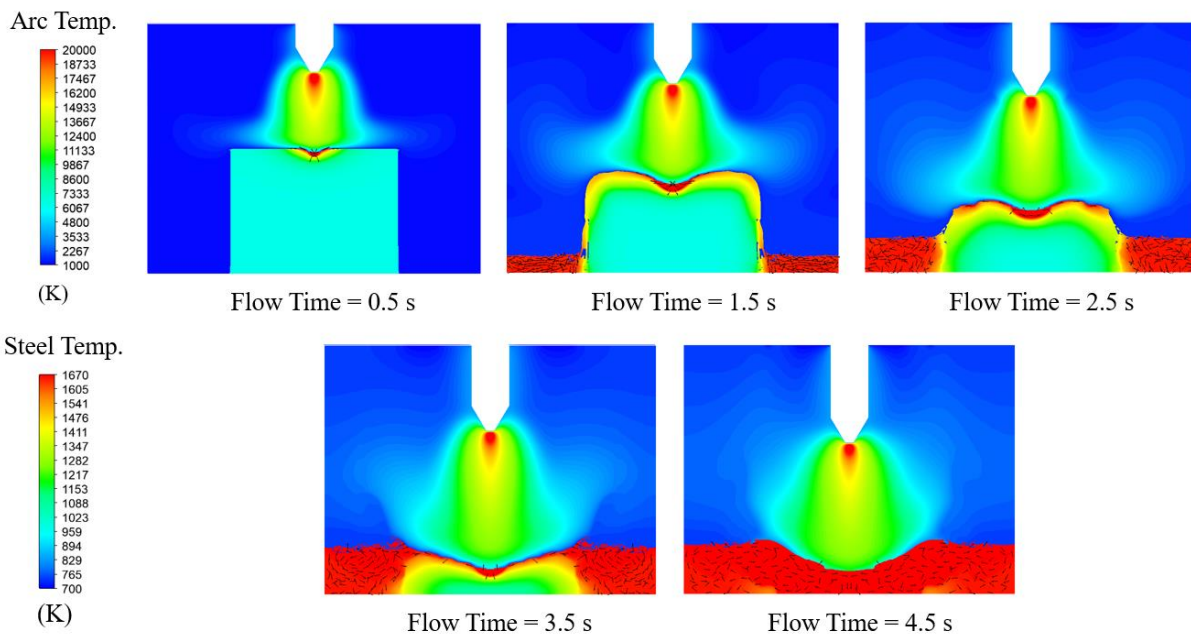


Figure 2.17. Steel ingot melting using electric arc under the dynamic moving electrode.

Generally, moving the electrode downward based on the melting rate to ensure a relatively stable arc length is one of the widely-accepted solutions in the actual operation and the most common example is the electrode bore-in during the melting stage in EAF. So far, there is no relevant literature known to the authors that has reported the numerical modeling of melting the steel ingot using the electric arc under the dynamic moving electrode. Thus, it is necessary to conduct further research on this. In the present study, the dynamic mesh is employed to achieve the electrode movement in the model. The electrode descend is assumed to be at a constant velocity of 0.0015 m/s downward in the simulation. The results are shown in **Figure 2.17**.

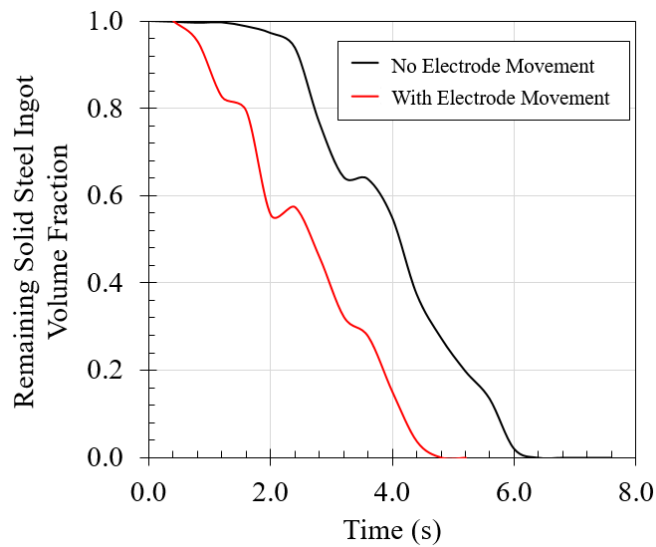


Figure 2.18. Comparison of steel ingot melting efficiency with and without dynamic moving electrode.

The distance between the electrode tip and the ingot top surface is maintained near the given value of the initial arc length during the entire melting stage. The relatively stable arc length enables the electric arc to sustain good thermodynamic characteristics, so that the arc can keep its original bell shape and melt the surface of the steel ingot with higher heat flux. Under the premise that the initial arc length is 0.01 m, as shown in **Figure 2.18**, the case with the dynamic electrode movement reduces the melting time from 6.4 s to 4.8 s, which has a total reduction of 25%.

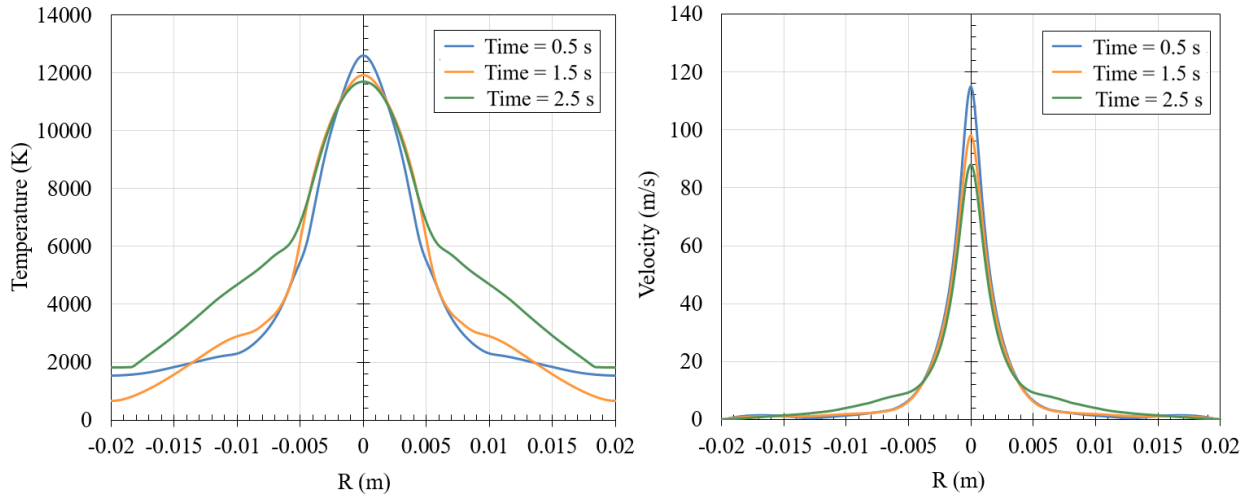


Figure 2.19. Axial temperature and velocity distribution at 0.0005 m above the ingot top surface with the dynamic moving electrode.

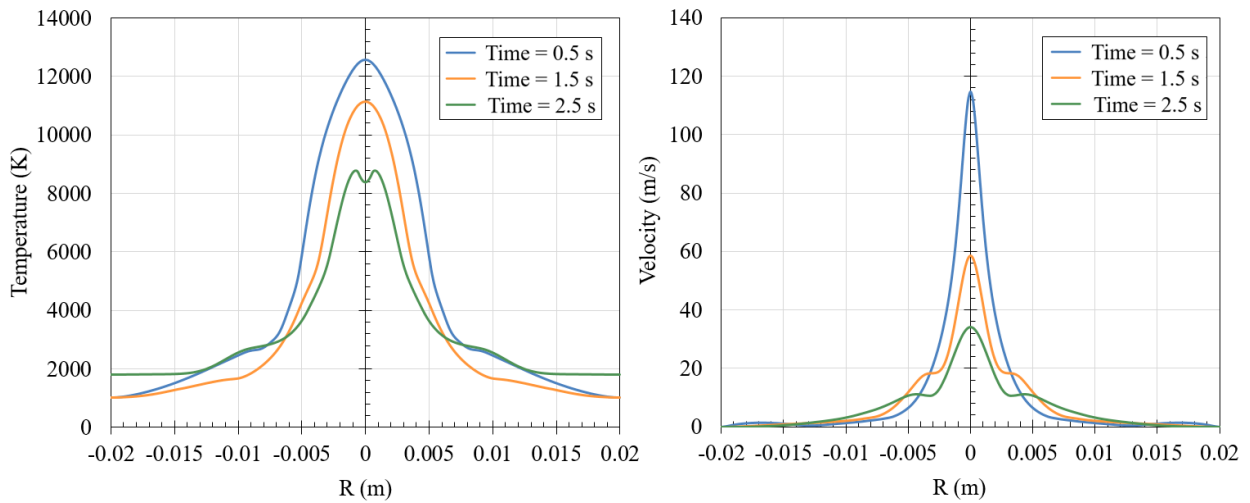


Figure 2.20. Axial temperature and velocity distribution at 0.0005 m above the ingot top surface without the dynamic moving electrode.

**Figure 2.19** and **Figure 2.20** show the axial temperature and velocity distribution at 0.0005 m above the ingot top surface with and without considering the dynamic movement of the electrode. Since the steel ingot itself continuously melts, the position of the ingot top surface also continuously declines. Thus, 0.0005 m mentioned in the present section is the relative distance from the ingot top surface at the current moment. Both figures show instantaneous temperature and velocity distributions at 0.5 s, 1.5 s, and 2.5 s for comparison. From the charts, the case

considering the dynamic electrode movement is able to maintain a relatively stable arc length, and the temperature and velocity distribution at the three plotted moments are concentrated and have a similar distribution and numerical range. On the contrary, for the case where the dynamic electrode movement is not considered, the distribution of instantaneous temperature and velocity reaching the ingot top surface is very different from each other. A large reduction can be found for both curves as the arc length continues to increase. According to the data given in **Figure 2.20**, the average peak temperature decreases up to 2000 K per second and the average peak velocity decreases up to 40 m/s per second meaning the original arc performance cannot be maintained in the sequent arc melting, which results in a significant negative impact on the melting efficiency.

## 2.5 Summary

The present chapter established a comprehensive EAF CFD model together with a direct-coupling methodology, which couples the solid steel melting model and the electric arc model (for lab-scale DC arc) together to dynamically simulate the entire steel ingot melting in the lab-scale DC EAF steelmaking process, which includes the continuous phase changing of solid steel, the surface deformation of steel ingot, and the close interaction between phases. The stationary DC electric arc and the arc-solid steel interface heat transfer and force interaction were validated respectively against the experimental data, which proved the accuracy of simulations. The relevant researches were conducted based on the validated models and the conclusions are given as follow:

- 1) The DC electric arc behavioral characteristics with varying arc lengths generated by the electrode movement were analyzed, which reveals that maintaining a reasonable and stable arc length will balance the electrode consumption rate and melting efficiency to achieve the highest economic benefit.
- 2) The effect of the initial arc length on the melting efficiency was studied, which demonstrates that the smaller initial arc length can provide higher instantaneous heat flux and current density and reduce the arc dissipation, meanwhile effectively avoid the accumulation of liquid steel in the surface depression thus more surface can be directly contacted with the arc to achieve the layer-by-layer melting, which greatly improves the overall melting efficiency.
- 3) The entire steel ingot melting process using the electric arc under the dynamic moving electrode was simulated, which illustrates that the case considering the dynamic

electrode movement can maintain the original arc performance near the ingot top surface in the sequent melting of the steel ingot, which results in a positive impact on the melting efficiency.

### 3. MODELING OF INDUSTRY-SCALE AC EAF

This chapter aims to establish a comprehensive EAF CFD model for simulating the industry-scale AC EAF. Compared with the lab-scale DC EAF, the steelmaking process in the industrial furnace is much more complex as it has not only arc melting but also burner-assisted preheating and melting, and the liquid steel refining follows afterward, where the supersonic coherent jet is adopted to stir and decarburize the bath meanwhile foaming the slag layer. Obviously, the steelmaking process in the industry-scale AC EAF involves dynamic multi-physics, in which AC electric arc plasma and coherent jet produced from the burners coexist creating a high temperature and velocity environment within the furnace. Different heat transfer mechanisms are tightly coupled and the phase change caused by melting and re-solidification constantly occur along with the chemical reactions in the molten bath and the post-combustion in the freeboard region. Therefore, the direct-coupling methodology proposed in the previous chapter cannot be applied for this comprehensive EAF CFD model establishment due to the physical complexity.

An original integration methodology was proposed in this chapter relying on the stage-by-stage approach, which developed six simulators to achieve the simulation of the entire industry-scale AC EAF steelmaking process. The six simulators are the scrap preheating simulator, the scrap melting simulator, the in-bath decarburization simulator, the freeboard post-combustion simulator, electric arc simulator, and the coherent jet simulator. Five models were established for six simulators so that each simulator can partially integrate the specific models to simulate the specific sub-processes in the industry-scale AC EAF. The simulators can perform the quantitative investigations for the coherent jet performance, the AC arc heat dissipation, the burner preheating characteristics, the scrap melting behavior, the in-bath decarburization efficiency, and the freeboard post-combustion status. Additionally, innovative numerical approaches were proposed and used in the above models, including the dual-cell approach and the stack approach for porous scrap pile melting and collapsing; the statistical sampling method for the total AC arc power delivery estimation; the CFD-compatible Monte Carlo method for the arc radiative heat dissipation estimation; the new electrode regulation algorithm for the instantaneous electrode movement prediction; the energetic approach for the prediction of the top-blown jet penetration and stirring.

### 3.1 Modeling Methodology

The present section delivers the integration methodology proposed and adopted in the comprehensive EAF CFD model for the industry-scale AC EAF. Due to the physical complexity, the direct-coupling methodology cannot be applied for the comprehensive model establishment in this chapter. The entire steelmaking process in the industry-scale AC EAF is simulated according to the innovative integration methodology given in **Figure 3.1**, which follows the stage-by-stage approach. Each stage is simulated by one or two simulators and each simulator partially integrates the specific models. The essence of the stage-by-stage approach is to use the results from the previous stage as the initial condition for the following stage. From the figure, both the scrap preheating stage and the scrap melting stage will use one simulator to simulate, respectively. The liquid steel refining stage will use two simulators to simulate including the freeboard post-combustion simulator and the in-bath decarburization simulator to reduce the computational intensity and simulation instability caused by the interaction of the supersonic jet and the bath. Based on the analysis of the basic multi-physics inside the furnace, five models need to be developed in total within those four simulators, including the scrap melting model, the electric arc model (for industry-scale AC arc), the coherent jet model, the oxidation model, and the slag foaming model. Each of model captures a phenomenon as can be recognized from the name of model and will be integrated with other models depending on the mass, energy, and momentum balance. In addition to the four simulators explained before, the electric arc model and the coherent jet model are two important models that can perform the separate simulation by themselves to provide the necessary inputs for other simulators. Therefore, two additional simulators were proposed regarding to those two models, and their corresponding studies are given in **Section 3.3.1** and **Section 3.3.2**. In summary, a total of six simulators were proposed in this chapter to simulate the sub-processes in the industry-scale AC EAF steelmaking process.

The principles of integration in each simulator are demonstrated as follows:

- 1) For the scrap preheating simulator, the developed coherent jet model can be directly coupled to the gas phase of the scrap melting model by simulating the momentum and energy from the gas injection and the oxy-fuel combustion. Integration details will be presented in **Section 3.2.3**, and simulation results will be given in **Section 3.3.3**.

- 2) The scrap melting simulator further introduces the electric arc model on the basis of the previous scrap preheating simulator, which is achieved by considering the arc heat transfer database and the arc momentum transfer database that are determined by the electric arc simulator. Integration details will be presented in **Section 3.2.2**, and simulation results will be given in **Section 3.3.4**.
- 3) For the in-bath decarburization simulator, the jet penetration cavity shape, oxygen delivery to the bath, and momentum transfer to the bath are all determined using the energetic approach based on the results from the coherent jet simulator. The above information defines the corresponding physical boundary and its boundary conditions that are used in the in-bath decarburization simulator. The oxidation model can be directly coupled to the liquid phase of the scrap melting model in the simulator to determine different species variations over time according to the decarburization reaction mechanisms. Details will be presented in **Section 3.2.4**, and simulation results will be given in **Section 3.3.5**.
- 4) The freeboard post-combustion simulator relies on the coherent jet model to capture the gas phase details, with the slag foaming model and the electric arc model respectively determining the exposed arc length as well as the radiative arc power delivery through the exposed arc, which is predefined as the boundary and its boundary condition. Details will be presented in **Section 3.2.5**, and simulation results will be given in **Section 3.3.6**.

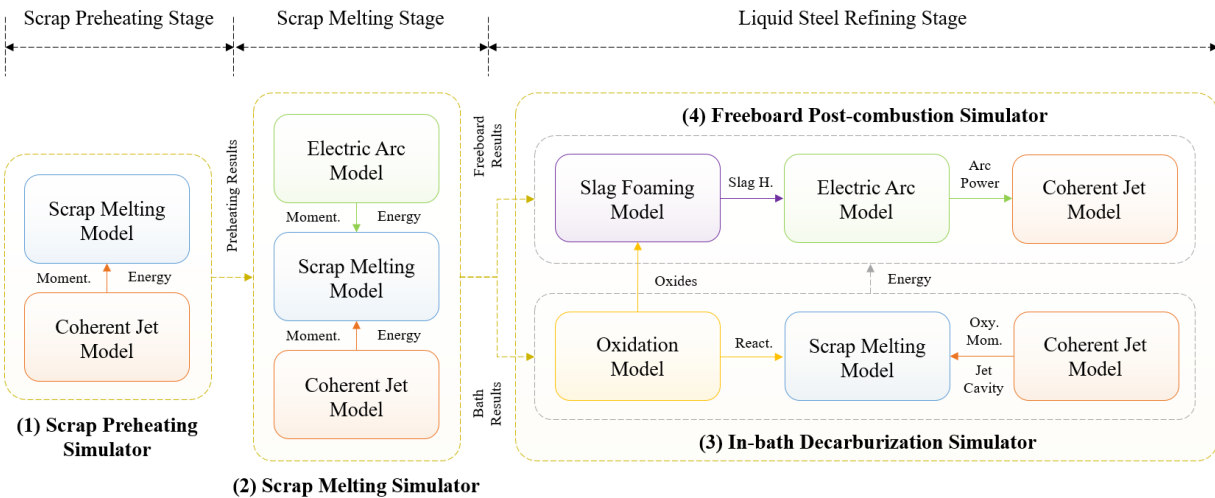


Figure 3.1. Integration methodology for the industry-scale AC EAF steelmaking process.

It should be emphasized that, in the present dissertation, the word “integrate” always represents that two models are not solved together in the same single simulation. Reversely, the word “couple” always represents that two models are solved together in the same single simulation.

## 3.2 Model Description

Five models involved in the above six simulators are illustrated in this part, including the scrap melting model, the electric arc model (for industry-scale AC arc), the coherent jet model, the oxidation model, the slag foaming model, and their integration/coupling details.

### 3.2.1 Scrap Melting Model

The present section describes the scrap melting model which is the key model in the comprehensive EAF CFD model. The hypotheses of the scrap melting model are established as follows:

- 1) The proposed model is based on the FVM CFD framework and the (ideal) principles of cell-based heat and mass transfer. The possible random processes are not considered.
- 2) All physical properties of both the solid phase (scrap) and the liquid phase (liquid steel) during the melting process are assumed to be constants including density, characteristic diameter, specific heat, thermal conductivity, and viscosity [14-16,111].
- 3) For a given scrap layer of the same scrap type (or a given scrap pile), the uniform porosity distribution is applied [15-16, 111-114].
- 4) Only vertical scrap collapse is considered due to its dominance in the collapse mechanism and the irregular random collapse at the edge of the melting pits is neglected [115].
- 5) The chemical reactions within or between solid and liquid phases are not involved in the present scrap melting simulation yet.

The scrap melting model can simulate the gas-liquid-solid three-phase system in the scrap preheating simulator, the scrap melting simulator, and the in-bath decarburization simulator. It can be coupled/integrated with the electric arc model, the coherent jet model, and the oxidation model. The details of its connections with other models are presented in **Figure 3.2**.

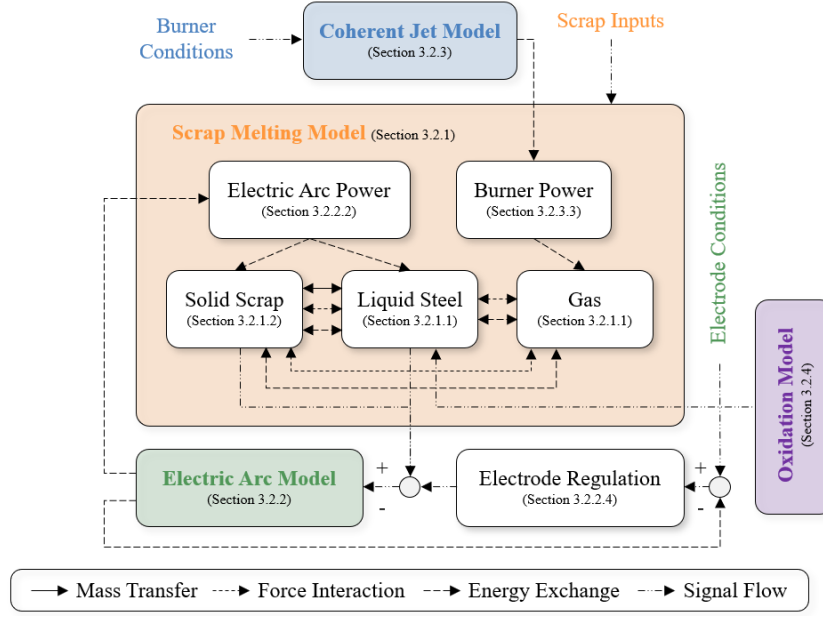


Figure 3.2. Connections of scrap melting model with other models.

### 3.2.1.1 Fluid Phases

The scrap melting model includes two fluid phases: the liquid steel phase ( $l$ ) and the gas phase ( $g$ ), both of which have fluid characteristics and are modeled using the Eulerian approach.

The mass conservation equation for fluid phases is:

$$\frac{\partial(\alpha_q \rho_q)}{\partial t} + \nabla \cdot (\alpha_q \rho_q \vec{v}_q) = \dot{m}_{s,mt} \quad (3-1)$$

where  $q$  denotes the subscript of the corresponding phase within the fluid phases; the phase volume fraction, density, velocity vector, and flow time are represented by  $\alpha_q$ ,  $\rho_q$ ,  $\vec{v}_q$ , and  $t$ , respectively;  $\dot{m}_{s,mt}$  describes the solid-liquid mass transfer rate, and is only available for the liquid steel phase.

The momentum conservation equation for fluid phases is:

$$\frac{\partial(\alpha_q \rho_q \vec{v}_q)}{\partial t} + \nabla \cdot (\alpha_q \rho_q \vec{v}_q \vec{v}_q) = -\alpha_q \nabla p + \nabla \cdot \bar{\tau}_q + \vec{F}_{q,df} + \alpha_q \rho_q \vec{g} \quad (3-2)$$

where  $p$  denotes the pressure for all fluid phases;  $\bar{\tau}_q$  signifies the phase stress-strain tensor; The drag force between phases is represented by  $\vec{F}_{q,df}$ . The acceleration of gravity in the vertical direction is denoted by  $\vec{g}$  in the vertical direction.

The energy conservation equation for fluid phases is:

$$\frac{\partial(\alpha_q \rho_q E_q)}{\partial t} + \nabla \cdot (\alpha_q \vec{v}_q (\rho_q E_q + p)) = \nabla \cdot \left( K_{eff,q} \nabla T_q - \sum_{i=1}^n h_{i,g} \vec{J}_{i,g} + \bar{\tau}_q \cdot \vec{v}_q \right) + Q_{q,ht} \quad (3-3)$$

where the phase energy, effective thermal conductivity, and temperature are denoted by  $E_q$ ,  $K_{eff,q}$ , and  $T_q$ , respectively;  $h_{i,g}$  and  $\vec{J}_{i,g}$  are the sensible enthalpy and the mass diffusion of species  $i$ , and their product represents the energy release due to the combustion reactions and is only available in the gas phase;  $Q_{q,ht}$  specifies the heat transfer between phases.

The flow field within the EAF exhibits high-temperature and high-speed characteristics under the typical EAF operation, thus the standard  $k - \varepsilon$  turbulence model is adopted to simulate the turbulent effect on the fluid phases, whose turbulent kinetic energy ( $k$ ) conservation equation and turbulent dissipation rate ( $\varepsilon$ ) conservation equation are expressed as follows:

$$\frac{\partial(\alpha_q \rho_q k_q)}{\partial t} + \nabla \cdot (\alpha_q \rho_q \vec{v}_q k_q) = \nabla \cdot \left( \alpha_q \left( \mu_q + \frac{\mu_{t,q}}{\sigma_k} \right) \nabla k_q \right) + \alpha_q G_{k,q} - \alpha_q \rho_q \varepsilon_q \quad (3-4)$$

$$\begin{aligned} \frac{\partial(\alpha_q \rho_q \varepsilon_q)}{\partial t} + \nabla \cdot (\alpha_q \rho_q \vec{v}_q \varepsilon_q) \\ = \nabla \cdot \left( \alpha_q \left( \mu_q + \frac{\mu_{t,q}}{\sigma_\varepsilon} \right) \nabla \varepsilon_q \right) + \alpha_q \frac{\varepsilon_q}{k_q} (C_{1\varepsilon} G_{k,q} - C_{2\varepsilon} \rho_q \varepsilon_q) \end{aligned} \quad (3-5)$$

where  $\mu_q$  and  $\mu_{t,q}$  represent molecular viscosity and turbulent viscosity, respectively;  $\sigma_k$ ,  $\sigma_\varepsilon$ ,  $C_{1\varepsilon}$ ,  $C_{2\varepsilon}$  are all constants in the standard  $k - \varepsilon$  turbulence model with values of 1.0, 1.3, 1.44, and 1.87, respectively.  $G_{k,q}$  denotes the kinetic energy produced by turbulence.  $\mu_{t,q}$  and  $G_{k,q}$  are evaluated as follows:

$$\mu_{t,q} = C_D' \rho_q \frac{k_q^2}{\varepsilon_q} \quad (3-6)$$

$$G_{k,q} = 2\mu_{t,q} S_{pq}^2 \quad (3-7)$$

where  $C_D'$  is a constant with the value of 0.09 and  $S_{pq}$  is the modulus of the mean rate-of-strain tensor.

### 3.2.1.2 Solid Phase

The solid phase ( $s$ ) in the scrap melting model refers to the solid scrap and is treated as a porous medium by the dual-cell approach to achieve its dynamic collapse during the melting process. The details of the scrap collapse simulation will be illustrated later. The dual-cell approach is a finite-volume-based approach and relies on the local mass and energy balance calculation between the solid phase and the gas/liquid phase. The thermal conductivity within the solid phase in between two neighbor computational cells was ignored since both scrap porosity and furnace scale are relatively large. The solid phase interacts with the fluid phases through the mass transfer and heat/force interactions. The following two equations are adopted to determine the status of the solid phase including the change of solid mass ( $m_s$ ) and solid energy ( $E_s$ ):

$$\frac{d(m_s)}{dt} = -\dot{m}_{s,mt} \quad (3-8)$$

where  $\dot{m}_{s,mt}$  is the cell-based solid mass transfer rate due to the solid scrap melting or liquid steel re-solidification. The scrap porosity ( $\gamma_s$ ) in each computational cell is determined by  $(1 - m_s/(\rho_s V_c))$ , where  $V_c$  is the cell volume.

The change of solid energy ( $E_s$ ) in each computational cell is calculated through:

$$\frac{d(E_s)}{dt} = \bar{Q}_s \quad (3-9)$$

where  $\bar{Q}_s$  presents the volumetric solid-fluid phase heat transfer, which includes the solid-gas heat transfer caused by the flame combustion, the solid-liquid heat transfer, and the solid-liquid phase energy exchange caused by the interphase mass transfer.

**Equations (3-8) to (3-9)** are solved simultaneously with the conservation equations for fluid phases to achieve the dynamic modeling of the solid-liquid-gas three-phase system.

### 3.2.1.3 Phase Interactions

The phase interactions in the scrap melting model involve the force interactions (drag forces) and the interphase heat transfers (energy exchanges).

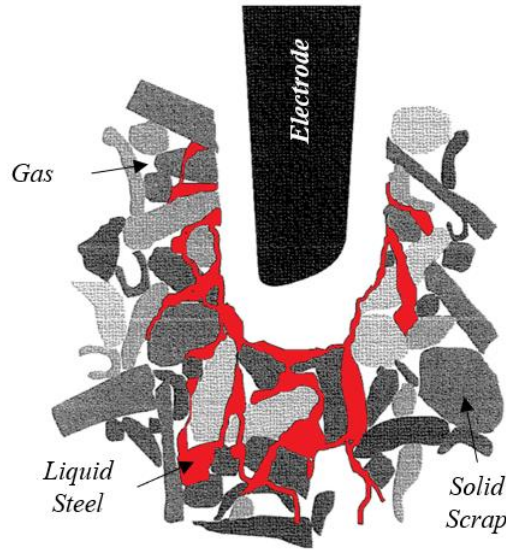


Figure 3.3. Phase interactions within gas-liquid-solid three-phase system.

The fluid phases flowing through the porous scrap pile are exerted the drag force on itself. The drag force can be described using the pressure drop governed by non-Darcian law for the flow with a high pore Reynolds number to consider the inertial losses correction as a function of the dynamic head [117]. The corresponding expression for the pressure drop is given by:

$$\nabla p_q = - \left( \frac{\mu_q}{\beta_s} \gamma_s \vec{v}_q + \frac{C_s \gamma_s^2}{2} \rho_q |\vec{v}_q| \vec{v}_q \right) \quad (3-10)$$

where  $\mu_q$ ,  $\beta_s$ , and  $C_s$  denote the corresponding phase viscosity, scrap permeability, and inertial resistance factor of scrap, respectively. The Ergun equation [118], which is a semi-empirical correlation valid across a large range of Reynolds numbers and for flow through porous media, is adopted to determine the latter two variables:

$$\beta_s = \frac{\gamma_s^3 d_s^2}{150(1 - \gamma_s)^2} \quad (3-11)$$

$$C_s = \frac{3.5(1 - \gamma_s)}{d_s \gamma_s^3} \quad (3-12)$$

where  $d_s$  is the characteristic diameter of the selected scrap whose value is taken to be 0.027 m for the shredded type based on the experimental measurement [18,112].

The drag force also takes place in between the flowing liquid and gas phase. As both liquid phase and gas phase has the potential to be dominant for every computational cell within the domain, the symmetric model is used to determine the liquid-gas force interaction:

$$\vec{F}_{gl} = \frac{C_D Re_{gl} \mu_{gl} A_{gl}}{8d_l} (\vec{v}_l - \vec{v}_g) \quad (3-13)$$

where  $Re_{gl}$  and  $\mu_{lg}$  are fluid phases' Reynolds number and viscosity, respectively;  $A_{gl}$  denotes the liquid-gas interfacial contact area which as determined using the symmetric model;  $C_D$  is the drag coefficient between the liquid phase and the gas phase and is evaluated through [119]:

$$C_D = \begin{cases} \frac{24(1 + 0.15Re_{gl}^{0.687})}{Re_{gl}} & (Re_{gl} \leq 1000) \\ 0.44 & (Re_{gl} > 1000) \end{cases} \quad (3-14)$$

**Equations (3-10) to (3-14)** are solved together before every time step to define momentum source terms in the aforementioned **Equation (3-2)** for the fluid resistance.

The heat transfers within the liquid-solid pair, the gas-liquid pair, and the gas-solid pair are evaluated along with the interphase force interactions. The liquid to solid/gas heat transfer is

mainly due to the direct contact between the hot liquid steel and the cold scrap/gas, causing the hot liquid steel itself to re-solidify, which in turn impacts the scrap bulk density and subsequent scrap melting patterns. The present model estimates the liquid-solid convective heat transfer coefficient ( $h_{ls}$ ) through the following as suggested by the previous research [120]:

$$h_{ls} = \begin{cases} \frac{(0.664Re_{ls}^{0.5}Pr_l^{0.333})\lambda_l}{d_s} & (\text{above} - \text{bath}) \\ \frac{2\gamma\sqrt{Re_{ls}Pr_l}\lambda_l}{(1.55\sqrt{Pr_l} + 3.09\sqrt{0.372 - 0.15Pr_l})d_s} & (\text{in} - \text{bath}) \end{cases} \quad (3-15)$$

where  $Pr_l$  and  $\lambda_l$  are the Prandtl Number and thermal conductivity of the liquid phase, respectively;  $\gamma$  is a scaling factor taken as 0.01 for typical EAF conditions. The gas-liquid heat transfer coefficient ( $h_{gl}$ ) is determined from a Nusselt correlation derived from the theoretical consideration by Ranz-Marshall [121], which is expressed as:

$$h_{gl} = \frac{(2 + 0.6Re_{gl}^{0.5}Pr_g^{0.333})\lambda_g}{d_l} \quad (3-16)$$

where  $d_l$  is the characteristic diameter of the liquid steel which is taken to be 0.001 m.

The gas-solid convective heat transfer coefficient ( $h_{gs}$ ) is critical in the present model since it dominates the scrap heating and melting rate and is affected by the combustion flame produced from the coherent jet burner and the overall gas flow status, thus the details are provided later in **Section 3.2.3** for better readability.

#### 3.2.1.4 Melting/Re-solidification

The numerical modeling of solid scrap melting and liquid steel re-solidification is achieved by the solid-liquid mass transfer. The triggering of the mass transfer is judged according to the phase temperature. For a target computational cell, the solid phase mass is completely transferred to the liquid phase when the temperature of the solid phase ( $T_s$ ) is higher than the liquidus temperature ( $T_{liquidus}$ ). Instead, the mass transfer path is reversed from the liquid phase to the solid phase when

the liquid phase temperature ( $T_l$ ) is lower than the solidus temperature ( $T_{solidus}$ ). The above mechanism is quantitatively expressed as:

$$\dot{m}_{s,mt} = \begin{cases} \frac{dm_s}{dt} & (T_s \geq T_{liquidus}) \\ -\frac{dm_l}{dt} & (T_l < T_{solidus}) \end{cases} \quad (3-17)$$

where  $m_s$  and  $m_l$  refer to the phase mass within the target cell and the negative sign denotes the opposite mass transfer direction.

The latent heat during the melting and re-solidification process is modeled by the effective specific heat capacity method assuming a non-isothermal phase change to prevent the singularity [15,122]. A higher effective specific heat capacity value in the melting range between solidus temperature and liquidus temperature is assigned to consider the extra supplied or extracted heat for the state change of a substance. The effective specific heat capacity ( $C_{p,eff}$ ) in the present model is given by:

$$C_{p,eff} = \begin{cases} C_{p,s} & (T < T_{solidus}) \\ C_{p,s} + \frac{h_{fusion}}{T_{liquidus} - T_{solidus}} & (T_{solidus} \leq T \leq T_{liquidus}) \\ C_{p,l} & (T > T_{liquidus}) \end{cases} \quad (3-18)$$

where  $C_{p,s}$  and  $C_{p,l}$  are the specific heat capacity for the solid phase and the liquid phase, respectively;  $h_{fusion}$  is the latent heat of fusion.

### 3.2.1.5 Scrap Collapse

Normally, the burners or electrodes are usually immersed inside the scrap pile to operate during the scrap heating or melting to maximize heat transfer efficiency, thus the scrap begins to melt near the heat source forming the cavities in the middle and lower parts of the pile, which consequently causes the scrap to collapse. The collapsed scrap refills the cavities generated and keeps absorbing the heat along to be melted, which triggers the next collapse. This melting-collapse-melting loop keeps settling the upper un-melted scrap down to the front of burners or

electrodes to melt, hence ignorance of scrap collapse cannot make the simulation be in line with the actual condition, which may result in the inaccurate melting results. Scrap collapse should be included as an essential feature in the scrap melting model.

According to Guo et al. [123], the scrap collapse mechanism can be subdivided into irregular random collapse and vertical collapse. The former mainly refers to the scrap slippage at the edge of the melting pit. The scale and frequency of this mechanism are relatively small and the process is random, which makes it difficult to be described and simulated using a mathematical model, therefore this collapse mechanism is not included in the model. The present study only considers the vertical collapse dominant in the scrap collapse mechanism, that is, a rapid scrap collapse in the vertical direction due to insufficient support to the upper scrap by the bottom.

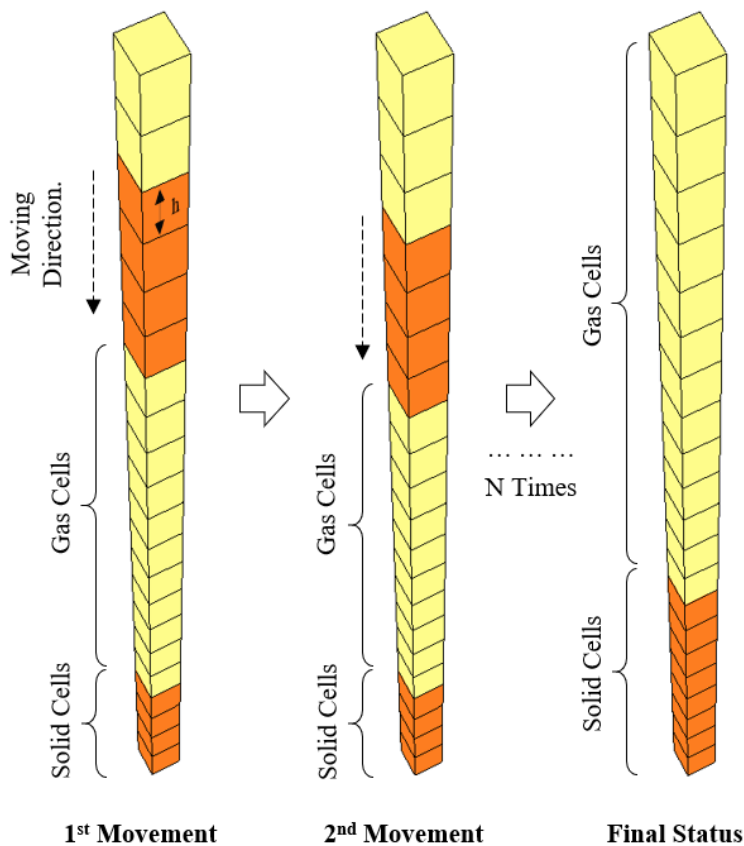


Figure 3.4. Sketch diagram of stack approach.

The present study proposed a numerical approach, the stack approach, which is compatible with the dual-cell approach, to dynamically implement the scrap collapse simulation in the scrap melting model. The basic principle of the stack approach is to scan the entire computational domain containing the fully-structured mesh layer by layer to locate the cells with zero solid volume fraction and fill them by settling the upper solid phase within the same stack. **Figure 3.4** and **Figure 3.5** demonstrates the schematic theoretical diagram of the aforementioned stack approach. To guarantee the mass conservation of solid phase when moving downward, the fully-structured mesh for the computational domain should have the same cell layer height ( $h_c$ ) and bottom projection shape, so that all cell volumes within the same stack can be consistent. Each execution of the stack approach makes the solid phase settlement occur between two adjacent cells. The continuous collapse can be achieved by executing the stack approach multiple times within a time step.

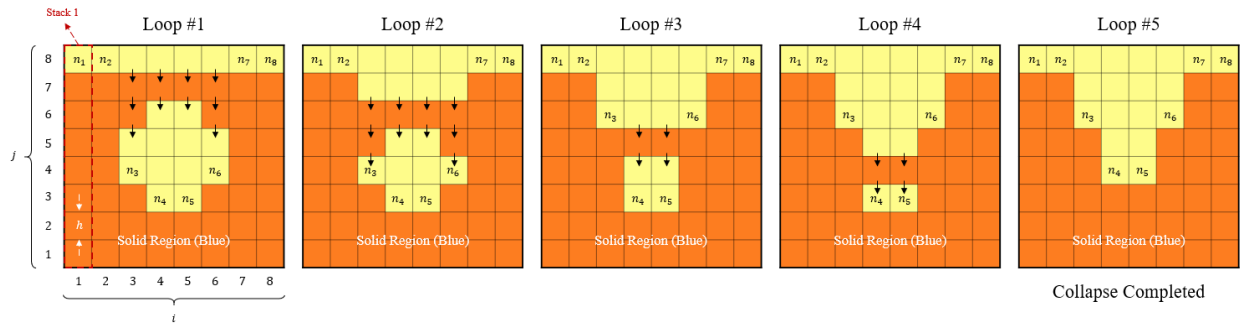


Figure 3.5. Application of stack approach for dynamic scrap collapse simulation.

The detailed algorithm for the stack approach is given below and the corresponding flow chart is shown in **Figure 3.6**:

- 1) Label all computational cells in the form of two-dimensional arrays  $(i, j)$ , where  $i$  is the vertical stack number, and  $j$  is the horizontal layer number whose smallest value locates at the bottom of each stack.
- 2) Determine  $n_i$  for the stack  $i$ , which indicates the first solid-phase-empty cell (solid-phase volume fraction = 0) closest to the bottom of the stack.
- 3) Move all solid-phase quantities in cells within the stack  $i$  meeting the horizontal layer number  $j > n_i$  a cell down, which is mathematically expressed as:

$$m_{s(i,j)} = m_{s(i,j+1)} \quad (j = n_i, n_i + 1, n_i + 2, \dots) \quad (3-19)$$

$$E_{s(i,j)} = E_{s(i,j+1)} \quad (j = n_i, n_i + 1, n_i + 2, \dots) \quad (3-20)$$

- 4) Loop step (2) to (3) until cells in the stack  $i$  with  $j > n_i$  are solid-phase-empty cells to complete the performance of scrap collapse within this target stack.
- 5) Repeat the above steps for all stack until the entire scrap pile collapsed.

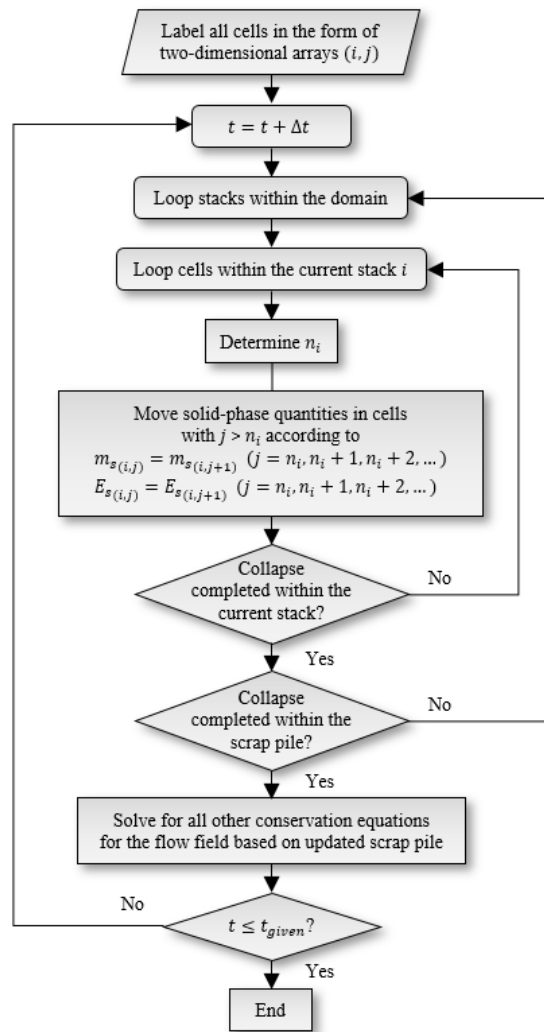


Figure 3.6. Algorithm of stack approach.

The scrap collapse simulation using the stack approach is triggered at beginning of each time step to update the solid phase distribution. The new scrap pile distribution is used for solving all other conservation equations in the current time step.

### **3.2.2 Electric Arc Model (for Industry-scale AC Arc)**

The present section describes the electric arc model developed for the comprehensive EAF CFD model. The electric arc simulator mentioned above is based on this model, which can perform a separate industry-scale AC arc simulation to determine the arc heat transfer database and the arc momentum transfer database for the scrap melting model. The real physical phenomena involved in the AC arc are complicated thus the following hypotheses were made when establishing the mathematical model in order to balance the computation time and the result accuracy:

- 1) The electric arc plasma is treated as an incompressible Newtonian fluid with temperature-dependent thermodynamic properties [44,46,47,125].
- 2) The electric arc plasma is optically thin and in a state of local thermodynamic equilibrium (LTE), that is, the temperature of the electron can be approximated as the temperature of heavy particles [44,46,47,125]. This assumption is valid in most regions within the arc column, except in the fine sheath close to the cathode/anode surface since the electron temperature there needs to be higher to maintain a conductor path between the arc column and the surface. To simplify the fine sheath modeling, the electrical conductivity of computational cells in the first layer adjacent to the cathode/anode surface is modified to be the same as that of the cathode/anode material so that the fine sheath can be considered as the Ohmic conductor to ensure the transition between the arc column and the cathode/anode surface [44,47,125].
- 3) The electric arc plasma is considered to be axisymmetric in the 2D configuration with the non-deformable flat electrode tip and scrap surface for the simplification purpose. Therefore, the cathodic white-hot spot is assumed to be fixed at the center of the cathode/anode surface for a better boundary condition allocation and future quantitative analysis [49,52].
- 4) The gravity effect is ignored for all cases in the electric arc simulator since the magnitude of electric arc plasma weight is much smaller compared with that of the axial pressure gradient during arcing [44,46,47,49,52,102,125].

### 3.2.2.1 Governing Equations

A set of time-dependent governing equations is proposed based on the above hypotheses to describe the AC electric arc plasma under the cylindrical coordinate.

The mass conservation equation is:

$$\frac{\partial(\rho)}{\partial t} + \frac{1}{r} \frac{\partial(r\rho v_r)}{\partial r} + \frac{\partial(\rho v_x)}{\partial x} = 0 \quad (3-21)$$

where  $\rho$ ,  $v$ ,  $t$  represent the density, the velocity vector component, and the flow time, respectively.

The momentum conservation equation is:

$$\begin{aligned} \frac{\partial(\rho v_x)}{\partial t} + \frac{1}{r} \frac{\partial(r\rho v_r v_x)}{\partial r} + \frac{\partial(\rho v_x^2)}{\partial x} \\ = -\frac{\partial p}{\partial x} + \frac{\partial}{\partial x} \left( 2\mu \frac{\partial v_x}{\partial x} \right) + \frac{1}{r} \frac{\partial}{\partial r} \left( r\mu \left( \frac{\partial v_x}{\partial r} + \frac{\partial v_r}{\partial x} \right) \right) + j_r B_\theta \end{aligned} \quad (3-22)$$

$$\begin{aligned} \frac{\partial(\rho v_r)}{\partial t} + \frac{1}{r} \frac{\partial(r\rho v_r^2)}{\partial r} + \frac{\partial(\rho v_x v_r)}{\partial x} \\ = -\frac{\partial p}{\partial r} + \frac{1}{r} \frac{\partial}{\partial r} \left( 2r\mu \frac{\partial v_r}{\partial r} \right) + \frac{\partial}{\partial x} \left( \mu \left( \frac{\partial v_r}{\partial x} + \frac{\partial v_x}{\partial r} \right) \right) - \frac{2\mu v_r}{r^2} - j_x B_\theta \end{aligned} \quad (3-23)$$

where  $p$  and  $\mu$  represent the pressure and the viscosity, respectively;  $j$  and  $B_\theta$  are the current density component and the azimuthal magnetic induction, respectively, and their product reflects the plasma acceleration effect on the flow field caused by the Lorentz force.

The energy conservation equation is:

$$\begin{aligned} \frac{\partial(\rho T)}{\partial t} + \frac{1}{r} \frac{\partial(r\rho C_p v_r T)}{\partial r} + \frac{\partial(\rho C_p v_x T)}{\partial x} \\ = \frac{1}{r} \frac{\partial}{\partial r} \left( r k_{eff} \frac{\partial T}{\partial r} \right) + \frac{\partial}{\partial x} \left( k_{eff} \frac{\partial T}{\partial x} \right) + \frac{j_x^2 + j_r^2}{\sigma} + \frac{5}{2} \frac{k_B}{e} \left( j_x \frac{\partial T}{\partial x} + j_r \frac{\partial T}{\partial r} \right) \\ - S_r \end{aligned} \quad (3-24)$$

where  $T$  is the temperature;  $C_p$  is the specific heat;  $k_{eff}$  is the effective thermal conductivity;  $\sigma$  is the electrical conductivity;  $k_B$  is the Boltzmann constant whose value is  $1.38 \times 10^{-23} J/K$  and  $e$  is the elementary charge whose value is  $1.6 \times 10^{-19} C$ . Last three terms included in this equation represent the Joule heating effect, the electronic enthalpic flux, and the radiation loss of plasma itself ( $S_r$ ), respectively.

Based on the estimation from Alexis et al. [46], and Wang et al. [47], Qian et al. [124], the industry-scale arc with the high current has a large temperature and velocity gradient, and its Reynolds number  $R_e$  can reach up to  $2.7 \times 10^5$ . Therefore, the standard  $k - \varepsilon$  turbulence model is adopted to describe the turbulent effect of plasma as suggested by the above researchers. The turbulent kinetic energy ( $k$ ) conservation equation and its dissipation rate ( $\varepsilon$ ) conservation equation can be expressed as:

$$\frac{\partial(\rho k)}{\partial t} + \frac{1}{r} \frac{\partial(r \rho v_r k)}{\partial r} + \frac{\partial(\rho v_x k)}{\partial x} = \frac{\partial}{\partial x} \left( \frac{\mu_{eff}}{\sigma_k} \frac{\partial k}{\partial x} \right) + \frac{1}{r} \frac{\partial}{\partial r} \left( r \frac{\mu_{eff}}{\sigma_k} \frac{\partial k}{\partial r} \right) - \rho \varepsilon + G \quad (3-25)$$

$$\begin{aligned} \frac{\partial(\rho \varepsilon)}{\partial t} + \frac{1}{r} \frac{\partial(r \rho v_r \varepsilon)}{\partial r} + \frac{\partial(\rho v_x \varepsilon)}{\partial x} \\ = \frac{1}{r} \frac{\partial}{\partial r} \left( r \frac{\mu_{eff}}{\sigma_\varepsilon} \frac{\partial \varepsilon}{\partial r} \right) + \frac{\partial}{\partial x} \left( \frac{\mu_{eff}}{\sigma_\varepsilon} \frac{\partial \varepsilon}{\partial x} \right) + \frac{\varepsilon}{k} (C_1 G - C_2 \rho \varepsilon) \end{aligned} \quad (3-26)$$

where  $\sigma_k$ ,  $\sigma_\varepsilon$ ,  $C_1$ ,  $C_2$  are all constants whose values are 1.0, 1.3, 1.44, and 1.87, respectively;  $\mu_{eff}$  represents the effective dynamic viscosity which is the sum of the molecular dynamic viscosity ( $\mu_l$ ) and the turbulent dynamic viscosity ( $\mu_t$ );  $G$  represents the volumetric generation of turbulent energy.  $\mu_t$  and  $G$  above are defined as:

$$\mu_t = C_D \rho \frac{k^2}{\varepsilon} \quad (3-27)$$

$$G = \mu_{eff} \left\{ 2 \left[ \left( \frac{\partial v_x}{\partial x} \right)^2 + \left( \frac{\partial v_r}{\partial r} \right)^2 + \left( \frac{v_r}{r} \right)^2 \right] + \left( \frac{\partial v_x}{\partial r} + \frac{\partial v_r}{\partial x} \right)^2 \right\} \quad (3-28)$$

where  $C_D$  is a constant equal to 0.09.

For the time-varying electromagnetic field excited in the AC electric arc system, the electric field and the magnetic field are governed by Maxwell's equations and can be expressed in the form of the  $A - \varphi$  formula as **Equations (3-29) to (3-30)** and **Equations (3-31) to (3-32)**, respectively:

$$\nabla \cdot \vec{E} = \frac{q}{\varepsilon_0} \quad (3-29)$$

$$\vec{E} = -\nabla\varphi - \frac{\partial\vec{A}}{\partial t} \quad (3-30)$$

$$\nabla \times \vec{H} = \vec{J} + \varepsilon_0 \frac{\partial\vec{E}}{\partial t} \quad (3-31)$$

$$\vec{H} = \frac{1}{\mu_0} \nabla \times \vec{A} \quad (3-32)$$

where  $\vec{E}$ ,  $q$ ,  $\varepsilon_0$  represent the electric intensity vector, the volume charge density, and the electric constant, respectively;  $\varphi$  and  $\vec{A}$  are the electrical potential and the magnetic vector potential, respectively;  $\vec{H}$  and  $\vec{J}$  are the magnetic intensity vector and the current density vector, respectively;  $\mu_0$  is the vacuum permeability.

By substituting **Equation (3-30)** into **Equation (3-29)** and **Equation (3-32)** into **Equation (3-31)**, following two equations can be obtained after derivation:

$$\nabla^2\varphi + \frac{\partial}{\partial t}(\nabla \cdot \vec{A}) = -\frac{q}{\varepsilon_0} \quad (3-33)$$

$$\nabla^2\vec{A} - \mu_0\varepsilon_0 \frac{\partial^2\vec{A}}{\partial t^2} = -\mu_0\vec{J} + \nabla\left(\nabla \cdot \vec{A} + \mu_0\varepsilon_0 \frac{\partial\varphi}{\partial t}\right) \quad (3-34)$$

where **Equation (3-33)** represents the variation of the electric field in the form of electrical potential and **Equation (3-34)** represents the variation of the magnetic field in the form of magnetic vector potential. In order to satisfy the one-to-one correspondence between the amount of time-varying electromagnetic field and the dynamic potential, the Lorenz gauge condition below is introduced to the above equation set:

$$\nabla \cdot \vec{A} = -\mu_0 \varepsilon_0 \frac{\partial \varphi}{\partial t} \quad (3-35)$$

so that **Equation (3-33)** to **Equation (3-34)** can be further derived as:

$$\nabla^2 \varphi - \mu_0 \varepsilon_0 \frac{\partial^2 \varphi}{\partial t^2} = -\frac{q}{\varepsilon_0} \quad (3-36)$$

$$\nabla^2 \vec{A} - \mu_0 \varepsilon_0 \frac{\partial^2 \vec{A}}{\partial t^2} = -\mu_0 \vec{j} \quad (3-37)$$

After applying the scale checking proposed by Rehmet et al. [126-127] on the current case, the second term on the left-hand side in both equations above can be eliminated since their magnitudes are much smaller than other terms. Additionally, the plasma is normally treated as a sufficiently conducting media ( $q \approx 0$ ), so that **Equations (3-36) to (3-37)** can be further simplified and expanded under the cylindrical coordinate as:

$$\frac{1}{r} \frac{\partial}{\partial r} \left( \sigma r \frac{\partial \varphi}{\partial r} \right) + \frac{\partial}{\partial x} \left( \sigma \frac{\partial \varphi}{\partial x} \right) = 0 \quad (3-38)$$

$$\frac{1}{r} \frac{\partial}{\partial r} \left( r \frac{\partial A_x}{\partial r} \right) + \frac{\partial}{\partial x} \left( \frac{\partial A_x}{\partial x} \right) = -\mu_0 j_x \quad (3-39)$$

$$\frac{1}{r} \frac{\partial}{\partial r} \left( r \frac{\partial A_r}{\partial r} \right) + \frac{\partial}{\partial x} \left( \frac{\partial A_r}{\partial x} \right) = -\mu_0 j_r + \frac{A_r}{r^2} \quad (3-40)$$

where **Equation (3-38)** and **Equations (3-39) to (3-40)** are known as the current continuity equation and the axial and the radial vector potential equations. They are in the same form as the generalized Patankar conservation equations, thus can be solved together with the other conservation equations, including mass, momentum, energy, and turbulence, to describe the AC electric arc plasma. The electrical current density component takes the following form:

$$\vec{j} = \sigma \vec{E} \quad (3-41)$$

and in order to close the system of equations, the azimuthal magnetic induction needs to be addressed as well. By calculating the Ampere's law using the radial and axial potential gradient obtained from **Equation (3-40)**, the azimuthal magnetic induction can be approximated as below:

$$B_{\theta} = \frac{\partial A_r}{\partial x} - \frac{\partial A_x}{\partial r} \quad (3-42)$$

and it is adopted to determine the Lorentz force which is described as the product of the electrical current density and the azimuthal magnetic induction.

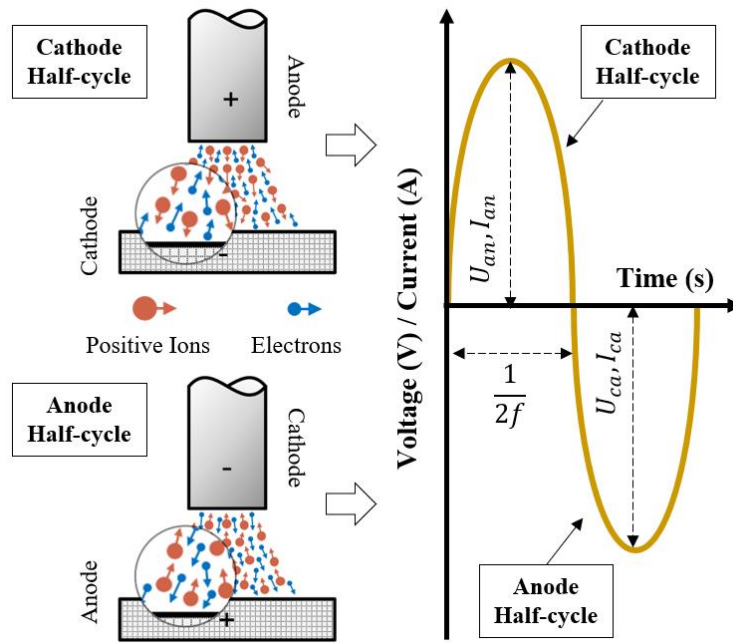


Figure 3.7. Variation of electrode polarity over time.

Considering that the electrode continuously reverses its polarity as shown in **Figure 3.7**, which causes the electrode and the scrap to serve as the cathode/anode and anode/cathode in turn, the current density ( $j$ ) of a parabolic distribution determined by the instantaneous current is successively applied on the electrode tip/scrap surface. The current density ( $j$ ) is given as:

$$j(r) = \begin{cases} 2J_c \left[ 1 - \left( \frac{r}{R_c} \right)^2 \right] & (r \leq R_c) \\ 0 & (r > R_c) \end{cases} \quad (3-43)$$

where  $J_C$  is taken as the average current density within the cathode white-hot spot ( $4.4 \times 10^7 \text{ A/m}^2$ ) [46-47];  $r$  is the distance from the axis of the computational domain;  $R_C$  is the cathode white-hot spot radius (or the cutoff radius) which can be defined as:

$$R_C = \sqrt{\frac{i}{\pi J_C}} \quad (3-44)$$

where  $i$  is the instantaneous value of current as a function of time and presented in the form of a sinusoidal waveform equation which is written as:

$$i(t) = \sqrt{2}I_{RMS}\sin(2\pi ft + \phi) \quad (3-45)$$

where  $I_{RMS}$  is the root mean square (RMS) of current;  $f$  is the frequency of current;  $\phi$  is the phase shift from a certain reference point and is taken as zero in this study.

It is noted that the high frequency of AC arc polarity variation (50 - 60 Hz) leads to an unaffordable total computational time for the scrap melting simulator if directly coupling the electric arc model into the gas phase of the scrap melting model. Therefore, the integration follows the method described below: a large number of separate industry-scale AC arc simulations will be performed first by the electric arc simulator, which is based on the electric arc model, according to the common-used electrical conditions to determine the arc heat dissipation database and the arc momentum transfer database. Afterward, the scrap melting simulator can directly retrieve the arc heat dissipation and momentum transfer amounts from the database and distribute them to the desired computational cells when simulating the scrap melting by the arc. The following two sections detail the evaluation of the arc heat dissipation and the arc momentum transfer.

### ***3.2.2.2 Arc Heat Dissipation***

During the arcing, the arc terminations keep wandering over the electrode tip surface and the scrap/liquid surface randomly. As shown in **Figure 3.8**, the twisted arc column in between releases a large amount of heat, which is normally dissipated in the form of convection ( $Q_c$ ), radiation ( $Q_r$ ), and electron flow ( $Q_e$ ), so that the solid scrap burden melts, accompanied by significant heating of the surrounding gas.

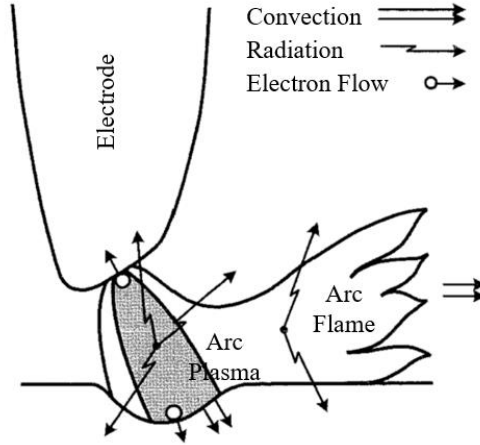


Figure 3.8. Arc heat dissipation mechanism.

Within the arc-scrap-gas system, the total arc power generation ( $Q_a$ ) will eventually go to the scrap/liquid steel or the surrounding gas by the aforementioned three heat dissipation mechanisms and their relationship can be mathematically expressed as:

$$Q_a = Q_c + Q_r + Q_e \quad (3-46)$$

In the present study, the Cassie-Mayr arc model is employed to determine the arc resistance  $R$  which is treated as a dynamic electric component in the AC circuit [46,128], and the corresponding simplified electrical schematic diagram is given in **Figure 3.9**. Therefore, the arc resistance together with the arc power generation can be governed by the following two equations:

$$\frac{dR}{dt} = \frac{R}{\tau} \left( 1 - \frac{ui}{2\pi^{0.5}\sigma^{0.5}l_a^{1.5}\sigma_{SB}T^4R^{-\alpha}} \right) \quad (3-47)$$

$$Q_a = ui = iR^2 \quad (3-48)$$

where  $\tau$  represents the cooling constant of the arc;  $l_a$  represents the arc length;  $\sigma_{SB}$  is the Stefan–Boltzmann constant;  $\alpha$  is equal to one for high current values;  $u$  and  $i$  represent the arc voltage and the arc current, respectively. The heat dissipation due to each aforementioned mechanism can be estimated by the following equations [59,61]:

$$Q_c = \pi r_a^2 \rho_a v_a (h_a - h_f) \quad (3-49)$$

$$Q_r = \pi r_a^2 l_a S_r \quad (3-50)$$

$$Q_e = i \left[ O_{an} + \frac{5 k_B T_a}{2 e} + U_{an} \right] \quad (3-51)$$

where  $r_a$ ,  $\rho_a$ ,  $\bar{v}_a$ ,  $h_a$ ,  $h_f$  are the arc radius, the arc density, the arc velocity, the arc specific enthalpy, and the surrounding gas specific enthalpy, respectively;  $i$  and  $T_a$  are the arc current and the arc temperature;  $O_{an}$  and  $U_{an}$  are the work function for the anode and the anode voltage drop equal to 4.75 V and 10 V, respectively.

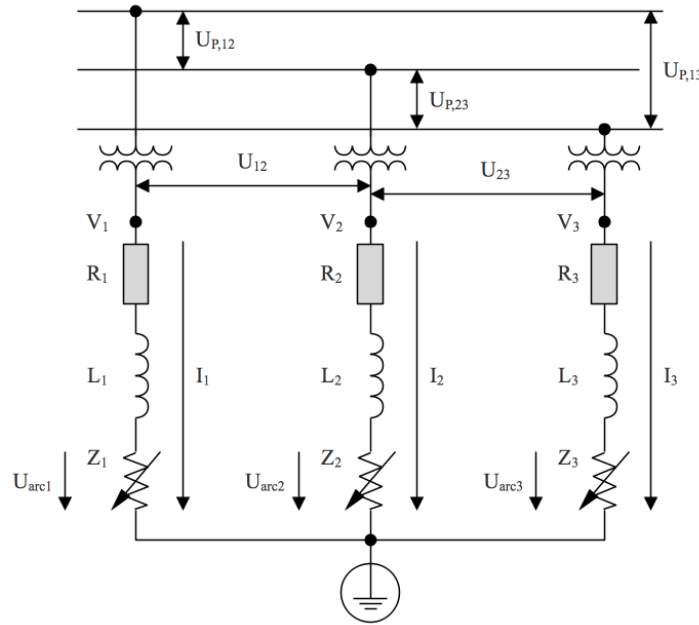


Figure 3.9. Simplified electrical schematic diagram for three-phase AC EAF.

It should be noted that the amount of arc radiative heat dissipation can also be obtained by subtracting the amount of convection and electron flow from the total arc power generation in order to strictly meet **Equation (3-46)**. In the evaluation of AC electric arc plasma, the time-averaged characteristics are considered to be more representative and meaningful than the instantaneous ones since they can objectively reflect the average performance of arc over a period of time. Therefore, the data sampling method for time statistics is introduced here to evaluate all

AC arc state variables including density, velocity, specific enthalpy, and temperature from the above arc simulation. Those state variables are assessed in the main body of the arc column, which is defined as the region where arc temperature is higher than 8000 K as suggested by Rehm et al. [127] and Bowman et al. [129]. To guarantee the accuracy, 10,000 samples covering 50 cathode half-cycles and anode half-cycles are taken during the simulation in order to get the time-averaged values. **Equations (3-47) to (3-51)** will adopt those variables for the estimation of different arc heat dissipation mechanisms. In order to ensure that the state variables used are all time-averaged, both the arc current and the arc voltage in the above estimations are also referred to the corresponding RMS values. The arc is assumed to be cylindrical and its radius is calculated through the equation below:

$$r_a = \sqrt{\frac{V_a}{\pi l_a}} \quad (3-52)$$

where  $V_a$  is the volume of arc column and also defined by the time-averaged arc temperature field.

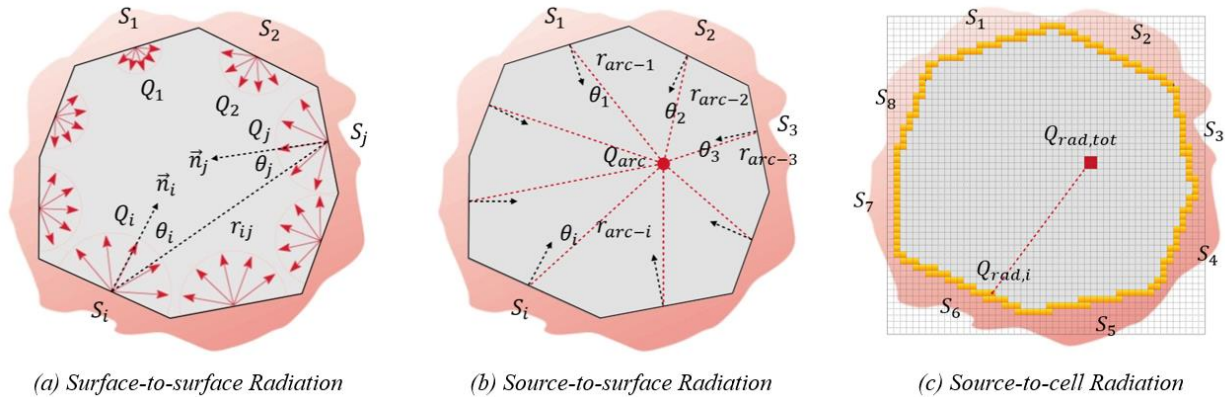


Figure 3.10. Comparison of surface-to-surface radiation, source-to-surface radiation, and source-to-cell radiation.

Additional attention should be paid to where different arc heat dissipation methods are received. The convective arc heat dissipation and electron flow are treated to be only received by the scrap/liquid surface beneath the electrode tip. While for the arc radiative heat dissipation, the heat normally can be received by all surfaces within the furnace consisting of solid scrap/liquid surface, furnace wall, and roof when they are visible to arc. The conventional CFD-compatible radiation

models, including the Surface to Surface (S2S) model, the Discrete transfer Surface (DTRM) model, the P1 model, and the Discrete Ordinates (DO) model, are only capable of simulating the radiative heat transfer between the physical boundaries of the computational domain. In the present case, the scrap/liquid surface appears as a series of interior cells instead of the physical boundaries of the computational domain, thus the area and normal vector angle of a specific surface cannot be discretized to be the cell-based variables as shown in **Figure 3.10 (c)**. Therefore, the aforementioned models cannot be employed to predict the arc-to-surface radiative heat transfer here. The present study adopts one idea from the previous research [130], applying the Monte Carlo (MC) statistical method to estimate the arc heat dissipation within the EAF, but further modifying it to be CFD-compatible. The strategy developed in the present model is illustrated as follows:

- 1) The center point of the electrode tip is configured to be the point that can randomly emit a certain number of radiation beams in the three-dimensional direction. The random emission of radiation beams is achieved by randomly selecting the azimuth and zenith angles under the spherical coordinate system.
- 2) The receiver cells include the cells marked as solid scrap surfaces, liquid bath surfaces, and the cells adjacent to the wall and roof that are not covered by scrap pile.
- 3) For a given radiation beam (e.g. beam #1), if the distance between the receiver cell center and the beam is smaller than the cell size, the cell is considered to have the potential to capture the current beam. On the straight-line propagation path of each beam, there may exist multiple receiver cells, all of which meet the criteria for capturing the current beam, but only the one closest to the emission point can serve as the receiver cell that ultimately captures the given radiation beam.
- 4) The above emission-decision-reception procedure for beam #1 is a complete evaluation period, and similar evaluation periods are adopted for all the rest of the radiation beams. After all beams are emitted and evaluated, the amount of arc radiative heat transfer  $Q_{a,i}$  on each receiver cell  $i$  can be computed through the number of radiation beams intercepted by cell  $i$  ( $N_i$ ) divided by the total number of radiation beam emissions ( $N_{tot}$ ), which is written as:

$$Q_{a,i} = \frac{N_i}{N_{tot}} Q_r \quad (3-53)$$

It should be noted that the larger the total number of radiation beams emitted, the higher the accuracy of this methodology, but it requires more computing power. The total number of radiation beams used in the present model is 50,000 to balance the result accuracy and the simulation speed.

### 3.2.2.3 Arc Impingement on Liquid Bath

Once the electrodes penetrate the scrap pile and reach the liquid bath, one of the arc terminals shifts to the liquid bath surface, and the direct contact results in the arc impingement effect (**Figure 3.11**) on the liquid bath, which causes the bath surface disturbance and further strengthens the liquid-solid convective heat transfer accelerating the in-bath scrap melting process.

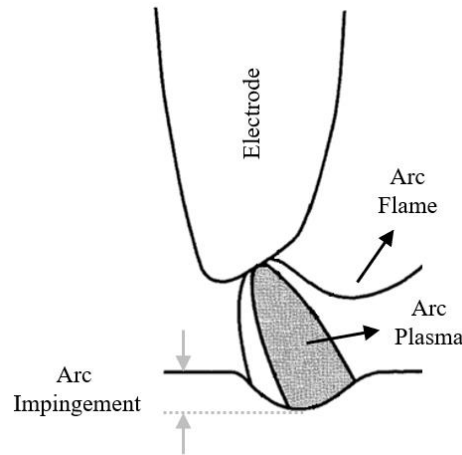


Figure 3.11. Arc impingement on liquid bath.

The above phenomenon is simulated by applying the corresponding momentum transfer  $P_l$  on the liquid bath surface beneath the electrode tips:

$$P_l = m_l \sqrt{\frac{\rho_a v_a^2}{\rho_l}} \quad (3-54)$$

where  $\rho_a$  and  $v_a$  are average AC arc density and velocity depending on the electric inputs.

### 3.2.2.4 Electrode Regulation

The typical control strategies of electrode regulation in the industry-scale EAF include the constant current control strategy, the constant impedance control strategy, and the constant power control strategy, among which the constant impedance control strategy is commonly used due to its strong anti-interference and high sensitivity.

The electrode regulation control strategy in the present model is based on the constant impedance control, whose basic principle is to keep the difference ( $\varepsilon$ ) between the measured arc voltage and the measured arc current at zero. Billings [131] deduced the similarity relation between the arc voltage measurement value and the arc length, expressed as a function of coefficient  $D'$ , and introduced the gain coefficient  $K$  of arc to link the arc current change and the arc length change. The above relation can be mathematically given as:

$$\varphi = (G_1 D' + G_2 \bar{G}) \Delta l_a \quad (3-55)$$

where  $\Delta l_a$  is the change of arc length. From the above expression, the essence of the constant impedance control strategy is to control the arc length to keep its deviation at a constant value (i.e. to make  $\varphi$  be zero by having the change of arc length  $\Delta l_a$  be zero). Therefore, the present electrode regulation strategy refers to using the instant arc length as the main value to control the electrode movement instead of calculating the impedance directly.

The strategy of achieving the constant impedance control is illustrated as follows and the corresponding sketch diagram is given in **Figure 3.12**:

- 1) Evaluate both the old electrode position from the previous time step ( $h_t'$ ) and the current scrap surface position beneath the electrode tip ( $h_s$ ) at the beginning of the time step.
- 2) Estimate the vertical height of the electrode from the difference between the old and new electrode positions, where the new electrode position ( $h_t$ ) is given by:

$$h_t = h_t' + ((h_t' - h_s) - l_a) \quad (3-56)$$

and  $l_a$  is the preset arc length suggested by the electrode manufacturer for AC EAF:

$$l_a = ((u - 40)/11.5) \quad (3-57)$$

- 3) Move the electrode to the new position to complete the electrode regulation in the current time step, and the new electrode position will be involved in the evaluation of the arc heat dissipation.

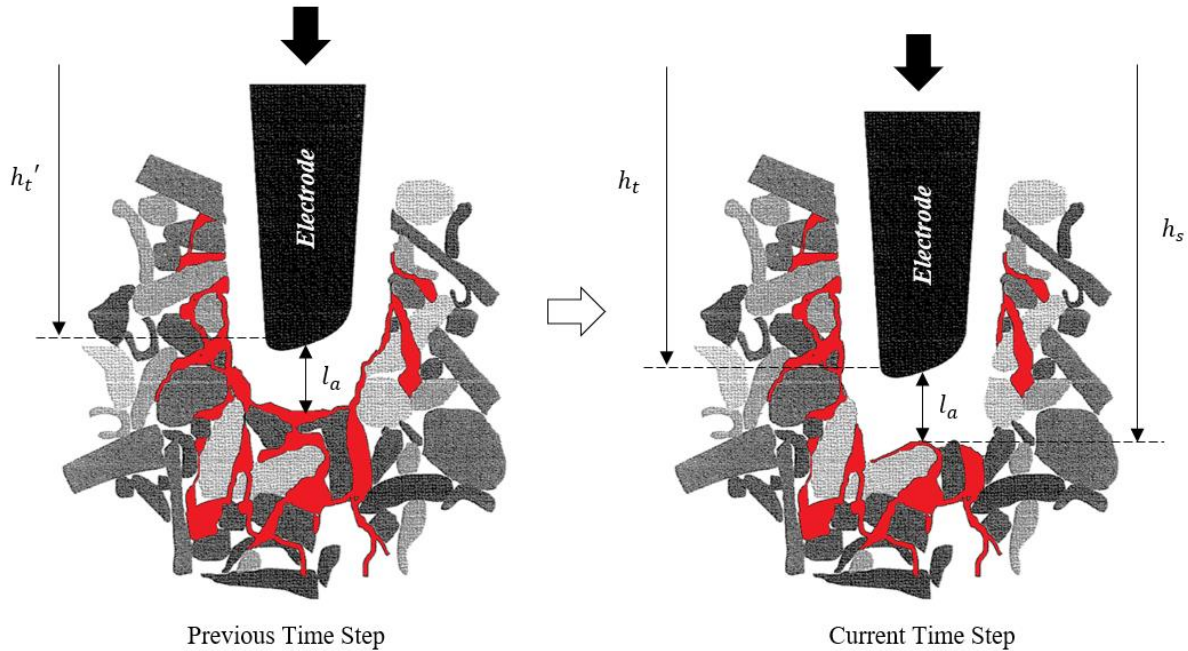


Figure 3.12. Constant impedance control for electrode regulation.

The above strategy ensures the electrode moves downwards as the scrap gradually melts beneath the electrode tip, meanwhile maintaining the distance between the electrode tip and the scrap surface equal to the preset arc length.

### 3.2.3 Coherent Jet Model

The coherent jet model developed for the comprehensive EAF CFD model is presented in this section, which is involved in all simulators except the electric arc simulator to:

- 1) Simulate the burner heating and melting process in the scrap preheating simulator and the scrap melting simulator by integrating the model into the gas phase of the scrap melting model;

- 2) Conduct a separate jet-only simulation in the coherent jet simulator to investigate the coherent jet performance or to define the physical boundary and its boundary conditions for the liquid steel refining;
- 3) Simulate the coherent jet and post-combustion for the gas region during the liquid steel refining stage in the freeboard post-combustion simulator.

### ***3.2.3.1 Shrouding Combustion Flame***

In contrast to the traditional burner, the coherent jet burner used in the modern EAFs creates the central jet shrouded by the combustion flame. The coherent jet burner is usually composed of the primary oxygen nozzle, the fuel nozzle, and the secondary oxygen nozzle. Three types of nozzles are arranged alternately in the radial direction. The primary oxygen nozzle is located in the center of the burner and is surrounded by a circle of fuel nozzles, which is further encircled by a circle of secondary oxygen nozzles. The coherent jet burner has both lance mode and burner mode. The lance mode is mostly used in the refining stage to agitate the liquid bath and deliver oxygen to the bath for the decarburization process. Under the lance mode, the primary oxygen nozzle with a high flow rate (around 1200 SCFM) produces the supersonic oxygen jet, while the corresponding flow rates of the fuel nozzle and the secondary oxygen nozzle are relatively low (around 80 SCFM), only to generate the shrouding combustion flame envelop to protect the central supersonic oxygen jet and slow the momentum decay in its traveling path. The burner mode is mainly adopted in the preheating and melting stage with the maximum burner power up to around 5 MW. Under this mode, the flow rate of the primary oxygen nozzle is reduced to around 300 SCFM so that the central oxygen jet is routinely to be in subsonic or sonic status. Instead, the corresponding flow rates through the fuel nozzles and the secondary oxygen nozzles are significantly elevated to be around 300 SCFM, which creates a larger flame and increases the burner power.

The shrouding flame around the central oxygen jet, as stated above, is the essential characteristic of the coherent jet compared to the conventional jet, greatly preventing entrainment of the ambient gas into the central oxygen jet and improving the jet potential core length, as shown in **Figure 3.13**. To simulate the shrouding flame created by the non-premixed combustion, the species transport model and the eddy-dissipation model with a 2-step natural gas-oxygen combustion mechanism are adopted to calculate the local mass fraction of each species ( $i$ ) and the heat release from the

combustion reactions, assuming that the mixing rate of the flow turbulence with the fuel and oxidizer is slower than their burning rate in the reaction zone.

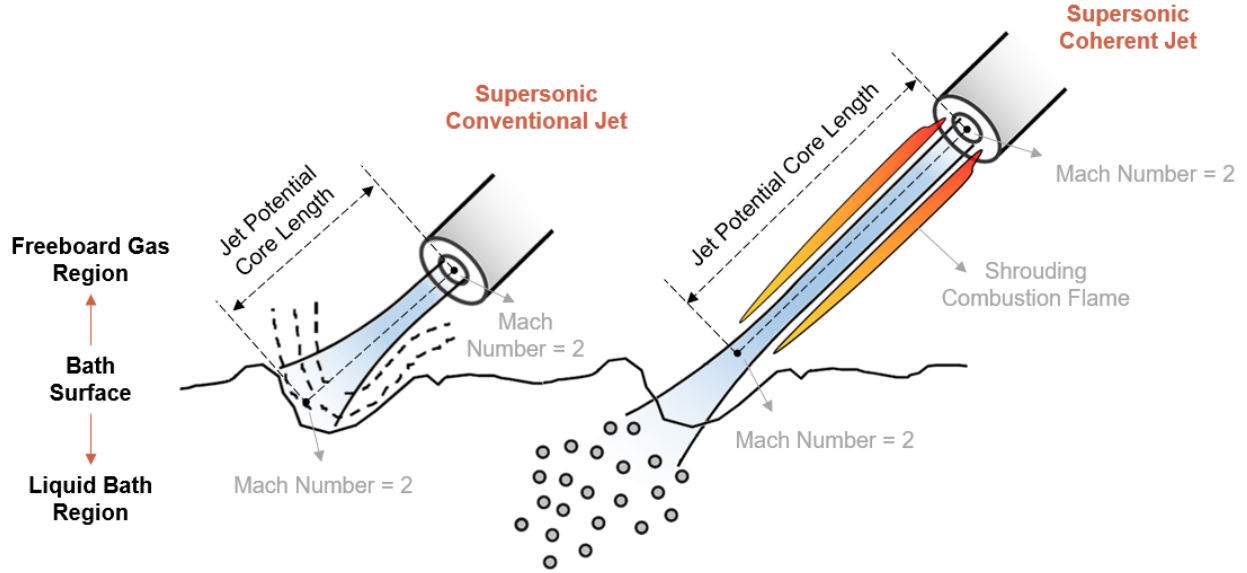


Figure 3.13. Comparison of conventional jet and coherent jet used in liquid steel refining stage.

The conservation equation of each species in the gas phase is expressed by:

$$\frac{\partial(\alpha_g \rho_g Y_{i_g})}{\partial t} + \nabla \cdot (\alpha_g \rho_g \vec{v}_g Y_{i_g}) = -\nabla \cdot \alpha_g \vec{J}_{i_g} + \nabla \cdot \left( \sum_{i=1}^n h_{i_g} \vec{J}_{i_g} \right) + \alpha_g R_{i,r_g} \quad (3-58)$$

where  $Y_{i_q}$  is the local mass fraction of each species;  $\vec{J}_{i_g}$  is the mass diffusion in turbulent flows due to gradients of concentration and temperature and can be calculated through:

$$\vec{J}_{i_g} = - \left( \rho_g D_{i,m_g} + \frac{\mu_{t_g}}{Sc_{t_g}} \right) \nabla Y_{i_g} - D_{T,i_g} \frac{\nabla T_g}{T_g} \quad (3-59)$$

where  $D_{i,m_g}$ ,  $Sc_{t_g}$ , and  $D_{T,i_g}$  are the mass diffusion coefficient for each species in the mixture, the turbulent Schmidt number, and the thermal (Soret) diffusion coefficient, respectively;  $R_{i_q}$  is the net rate of production of each species by chemical reaction and can be estimated through the smaller value of the following two expressions (the eddy-dissipation model):

$$R_{i,r_g} = v'_{i,r_g} M_{w,i_g} A \rho_g \frac{\varepsilon_g}{k_g} \min \left( \frac{Y_{\mathcal{R}_g}}{v'_{\mathcal{R},r_g} M_{w,\mathcal{R}_g}} \right) \quad (3-60)$$

$$R_{i,r_g} = v'_{i,r_g} M_{w,i_g} A B \rho_g \frac{\varepsilon_g}{k_g} \frac{\sum_P Y_{P_g}}{\sum_j v''_{j,r_g} M_{w,j_g}} \quad (3-61)$$

where  $v'_{i,r_g}$  and  $v'_{\mathcal{R},r_g}$  are the stoichiometric coefficients for reactant  $i$  and  $\mathcal{R}$  in reaction  $r$ , while  $v''_{j,r_g}$  is the stoichiometric coefficient for product  $j$  in reaction  $r$ ;  $M_{w,i_g}$  and  $M_{w,\mathcal{R}_g}$  are the molecular weight of species  $i$  and  $\mathcal{R}$ , while  $M_{w,j_g}$  is the molecular weight of product  $j$ ;  $A$  and  $B$  are the empirical constant equal to 4.0 and 0.5 in the model;  $Y_{\mathcal{R}_g}$  and  $Y_{P_g}$  are the mass fraction of a particular reactant  $\mathcal{R}$  and a particular product species  $P$ .

The Discrete Ordinates (DO) radiation model is used to capture the radiative heat transfer due to the shrouding combustion flame in the gas phase. The corresponding conservation equation to calculate the radiation intensity ( $I$ ) in the given beam direction ( $\vec{s}$ ) and the position ( $\vec{r}$ ) is given by:

$$\nabla \cdot [I(\vec{r}, \vec{s}) \vec{s}] + (a + \sigma_s) I(\vec{r}, \vec{s}) = a n'^2 \frac{\sigma T_g^4}{\pi} + \frac{\sigma_s}{4\pi} \int_0^{4\pi} I(\vec{r}, \vec{s}') \phi(\vec{s} \cdot \vec{s}') d\Omega' \quad (3-62)$$

where  $\sigma_s$ ,  $n'$ ,  $\sigma$ ,  $\phi$ , and  $\Omega'$  denote the scattering coefficient of the gas, the refractive index of the gas, the Stefan-Boltzman constant, the phase function, and the solid angle, respectively;  $a$  represents the absorption coefficient, which is defined through:

$$a = - \frac{l n(1 - \varepsilon')}{s} \quad (3-63)$$

where the total emissivity ( $\varepsilon'$ ) over the path length ( $s$ ) above is determined by the weighted-sum-of-gray-gases model (WSGGM) which considers the particular absorption bands for the combusting flow in the gas phase:

$$\varepsilon' = \sum_{i=0}^I a_{\varepsilon,i}(T_g) (1 - e^{-k'_i P_g S}) \quad (3-64)$$

where  $k'_i$  is absorption coefficient of the  $i$ th fictitious gray gas;  $P_g$  denotes the sum of the partial pressures of all absorbing gases;  $a_{\varepsilon,i}$  is the emissivity weighting factor which is dependent of gas temperature and is estimated through:

$$\varepsilon' = \sum_{i=0}^I a_{\varepsilon,i}(T_g) (1 - e^{-k'_i P_g S}) \quad (3-65)$$

where  $b_{\varepsilon,i,j}$  is the emissivity gas temperature polynomial coefficients.

### 3.2.3.2 Turbulence Viscosity Correction

The previously introduced standard  $k - \varepsilon$  turbulence model does not account for the influence of temperature gradients on the turbulent mixing zone within the gas phase, thus the mixed growth rate of the shear layer near the shrouding flame cannot be correctly captured for the coherent jet. The temperature corrected method is adopted in the current model to modify the gas turbulence viscosity ( $\mu_t$ ) based on Alarm's research work [69] to make the gas flow be sensitive to the shrouding flame. Therefore, the gas turbulent viscosity in **Equation (3-6)** is modified as:

$$\mu_{t,g} = \frac{0.09 \rho_g k_g^2}{C_T \varepsilon_g} \quad (3-66)$$

where  $C_T$  is characterized as a function of the gas temperature and velocity field, as follows:

$$C_T = 1 + \frac{C_1 T_g^\xi}{1 + C_2 f(M_\tau)} \quad (3-67)$$

where  $C_1$ ,  $C_2$  and  $\xi$  above are constantly equal to 1.2, 1.0 and 0.6, respectively;  $T_g$  and  $f(M_\tau)$  are the normalized local total gas temperature gradient and the function considering the influence of turbulent Mach number, respectively, and they can be estimated as follows:

$$T_g = \frac{k_g^{\frac{3}{2}} |\nabla T_{t,g}|}{\varepsilon_g T_{t,g}} \quad (3-68)$$

$$f(M_\tau) = (M_\tau^2 - M_{\tau 0}^2) H(M_\tau - M_{\tau 0}) \quad (3-69)$$

where  $T_{t,g}$ ,  $H(x)$ , and  $M_{\tau 0}$  represent the local gas total temperature, the Heaviside function, and a constant equal to 0.1 [132], respectively;  $M_\tau$  is the turbulent Mach number defined as follows:

$$M_\tau = \frac{\sqrt{2k_g}}{a_g} \quad (3-70)$$

where  $a_g$  is the gas acoustic velocity.

### 3.2.3.3 Gas-solid Heat Transfer

The coherent jet model is integrated into the gas phase of the scrap melting model to simulate the scrap heating and melting by the coherent jet burner, thus the gas-solid heat transfer needs to be considered.

Obviously, the heat for melting the solid scrap mainly comes from the combustion flame produced by the coherent jet burner. The convective gas-solid heat transfer adopted in the present model is referred to the studies from Wakao et al. [133] and Mandal [113] to account for the effect of porous scrap pile on the heat transfer coefficient. Two different temperature ranges are considered in the estimation of the heat transfer coefficient based on the gas temperature and flow status: if the gas temperature is lower than 1373 K, the gas-solid heat transfer coefficient ( $h_{gs}$ ) is determined through:

$$h_{gs} = K_g \frac{(2 + 1.1Pr_g^{0.333} Re_{gs}^{0.6})}{d_s} \quad (T_g \leq 1373K) \quad (3-71)$$

where  $K_g$  is the gas thermal conductivity. While if the gas temperature is higher than 1373 K, the gas-solid heat transfer coefficient is defined through the volumetric heat transfer coefficient ( $h_{vgs}$ ) derived by Furnas [134] and Kitaev et al. [135] through the experimental works:

$$h_{v_{gs}} = h_{gs}A_{gs} = \frac{Af(\omega)|\vec{v}_g|^{0.9}T_g^{0.3}}{d_s^{0.75}} \quad (T_g > 1373K) \quad (3-72)$$

where  $A_{gs}$  is the gas-solid interfacial contact area;  $A$  is a coefficient related to the material type which is taken as a constant 160;  $f(\omega)$  is also a coefficient dependent on material porosity and is taken as 0.03 for the scrap melting in EAF.

It is noted that, based on the research by Mandal [18], the result difference between the case with and without gas-solid radiative heat transfer is 4% after 1-hour burner heating, and the result difference at 5 min (same as the operating time in the present study) is only about 1.3%. Moreover, the coherent jet burner under the burner mode has a much higher operating flow rate compared with the burner studied in the reference paper, thus the gas-solid convective heat transfer is dominant. Therefore, the present work did not consider the gas-solid radiative heat transfer.

The above two equations are also solved before every time step to define energy source terms for the aforementioned **Equation (3-3)** and **Equation (3-9)** to achieve the dynamic energy exchange between the gas phase and the solid phase.

#### ***3.2.3.4 Jet Penetration in Liquid Bath***

The adoption and integration of the coherent jet model in the in-bath decarburization simulator are illustrated in this sub-section. The complex phenomena of the in-bath decarburization during the liquid steel refining stage can be classified into three categories based on their major physical principles, including (1) the supersonic coherent jet above the liquid steel bath; (2) the interaction between the coherent jet and the liquid steel; (3) the in-bath stirring and decarburization.

Due to the numerical instability of simulation and the extremely high computational costs, the attempt to concurrently capture all those phenomena within a single simulation is difficult as expected. The integration of the coherent jet model in the in-bath decarburization simulator is based on the energetic approach, whose procedures are described as below and shown in **Figure 3.14**:

- 1) The separate jet-only simulation is firstly performed by the coherent jet simulator, which is based on the coherent jet model, in an open space under the actual high ambient temperature conditions inside the furnace to obtain the jet characteristics.
- 2) A theoretical interface is then calculated to represent the jet penetration cavity inside the liquid steel bath according to the previous jet-only simulation results. This method is based on the energy balance between the injected jet and penetrated bath.
- 3) The computational domain of the bath region with the above-estimated jet cavity is established for the in-bath decarburization simulator and the boundary conditions including the oxygen delivery and mass transfer through the cavity surface are also estimated from the previous jet-only simulation results so that the in-bath thermodynamic and kinetic coupled multiphase reacting flow simulation can be performed.

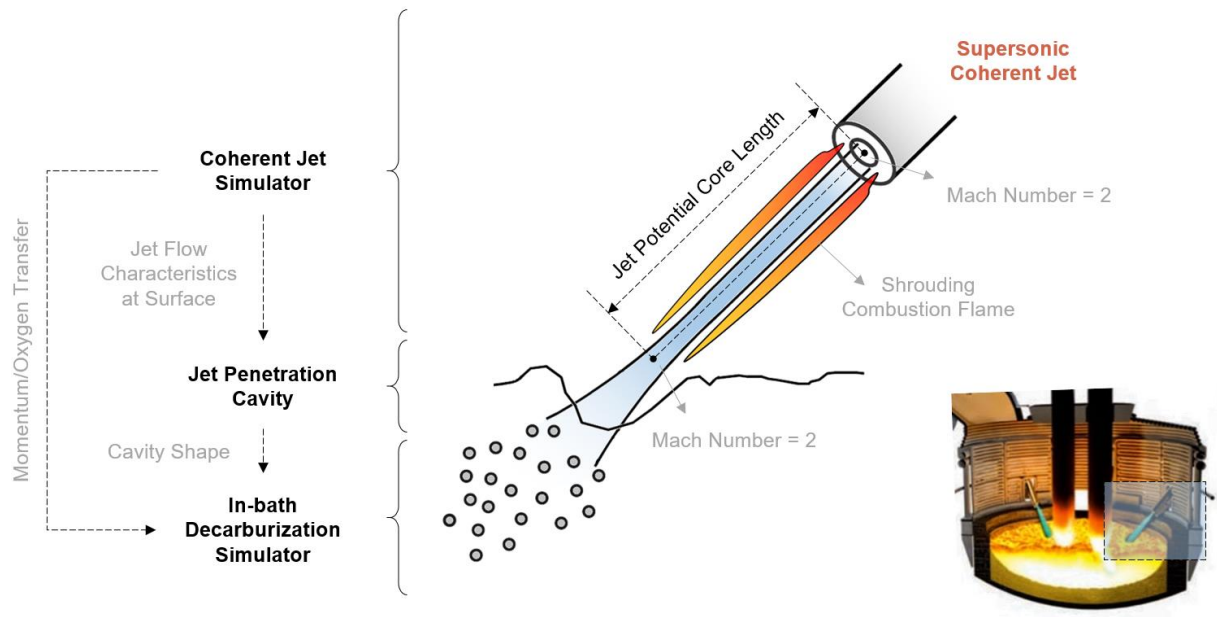


Figure 3.14. Integration of coherent jet model in the in-bath decarburization simulation.

The shape of the jet penetration cavity interface is assumed to be a revolution paraboloid based on the suggestions from Memoli et al. [90], which is more precise for the coherent jet with high momentum, as its penetration depth is greater than the radius of its cross-section. The three-

dimensional mathematical expression of a revolution paraboloid in Cartesian coordinate can be written as:

$$z = \frac{x^2 + y^2}{c} \quad (3-73)$$

where  $c$  is the constant need to be defined by a given volume of the jet penetration cavity and the penetration depth.

The volume of the jet penetration cavity  $V$  can be determined by calculating liquid steel replaced by the gas flow based on the impulsive balance at the cavity interface if ignoring the impact of the liquid steel surface tension [136]. The expression of the jet cavity volume can be written as:

$$V = \frac{\pi \rho_j v_j^2 d_j^2}{4g\rho_s} \quad (3-74)$$

where  $\rho_j$  and  $\rho_s$  are the density of primary oxygen jet and liquid steel, respectively;  $v_j$  and  $d_j$  are the primary oxygen jet velocity and diameter when at bath surface, which can be determined through the supersonic coherent jet modeling of a given distance from the nozzle exit to the bath.

Jet penetration depth  $D$  refers to an empirical formula derived by Ishikawa et al. [136], which describes the penetration depth created by the turbulent jet. For the supersonic coherent jet, the constants in the formula need to be modified accordingly. The empirical formula shows the relationship between the jet penetration depth of a single-hole or multi-holes nozzle and the burner operating conditions, which can be expressed as:

$$D = \gamma_{h_0} e^{-\frac{\sigma_1 L}{\gamma_{h_0} \cos \theta}} \quad (3-75)$$

$$\gamma_{h_0} = \sigma_2 \left( \frac{\dot{V}}{\sqrt{3}nd} \right) \quad (3-76)$$

where  $L$  is the axial distance between the nozzle exit to the bath surface;  $\theta$  is the angle of the jet inclination;  $\dot{V}$  is the volume flow rate of primary oxygen jet;  $n$  is the number of the nozzle and

equal to 1 for the current study;  $d$  is the nozzle exit diameter for primary oxygen jet;  $\sigma_1$  and  $\sigma_2$  are two constants originally equal to 1.77 and 1.67 in Ishikawa et al.'s work and those two parameters used in the present study are corrected specifically through experiments for the given type of coherent jet burner.

The actual liquid steel refining stage has the slag layer covering the liquid steel bath to protect the arc and reduce heat radiation loss. The coherent jet needs to pass through the slag layer before reaching the liquid steel bath. During this period, the jet will lose some of its momentum. Therefore, the jet penetration depth should be shorter than the one without the slag layer. In the current model, the slag layer is assumed to be converted equivalently to a corresponding liquid steel layer to include its effect on the jet penetration depth. The equivalent slag layer height  $h_s$  can be estimated by:

$$h_s = \frac{\rho_{sl}}{\rho_s} h_{sl} \quad (3-77)$$

where  $\rho_{sl}$  and  $h_{sl}$  are the values for slag layer density and slag layer height, respectively. The actual jet penetration depth  $D_{act}$  reads as:

$$D_{act} = D - h_s \quad (3-78)$$

Once the constant  $c$  is determined by solving **Equations (3-73) to (3-78)**, the theoretical parabolic jet cavity interface can be defined and included as the physical boundary of the computational domain for the in-bath decarburization simulator, which eliminates the direct consideration of supersonic jets and its interaction with the liquid surface in the simulation largely shortening the total computational time. The estimation of the three-dimensional jet penetration cavity based on actual burner operating conditions is illustrated in **Figure 3.15** and the computational domain with five jet penetration cavities established according to the actual burner arrangement provided by the industry is given in **Figure 3.16**. This computational domain will be used for the in-bath decarburization simulator.

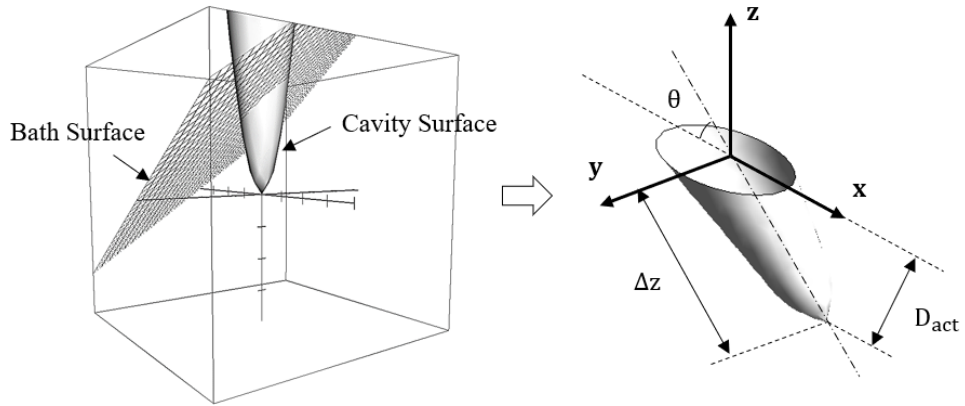


Figure 3.15. Sketch of 3D jet penetration cavity estimation.

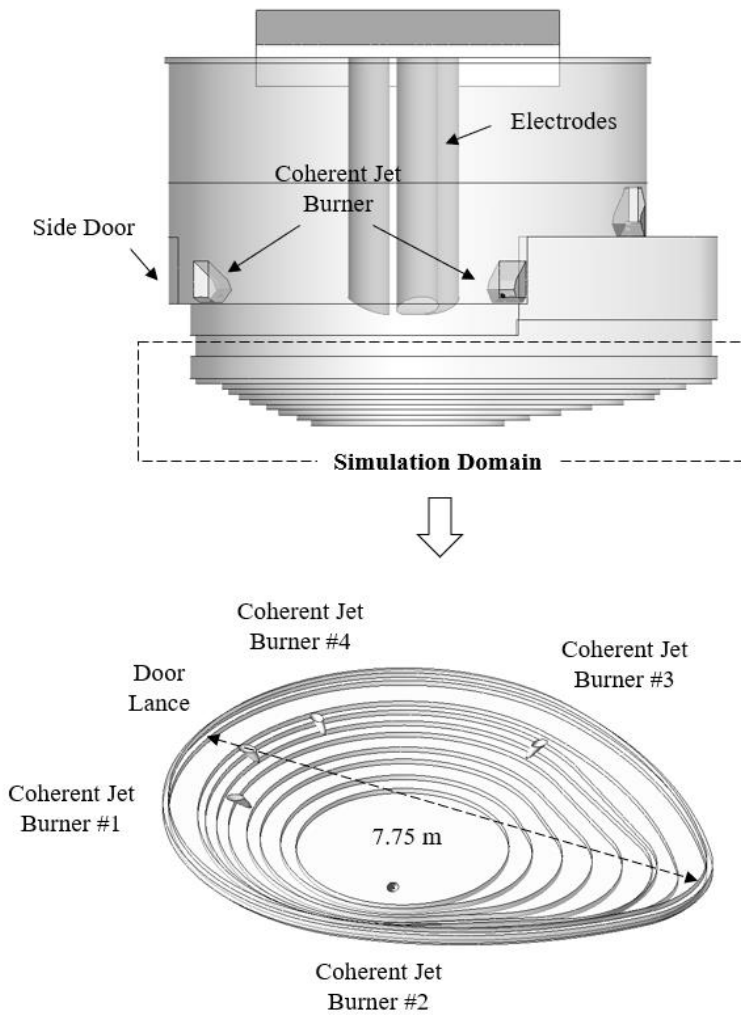


Figure 3.16. 3D computational domain with jet penetration cavities for the in-bath decarburization simulator.

The exchange of energy and substance occurs intensively between the gas phase and liquid phase when the supersonic coherent jet impinges on the liquid steel bath forming the jet penetration cavity. Therefore, the jet penetration cavity surface, as the physical boundary of the computational domain, needs to establish appropriate boundary conditions to consider the energy and substance transfer during the jet impingement. In the present study, both jet momentum transfer and delivery of the oxygen were considered. Based on the energy balance on the cavity surface, the jet momentum transferred to the liquid steel bath  $P_{s,avg}$  can be expressed as:

$$P_{s,avg} = \alpha \rho_{O_2} v_{O_2}^2 A = \frac{\alpha \rho_{O_2}^2 A}{\rho_s} \left[ \frac{1}{\Delta z} \int_{z_2}^{z_1} v_{O_2}(z) dz \right]^2 \quad (3-79)$$

where  $\alpha$  is the transferable percentage of the jet total momentum at liquid steel bath, which is 0.06 according to the reference [137];  $v_{O_2}$  is average jet velocity along cavity centerline;  $A$  is the cavity surface area;  $\Delta z$  is the length of the cavity centerline, which is equal to  $z_1 - z_2$ .

The amount of oxygen delivered to the liquid steel  $m_{O_2,avg}$  through the jet cavity can be estimated by calculating the average oxygen distribution along the cavity centerline:

$$m_{O_2,avg} = \frac{1}{\Delta z} \int_{z_2}^{z_1} m_{O_2}(z) dz \quad (3-80)$$

### 3.2.4 Oxidation Model

The present section describes the oxidation model developed for the comprehensive EAF CFD model to simulate the decarburization process during the liquid steel refining stage in the in-bath decarburization simulator. **Figure 3.17** shows the detailed mechanism and phenomena of the in-bath exothermic oxidation reactions during the liquid steel refining stage.

The oxidation model can be directly coupled to the liquid phase of the scrap melting model to consider a liquid steel-oxygen two-phase reacting flow system, in which the oxygen enters the domain through the pre-defined jet penetration cavity surface to react with carbon and other impurities. The injected oxygen results in two main effects on the system including the stirring of

the liquid steel bath and the bath temperature rise due to the oxidation exothermic reactions, which will be detailed in the following two sections.

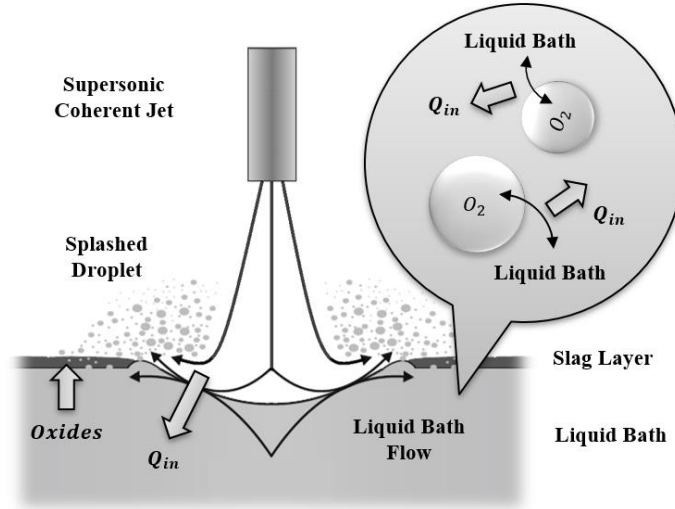


Figure 3.17. Exothermic oxidation reactions in liquid bath.

### 3.2.4.1 Reaction Mechanisms

The present study considered the species (elements) including carbon ( $C$ ), iron ( $Fe$ ), and manganese ( $Mn$ ) as a mixture in the liquid phase, whose corresponding oxidation reactions are listed in **Table 3.1**.

Table 3.1. Oxidation reaction mechanism in the oxidation model.

Reaction #	Chemical reaction equation
[A]	$C + 0.5O_2(g) = CO(g)$
[B]	$Fe + 0.5O_2(g) = FeO$
[C]	$Mn + 0.5O_2(g) = MnO$

The order of the above reactions is evaluated according to the Ellingham diagram given in **Figure 3.18**, that is, the oxidation tends to react first if its product oxide has a larger absolute value of free energy of formation.

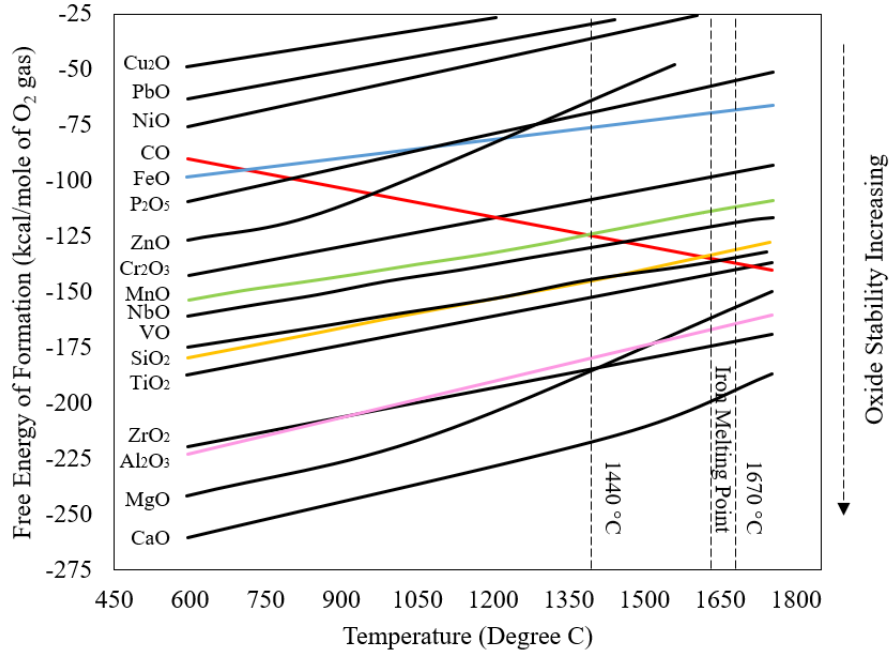


Figure 3.18. Ellingham diagram for determining the reaction orders.

The species variation over time in the liquid phase is handled by the species transport model coupled in the scrap melting model, whose conservation equation of each species is expressed by:

$$\frac{\partial(\alpha_l \rho_l Y_{i_l})}{\partial t} + \nabla \cdot (\alpha_l \rho_l \vec{v}_l Y_{i_l}) = -\nabla \cdot \alpha_l \vec{J}_{i_l} \quad (3-81)$$

where  $Y_{i_l}$  is the local mass fraction of each species;  $\vec{J}_{i_l}$  is the mass diffusion in turbulent flows due to gradients of concentration and temperature and can be calculated through:

$$\vec{J}_{i_l} = - \left( \rho_l D_{i,m_l} + \frac{\mu_{t_l}}{Sc_{t_l}} \right) \nabla Y_{i_l} - D_{T,i_l} \frac{\nabla T_l}{T_l} \quad (3-82)$$

where  $D_{i,m_l}$ ,  $Sc_{t_l}$ , and  $D_{T,i_l}$  are the mass diffusion coefficient for each species in the mixture, the turbulent Schmidt number, and the thermal (Soret) diffusion coefficient, respectively.

Oxidation reactions take place in the computational cells that contain the oxygen. The oxidation rates of carbon, iron and manganese at high carbon content are mainly limited by the cell-based

amount of oxygen. If the oxygen is sufficient, the rate equations can be written as suggested by Wei and Zhu [138]:

$$-\frac{W_s}{100 M_C} \frac{d[\%C]}{dt} = \frac{2\eta_C Q_{O_2}}{22,400} x_C \quad (3-83)$$

$$-\frac{W_s}{100 M_{Mn}} \frac{d[\%Mn]}{dt} = \frac{2\eta_{Mn} Q_{O_2}}{22,400} x_{Mn} \quad (3-84)$$

where  $W_s$  and  $Q_{O_2}$  is the mass of liquid steel and the volume of oxygen in the corresponding cell, respectively;  $M_i$  is the mole mass of each substance;  $\eta_i$  is the efficiency factor of each substance, which is a function of total mixing of the system and can be estimated based on the work done by Shukla et al. [139];  $x_i$  is the oxygen distribution ratios of each substance and is assumed to be proportional to the Gibbs free energies of corresponding oxidation reactions:

$$x_C = \frac{\Delta G_C}{\Delta G_C + \Delta G_{Fe} + \Delta G_{Mn}} \quad (3-85)$$

$$x_{Mn} = \frac{\Delta G_{Mn}}{\Delta G_C + \Delta G_{Fe} + \Delta G_{Mn}} \quad (3-86)$$

where the Gibbs free energies  $\Delta G_i$  of respective substance can be defined as:

$$\Delta G_C = \Delta G_C^0 + RT \ln \left[ \frac{P_{CO}}{a_C \cdot a_{O_2}^{0.5}} \right] \quad (3-87)$$

$$\Delta G_{Fe} = \Delta G_{Fe}^0 + RT \ln \left[ \frac{a_{FeO}}{a_{Fe} \cdot a_{O_2}^{0.5}} \right] \quad (3-88)$$

$$\Delta G_{Mn} = \Delta G_{Mn}^0 + RT \ln \left[ \frac{a_{MnO}}{a_{Mn} \cdot a_{O_2}^{0.5}} \right] \quad (3-89)$$

where  $\Delta G_i^0$  and  $a_i$  is the standard Gibbs free energy and the activity of each substance in the bath respectively;  $R$  is gas constant;  $P_{CO}$  is the partial pressure of carbon monoxide.

At low carbon content, the oxidation rate of carbon is no longer controlled by the oxygen contained in the cell. Instead, the mass carbon transfer rate to liquid steel will directly impact the decarburization rate, which can be expressed as:

$$-W_s \frac{d[\%C]}{dt} = -\rho_s k_C A_{inter} ([\%C] - [\%C]_e) \quad (3-90)$$

where  $A_{inter}$  is the bubble inter-surface area;  $[\%C]_e$  is carbon equilibrium concentration in the molten bath;  $k_C$  is the carbon mass transfer coefficient through the oxygen bubble surface which can be calculated by [140]:

$$k_C = 0.59 \cdot [D_C \cdot (u_{rel}/d_B)]^{0.5} \quad (3-91)$$

where  $D_C$  is the diffusion coefficient of carbon;  $u_{rel}$  is relative velocity of liquid steel;  $d_B$  is the bubble diameter.

The product oxides ( $CO$ ,  $FeO$ , and  $MnO$ ) formed through **Reaction (A)** to **Reaction (C)** gradually float upwards with the liquid flow until reaching the top surface of the domain (i.e. the lower surface of the slag layer), where they will be eliminated by the degassing approach to represent their absorption by the slag layer. The absorption amounts are used in the slag foaming model to predict the slag forming height. The demonstration of the oxide absorption process is given in **Figure 3.19** for better readability.

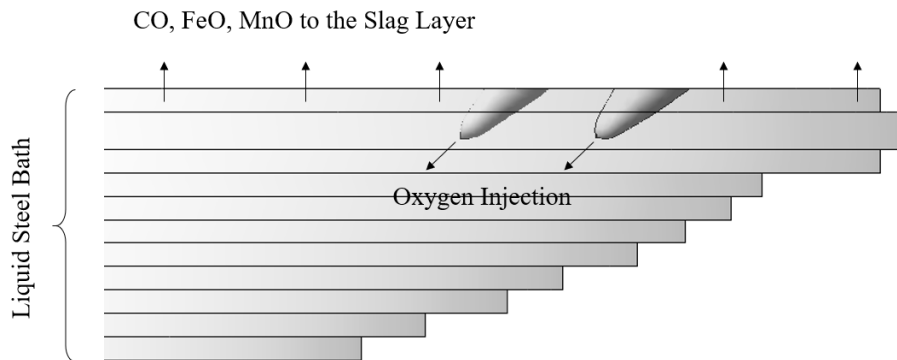


Figure 3.19. Oxygen injection through jet penetration cavities and absorption of oxides.

### 3.2.4.2 Bath Temperature Rise

The liquid bath temperature will rise during the liquid steel refining stage due to the exothermic oxidation reactions. The bath temperature is treated as one of the crucial criteria to determine the time for tapping, whose range is normally from 1900 K to 1950 K. The amount of energy released to the bath can be estimated dependent on both oxidation rates and the oxidation enthalpies of each reaction, and the latter is a function of bath temperature, which is given in **Figure 3.20**.

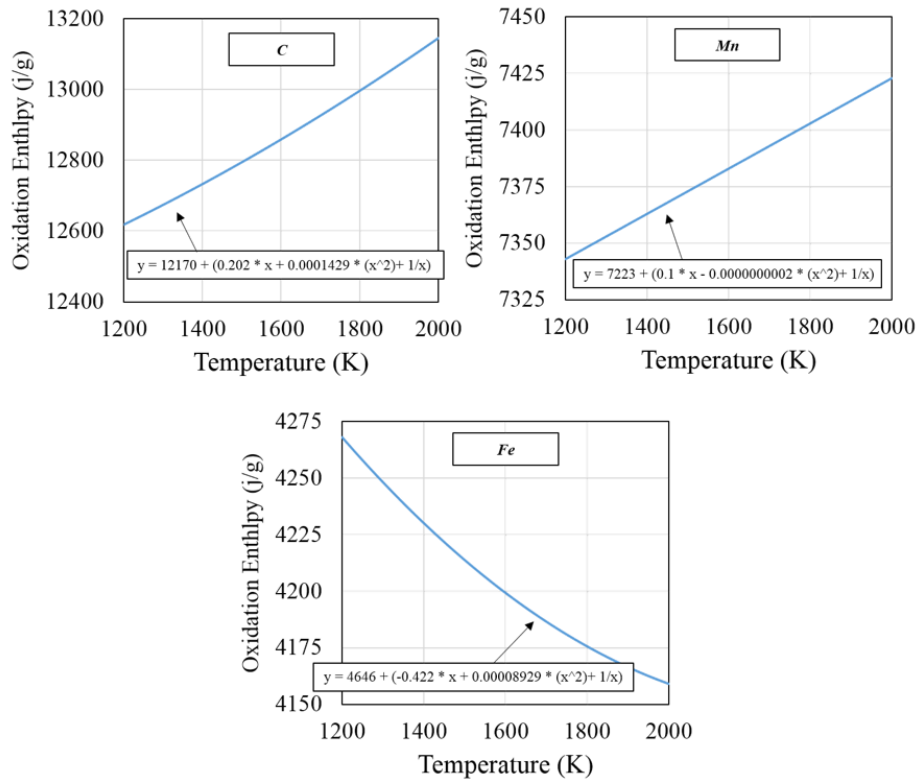


Figure 3.20. Oxidation enthalpies for each reaction [141].

The rate of cell-based energy generation due to the oxidation exothermic reactions is the sum of all three oxidation reactions considered, can be expressed as follows:

$$\frac{dE_{reac}}{dt} = \sum \Delta H_i W_s \frac{d[\%i]}{dt} \quad (3-92)$$

where  $\Delta H_i$  is the oxidation enthalpy;  $W_s$  is the weight of the liquid phase. **Equation (3-92)** is used to define the energy source term, which is added to the liquid phase energy conservation equation of the scrap melting model used in the in-bath decarburization simulator.

### 3.2.5 Slag Foaming Model

The present section describes the slag foaming model developed for the comprehensive EAF CFD model to estimate the slag foaming effect and the consequently exposed arc length for the freeboard post-combustion simulator.

#### 3.2.5.1 Slag Foaming Height

The slag is a layer of melt that floats on the surface of the liquid steel bath during the liquid steel refining stage. The typical slag compositions in the EAF steelmaking process involve CaO, FeO, Al<sub>2</sub>O<sub>3</sub>, SiO<sub>2</sub>, MgO, and MnO. The initial height of the slag layer is relatively thin but will gradually elevate over time, which is mainly due to the absorption of CO in the slag layer leading to the so-called foaming effect. The foamed slag layer divides the entire furnace into the freeboard region and bath region, which can be simulated by the freeboard post-combustion simulator and the in-bath decarburization simulator, respectively. Previous researchers have derived an empirical equation to calculate the slag foaming height from the foaming index ( $\Sigma$ ) and the superficial velocity ( $v_g$ ) [142]:

$$H_f = \Sigma \cdot v_g \quad (3-93)$$

Considering that the foaming effect is mainly caused by CO, the superficial velocity can be estimated through the total CO absorption amount by the slag layer simulated from the in-bath decarburization simulator to achieve the model-to-simulator integration. The foaming index denotes the average gas traveling time in the foamed slag layer, which is dependent on the slag properties and can be calculated through the following empirical formula as suggested by Jiang and Fruehan [143]:

$$\Sigma = 150 \frac{\mu_s}{\sqrt{\sigma_s \rho_s}} \quad (3-94)$$

In the above formula,  $\sigma_s$  and  $\rho_s$  express the slag surface tension and the slag density, respectively, which are dependent on the temperature as presented in **Table 3.2**.

Table 3.2. Temperature-dependent slag surface tension and density [144-145].

Species	Surface Tension $\sigma_s$ (mN/m)	Slag Density $\rho_s$ (kg/m <sup>3</sup> )
<i>CaO</i>	$791 - 0.094 T (K)$	$3240 - 0.2 T (K)$
<i>FeO</i>	$504 + 0.098 T (K)$	$1950 + 1.86 T (C)$
<i>Al<sub>2</sub>O<sub>3</sub></i>	$1020 - 0.177 T (K)$	$3040 - 1.15 (T - 2303) (K)$
<i>SiO<sub>2</sub></i>	$243 + 0.031 T (K)$	$2510 - 0.213 T (C)$
<i>MgO</i>	$1770 - 0.636 T (K)$	3600
<i>MnO</i>	$988 - 0.179 T (K)$	5400

The slag viscosity has a significant effect on the slag foaming process, while the contents of CaO and MgO in the slag impact the slag viscosity. At the beginning of the foaming stage, the presence of CaO and MgO makes the solid particles in the slag easier to be accumulated, which extends the residual time of the bubbles in the slag, so that the foaming height elevates with the slag viscosity increase. However, the further increase of viscosity, in turn, makes CaO and MgO over-saturated which is not conducive to the continued occurrence of the slag foaming process. The current model estimates the slag viscosity before the over-saturation of CaO and MgO happens according to the following equation:

$$\mu_s = A T \exp\left(\frac{1000 B}{T}\right) \quad (3-95)$$

where  $T$  is slag temperature; the relationship of  $A$  and  $B$  follows the expression below:

$$-\ln A = 0.2693 B + 11.6725 \quad (3-96)$$

and  $B$  can be further evaluated through:

$$B = \frac{X_{MnO} \overline{B_{MnO}} + X_{CaO} \overline{B_{CaO}} + X_{MgO} \overline{B_{MgO}}}{X_{CaO} + X_{MgO} + X_{MnO}} \quad (3-97)$$

$$\bar{B}_i = B_0 + B_1X_i + B_2X_i^2 + B_3X_i^3 \quad (i = MnO, CaO, MgO) \quad (3-98)$$

where  $X_i$  is the mole fraction of its corresponding oxide and  $B_j$  ( $j = 0,1,2,3$ ) is determined by:

$$B_j = a_j + b_j \frac{X_M}{X_M + X_A} + c_j \left( \frac{X_M}{X_M + X_A} \right)^2 \quad (3-99)$$

In the above expression, the values for the coefficients  $a_j$ ,  $b_j$ , and  $c_j$  can be referred to **Table 3.3**, while  $X_M$  and  $X_A$  can be further calculated through:

$$X_M = X_{CaO} + X_{MgO} + X_{FeO} + X_{MnO} \quad (3-100)$$

$$X_A = X_{Al_2O_3} \quad (3-101)$$

Table 3.3. Coefficient values [146].

i	a <sub>i</sub>		b <sub>i</sub>			c <sub>i</sub>	
	All	Mg	Ca	Mn	Mg	Ca	Mn
0	13.2	15.9	41.5	20.0	-18.6	-45	-25.6
1	30.5	-54.1	-117.2	26	-104.6	130	-56
2	-40.4	138	232.1	-110.3	-112	-298.6	186.2
3	60.8	-99.8	-156.4	64.3	97.6	213.6	-104.6

### 3.2.5.2 Exposed Arc Length

The slag foaming model helps to evaluate the exposed arc length used in the freeboard post-combustion simulator, so that the arc radiation predicted by the electric arc simulator can be correctly assigned through the determined exposed arc, which is presented as a small cylinder beneath the electrode tip as shown in **Figure 3.21**. The exposed arc exists in the freeboard region when the slag foaming is insufficient, that is, the total arc length (the distance from the electrode tip to the liquid bath) is higher than the slag foaming height. Inversely, there will be no arc exposure

if the slag foaming height is higher than the total arc length. The above statement is mathematically expressed as:

$$l_{exp} = l_a - H_f = \begin{cases} > 0 & (\text{with arc exposure}) \\ \leq 0 & (\text{no arc exposure}) \end{cases} \quad (3-102)$$

where  $l_{exp}$  is the exposed arc length;  $l_a$  is the total arc length determined in **Section 3.2.2**;  $H_f$  is the slag foaming height.

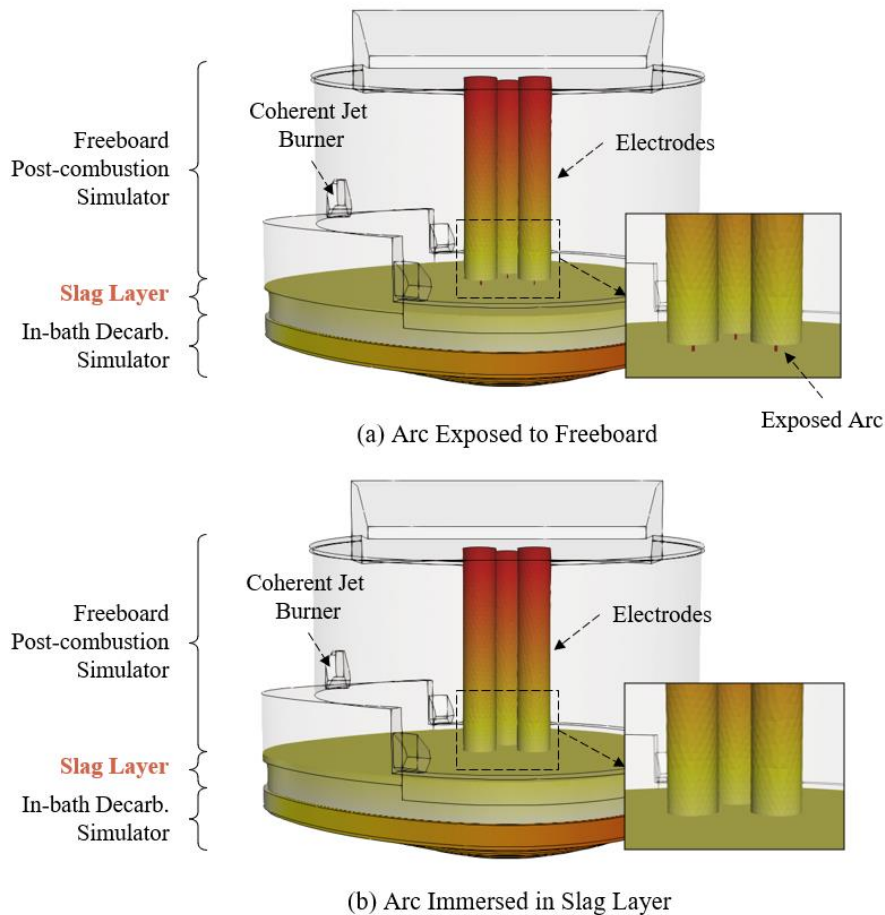


Figure 3.21. Exposed arc to freeboard.

### 3.3 Results and Discussions

The present part includes six sections. The first two sections present the results from the electric arc simulator and the coherent jet simulator, which investigate the AC arc heat dissipation (**Section 3.3.1**) and the coherent jet performance (**Section 3.3.2**), respectively. Afterward, the results of the

rest four simulators are provided in the subsequent four sections (**Section 3.3.3** for scrap preheating simulator, **Section 3.3.4** for scrap melting simulator, **Section 3.3.5** for in-bath decarburization simulator, and **Section 3.3.6** for freeboard post-combustion simulator) to achieve the simulation of the entire steelmaking process in the industry-scale AC EAF according to the integration methodology demonstrated in **Section 3.1**.

### 3.3.1 Electric Arc Simulator

This section presents the results from the electric arc simulator, which performs a separate simulation of industry-scale AC electric arc plasma for investigating its arc heat dissipation.

#### 3.3.1.1 Simulation Conditions

A typical view consisting of one of the three electrodes and the scrap surface is presented in **Figure 3.22**. After the arc ignition, the electrode will continuously reverse its polarity according to the current half-cycle to which it belongs so that both electrode and scrap surface successively act as cathode/anode and anode/cathode to generate the AC electric arc plasma in between. The arc terminations of both the electrode side and the scrap side normally wander over its corresponding surface centered on the electrode, meanwhile, the twisted arc column between the arc terminations releases a large amount of heat to the surroundings showing as the aureole region in observation.

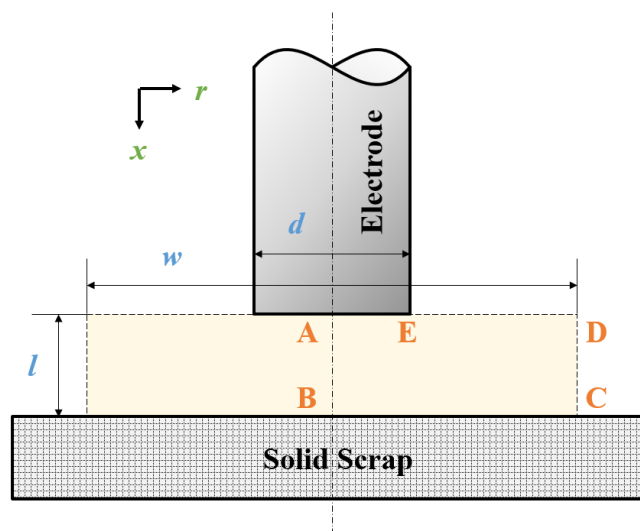


Figure 3.22. Schematic diagram of computational domain for AC arc modeling.

To capture and investigate the described AC electric arc plasma and its heat distribution mechanisms, it is appropriate to restrict the computational domain to within the yellow region marked in **Figure 3.22**. In the present study, the entire computational domain is considered to be axisymmetric, hence only half of the domain is included in the simulation. As shown, the domain is connected to the furnace atmosphere through CD and DE. The electrode tip AE and the scrap surface BC are all treated as flat surfaces. The electrode diameter ( $d$ ) and scrap surface diameter ( $w$ ) are 1.2 m and 2.0 m, respectively. The arc length ( $l$ ) is fixed as a constant and variant values are allocated to it case-by-case. The simulation is conducted under the cylindrical coordinate ( $r, x$ ) with the origin at the center of the electrode tip. A structured mesh has been developed for the entire computational domain; and after a mesh sensitivity study, a mesh with a total of 467,880 was selected.

Table 3.4. Boundary conditions.

	AB	BC	CD	DE	EA
$v_x$ (m/s)	0	0	( $p = 1atm$ )	0	0
$v_r$ (m/s)	$\partial v_r / \partial r = 0$	0	( $p = 1atm$ )	0	0
$T$ (K)	$\partial T / \partial r = 0$	2000	2000	2000	4000
$\varphi$ (V)	$\partial \varphi / \partial r = 0$	<b>Eqn.(3-43)</b> (Cathode) $\partial \varphi / \partial x = 0$ (Anode)	$\partial \varphi / \partial r = 0$	$\partial \varphi / \partial x = 0$	$\partial \varphi / \partial x = 0$ (Anode) <b>Eqn. (3-43)</b> (Cathode)

Time-dependent conditions for the variables ( $u, v, T, \varphi$ ) must be assigned along the boundaries of the computational domain ABCDE to solve the mathematical model proposed. As illustrated, only half of the domain is included due to the axisymmetric condition. Therefore, zero fluxes are set for all variables along the radial direction at the axis of symmetry AB. The domain connects to the furnace atmosphere through CD and DE, thus CD is set as a velocity inlet with 2000 K, the same as the temperature of furnace atmosphere; while DE is defined as the pressure outlet with 2000 K as well. The temperatures along the scrap surface BC and the electrode tip surface AE are

held as constants equal to 2000 K and 4000 K respectively based on the real EAF conditions [49]. The complete set of boundary conditions are summarized in **Table 3.4**.

As reported by Ramirez and Trapaga [148], all material properties in the above conservation equations in Section 2.1.2 should be temperature-dependent in the simulation. Therefore, the values of all material properties in the present AC arc modeling are considered to be functions of arc temperature field and are taken from literatures [103,110,147]. Details are indexed in **Table 3.5**. All material properties are added to the solver by the linear interpolation between two given points in the plots and are consistently updated at every iteration based on the instantaneous arc temperature field before solving all conservation equations.

Table 3.5. Material properties.

Material Properties	Units	Values in Air/Argon
$\rho$	$kg/m^3$	
$C_p$	$J/kg-K$	<i>Reference [103]</i>
$k$	$W/m-K$	
$\mu$	$kg/m-s$	
$S_r$	$W/m^3$	<i>Reference [110]/ Reference [147]</i>
$\sigma$	$A/V-m$	<i>Reference [103]</i>

### 3.3.1.2 Validations

To prove the validity of the modeling methodology, the simulator is used to simulate both DC arc in the air and AC arc in the argon and compare the results against either the published experimental data or simulation results in the literature.

The stationary DC arc modeling in air with arc length equal to 0.07 m is presented. The arc velocity predicted by the simulation is compared to the arc velocity measured by Bowman [149] in his experiment. In the experiment, the steel ball was released above the horizontal arc and the ball was deflected horizontally after contacting the arc. The ball's landing location was recorded to derive

the arc axial velocity. The arc velocities for three different measurement positions (0.02, 0.038, and 0.055 m) and three different arc currents (520, 1150, and 2160 A) reported by Bowman are plotted as points in **Figure 3.23**.

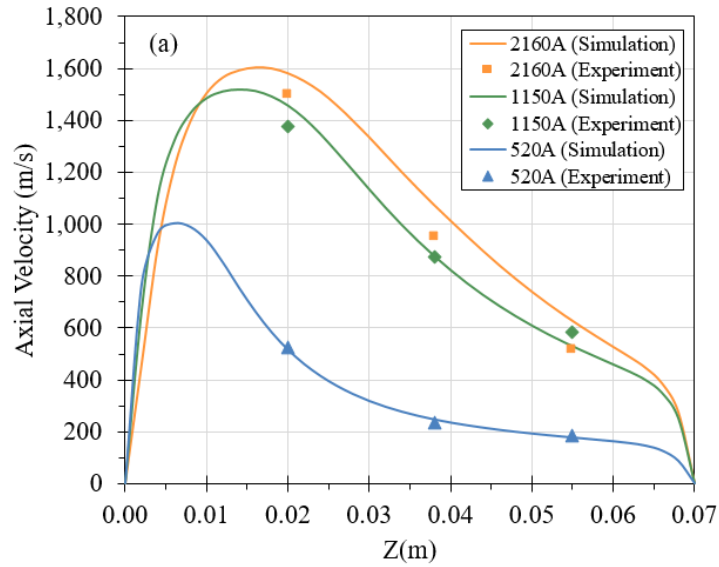


Figure 3.23. Comparison of simulated arc axial velocity and measurement data [149].

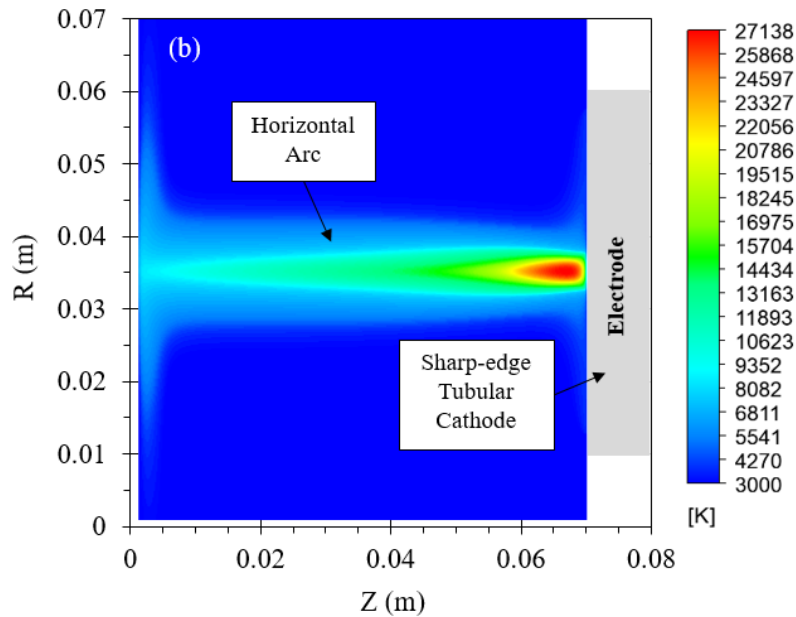


Figure 3.24. Arc temperature field for 1150 A current case.

Based on the experiment setup, the same computational domain is adopted in the simulation with consistent arc operating conditions and working gas. To model the DC arc, the electrode tip is fixed as the cathode with the application of the estimated current density illustrated above. The scrap surface is fixed as the anode. The arc velocity along the electrode centerline is obtained from the simulation and plotted as the line to compare with the experimental raw data. As can be seen from **Figure 3.23**, the axial velocity of the arc reaches a peak near the anode and then gradually decreases to the cathode. The overall arc axial velocity is significantly affected by the current. The higher arc current results in higher overall arc axial velocity. This is because the higher arc current contributes to higher current density through the entire arc column, which in turn leads to a larger Lorentz force in the working gas and a significant acceleration. Furthermore, doubling the arc current from 520 A to 1150 A can elevate the peak axial velocity from 1000 m/s to 1500 m/s, while further doubling the arc current only gives a slight increase of the peak axial velocity from 1500 m/s to 1600 m/s. The present simulation results have a good agreement with the reported three groups' data with an average percentage error of 4.9%. **Figure 3.24** shows the simulated arc temperature field at 1150 A current. It can be seen that the simulated horizontal arc roots from a sharp-edge tubular cathode surface. The high-temperature and high-speed plasma jet hits the surface of the anode and disperses in the vertical direction. According to the previous definition of the main body of the arc column (the region where arc temperature is higher than 8000 K), the simulated arc shape and behavior are very close to that in the photo taken in the experiment [149], which further proves the accuracy of arc modeling in the present study.

The AC arc modeling in argon with arc length equal to 0.01 m is presented here and is compared with the published simulation results by Larsen et al. [49] for the arc temperature field. The simulation setup in the present study is consistent with that in the reference paper including the dimensions of the computational domain and the boundary conditions. The RMS arc current is set to be 70 kA according to the real operating conditions. Four snapshots of the simulation results are plotted and compared to the work by reported by Larsen et al. in **Figure 3.25**. The isotherms range from 9000 K to 19000 K are marked out in the plotted arc temperature contours for the comparison. The first two snapshots correspond to the cathode half-cycle near the positive current peak ( $i = 86$  kA and 43 kA) and the others correspond to the anode-half cycle near the negative current peak ( $i = -79$  kA and -42 kA).

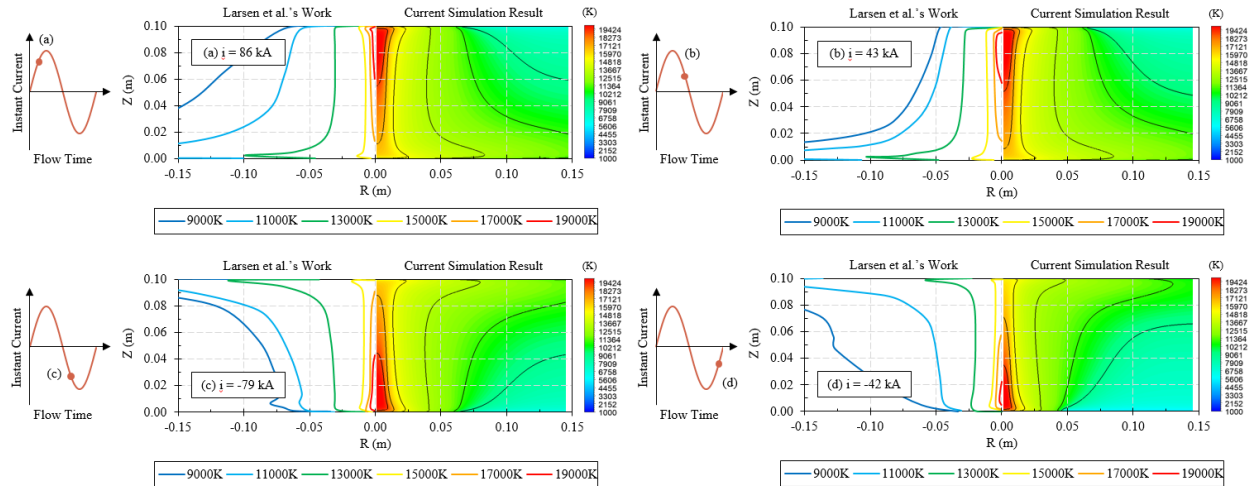


Figure 3.25. Validation of AC arc in Argon.

(a) current = 86 kA; (b) current = 43 kA; (c) current = -79 kA; (d) current = -42 kA.

As can be seen from the four snapshots, the high temperature caused by the combination of the Joule heating effect and the electronic enthalpic flux first occurs near the upper surface (the electrode tip) in the cathode half-cycle. When the instantaneous arc current increases, the red region in the temperature contour increases then slowly reduces as the instantaneous arc current decreases. This is because the working gas at this moment is sufficiently ionized, enabling the plasma to maintain the conductivity as well as the high temperature. Due to this characteristic, the high-temperature region keeps a similar shape even when the instantaneous arc current is reduced from 86 kA in **Figure 3.25 (a)** to 43 kA in **Figure 3.25 (b)**. During this period, the AC arc resembles the DC arc and is stiffened by the plasma jet directed to the bottom surface (the scrap surface). After the instantaneous arc current passing the zero point, the bottom surface now becomes the cathode. The AC arc goes into the anode half-cycle, thereby making the region near the upper surface gradually cool down and the region near the bottom surface start to heat up. The corresponding arc temperature fields at -79 kA and -42 kA near the minimum arc current can be found in **Figure 3.25 (c)** and **Figure 3.25 (d)**. It should be noted that the arc behavior in the anode half-cycle is observed to be extremely unstable in reality. The present prediction still gives a DC-arc-like behavior in the anode half-cycle but with the smaller high-temperature region in the contour. This is considered to be a limitation of the proposed model but subsequent estimates of arc heat distribution are still generally acceptable. To sum up, the overall comparisons of the four

plots illustrate that the simulated arc temperature fields are in a fairly good agreement with Larsen's works and the average percentage error is less than 11.8%.

With the validated arc modeling, AC arc state variables can be obtained from the arc simulations by data sampling methods for time statistics so that the arc power delivery, arc performance, and arc heat dissipation can be further estimated quantitatively and the results will be presented in the following sections.

### 3.3.1.3 AC Arc Power Delivery

This section discusses the results of the total AC arc power delivery obtained in the present study. As described above, due to the continuous reversal of the electrode polarity, AC arc roots are alternately generated on the electrode tip surface and the scrap surface, resulting in the arc behavior different from the DC case. The sinusoidal waveform of the arc current is considered to be the direct cause of the electrode polarity reversal.

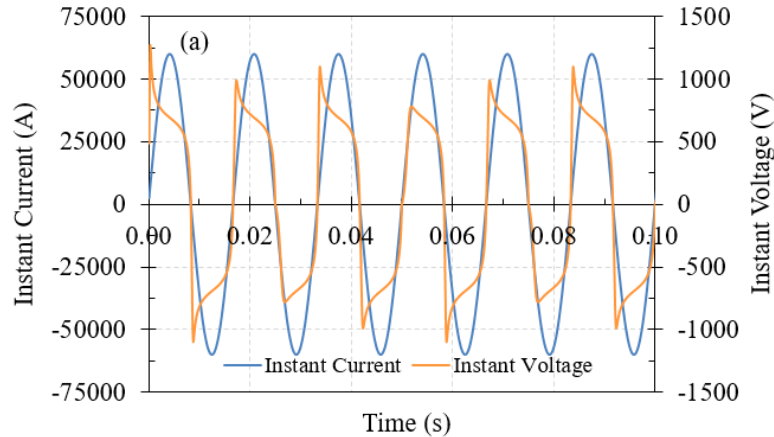


Figure 3.26. Instantaneous arc current/voltage variation over time (arc length = 0.4 m and RMS arc current = 60 kA).

**Figure 3.26** demonstrates both instantaneous arc current and arc voltage variations over time within 6 cycles for the ideal case when the arc length is 0.4 m and the RMS arc current is 60 kA. As can be seen from the plot, the arc current appears as a sinusoidal waveform while the arc voltage appears as a more square-shaped waveform which is commonly found in the literature. They both

have the same frequency and are positive at the anode half-cycle and negative at the cathode half-cycle. **Figure 3.27** gives the corresponding instantaneous arc power delivery variation over time calculated based on the arc current and arc voltage. For the present case (arc length = 0.4 m, RMS arc current = 60 kA), the AC arc power delivery can reach a maximum value of 41.9 MW near the peak of the arc current and drop to zero at the current zero points. Therefore, the RMS arc power delivery from a time-averaged perspective is 29.6 MW.

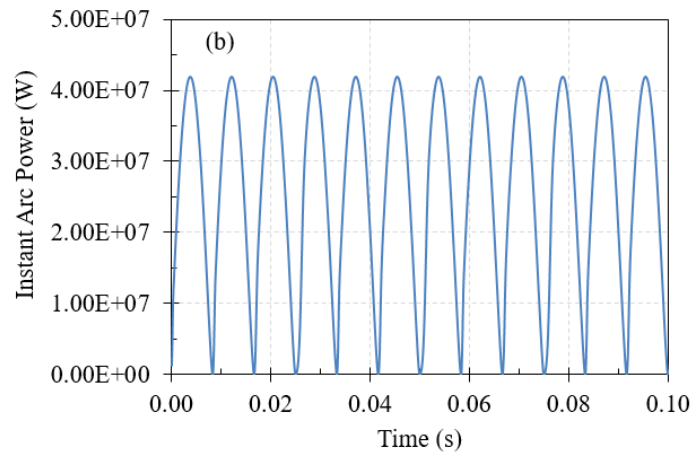


Figure 3.27. Instantaneous arc power delivery variation over time (arc length = 0.4 m and RMS arc current = 60 kA).

The arc current and the arc length are considered to be two major factors impacting the final total arc power delivery. **Figure 3.28** illustrates the relationship between the total arc power delivery, arc length, and RMS arc current. The X-axis in the plot represents the arc length covering the range from 0.25 m to 0.5 m which is the common arc length during the real EAF operation as suggested by Sanchez et al. [59]. The Y-axis is the RMS arc current covering the range from 30 kA to 80 kA. At a given arc length and the RMS arc current, the corresponding amount of total arc power delivery is given in the Z-axis. It can be seen that increasing the arc length elevates the total arc power delivery since the longer arc increases the arc resistance, resulting in a higher voltage drop to deliver higher power based on **Equation (3-48)**. On the other hand, increasing the RMS arc current also has a positive effect on the elevation of total arc power delivery. Therefore, from the point with the lowest arc current and the shortest arc length to the point with the highest arc current and the longest arc length, the total arc power delivery represented by the surface in **Figure 3.28**

shows a gradual increase from 10.4 MW to 46.7 MW. In addition, the faster growth of arc power delivery appears when having higher arc current or longer arc length.

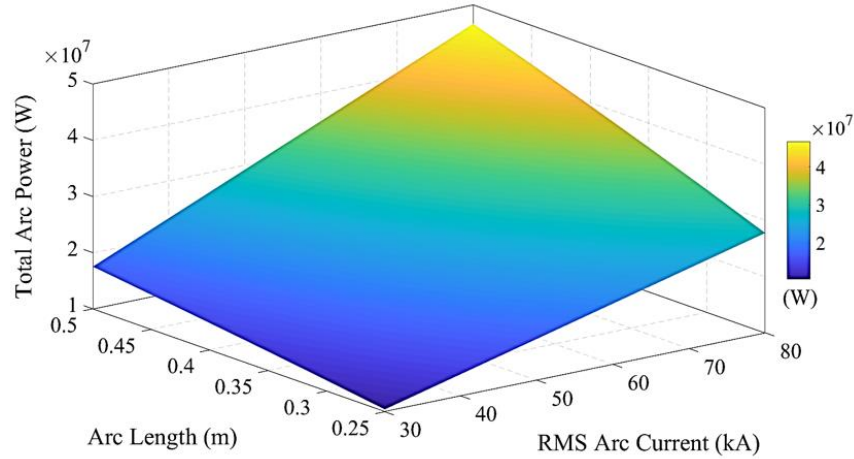


Figure 3.28. Relationship between the total arc power delivery, arc length, and RMS arc current.

### 3.3.1.4 AC Arc Performance

Simulation results in **Figure 3.29** shows the contours of time-averaged AC arc state variables including arc density, arc velocity, arc specific enthalpy, and arc temperature after 10,000 times data sampling covering 50 cathode half-cycles and anode half-cycles in total. All contours are from the case whose arc length is equal to 0.4 m and RMS arc current is equal to 60 kA. It can be seen that the AC arc state variables obtained by the data sampling method consider the impact from the anode half-cycle and the cathode half-cycle at the same time. The rapid polarity reversal allows electrons and positive ions to continuously transfer between the electrode tip surface and the scrap surface, thereby forming a conductive arc column. Within this column, the flow field is significantly affected by the Lorentz force and Joule heating effect. The electrode tip surface and the scrap surface are connected by high-temperature and high-speed flow. The high temperature increases the specific enthalpy of the working gas and reduces its density which further aggravates the influence of the Lorentz force on the flow field. Therefore, under the comprehensive impact from various factors, the conductive arc column has the characteristics of high temperature, high velocity, high specific enthalpy, and low density, which are depicted in **Figure 3.29**. With the aforementioned 8000 K temperature isotherm to define the main body of the arc column [127,129], the averaged AC arc state variables can be evaluated within the defined arc column, whose average

arc radius is calculated to be around 0.044 m. Under the current arc operating conditions, the average arc density, velocity, specific enthalpy, and temperature within the defined arc column are also found to be around  $0.017 \text{ kg/m}^3$ ,  $929 \text{ m/s}$ ,  $6.06 \times 10^7 \text{ J/kg}$ , and  $10718 \text{ K}$ , respectively. By using the approach described in Section 2.2 to estimate the arc heat dissipation in the present case, the share of convection is 19% and the share of electron flow is 3.5% and the share of radiation is 77.5%. The estimation results coincide with the reported values in the literature [129].

In the next two subsections, the effects of arc length and RMS arc current on the AC arc state variables as well as the arc heat dissipation are further investigated and illustrated to understand the potential impact on the arc operation.

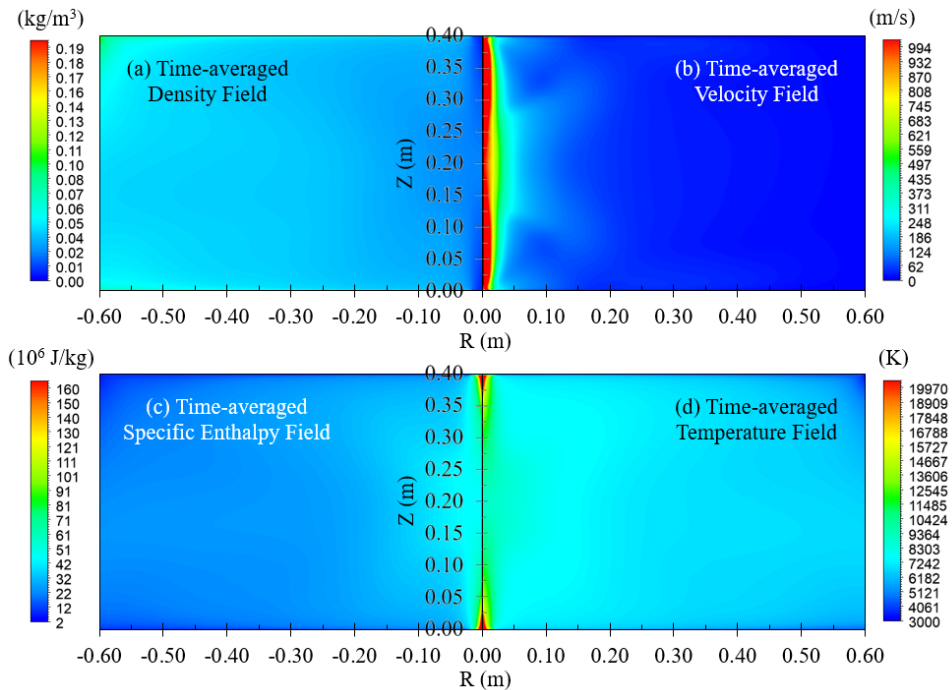


Figure 3.29. Time-averaged AC arc state variables (arc length = 0.4 m, RMS arc current = 60 kA). (a) Density field; (b) Velocity field; (c) Specific enthalpy field; (d) Temperature field.

### 3.3.1.5 Effect of Arc Length

In this group, the study is conducted for arc length from 0.25 m to 0.5 m with a fixed RMS arc current equal to 60 kA. **Figure 3.30** shows the arc column shape under different arc lengths, which

is defined by 8000 K isotherm from the time-averaged temperature field on the right-hand side of each plot.

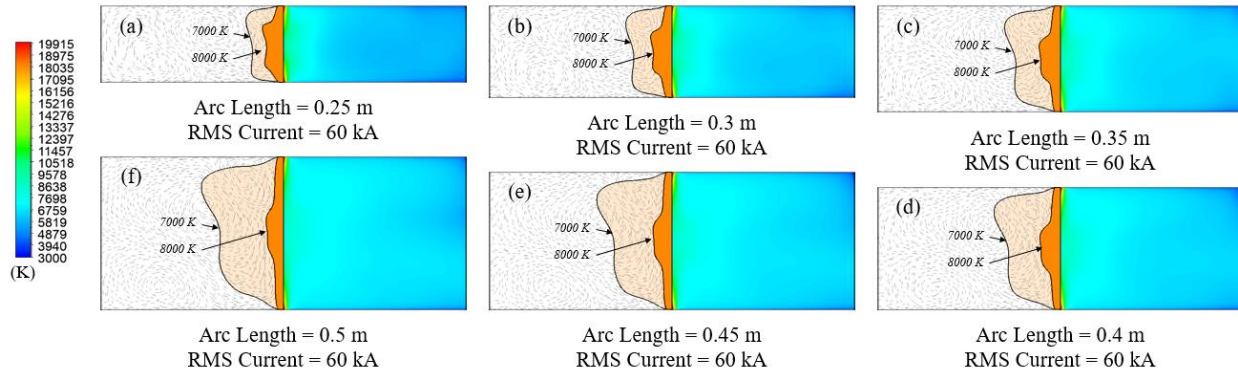


Figure 3.30. Effect of arc length on AC arc performance.

As can be revealed, increasing the arc length stretches the arc column leading to the reduction of arc radius. When the electrode tip and the scrap surface are relatively close, the narrow gap in between facilitates ionization and rapid heating of the working gas. However, when the distance between the electrode tip and the scrap surface is extended, the above effect will be weakened and the arc radius will be directly reduced. The dark blue line in **Figure 3.31** indicates the trend of arc radius decreasing. It can be seen that extending the arc length from 0.25 m to 0.5 m decreases the arc radius from 0.0516 m to 0.0373 m, with a percentage decrease of about 27.7%. **Figure 3.31** also demonstrates the consequences of changing the arc length on other AC arc state variables including the average arc density, velocity, specific enthalpy, and temperature. With a longer arc length, the arc temperature is reduced from 11469 K to 10365 K along with the decrease of arc velocity from 1034.2 m/s to 890.7 m/s and the arc specific enthalpy from  $6.81 \times 10^7$  J/kg to  $5.76 \times 10^7$  J/kg. However, the arc density is increased from  $0.0157 \text{ kg/m}^3$  to  $0.0178 \text{ kg/m}^3$ , which is because the physical property of arc density is inversely proportional to arc temperature. **Figure 3.32** illustrates the variations of AC arc heat distribution under different arc lengths. It can be seen that, as the arc length is increased from 0.25 m to 0.5 m, the share of arc heat dissipation by electron flow is slightly decreased, while the share of arc radiative heat dissipation is increased from 52 % to 86 % accompanied by the decrease of the share of arc convective heat dissipation from 43 % to 11 %. Further extension of the arc length slows down the growth of the radiation share and the reduction of the convection share, which may also cause arc instability or even arc extinguishing

in the actual EAF operation process. The changing trend of the share for different arc heat dissipation mechanisms with the arc length is consistent with the actual arc operation conventions: a short arc is used initially when the electrode first bores down to minimize arc radiation to the roof and side walls from the exposed arc while leveraging convective heating of the gasses near the arc and scrap; a longer arc is used after the electrode has bored down into the scrap when the radiated power will be dissipated to the surrounding scrap more effectively and convective transfer decreases in efficiency due to the long arc length and the reduced effective scrap porosity.

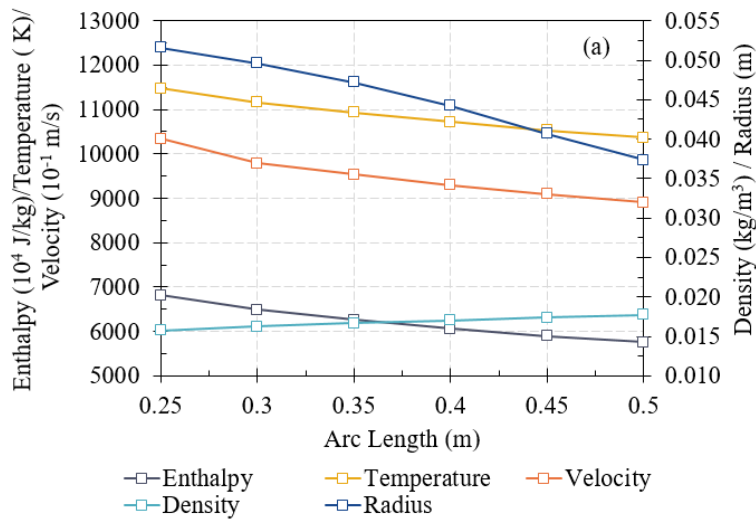


Figure 3.31. Effect of arc length on AC arc state variables.

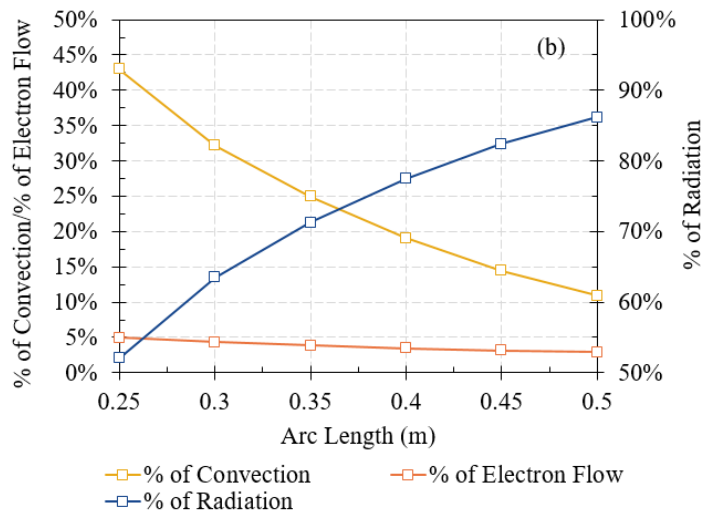


Figure 3.32. Effect of arc length on AC arc heat dissipation.

### 3.3.1.6 Effect of Arc Operating Current

In this group, the study is conducted for the effect of RMS arc current from 30 kA to 80 kA. The different arc column shapes under different RMS arc currents are given in **Figure 3.33** and the arc length is fixed at 0.4 m for all cases.

Obviously, a higher RMS arc current increases the radius of the arc column since a larger cathode white-hot spot appears on the electrode tip/scrap surface, thereby ionizing a larger area of gas and obtaining a higher arc temperature. The variation of arc radius in value is indicated by the dark blue line in **Figure 3.34**. From the plots, the arc radius grows from 0.0247 m to 0.0530 m when the RMS arc current is increased from 30 kA to 80 kA. Similar to the previous group, **Figure 3.34** also demonstrates the impact of changing the RMS arc current on other AC arc state variables. With a higher RMS arc current, the arc temperature is increased from 10199 K to 10928 K along with the increase of arc velocity from 636.9 m/s to 1076.4 m/s and the arc specific enthalpy from  $5.64 \times 10^7$  J/kg to  $6.25 \times 10^7$  J/kg. On the contrary, the arc density is decreased from  $0.0182 \text{ kg/m}^3$  to  $0.0166 \text{ kg/m}^3$ , which is due to the arc temperature increasing as explained above.

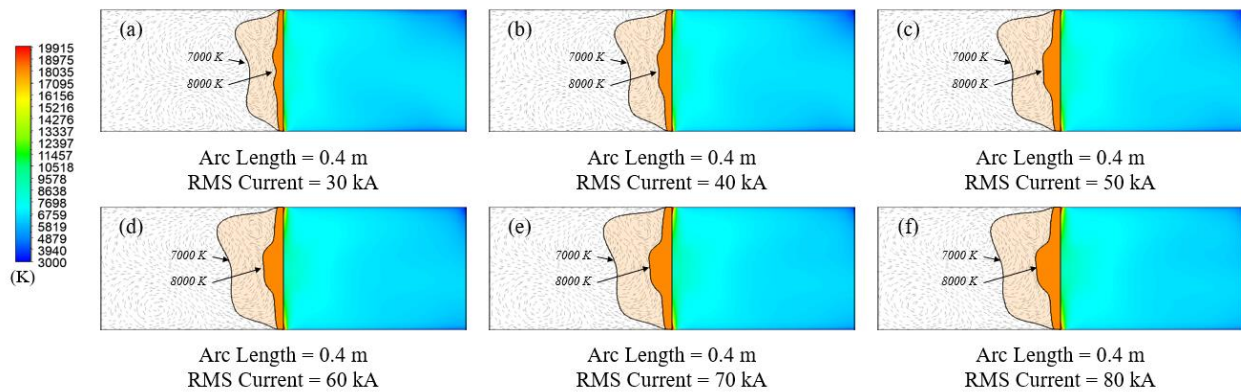


Figure 3.33. Effect of RMS arc current on AC arc performance.

The effect of RMS arc current on heat dissipation is illustrated in **Figure 3.35**. It can be seen that the changing trends of the share of convection and radiation are opposite compared with the results in the previous group. With the quantitative analysis, increasing the RMS arc current from 30 kA to 80 kA elevates the share of arc convective heat dissipation from 8% to 24% but reduces the share of arc radiative heat dissipation from 88% to 72%. This is because the higher arc current

reinforces the Lorentz force and Joule heating effect applied on the flow field. As a result, the arc plasma have stronger impingement on the cathode/anode surface which increases the share of convection while reduces the share of radiation. Additionally, continuously increasing the RMS arc current also slows down the decrease in the radiation share and the increase in the convection share, which can be reflected by the slopes of two curves. In reality, such operations may also result in the splashing of slag/liquid steel near the electrode and the waste of electrical energy.

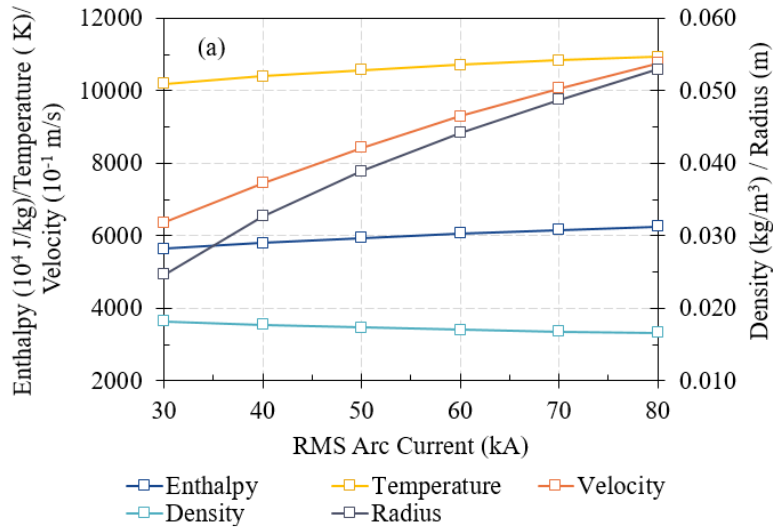


Figure 3.34. Effect of RMS arc current on AC arc state variables.

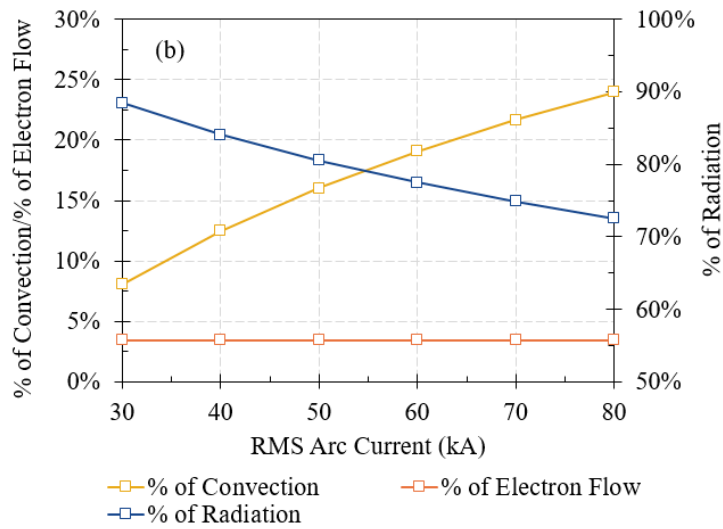


Figure 3.35. Effect of RMS arc current on AC arc heat dissipation.

### 3.3.1.7 AC Arc Heat Dissipation Database and Arc Momentum Transfer Database

This section discusses the variation of share for different AC arc heat dissipation mechanisms with the comprehensive effects of both arc length and arc operating current. The results are used to generate the AC arc heat dissipation database. The study covers the arc length from 0.25 m to 0.5 m and the RMS arc current from 30 kA to 80 kA. The share for different AC arc densities and velocities varied with those two variables are also plotted in **Figure 3.36** and **Figure 3.37**, which can be used to generate the arc momentum transfer database.

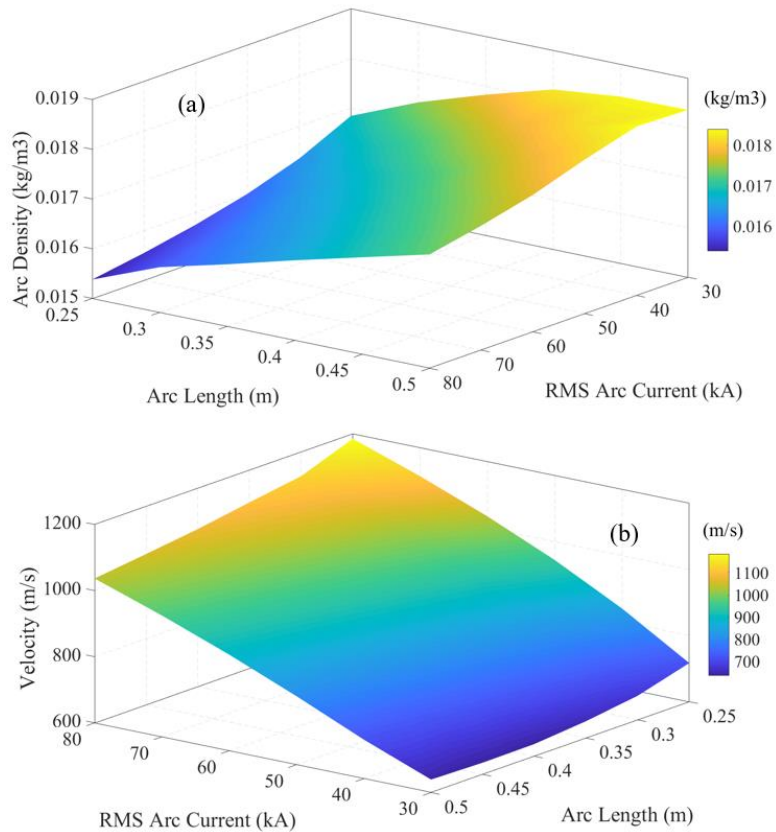


Figure 3.36. Variations of arc density/velocity with different arc lengths and RMS arc currents.

As it can be observed in **Figure 3.37 (a)**, the amount of arc heat dissipated by the convection is reduced with the increase of arc length and with the decrease of RMS arc current. This is because both longer arc and lower arc operating current weaken the arc plasma impingement on the cathode/anode surface, thus the highest share of arc convective heat dissipation appears with a high current and short arc. The amount of share for arc heat dissipated by the electron flow is

revealed in **Figure 3.37 (b)**. Adjusting the RMS arc current has a limited impact on its share. This is because the increase in the total arc power delivery is much greater than the increase in the power lost by the electron flow with the same RMS arc current increasing. Instead, increasing the arc length has a more obvious impact. With a 0.25 m increase of arc length, the share of arc heat dissipation by electron flow is reduced from 5% to 3%. **Figure 3.37 (c)** gives the share variation of arc heat dissipated by the radiation, and its amount occupies the largest part among the three arc heat dissipation mechanisms. It can be seen that its share is increased with the increase of arc length and with the decrease of RMS arc current, which is totally opposite with that in the arc convective heat dissipation. Overall, the share of arc radiative heat dissipation lies in the range of 46% to 93%, with the mean value of 69.5%.

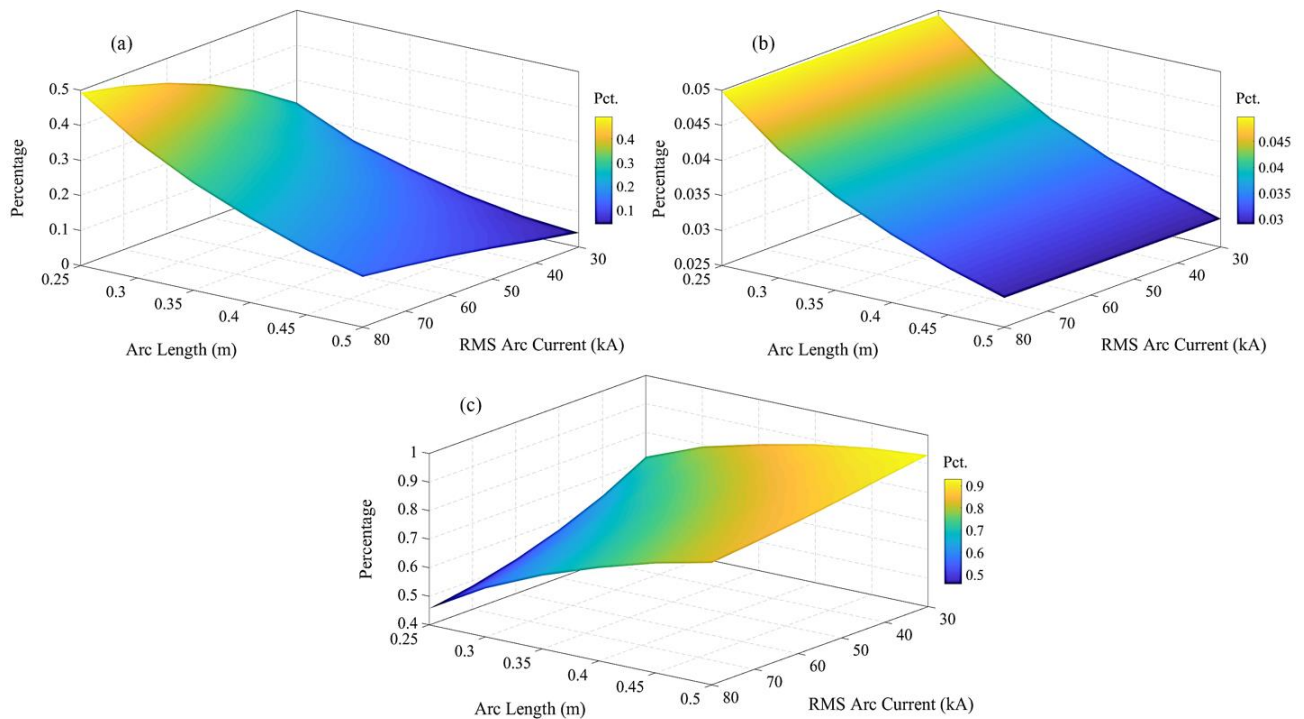


Figure 3.37. Variation of the share for different heat dissipation mechanisms with different arc lengths and RMS arc currents. (a) Convection; (b) Electron flow; (c) Radiation.

One of the main tasks of the present study is to deduce the relationship between arc operating current, arc length, and the shares of different arc heat dissipation mechanisms. The results will be used to generate the AC arc heat dissipation database and integrated into the scrap melting model to dynamically allocate the share for different arc heat dissipation mechanisms according to the

instantaneous arc operations, so as to correctly predict the scrap melting rate. Based on the three plots given in **Figure 3.37**, the aforementioned relationship between the shares for three AC arc heat dissipation mechanisms and the arc length and the RMS arc current can be derived by surface fitting and they can be mathematically described by the following generalized equation:

$$Ptc(I_{RMS}, l) = AI_{RMS}^2 + Bl^2 + CI_{RMS}l + DI_{RMS} + El + F \quad (3-103)$$

where  $A, B, C, D, E, F$  are constants, whose values are different for each arc heat transfer mechanism and can be found in **Table 3.6**. As previously mentioned, **Equation (3-103)** will be integrated into the scrap melting model so that it can be called at the beginning of each time step.

Table 3.6. Coefficients in the equation.

	A	B	C	D	E	F
<i>Convection</i>	-3.27E-05	3.071	-0.012	0.0116	-2.79	0.5252
<i>Electron Flow</i>	-5.40E-08	0.1972	-2.21E-05	2.08E-05	-0.2271	0.09313
<i>Radiation</i>	3.27E-05	-3.268	0.01202	-0.01162	3.017	0.3817

### 3.3.1.8 Summary

The present study validated the electric arc simulator against experimental data with 4.9% average percentage error. A statistical method based on data sampling was proposed to determine the AC arc state variables from results in order to approximate and evaluate the arc heat dissipation. The analysis of arc performance was conducted under different arc operating currents and arc lengths and generated the AC arc heat dissipation database and the arc momentum transfer database for the scrap melting model. The main conclusions from the parametric study are given below:

- 1) Increasing the arc length elevates the total arc power delivery since the longer arc increases the arc resistance, and increasing the RMS arc current also has a positive effect on the elevation of total arc power delivery. The faster growth of arc power delivery appears when having a higher arc current or longer arc length.
- 2) Longer arc length has a positive impact on increasing the arc radiation but a negative impact on increasing the arc convection and electron flow. Therefore, a short arc should

be used initially when the electrode first bores down to minimize radiative heat dissipation to the roof and side walls from the exposed arc. A longer arc should be used after the electrode has bored down into the scrap to make the radiated power dissipate to the surrounding scrap more effectively.

- 3) The higher arc current reinforces the Lorentz force and Joule heating effect applied on the flow field leading to the arc plasma having stronger impingement on the cathode/anode surface and increasing the share of convection but reducing the share of radiation.

### 3.3.2 Coherent Jet Simulator

This section presents the results from the coherent jet simulator, which performs a separate simulation of the coherent jet produced from an industry-scale burner to investigate its jet performance.

#### 3.3.2.1 Simulation Conditions

The computational domain used in the coherent jet simulator is shown in **Figure 3.38**, which contains 3 million computational cells in total determined from the mesh sensitivity study. Total computational time is around 15 hours if using 80 cores in the high-performance computing (HPC) cluster to obtain the converged results.

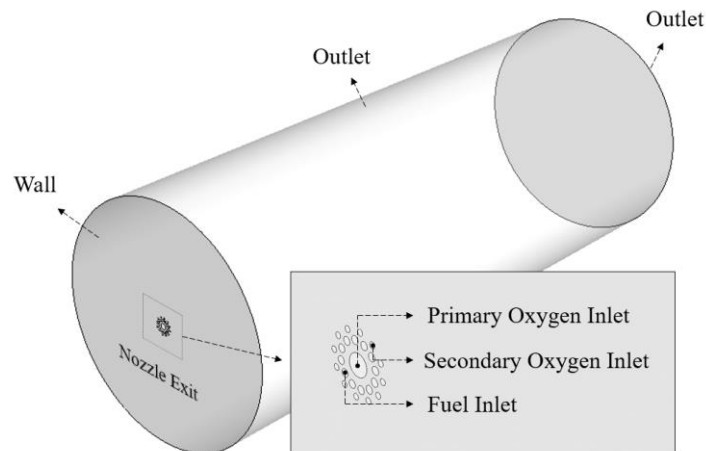


Figure 3.38. Computational domain for separate coherent jet simulation.

The simulation domain is a cylindrical-shaped vessel originating from the exit of the converging-diverging nozzle where the nozzle structure is ignored. The dimension of the vessel is much larger than the burner, which can be used to simulate the supersonic coherent jet behavior in the open space. Therefore, the other walls of the vessel are set as outlets except for the wall where the nozzle exit is located. The present study investigates the jet performance under the lance mode, in which the primary oxygen nozzle with a high flow rate produces the supersonic oxygen jet, while the corresponding flow rates of the fuel nozzle and the secondary oxygen nozzle are relatively low, only to generate the shrouding combustion flame envelop to protect the central supersonic oxygen jet and slow the momentum decay in its traveling path. The boundary conditions used are given in **Table 3.7**.

Table 3.7. Boundary conditions for lance mode.

Name	Parameter	Value
<i>Primary oxygen nozzle</i>	<i>Stagnation pressure</i>	<i>929,000 Pa</i>
	<i>Mach number</i>	<i>2.1</i>
	<i>Total temperature</i>	<i>300 K</i>
	<i>Oxygen mass fraction</i>	<i>100%</i>
<i>Secondary oxygen nozzle</i>	<i>Flow rate</i>	<i>0.006383 kg/s</i>
	<i>Total temperature</i>	<i>300 K</i>
	<i>Oxygen mass fraction</i>	<i>100%</i>
<i>Fuel nozzle</i>	<i>Flow rate</i>	<i>0.01277 kg/s</i>
	<i>Static temperature</i>	<i>300 K</i>
	<i>CH<sub>4</sub> mass fraction</i>	<i>100%</i>

### 3.3.2.1 Validations

The validation of the coherent jet simulation is based on the experiment by Anderson et al. [65], including the establishment of the identical geometry and the use of the same operations for the burner as in the experiment. Since the referred experiment only includes the burner without

considering the solid scrap and the liquid steel, the initial volume fractions of both solid and liquid phases in this numerical validation are set to zero. The jet potential core length produced by the burner is defined as the jet travel length when the axial velocity of the central jet drops to 90% of the initial velocity. Anderson et al. measured the impact of the shrouding flame on the jet potential core length in the ambient air to reflect the sensitivity of the jet performance to the shrouding flame. The validation in this section quantifies the modeling accuracy of the coherent jet by comparing the jet potential core length under two different operating conditions according to the experimental setup.

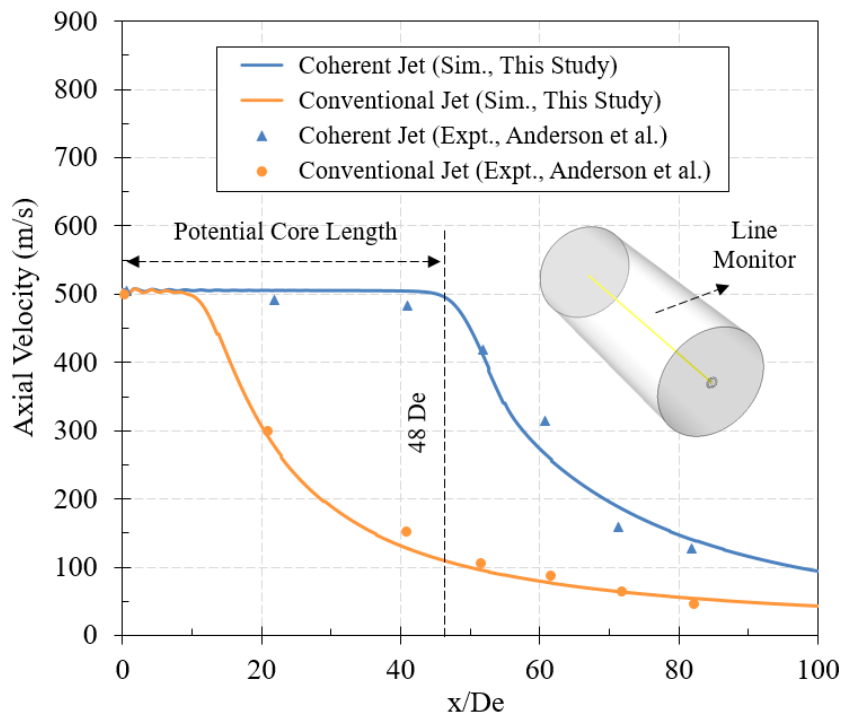


Figure 3.39. Coherent jet validation – axial velocity distribution.

The comparison between the simulation results and the measured data of the axial velocity distribution for both coherent jet and conventional jet is shown in **Figure 3.39**, the corresponding coherent jet velocity, temperature, and density contours are given in **Figure 3.40**. The conventional jet without the shrouding flame is easy to have direct contact with the environment so that the shear layer at the boundary of the central jet tends to have higher vorticity, resulting in more intense fluid mixing and turbulence effects that entrains more ambient gas into the central jet, which in turn makes the decay of central jet momentum. The above effects significantly reduce the jet

potential core length of the conventional jet compared with that of the coherent jet. From the comparison, the jet potential core length of the coherent jet is 48  $D_e$  (where  $D_e$  is the diameter of the convergent-divergent nozzle exit), which is 2.5 times longer than that of the conventional jet. The average difference between the simulation results and the measured data is 5.9%, which indicates a good accuracy in the coherent jet modeling including the turbulence viscosity correction and the shrouding flame combustion simulation.

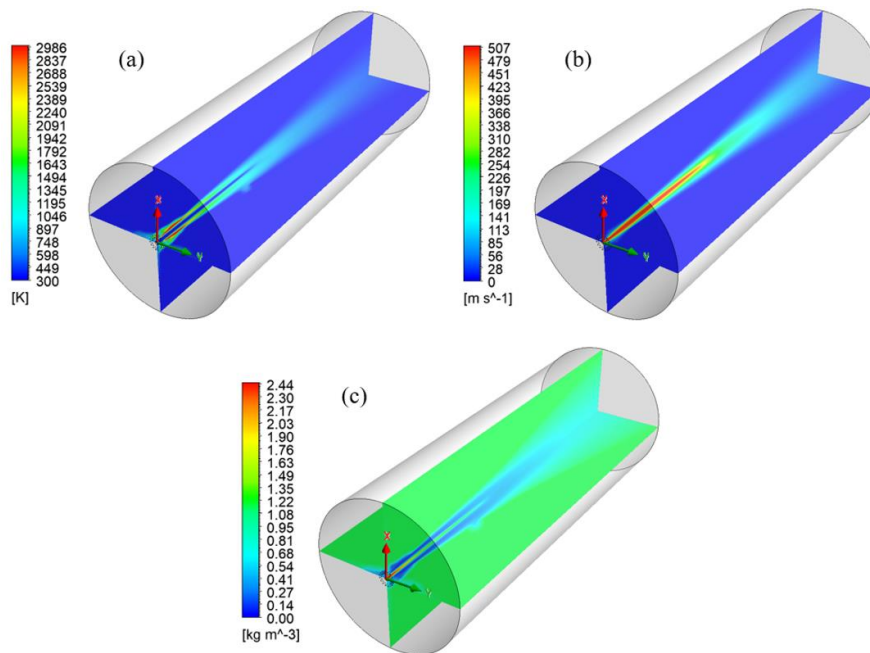


Figure 3.40. Coherent jet validation – (a) temperature distribution; (b) velocity distribution; (c) density distribution.

### 3.3.2.3 Effect of Freeboard Ambient Temperature

The utilization of burners to generate coherent jets in the refining stage mainly aims to deliver more oxygen and jet kinetic energy to the bath for better stirring and decarburization. The main body of the coherent jet during this stage is exposed to the freeboard region, which may be impacted by the freeboard environment leading to further impacts on the delivery of oxygen and kinetic energy. Generally, the difference in the freeboard environment is eventually comprehensively reflected in the variations in the freeboard ambient temperature. Therefore, this section evaluates the jet performance under different freeboard ambient temperatures from 300 K to 1922 K to reveal the relevant impacts.

**Figure 3.41** shows the variations of jet potential core length under 5 target freeboard ambient temperatures. The jet potential core length is extended with the increase of freeboard ambient temperature, in which the jet potential core length at 1922 K is 1.2 times longer than that at 300 K. In addition, the correlation between the freeboard ambient temperature and the jet potential core length grows exponentially, that is, compared with the low ambient temperature, the increase in the jet potential core length is much larger in the high ambient temperature for each degree elevation of ambient temperature. The results can be explained by the fact that the turbulent viscosity and density of ambient gas are significantly reduced in the high ambient temperature environment, meanwhile, the heat transfer between the shrouding combustion flame and the environment is strengthened instead, leading to more effective protection of the center jet. The aforementioned combined effects allow the center jet to travel farther in the freeboard consequently, as can be seen from both **Figure 3.42**. A high-temperature freeboard environment can often be obtained by properly installing the burner for sufficient post-combustion, which is beneficial to prolong the jet potential core length while reducing the emissions of carbon monoxide. However, the excessive freeboard temperature often means higher heat loss, which may be caused by the large arc exposure to the freeboard region. This scenario can cause potential damage to the water-cooling panel system on the furnace side wall, which is studied in detail in the subsequent **Section 3.3.6**.

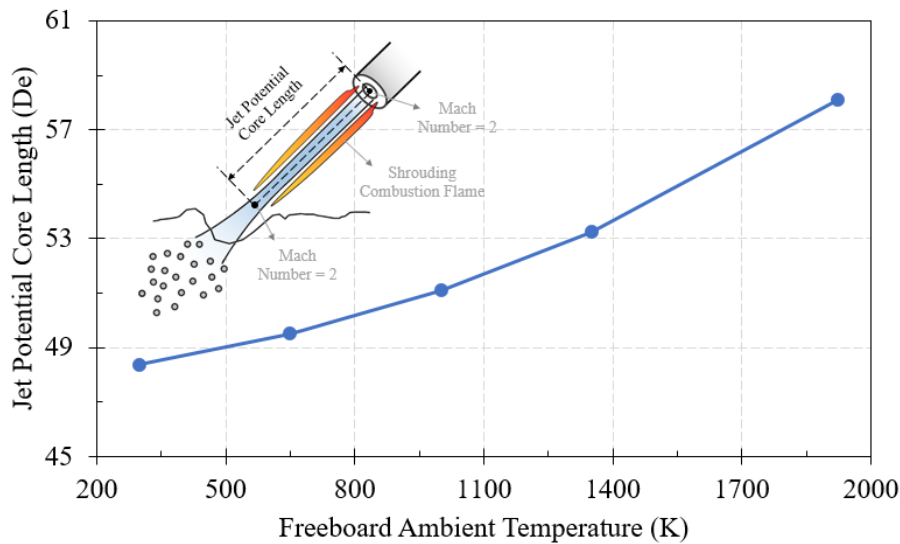


Figure 3.41. Comparison of jet potential core length under different ambient temperatures.

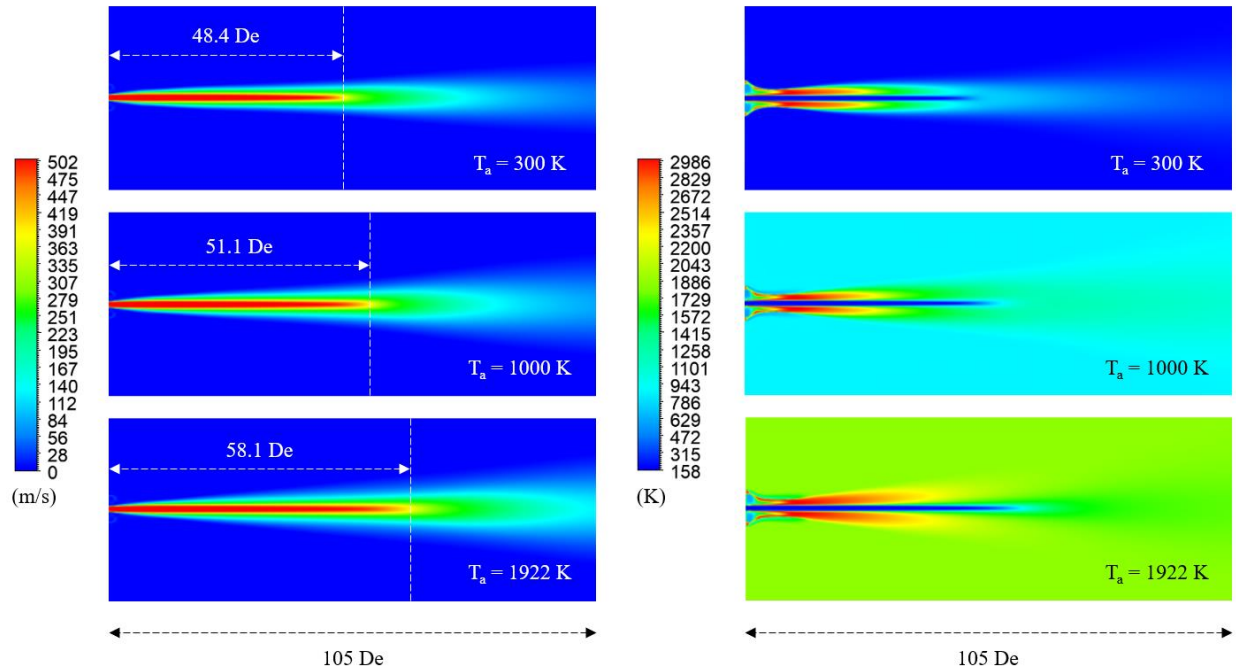


Figure 3.42. Coherent jet simulation results under different ambient temperatures.

### 3.3.2.4 Effect of Fuel Input

The main difference between the supersonic coherent jet and the supersonic conventional jet lies in the combustion flame envelope around the central jet, while the fuel input directly impacts the combustion flame status. To this fact, it is necessary to evaluate the effectiveness of fuel input to determine the optimal flow rate of the given burner from the industry collaborator. The present study considers eight different fuel inputs at the freeboard ambient temperature of 1922 K, and the fuel input is represented through the different percentages of the given total primary oxygen volumetric flow rate. The jet potential core length varied with the fuel input amount is given in **Figure 3.43** and the corresponding CFD simulation results are shown in **Figure 3.44**.

It can be seen that the low fuel input makes the burner difficult to form an effective flame envelope to protect the center jet, thus a large amount of the gas entrainment from the ambient disturbs the center jet leading to a short jet potential core length. With the gradual increase of fuel input, a stable flame envelope is generated promoting the increase of jet potential core length. When the fuel/primary oxygen volumetric flow ratio exceeds 6.5%, the growth of the core length slows down considerably. Further increase of the fuel input by 10% can only extend the jet potential core length

by 0.8%, which lacks the economy of the burner operation. Therefore, under the current high ambient temperature conditions, the fuel input plays an important role in determining the jet potential core length, and insufficient fuel input significantly reduces the coherent jet performance, leading to poor oxygen delivery and bath stirring intensity.

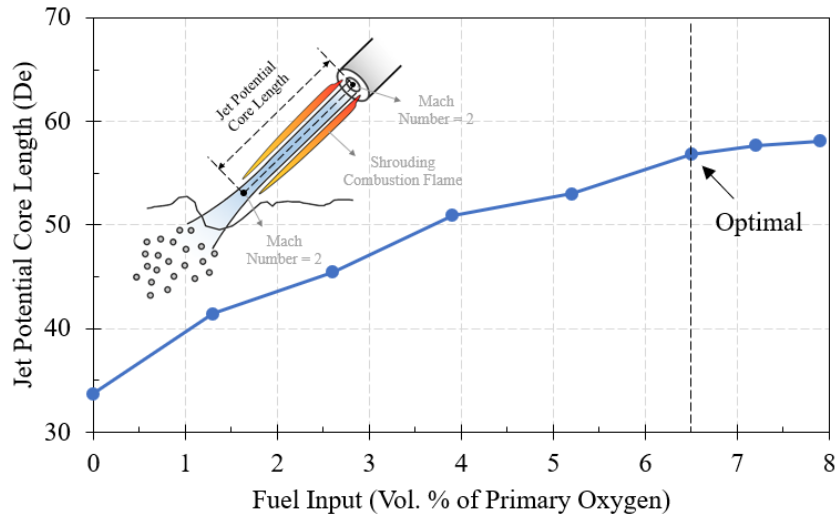


Figure 3.43. Comparison of jet potential core length under different fuel input.

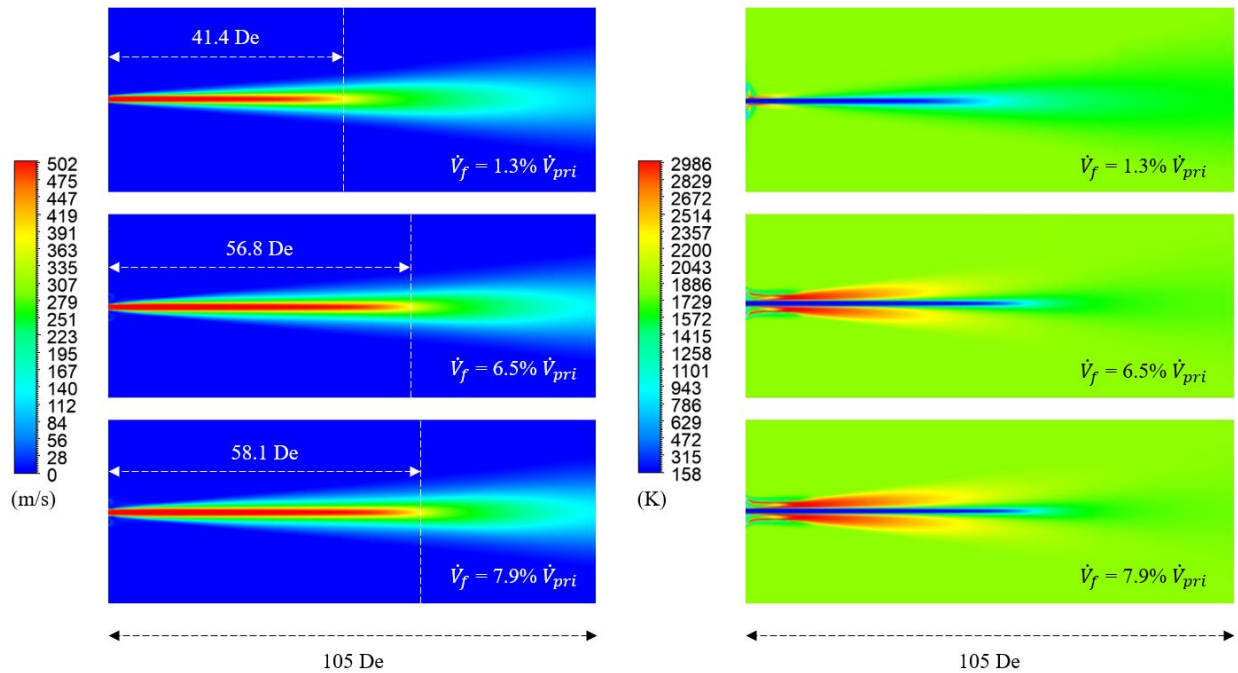


Figure 3.44. Coherent jet simulation results under different fuel input.

### 3.3.2.5 Summary

The present study validated the coherent jet simulator against experimental data with 5.9% average percentage error. The investigations were conducted for the given burner to reveal the effects of freeboard ambient temperature and the fuel input on the jet potential core length. The main conclusions from the parametric study are given below:

- 1) The turbulent viscosity and density of ambient gas are significantly reduced in the high ambient temperature environment, meanwhile, the heat transfer between the shrouding combustion flame and the environment is strengthened instead, leading to more effective protection of the center jet. Therefore, the relatively high freeboard ambient temperature increases the jet potential core length and improve the jet performance during the refining stage, which can achieve a better oxygen delivery and jet kinetic energy to the bath.
- 2) Under the current high ambient temperature conditions, the fuel input plays an important role in determining the jet potential core length, and insufficient fuel input significantly reduces the coherent jet performance, leading to poor oxygen delivery and bath stirring intensity. For the given burner, the optimal fuel input can be achieved when the fuel/primary oxygen volumetric flow ratio exceeds 6.5%.

### 3.3.3 Scrap Preheating Simulator

This section presents the results from the scrap preheating simulator, which couples the scrap melting model and the coherent jet model to simulate the scrap preheating stage, that is, the scrap preheating and melting by the industry-scale coherent jet burner.

#### 3.3.3.1 Simulation Conditions

The simulator are used to simulate a 150-ton NLMK industrial AC EAF. **Figure 3.45** and **Figure 3.46** shows the internal structure of the target furnace and the corresponding computational domain which is established according to the actual dimensions.

Complex geometric structures, including burner station, furnace lid, and wall, bottom refractory surface, are appropriately simplified to ensure the quality of the full-structure mesh. The optimal

mesh contains 0.6 million computational cells in total after conducting a mesh sensitivity study. Considering that electrode melting is not involved in the study, the three electrodes located in the center of the furnace are not presented in the computational domain. Four burners are distributed 90 degrees apart on the four corners of the furnace wall so that the scrap can be melted from the surrounding cold spots to the center of the furnace.



Figure 3.45. NLMK EAF with scrap charged;

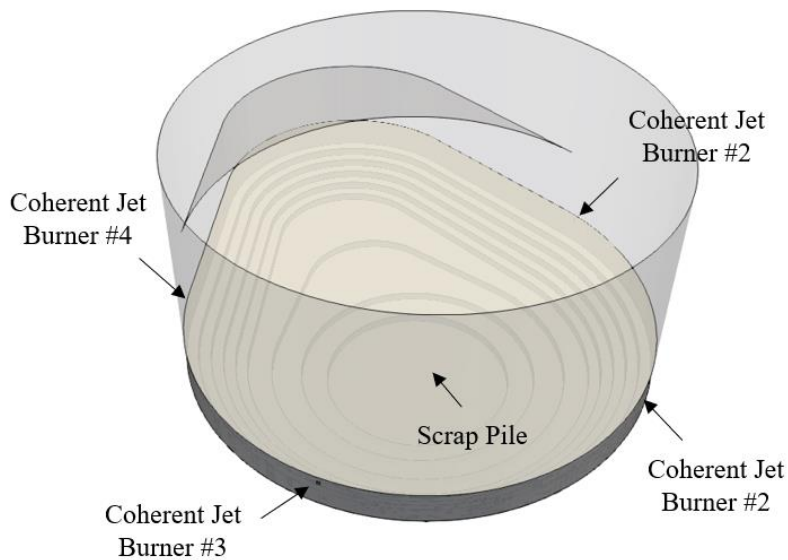


Figure 3.46. Computational domain with scrap charged.

Table 3.8. Baseline burner condition (3.2 MW under burner mode).

Name	Parameter	Value
<i>Primary oxygen nozzle</i>	<i>Flow rate</i>	<i>210 SCFM</i>
	<i>Total temperature</i>	<i>300 K</i>
	<i>Oxygen mass fraction</i>	<i>100%</i>
<i>Secondary oxygen nozzle</i>	<i>Flow rate</i>	<i>210 SCFM</i>
	<i>Total temperature</i>	<i>300 K</i>
	<i>Oxygen mass fraction</i>	<i>100%</i>
<i>Fuel nozzle</i>	<i>Flow rate</i>	<i>250 SCFM</i>
	<i>Static temperature</i>	<i>300 K</i>
	<i>CH<sub>4</sub> mass fraction</i>	<i>100%</i>

Table 3.9. Key parameters in scrap melting model.

Parameters	Value
$\rho$	<i>Steel density</i> 7500 kg/m <sup>3</sup>
$C_{p,s}/C_{p,l}$	<i>Steel specific heat</i> 696.4 j/kg-K
$T_{solidus}$	<i>Solidus temperature</i> 1670 K
$T_{liquidus}$	<i>Liquidus temperature</i> 1809 K
$h_{fusion}$	<i>Latent heat of fusion</i> 275000 j/kg
$K_l$	<i>Steel thermal conductivity</i> 35 W/(m-K)
$\mu_l$	<i>Steel viscosity</i> 0.007 kg/m-s
$d_s$	<i>Solid phase characteristic diameter</i> 0.027 m
$d_l$	<i>Liquid phase characteristic diameter</i> 0.001 m

For the baseline case, the power of each burner is 3.2 MW, and its corresponding operating conditions are shown in **Table 3.8**. The scrap used for preheating consists of a single scrap type

and assumes a uniform distribution throughout the entire pile. According to the plant data, the initial scrap charge for the baseline simulation is 70 tons of scrap without the external preheating ( $T_s = 300\text{ K}$ ), and the key material parameters in the model are shown in **Table 3.9**.

### 3.3.3.2 Validations

#### 3.3.3.2.1 Gas-solid Heat Transfer

The validation of the gas-solid heat transfer and scrap heating simulation is based on experiments by Mandal et al. [112]. The experiment was carried out in a laboratory-scale cubic furnace, which is filled with scrap initially. The experiment only focuses on the process of scrap heating using a single traditional burner and tries to avoid the occurrence of scrap melting. A single conventional burner was inserted through the hole in the middle-lower part at the front wall of the cubic furnace, and a number of thermocouples were inserted from the side of the furnace to record the temperature variation inside during the experiment.

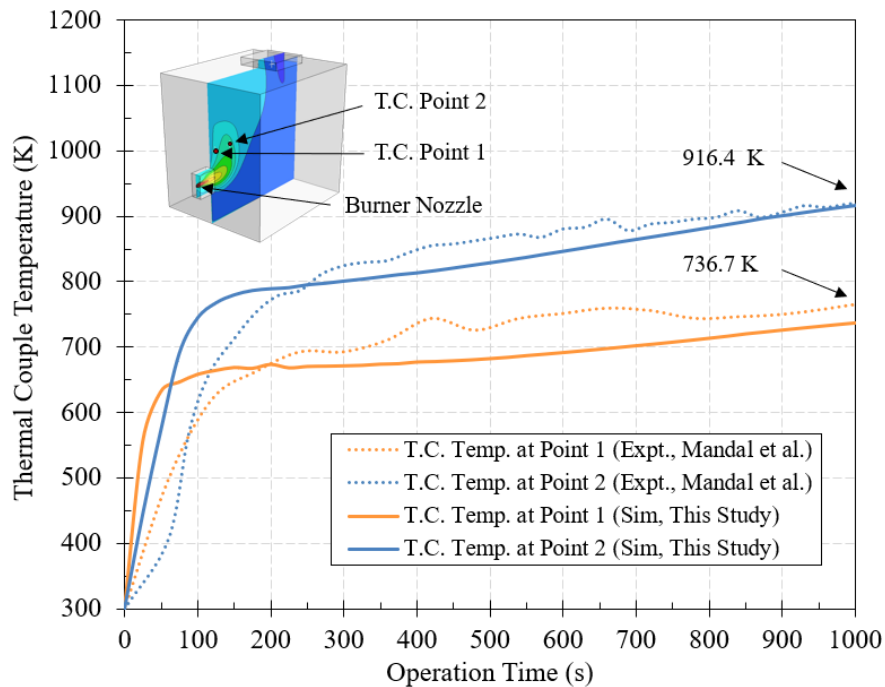


Figure 3.47. Gas-solid heat transfer validation – thermocouple temperature reading comparison.

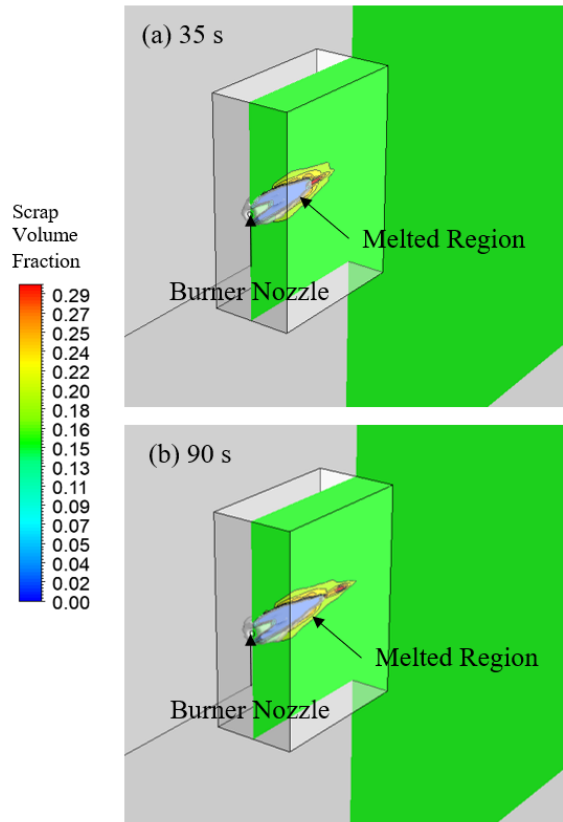


Figure 3.48. Gas-solid heat transfer validation – (a) melted region at 35 s;  
 (b) melted region at 90 s.

The validation in this section establishes the identical geometry as the furnace used in the experiment, and uses the same burner operations to heat the scrap, and compares the thermocouple temperature readings with the simulation results at the same measurement locations. **Figure 3.47** shows the comparison of the thermocouple temperature readings over time at monitoring point 1 and 2 for the shredded scrap heating case under 8.3 kW burner power. The temperature readings for both monitoring points rise rapidly in the first 100 seconds and a turning point occurs at around 100 seconds. The temperature gradually stabilizes after 100 seconds and the final temperatures for monitoring point 1 and 2 are 916.4 K and 736.7 K, respectively, after 1000 seconds of heating. It can be revealed from the comparison that the simulated heating curve is consistent with the experimental data, and the average difference of the final thermocouple temperature prediction is about 2.1%. The simulated scrap melting region is also demonstrated in **Figure 3.48**. Based on the statement from Mandal et al., a small melting cavity was observed in front of the burner within a few minutes during the experiment but grew no larger afterward. The simulation results show a

similar growth rate of the melting cavity. The cavity can be fully developed within 60 seconds, and its size at 90 seconds remains close to the size at 60 seconds. The shape of the cavity matches the photos (35 s and 90 s) provided in their research, indicating a good accuracy of the gas-solid heat transfer and scrap heating simulation.

### 3.3.3.2.2 Non-immersed Burner Preheating

A non-immersed burner preheating experiment was designed and implemented in an industrial-scale 150-ton NLMK AC EAF to collect the necessary data for the simulator validation. The furnace operations were altered specifically in the trial with the intention of achieving parameter controls and data measurements, which was different from the normal furnace setup in NLMK: 50 tons of shredded scrap was charged into a cold and empty furnace with the roof open; the surface of charged scrap was about 0.6 m away from the burner vertically; only one 3.2 MW burner was adopted for the scrap preheating and the three electrodes were powered-off and swung together with the furnace roof to one side; the coherent jet burner was on for 5 minutes to conduct the consecutive scrap preheating during the trial.

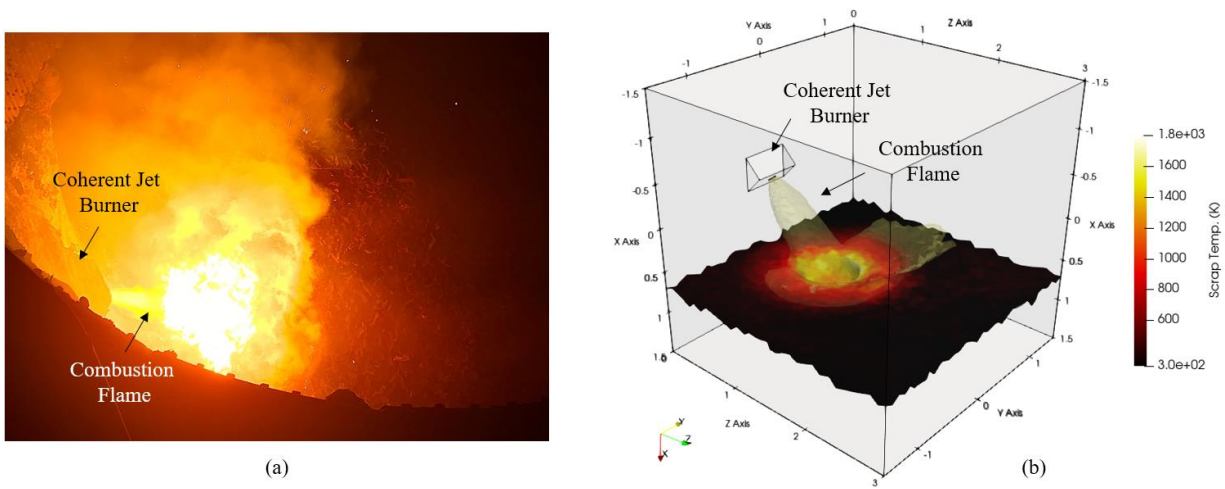


Figure 3.49. Scrap preheating trial using coherent jet burner – (a) experiment; (b) CFD results.

**Figure 3.49 (a)** shows a photograph of scrap preheating using the coherent jet burner taken during the experiment, and the corresponding CFD result from the simulator is given in **Figure 3.49 (b)**. The operating conditions for burner and scrap are consistent in both experiment and simulation. It

can be seen that the high-temperature flame produced by the burner gradually heated and melted the scrap forming a cavity inside. The inner surface of the cavity was bright yellow whose temperature was much higher than elsewhere away from the cavity. The flame was deflected after hitting the cavity and was producing a thick plume of fume during the whole trial. The CFD result correctly reflects the phenomena observed in the experiment.

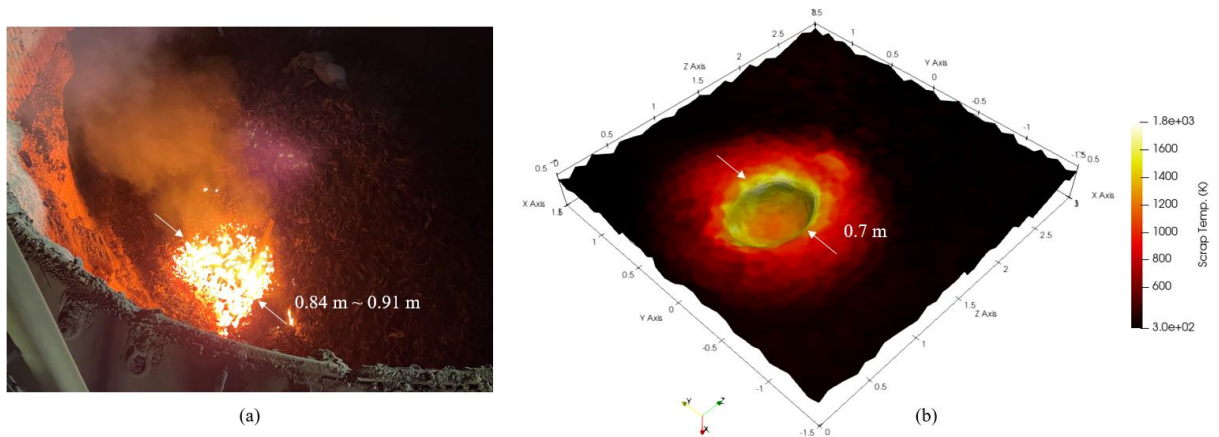


Figure 3.50. Scrap melting cavity at 500 s – (a) experiment; (b) CFD results.

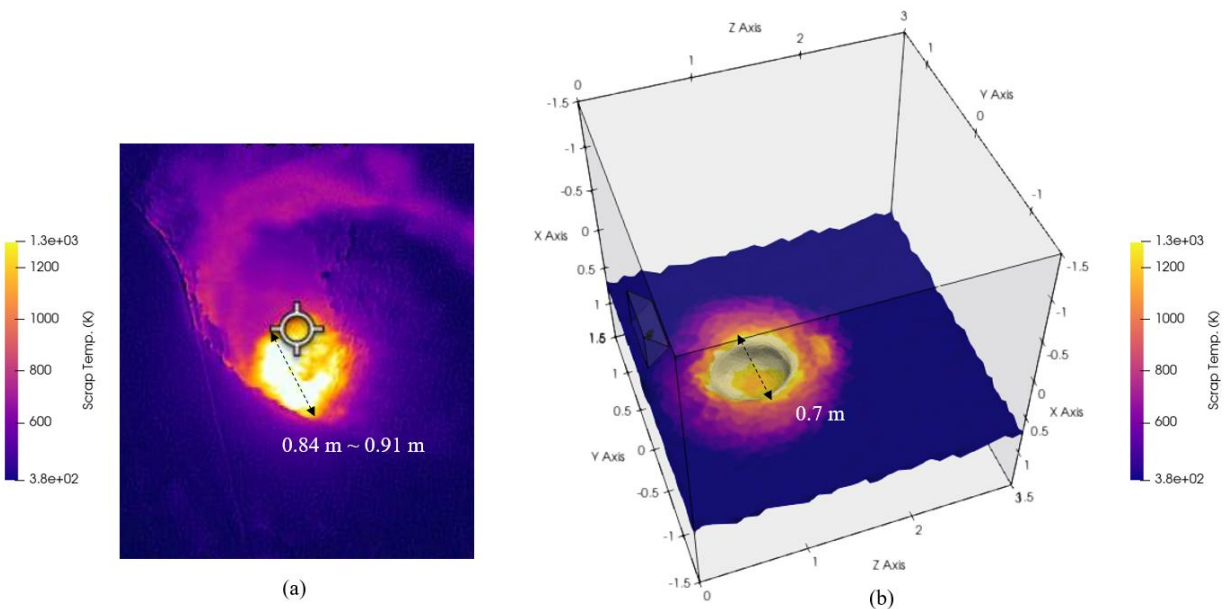


Figure 3.51. Scrap temperature distribution at 500 s – (a) by industrial high-temperature thermal camera FLIR TG297; (b) by CFD simulation.

The evaluation of the simulator accuracy is conducted by comparing the final melted cavity diameter after 5 minutes of consecutive burner preheating and the results are given in **Figure 3.50**. The observed melted cavity diameter is about 0.84 m to 0.91 m in the optical image while the simulated melted cavity is smaller with a diameter of 0.7 m. The percentage error is estimated to be 16.7% to 23.1%. The error is mainly due to ignorance of the jet pushing effect on the scrap surface, which can further enlarge the cavity size.

**Figure 3.51** shows the thermal images for the comparison of scrap temperature distribution at 500 s. The thermal image was taken by the handheld industrial high-temperature thermal camera FLIR TG297 with an accuracy range from 100 °C to 1030 °C (373 K to 1303 K) under the high-temperature mode. The color scale of the simulation result was re-arranged to fit the provided accuracy. The color observed from the thermal image was bright white inside the melting cavity with a similar diameter estimated previously in the optical image.

#### *3.3.3.2.3 Immersed Burner Preheating*

Generally, the height of the scrap charged for the EAF typical run is higher than the vertical height from the burner to the furnace bottom, allowing the burner to be immersed in the scrap pile to maximize heat transfer efficiency during operation. The burner starts to preheat and melt the front scrap from the lower part of the pile forming a cavity, which makes the upper scrap collapse into it under the effect of gravity and continue to be heated and melted. To reproduce the actual phenomenon described above, the burner in this experimental validation was also immersed in the scrap pile to operate to evaluate the simulation results of scrap melting and collapse. Considering the economy of the experiment, only one burner (burner #4) was used for melting while the other three burners were turned off. To facilitate observation and measurement, the height of the scrap pile was controlled at the position just immersing the burner station, and the electrode power supply was off with all electrodes swung to the side along together with the furnace lid. The scrap type used in this experiment is shredded scrap whose average porosity is 0.86 and the entire experiment lasted 12 minutes.

Due to the interference of heavy high-temperature dust and reflected flame radiation when operating the burner, it was difficult to observe the evolution of the melting pit growth during the

experiment. Therefore, in the present experimental validation, the shape of the melting pit was recorded and measured 2 minutes after the burner was turned off and the dust had dissipated in the freeboard region (i.e. the 14<sup>th</sup> minutes from the burner ignition). **Figure 3.52 (a)** shows a thermal image also taken with a handheld industrial high-temperature thermal camera FLIR TG297. The figure demonstrates a bright-yellow pit melted under the burner, whose temperature inside is estimated to be above 1303 K, and a large amount of high-temperature dust still rises up from the melting pit. The edge of the pit is purple-yellow, while the majority part of scrap pile outside the melting pit still remains dark-purple indicating the scrap there was not heated by the burner yet. **Figure 3.52 (b)** shows the corresponding figure captured using an optical camera. By measuring the distance from the front edge of the melting pit to the furnace wall, 12 minutes of consecutive burner operation created a melting pit with a diameter of 1.1 m along the x-direction. The diameter of the melting pit perpendicular to the x-direction is relatively hard to be measured due to the block by rising high-temperature dust in the figure.

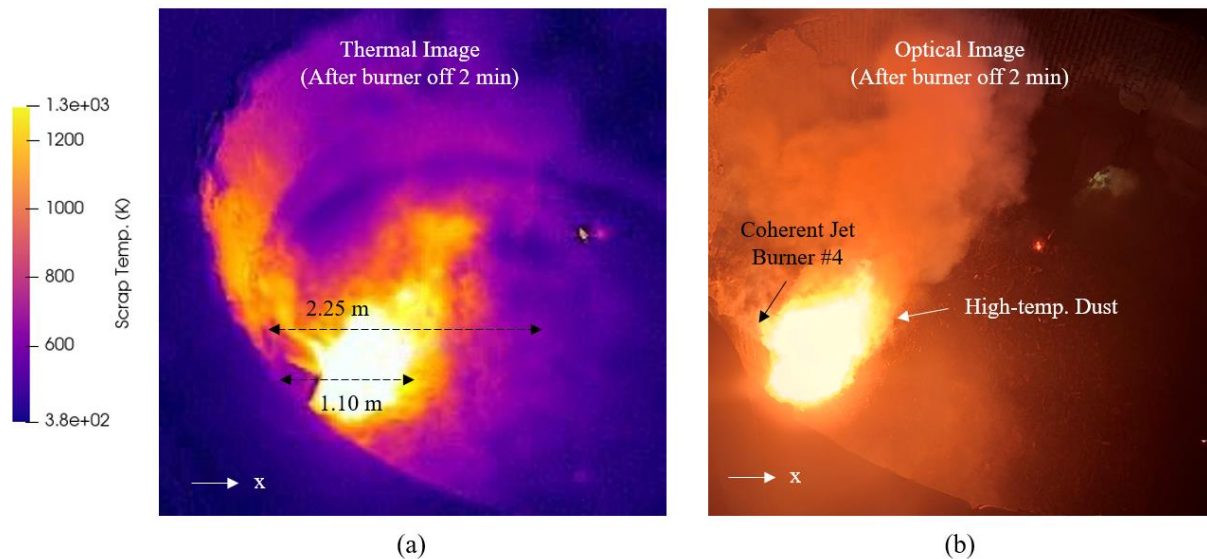


Figure 3.52. Experiment observation – (a) thermal image; (b) optical image.

**Figure 3.53** shows the results of the CFD simulation using the same conditions according to the experimental setup. The figure indicates that the shape, size, and position of the simulated melting pit are relatively consistent with the actual observation in the experiment. With the same range of the temperature scale, the color inside the melting pit shows as bright-yellow, the edge is purple-

yellow, and the rest of the scrap pile outside the melting pit is dark-purple. The present scrap temperature distribution is similar to that given in the thermal image above. The results also reveal that the upper part of the melting pit was slightly larger than the lower part after the scrap collapse showing a U-shape. The diameter of the melting pit is measured in the same x-direction, whose value is 1.24 m and is slightly larger than the experimental observation. The difference in diameter comparison is 12.7% which shows relatively good model accuracy in predicting scrap preheating/melting rate and scrap collapse.

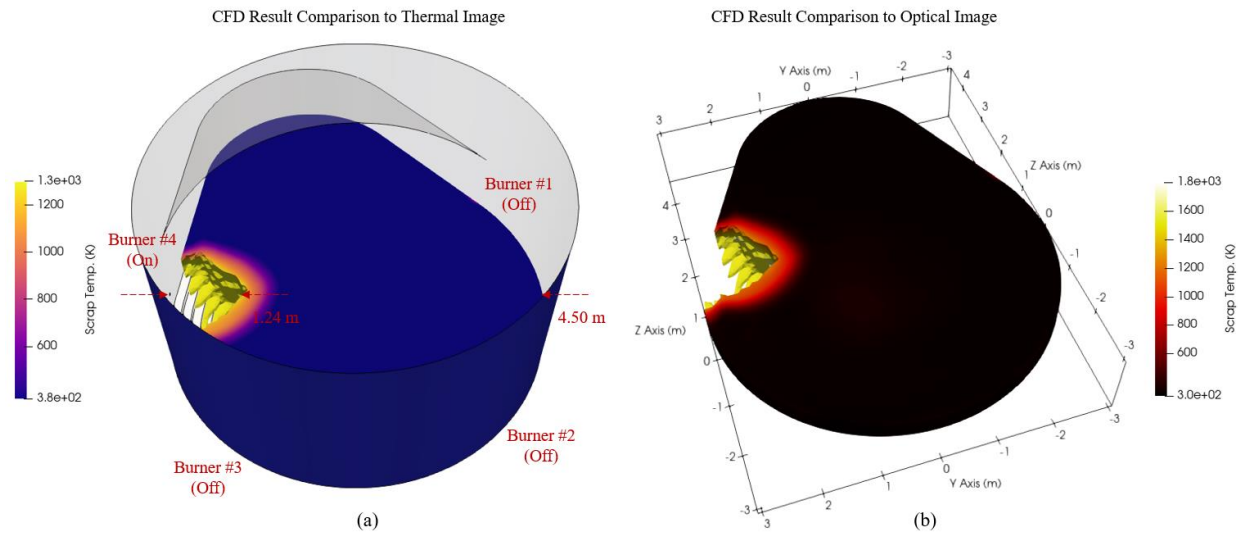


Figure 3.53. CFD results – (a) thermal image; (b) optical image.

### 3.3.3.3 Baseline Results

To explore the scrap preheating stage in NLMK EAF, the NLMK baseline condition is first simulated in the present study, i.e. 70 tons scrap of ambient temperature (300 K) preheated by four 3.2 MW burners for 10 minutes in a full-scale industrial EAF, whose preheating duration is close to the typical burner operation time in NLMK first bucket charge for preheating. Electrode melting is not included in this simulation hence the analysis can focus on the preheating/melting results only caused by the burners.

**Figure 3.54** shows the simulated evolution of the melting pits in front of four burners during the scrap preheating stage, with each plot interval of 100 seconds. The scrap pile is colored with solid phase temperature and the streamlines in the freeboard region are colored with gas phase

temperature. From the results, the burners immersed near the lower part of the pile gradually preheat and melt the scrap in front of them, so that the un-melted scrap above can collapse and form a melting pit. Over time, the diameters of the melting pits increase, and the hot combustion gas that is not sufficiently heat-exchanged with the scrap rises through the openings of the pits into the freeboard region to mix and heat the cold gas there. Under the current baseline conditions, the scrap temperature rise, the melted percentage, and the burner efficiency at 10 minutes are 65.83 K, 3.8%, and 79.56%, respectively. These three indicators are the three main evaluation indexes to judge the quality of the burner preheating process, which are also used for subsequent analysis and optimization. The scrap temperature rise is calculated based on the volume-average temperature of the entire scrap pile. The melted percentage is the ratio of the melting pit volume to the initial scrap pile volume. The burner efficiency is defined as the ratio of the total gas-solid heat transfer amount to the total burner power input. The former two evaluation indexes mainly reflect the scrap heating and melting efficiency, while the latter one mainly reflects the burner performance. The main purpose of the present study is to provide the operational guide for NLMK based on the CFD simulation results to improve both scrap heating/melting efficiency and burner performance.

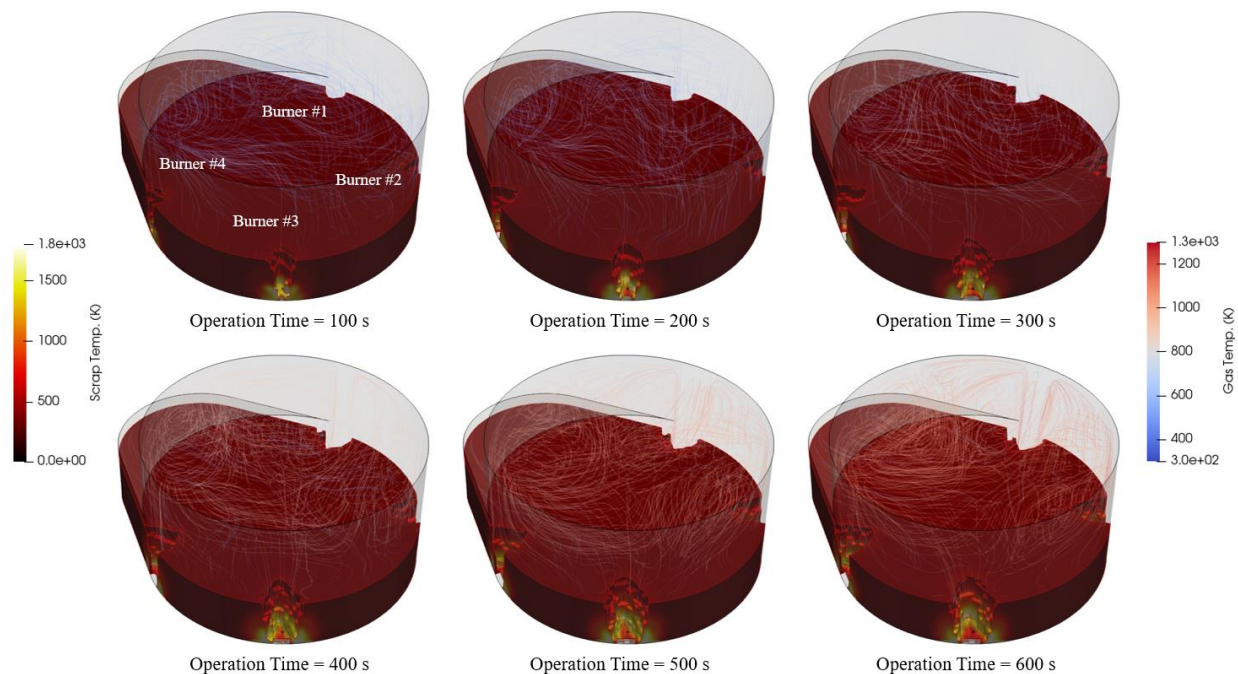


Figure 3.54. Evolution of melting pits in front of four burners (baseline).

### *3.3.3.4 Effects of Single Factors on Scrap Preheating Characteristics*

This section investigates the effects of three main single factors (burner power, scrap initial temperature, and scrap porosity) on the scrap preheating characteristics based on the control variates. Quantitative analysis is performed by comparing three evaluation indexes (scrap temperature rise, melted percentage, and burner efficiency) introduced before.

#### *3.3.3.4.1 Burner Power*

Burner power is considered to be the most crucial factor affecting the scrap preheating stage. Practical EAF operation tends to increase burner power to accelerate the scrap heating and melting rate per heat, which may not be cost-effective. To this fact, three commonly-used burner powers (2.4 MW, 3.2 MW, and 4.0 MW) are selected to evaluate the corresponding preheating results in a full-scale furnace under the same scrap pile conditions (porosity 0.81, initial scrap temperature 300 K).

**Figure 3.55** shows the variations of the above three evaluation indexes in a 10-minute burner operation. Under the same burner power, both the scrap temperature and the size of the melting pit increase with time, while the burner efficiency gives an opposite trend. This can be explained by the fact that the larger melting pit increases the effective traveling distance of the hot combustion gas to its front solid scrap, and the long traveling distance further weakens the gas momentum, thereby reducing the gas-solid heat transfer rate. Additionally, the larger opening of the melting pit also makes it easier for the hot combustion gas to escape to the freeboard region, resulting in potential energy loss. Under different burner powers, increasing burner power helps to speed up the heating and melting of the scrap pile, but reduces the burner efficiency. As the burner power increased from 2.4 MW to 4.0 MW (1.6 times increase in the total burner power input), the scrap temperature increases by 1.1 times at 10 minutes, the melted percentage increases by 1.56 times, and the burner efficiency averaged within 10 minutes decreases by 7.8%. This is mainly due to the fact that the elevation of the total burner power input is greater than the increase in gas-solid heat transfer amount, and a portion of the input power cannot be effectively used to heat and melt the scrap pile. Therefore, higher burner power can accelerate the scrap heating and melting, but it is less economic if considering the burner efficiency.

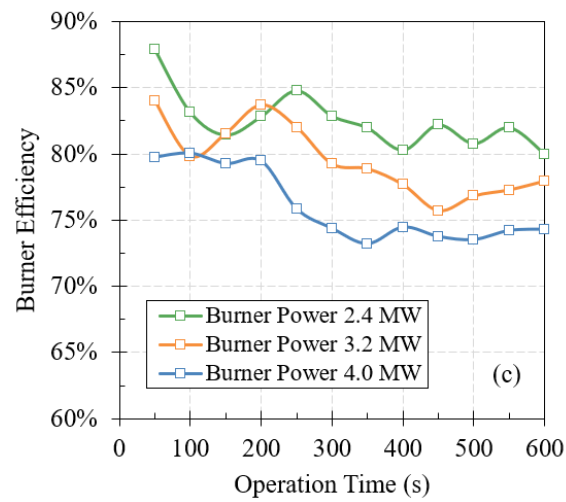
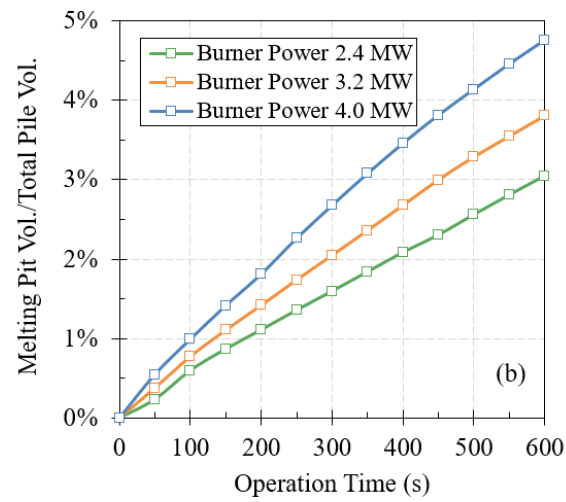
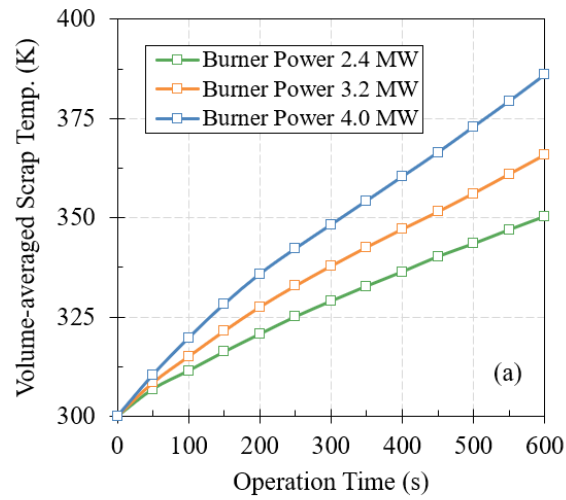


Figure 3.55. Impact of burner power – (a) scrap temperature rise; (b) melted percentage; (c) burner efficiency.

**Figure 3.56** shows a comparison of both final melting pit size and gas temperature in the freeboard region at 10 minutes under different burner powers. The melting pit size is larger and the gas temperature in the freeboard region is likewise higher when the burner power is increased.

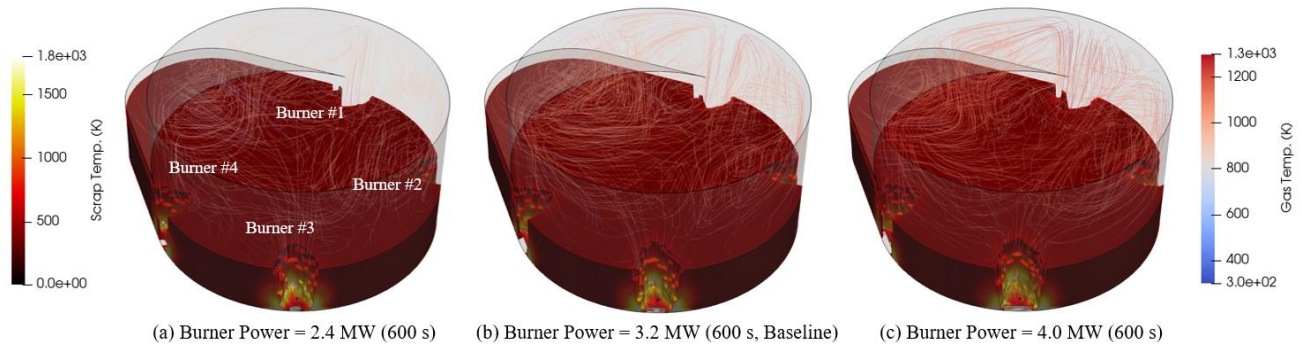


Figure 3.56. Comparison of final melting pit at 600 s – (a) 2.4 MW; (b) 3.2 MW; (c) 4.0 MW.

#### 3.3.3.4.2 Initial Scrap Temperature

Initial scrap temperature impacts the furnace performance in the scrap preheating stage. The external heating or ambient temperature change can affect the initial scrap temperature. This group investigates the effect of different initial scrap temperatures (300 K, 450 K, and 600 K) on three evaluation indexes under the same burner power (3.2 MW) and scrap porosity (0.86). From **Figure 3.57**, when the initial scrap temperature is increased by 2 times, the scrap temperature rise at 10 minutes decreases slightly but the melted percentage increases instead by 1.12 times. This is because the higher initial scrap pile temperature reduces the temperature difference between solid and gas, resulting in a lower total gas-solid heat transfer amount and a slower scrap heating rate. On the other hand, higher initial scrap pile temperatures make the scrap require less energy to be melted within the same amount of time, leading to a larger melted percentage. The trend in burner efficiency analysis is similar to that in the scrap temperature rise analysis. The higher initial scrap temperature reduces the burner efficiency, and the time-averaged burner efficiency decreases by 3.64% within 10 minutes of burner operation when the initial scrap temperature is elevated from 300 K to 600 K. Therefore, there also has the pros and cons when charging the scrap with a high initial temperature in the EAF, that is, the higher initial scrap temperature benefits the faster melting rate, while the lower initial scrap temperature is good for improving the burner efficiency.

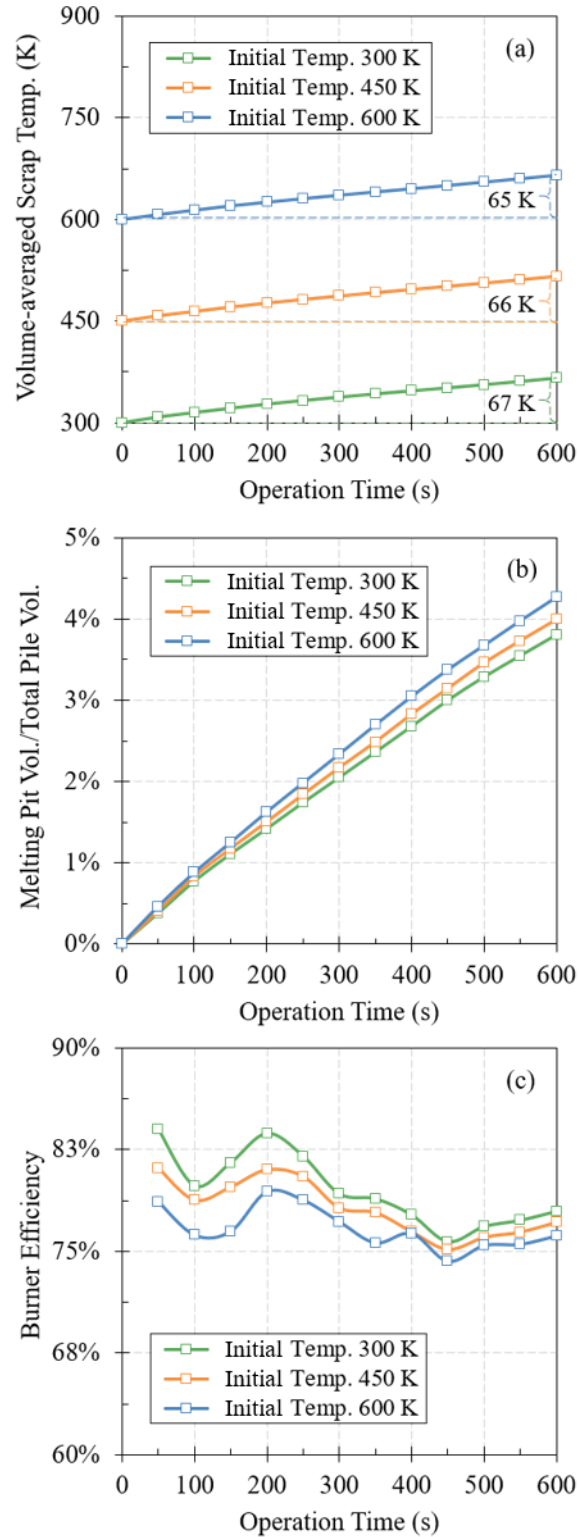


Figure 3.57. Impact of initial scrap temperature – (a) scrap temperature rise; (b) melted percentage; (c) burner efficiency.

**Figure 3.58** shows a comparison of both final melting pit size and gas temperature in the freeboard region at 10 minutes under different initial scrap temperatures. At higher initial scrap temperatures, the pit size is larger and the gas temperature in the freeboard region is higher.

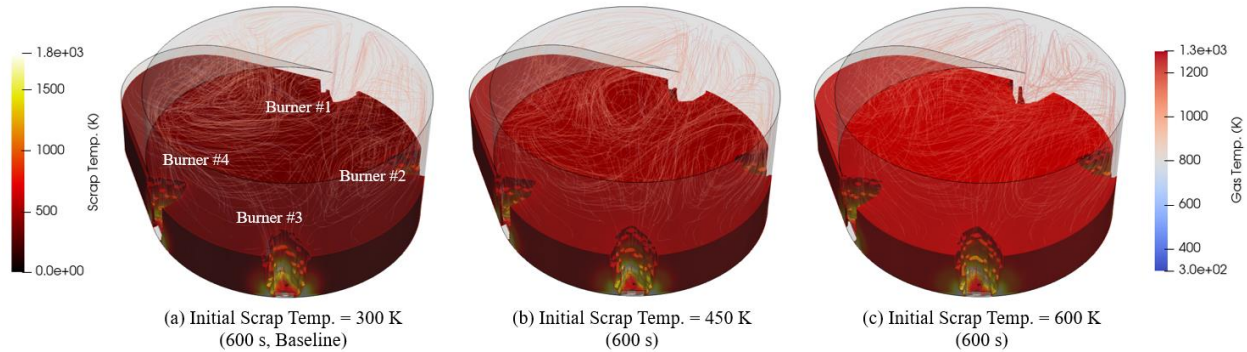


Figure 3.58. Comparison of final melting pit at 600 s – (a) 300 K; (b) 450 K; (c) 600 K.

#### 3.3.3.4.3 Scrap Porosity

The EAF scrap supply stream is constantly evolving with the market. Different types of scrap tend to have different porosity, which can affect the basic physical properties of the charged scrap pile and lead to differences in melting and burner efficiency. Analysis of the effect of scrap porosity helps understand how to proactively adjust furnace operations to achieve higher furnace performance and provide greater flexibility and sustainability to the furnace steelmaking process. Therefore, this group investigates how the scrap with different scrap porosity (0.76, 0.81, and 0.86) impacts three evaluation indexes under the same burner power (3.2 MW) and room temperature (300 K). From **Figure 3.59**, under the same amount of charged scrap (70 tons), the elevation of the scrap porosity (i.e. using less dense scrap) improves the void passage rate of the hot combustion gas and the gas residence time inside the scrap pile, so that the gas-solid heat transfer rate is significantly increased and the scrap can be melted faster. Meanwhile, under the same total burner power input, a higher gas-solid heat transfer rate also means a higher burner efficiency. After 10 minutes of burner melting, 1.13 times increase in the scrap porosity can boost both the melted percentage and the burner efficiency by 1.19 times. Therefore, no matter from the perspective of scrap melting efficiency or burner energy utilization, it is recommended to use less dense scrap (such as busheling) for melting when the capability of the crane and furnace allows.

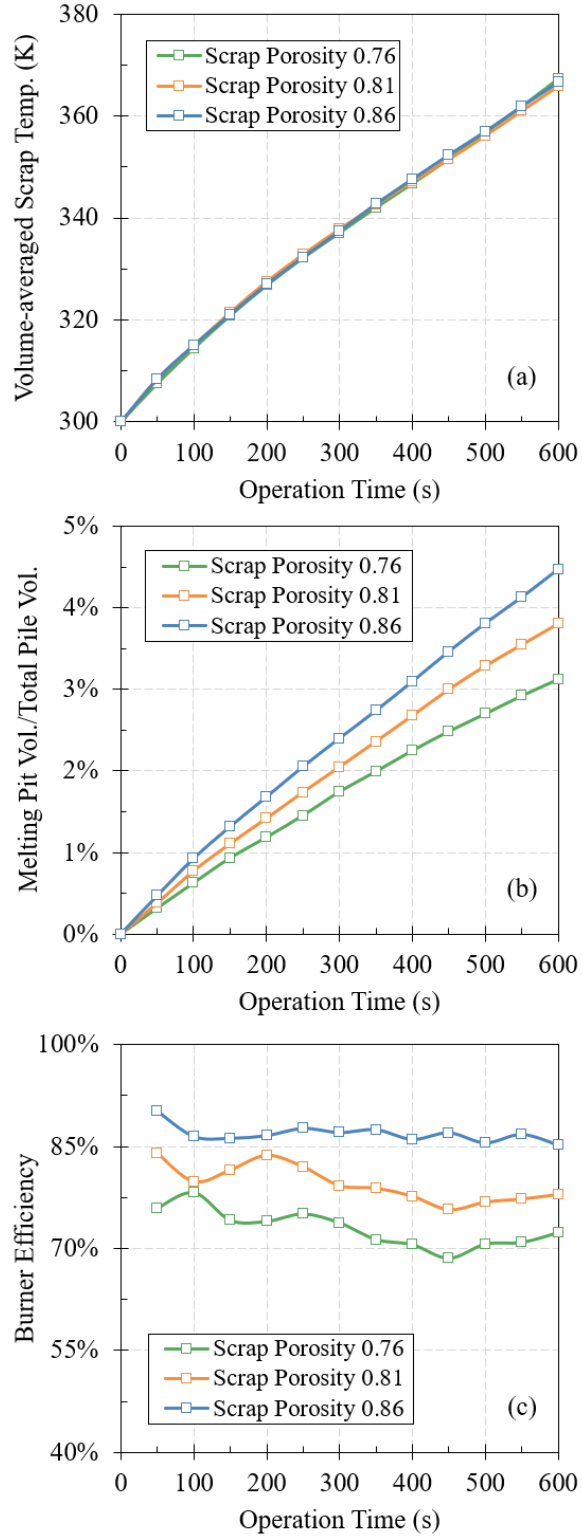


Figure 3.59. Impact of scrap porosity – (a) scrap temperature rise; (b) melted percentage; (c) burner efficiency.

**Figure 3.60** shows a comparison of both final melting pit size and gas temperature in the freeboard region at 10 minutes for different scrap porosity scenarios. A higher porosity has a larger scrap pile volume and a higher scrap pile height. It can also be seen that the scrap pile with higher porosity gives a longer gas residence time in the scrap pile, a larger melting pit size, and a lower gas temperature in the freeboard region.

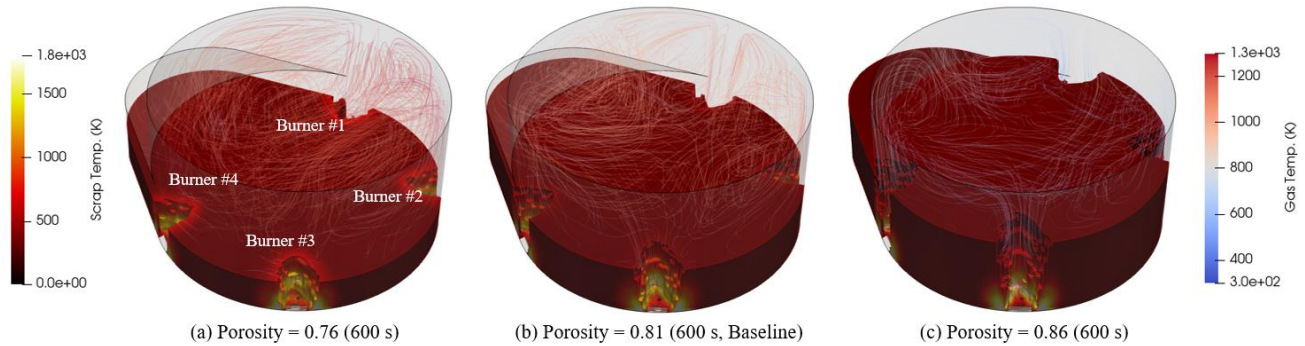


Figure 3.60. Comparison of final melting pit at 600 s – (a)  $\gamma_s = 0.76$ ; (b)  $\gamma_s = 0.81$ ; (c)  $\gamma_s = 0.86$ .

#### 3.3.3.4.3 Scrap Blockage

This sub-section discussed a special scenario in the actual EAF operation, that is, the scrap blockage in front of the burner during the scrap preheating stage, which may be caused by the scrap collapse or the improper scrap charging. The present study assumes that the scrap blockage is caused by a solid cubic scrap, whose distance is 0.4 m away from the furnace wall. The scenario with and without the scarp blockage is compared under the same burner power (3.2 MW), scrap porosity (0.86), and initial scrap temperature (300 K). The scrap blockage has a significant impact on the burner efficiency as shown in **Figure 3.61 (a)**. The burner efficiency is reduced by 22.5% after 5 minutes of burner operation compared with the baseline case. Moreover, the short effective heat penetration distance due to the scrap blockage makes it difficult to heat scrap piles deeper in the middle and back, which reduces scrap heating rate as can be seen from **Figure 3.61 (b)**. The serious flame deflection can also be detected as given in **Figure 3.62 (b)**, which is known as the flame back-blow. The flame back-blow results in a broad region of local high temperature on the sidewall near the burner, with the peak temperature up to 2431 K.

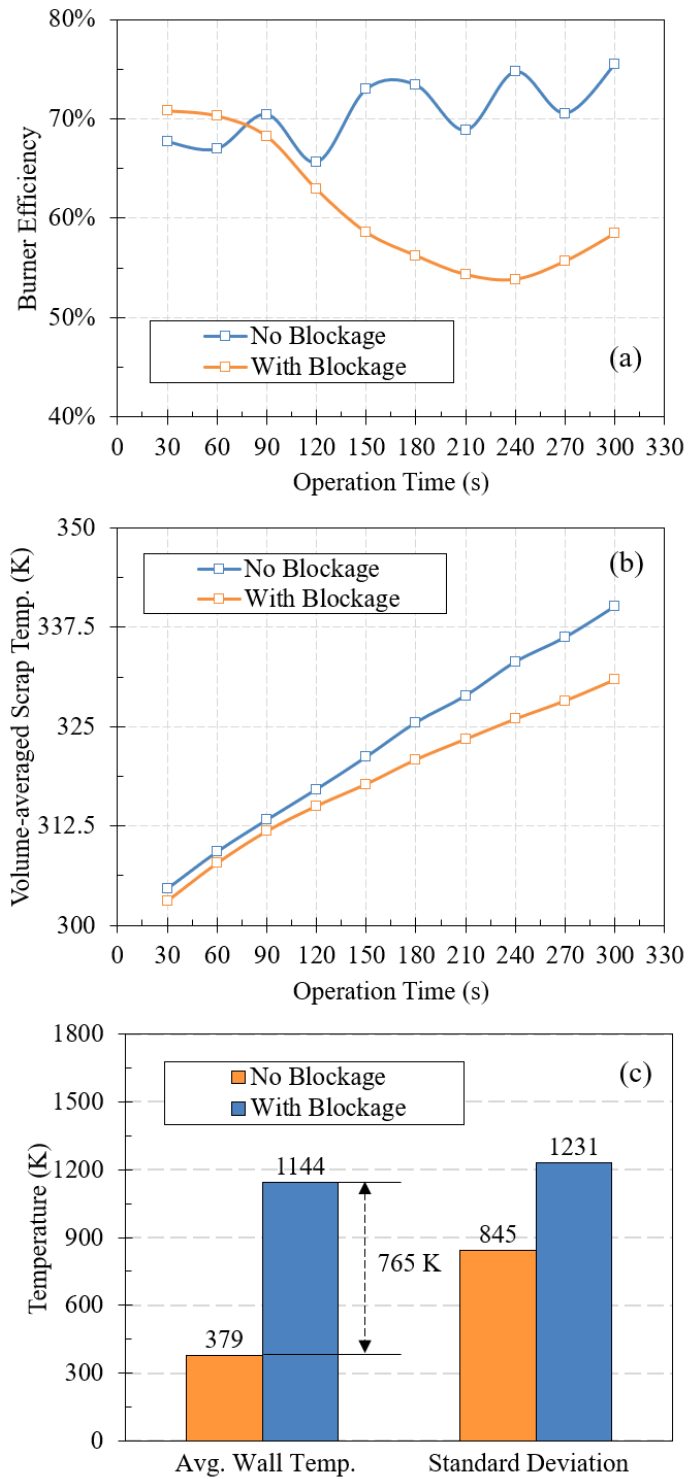


Figure 3.61. Impact of scrap blockage – (a) burner efficiency; (b) scrap heating rate; (c) sidewall temperature distribution.

From **Figure 3.61 (c)**, the flame back-blow raises the average temperature of the side wall 3 times with the current 3.2 MW coherent jet burner, causing serious ablation of the burner and surrounding refractories. Moreover, the flame back-blow may even overheat the water-cooling panel above the burner, triggering the temperature-control alarm to stop the furnace from operating, which has a substantial impact on productivity. Therefore, maintaining a uniform distribution of scrap porosity in the furnace can effectively reduce the probability of scrap blockage, thereby better-protecting facilities and avoiding occurrences of safety accidents.

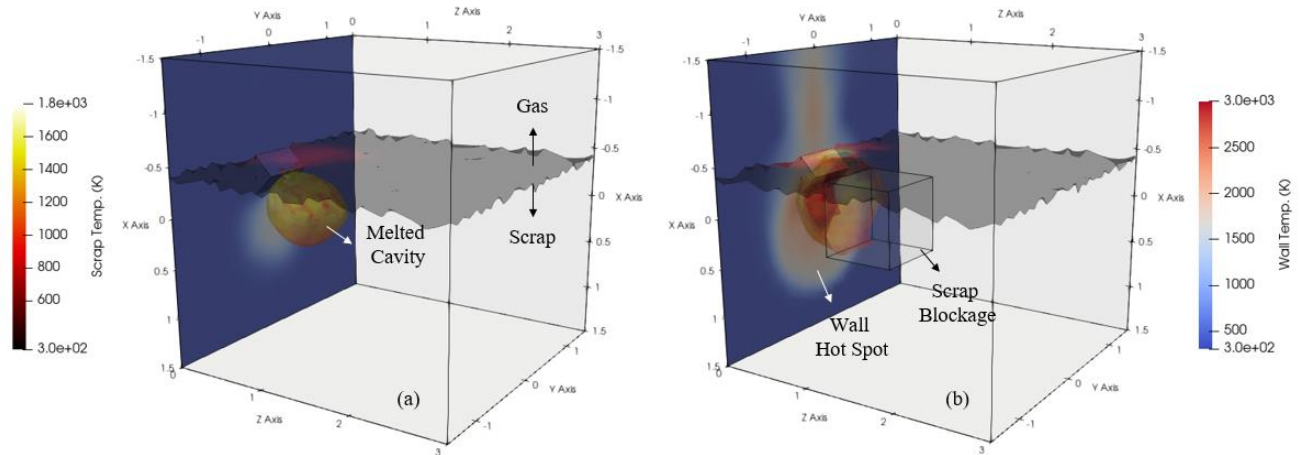


Figure 3.62. Scrap cavity and sidewall temperature distribution with and without scrap blockage.

### 3.3.3.5 Optimization of Scrap Preheating Stage

Generally, the scrap preheating stage is not only affected by a single factor, thus the optimization should always comprehensively consider the impacts of multiple factors to ensure the conclusions are representative. To this fact, the present study adopts the orthogonal design method, which is a mathematical method for multi-factor and multi-level optimization. Compared to the full design method, the orthogonal design method evenly selects representative points according to the orthogonality, which is relatively efficient and accurate. Based on the studies of single factors in the earlier sections, a three-level orthogonal design structure with 3 main factors (burner power, initial scrap temperature, and scrap porosity) same as before is considered to optimize the NLMK burner preheating process. The factor configurations and the corresponding levels are given in **Table 3.10**:

Table 3.10. Factor configurations for optimization.

Factor #	Descriptions	Level 1	Level 2	Level 3
1	<i>Burner Power (MW)</i>	<i>2.4</i>	<i>3.2</i>	<i>4.0</i>
2	<i>Scrap Porosity</i>	<i>0.86</i>	<i>0.81</i>	<i>0.76</i>
3	<i>Initial Scrap Temperature (K)</i>	<i>300</i>	<i>450</i>	<i>600</i>

The  $L_9 (3^3)$  orthogonal design table is used to determine the permutations for basic conditions of both burner operation and charged scrap in each case according to the orthogonality of factor configuration [243], and the corresponding detailed trial information is given in **Table 3.11**:

Table 3.11.  $L_9 (3^3)$  orthogonal design table for CFD simulations.

Trial #	Burner Power (MW)	Scrap Porosity	Initial Scrap Temperature (K)
1	<i>2.4</i>	<i>0.86</i>	<i>300</i>
2	<i>2.4</i>	<i>0.81</i>	<i>450</i>
3	<i>2.4</i>	<i>0.76</i>	<i>600</i>
4	<i>3.2</i>	<i>0.86</i>	<i>450</i>
5	<i>3.2</i>	<i>0.81</i>	<i>600</i>
6	<i>3.2</i>	<i>0.76</i>	<i>300</i>
7	<i>4.0</i>	<i>0.86</i>	<i>600</i>
8	<i>4.0</i>	<i>0.81</i>	<i>300</i>
9	<i>4.0</i>	<i>0.76</i>	<i>450</i>

Nine trials in total are conducted in the present orthogonal design and three main evaluation indexes (burner efficiency, scrap temperature rise, and melted percentage) same as before is used to evaluate the CFD simulations of each trial, whose results are given in **Table 3.12**:

Table 3.12. CFD simulation results presented by three evaluation indexes.

Trial #	Burner Efficiency	Scrap Temperature Rise (K)	Melted Percentage
1	89.37%	50.99	3.57%
2	81.83%	51.39	3.18%
3	74.05%	51.05	2.82%
4	85.65%	67.29	4.66%
5	77.07%	65.28	4.27%
6	72.96%	67.27	3.12%
7	80.27%	85.11	6.21%
8	76.04%	86.04	4.76%
9	67.14%	86.83	4.08%

In the present multi-objective optimization, the results of three evaluation indexes corresponding to each trial are quite different, thus determining the weight of each evaluation index is critical in the selection of the optimal burner and scrap conditions.

The range analysis and the matrix method are adopted here to calculate the contributions of each factor to three evaluation indexes so that the effect of each factor on the final optimization can be considered. The range analysis results are listed in **Table 3.13**, where  $K_i$  is the average CFD results of each evaluation index for the given factor level  $i$ , and  $G$  is the extreme difference of  $K_i$  within three factor levels. The higher  $G$  value, the more dominant the factor is in impacting the corresponding evaluation index.

Table 3.13. Range analysis results.

		Burner Power	Scrap Porosity	Initial Scrap Temperature
Burner Efficiency	$K_1$	0.818	0.851	0.795
	$K_2$	0.786	0.783	0.782
	$K_3$	0.745	0.714	0.771
	$G$	0.073	0.137	0.023
Scrap Temperature Rise	$K_1$	51.141	67.797	68.098
	$K_2$	66.615	67.569	68.501
	$K_3$	85.991	68.382	67.148
	$G$	34.851	0.813	1.352
Melted Percentage	$K_1$	0.032	0.048	0.038
	$K_2$	0.040	0.041	0.040
	$K_3$	0.050	0.033	0.044
	$G$	0.018	0.015	0.006

The range analysis results are visualized in **Figure 3.63**. As can be seen that adjusting the scrap porosity impacts the burner efficiency more than the other two factors. Burner power has absolute dominance in raising the scrap temperature, whose  $G$  value can reach to 34.851. The effect of the three factors on the melted percentage is steadily diminishing, but the burner power still maintains the greatest impact.

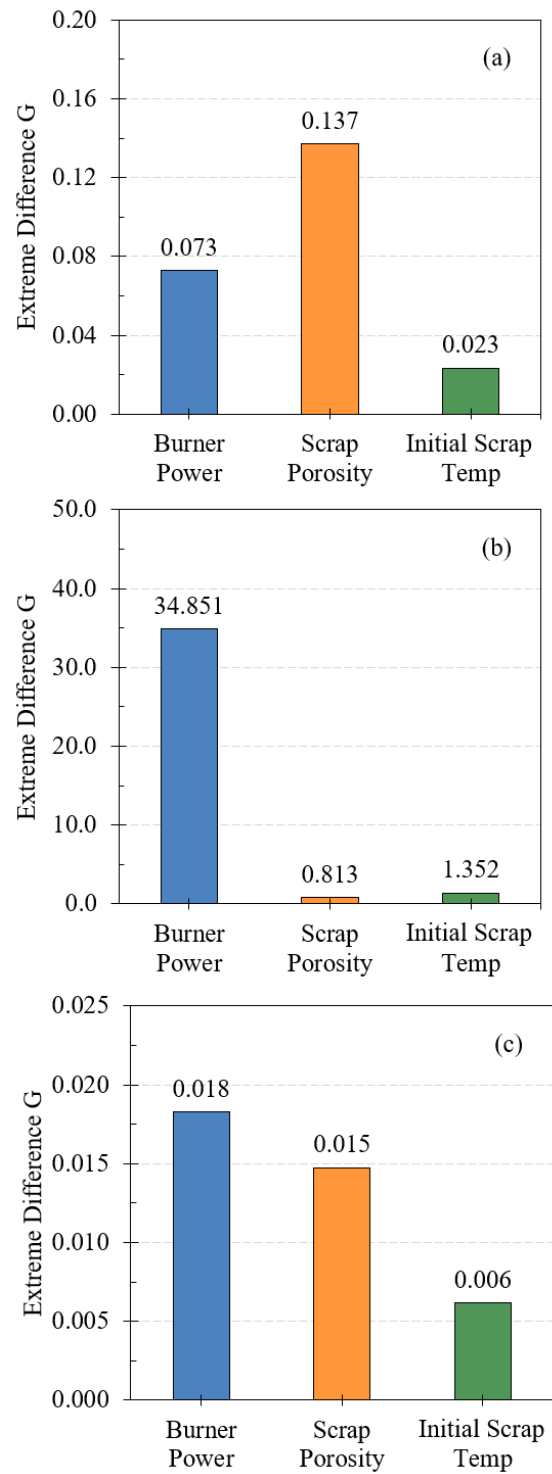


Figure 3.63. Contributions of different factors on impacting – (a) burner efficiency; (b) scrap temperature rise; (c) melted percentage.

The matrix method is demonstrated below to find the optimal burner and scrap conditions from the given factor configuration. A three-layer data structure, as shown in **Table 3.14**, is built up and three key matrixes including the experimental evaluation index layer matrix ( $M$ ), the factor layer matrix ( $F$ ), and the level layer matrix ( $L$ ) are established accordingly to calculate the weight matrix ( $\omega$ ). For the evaluation of burner efficiency as an example, the corresponding matrix definitions and calculation procedures are given below.

Table 3.14. Three-layer data structure for optimization.

1 <sup>st</sup> Layer	Experimental Evaluation Indexes		
2 <sup>nd</sup> Layer	Factor $A_1$	Factor $A_2$	Factor $A_3$
3 <sup>rd</sup> Layer	$A_{11}, A_{12}, A_{13}$	$A_{21}, A_{22}, A_{23}$	$A_{31}, A_{32}, A_{33}$

The experimental evaluation index layer matrix ( $M_1$ ): assuming there are  $i$  factors in total for the optimization and each factor has  $m$  levels, the average value of the evaluation index at the  $j$  level of factor  $A_i$  is denoted as  $K_{ij}$ . In the present study, the larger the evaluation index, the better the burner melting results, thus establishing the matrix  $M_1$  as follow:

$$M_1 = \begin{bmatrix} K_{11} & 0 & 0 \\ K_{12} & 0 & 0 \\ K_{13} & 0 & 0 \\ 0 & K_{21} & 0 \\ 0 & K_{22} & 0 \\ 0 & K_{23} & 0 \\ 0 & 0 & K_{31} \\ 0 & 0 & K_{32} \\ 0 & 0 & K_{33} \end{bmatrix} = \begin{bmatrix} 0.817505502 & 0 & 0 \\ 0.785586825 & 0 & 0 \\ 0.744814524 & 0 & 0 \\ 0 & 0.850963786 & 0 \\ 0 & 0.783095242 & 0 \\ 0 & 0.713847823 & 0 \\ 0 & 0 & 0.794552541 \\ 0 & 0 & 0.78206593 \\ 0 & 0 & 0.77128838 \end{bmatrix} \quad (3-104)$$

The factor layer matrix ( $F_1$ ): the elements in the matrix can be then determined through  $1/\sum_{j=1}^m K_{ij}$  from the values in  $M_1$ :

$$\begin{aligned}
 F_1 &= \begin{bmatrix} \frac{1}{K_{11} + K_{12} + K_{13}} & 0 & 0 \\ 0 & \frac{1}{K_{11} + K_{12} + K_{13}} & 0 \\ 0 & 0 & \frac{1}{K_{11} + K_{12} + K_{13}} \end{bmatrix} \\
 &= \begin{bmatrix} 0.425911275 & 0 & 0 \\ 0 & 0.425911275 & 0 \\ 0 & 0 & 0.425911275 \end{bmatrix}
 \end{aligned} \tag{3-105}$$

The level layer matrix ( $L_1$ ): the elements in the matrix can be then determined through  $G_i / \sum_{i=1}^i G_{ij}$  based on the range analysis results to compute the ratio of the extreme difference of factor  $A_i$  to the total of all extreme differences:

$$L_1 = \begin{bmatrix} \frac{G_1}{G_1 + G_2 + G_3} \\ \frac{G_2}{G_1 + G_2 + G_3} \\ \frac{G_3}{G_1 + G_2 + G_3} \end{bmatrix} = \begin{bmatrix} 0.311883272 \\ 0.588301002 \\ 0.099815726 \end{bmatrix} \tag{3-106}$$

The weight matrix ( $\omega_1$ ): the weights of three factors within all three levels can be determined by multiplying three matrixes above:

$$\omega_1 = M_1 F_1 L_1 = \begin{bmatrix} 0.108593018 \\ 0.104353113 \\ 0.098937141 \\ 0.213220915 \\ 0.1962155 \\ 0.178864587 \\ 0.033778529 \\ 0.03324769 \\ 0.032789508 \end{bmatrix} \tag{3-107}$$

For the evaluations of scrap porosity and initial scrap temperature, the same procedure can be performed to calculate  $\omega_2$  and  $\omega_3$ :

$$\omega_2 = M_2 F_2 L_2 = \begin{bmatrix} 0.23631742 \\ 0.307823259 \\ 0.397359412 \\ 0.007309772 \\ 0.007285178 \\ 0.007372853 \\ 0.012210119 \\ 0.012282225 \\ 0.012039761 \end{bmatrix} \quad (3-108)$$

$$\omega_3 = M_3 F_3 L_3 = \begin{bmatrix} 0.121763051 \\ 0.153180371 \\ 0.191400643 \\ 0.148217997 \\ 0.125294203 \\ 0.102858986 \\ 0.049123841 \\ 0.051115629 \\ 0.057045279 \end{bmatrix} \quad (3-109)$$

The final weight matrix used to determine the optimal burner and scrap conditions is given as:

$$\omega = \frac{1}{3} \times (\omega_1 + \omega_2 + \omega_3) = \begin{bmatrix} 0.15555783 \\ 0.188452248 \\ 0.229232399 \\ 0.122916228 \\ 0.109598294 \\ 0.096365475 \\ 0.031704163 \\ 0.032215181 \\ 0.033958183 \end{bmatrix} \quad (3-110)$$

Table 3.15. CFD results comparison before and after the optimization.

	Burner Efficiency	Scrap Temp. Rise (K)	Melted Percentage
Before Optimization	79.56%	65.83	3.80%
After Optimization	80.27%	85.11	6.21%
% of Improvement	0.01%	29.29%	63.42%

From **Equation (3-110)**, the comprehensive contribution rates of each factor on the scrap preheating results are given in **Figure 3.64** with the burner power having the greatest impact at 57.3%, the scrap porosity contributing 32.9%, and the initial scrap temperature remaining a relatively minor impact at 9.8%.

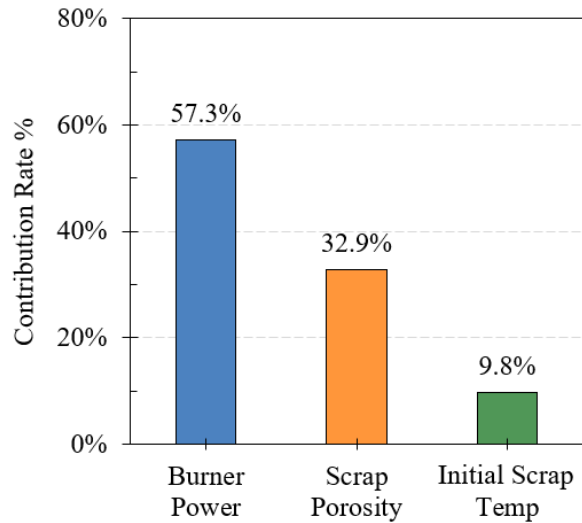


Figure 3.64. Comprehensive contribution rates of each factor on burner preheating results.

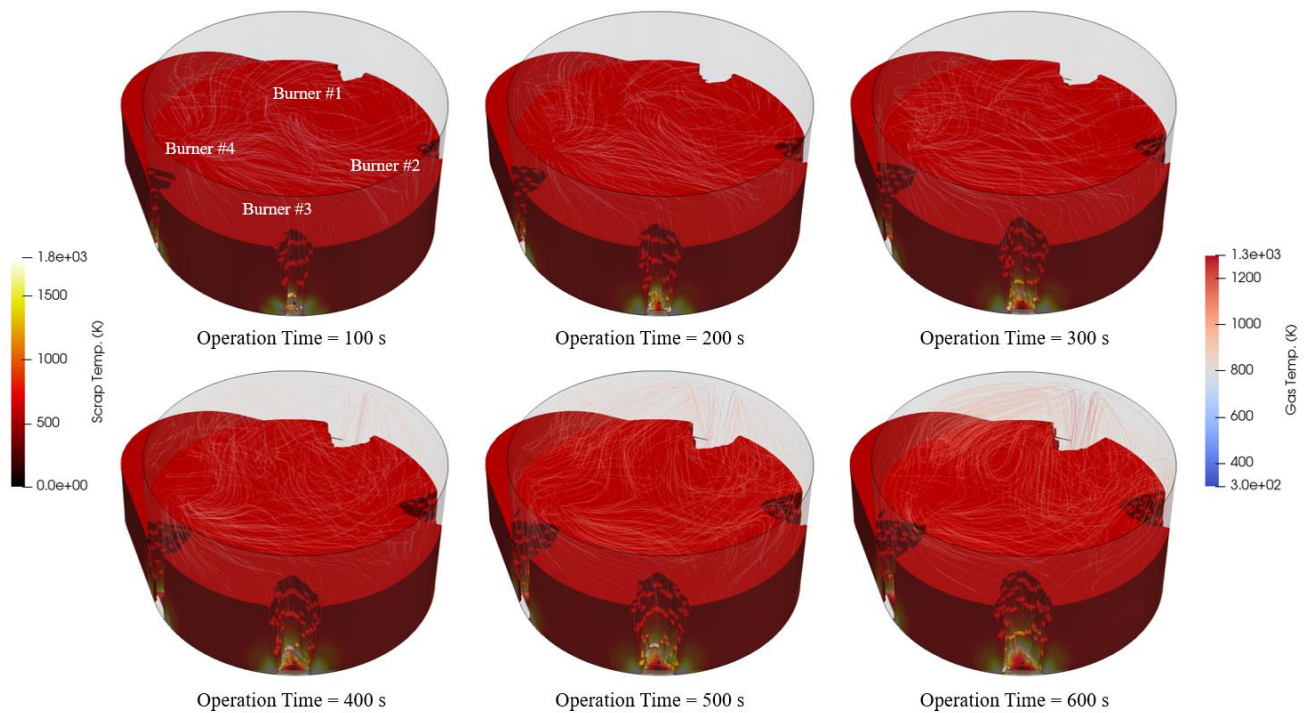


Figure 3.65. Evolution of melting pits in front of four burners (after optimization).

To achieve a better scrap preheating, a higher burner efficiency with a higher scrap temperature rise and a larger melted percentage is preferred for the final results. Considering the above contribution rates of each factor, the optimal burner and scrap conditions are suggested to be 4.0 MW burner power with 0.86 scrap porosity and 600 K initial scrap temperature for NLMK EAF, which means increasing the original burner power by 1.25 times, the original initial scrap temperature by 2 times, and the original scrap porosity by 1.06 times. The CFD results comparison before and after the optimization is presented in

**Table 3.15.** It is noted that the scrap temperature rise and melted percentage have been significantly improved while the burner efficiency enhancement stays almost the same. The evolution of melting pits after optimization is given in **Figure 3.65**.

### **3.3.3.6 Summary**

This section presents the results from the scrap preheating simulator, which simulates the scrap preheating stage. The non-immersed and immersed burner preheating experiments were first time conducted in an NLMK industrial furnace to validate the scrap preheating simulator, whose differences are of 12.7% to 23.1% showing a relatively good model accuracy. The simulator was applied to help NLMK investigate its burner preheating/melting characteristics, and the orthogonal design method was adopted to optimize the process. The main conclusions from the parametric study and optimization are given below:

- 1) The burner efficiency decreases over time during the entire scrap preheating stage. For the baseline NLMK burner and scrap conditions, it is reduced from 84.02% to 77.96% within 10 minutes of operation.
- 2) Under different burner powers, higher burner power can accelerate the scrap heating and melting, but it is less economic if taking the burner efficiency into account.
- 3) Higher initial scrap temperature makes the scrap require less energy to be melted within the same amount of time, leading to a larger final melted percentage. However, the corresponding reduced gas-solid heat transfer rate results in a lower scrap heating rate and burner efficiency. Therefore, the higher initial scrap temperature benefits the faster melting rate, while the lower initial scrap temperature is good for improving the burner efficiency.

- 4) Using less dense scrap improves the void passage rate of the hot combustion gas and the gas residence time inside the scrap pile so that the gas-solid heat transfer rate is significantly increased. Therefore, no matter from the perspective of scrap melting efficiency or burner energy utilization, it is recommended to use high-porosity scrap for melting.
- 5) Adjusting the scrap porosity impacts the burner efficiency more than the burner power and the initial scrap temperature does. Burner power has absolute dominance in raising the scrap temperature and relatively the greatest impact on the melted percentage.
- 6) Although the scrap blockage does not impact the burner efficiency within a short time, it still needs to be avoided during the operation. The scrap blockage not only makes it difficult to heat the scrap pile deeper in the middle and back, which reduces scrap heating rate but also causes the flame blow-back, which leads to a serious ablation of the burner and surrounding refractories as well as the water-cooling panel overheat above the burner
- 7) For the comprehensive contribution rates of each factor on the scrap preheating stage, the burner power having the greatest impact at 57.3%, the scrap porosity contributing 32.9%, and the initial scrap temperature having a relatively minor impact at 9.8%.
- 8) For NLMK EAF, it is suggested to increase the burner power by 1.25 times, the initial scrap temperature by 2 times, and the scrap porosity by 1.06 times, which can improve overall scrap temperature rise and melted percentage by 29.29% and 63.42%, respectively.

### **3.3.4 Scrap Melting Simulator**

This section presents the results from the scrap melting simulator, which couples/integrates the scrap melting model, the electric arc model, and the coherent jet model to simulate the scrap melting stage, that is, the scrap melting by both AC electric arc and coherent jet burner.

#### ***3.3.4.1 Simulation Conditions***

The scrap melting simulator simulates the baseline case in an industry-scale NLMK 150-ton AC EAF with three electrodes of 0.3 m radius and four coherent jet burners mounted on the furnace

wall. The computational domain is constructed according to the real furnace dimensions and is given in **Figure 3.66**. Some complicated structures are simplified for a better mesh quality. The full structure mesh is generated in the entire computational domain with a total element number of 0.6 million after the mesh sensitivity study.

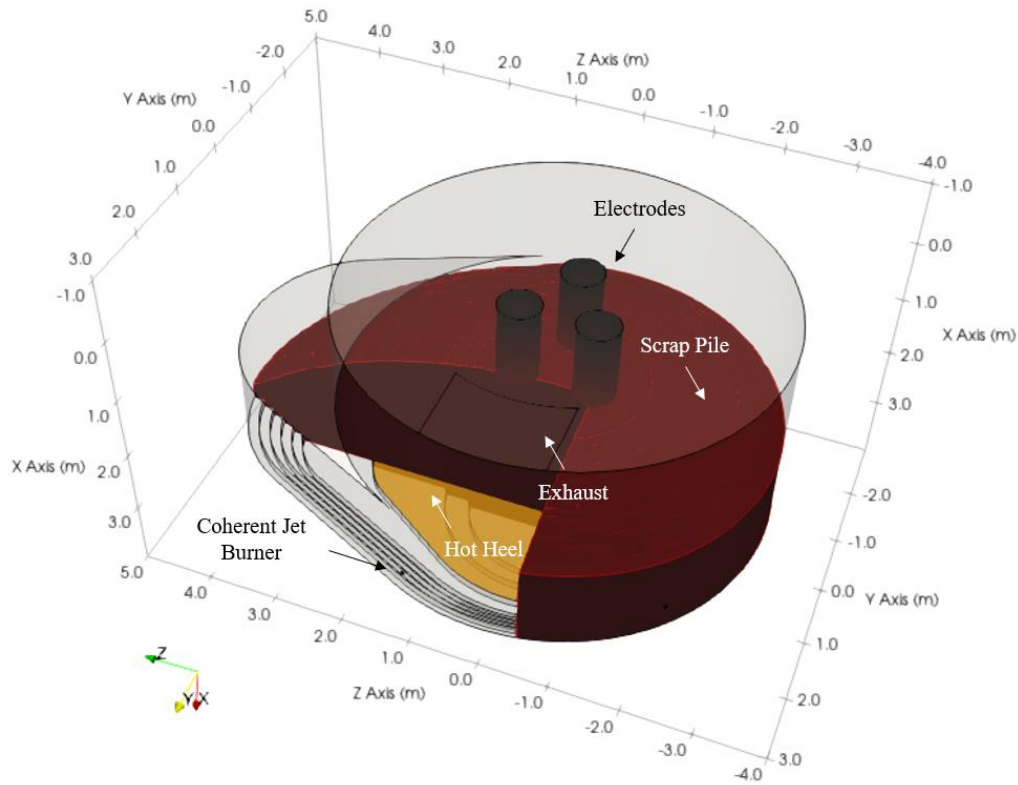


Figure 3.66. Computational domain of industry-scale NLMK AC EAF.

The baseline case refers to the typical run in NLMK EAF, which charges 65 tons of scrap mixes for the first bucket and another 20 tons of scrap mixes for the back-charge. 20 tons of hot heel is left at the bottom of the furnace as the initial.

The operation conditions of the coherent jet burner and the electrodes are extracted from real industrial data in order to reproduce the case by the simulation. Four burners are under the burner mode during the melting stage with the burner power input of 3.8 MW/each. The instant phase current and phase voltage, together with the corresponding arc power and arc length calculated from the electric arc model, are shown in **Figure 3.67**. This figure also reflects the real NLMK

furnace operation timeline, including the first-time electrode bore-in (0 – 350 s), the scrap melting stage for the first bucket (350 s – 900 s), the back charge of the second bucket (900 s), the second-time electrode bore-in (900 – 1250 s), and the main scrap melting stage and the liquid steel refining stage (1250 – 2400 s).

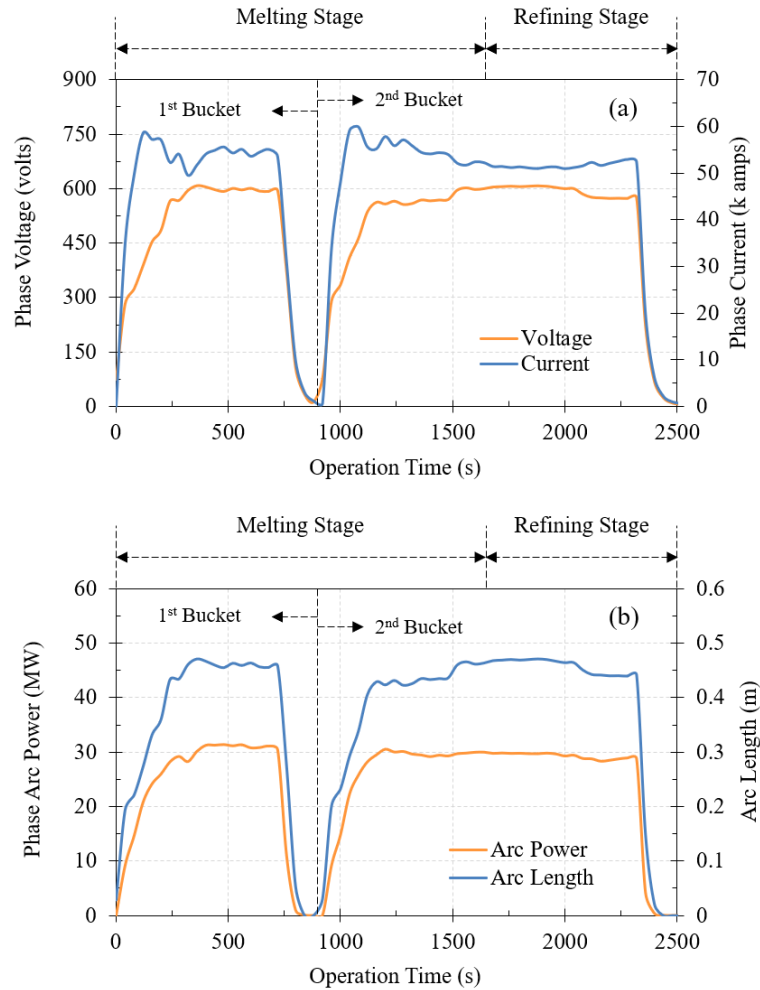


Figure 3.67. Electrical inputs – (a) phase current and phase voltage; (b) arc power and arc length.

**Table 3.16** summarizes the key properties and model parameters involved in the baseline simulation. The present CFD simulations were performed in the commercial software package ANSYS Fluent with intensive model re-developments using user-defined functions (UDFs) to achieve the scrap melting and collapse simulation, the phase interactions, the arc heat dissipation simulation, the electrode regulation, the arc impingement, and the coherent jet simulation.

Table 3.16. Key properties and parameters in the model.

Name of Parameter	Value
<i>Steel density (<math>\rho</math>)</i>	<i>7500 kg/m<sup>3</sup></i>
<i>Average scrap bulk density (<math>\rho_b</math>)</i>	<i>900 kg/m<sup>3</sup></i>
<i>Steel specific heat (<math>C_{p,s}/C_{p,l}</math>)</i>	<i>696.4 j/kg-K</i>
<i>Solidus temperature (<math>T_{solidus}</math>)</i>	<i>1670 K</i>
<i>Liquidus temperature (<math>T_{liquidus}</math>)</i>	<i>1809 K</i>
<i>Latent heat of fusion (<math>h_{fusion}</math>)</i>	<i>275000 j/kg</i>
<i>Steel thermal conductivity (<math>K_l</math>)</i>	<i>35 W/(m-K)</i>
<i>Steel viscosity (<math>\mu_l</math>)</i>	<i>0.007 kg/m-s</i>
<i>Solid phase characteristic diameter (<math>d_s</math>)</i>	<i>0.027 m</i>
<i>Liquid phase characteristic diameter (<math>d_l</math>)</i>	<i>0.001 m</i>

### 3.3.4.2 Validations

This section presents experiments designed and implemented in the NLMK 150-ton EAF to validate the scrap melting simulator. It should be emphasized that the furnace operation in the experiments was altered with the specific intention of achieving parameter controls and data measurements, which is different from the normal furnace setup in NLMK.

The process of scrap melting by the coherent jet burner in the scrap melting simulator is the same as that in the scrap preheating simulator, which has been validated in **Section 3.3.3**. The experimental validation in the present section is to validate the process of scrap melting by the electric arc.

The experimental validation for scrap melting by the electric arc considers the melting in the electrode bore-down phase since this process is relatively controllable, and the visualization and data achievement of the melting process is relatively simple. Validations include the comparisons

of both the electrode descending speed and the final electrode pit size. The electrode descending speed can indirectly indicate the scrap melting rate near the electrode region, while the final electrode pit size can reflect the arc radiative heat transfer to the scrap surfaces which is parallel to the electrode during the bore-in. The stronger the arc radiation, the larger the size of the electrode pit.

To limit the variables and reduce the unnecessary factors in the experiments, all burners were off to ensure that the arc is the only source of energy input for melting. About 70 tons of the shredded scrap or 50 tons of the busheling scrap were charged for melting separately. A total of five trials with different amperage set points and nominal voltages were performed to record the scrap melting rate under different electric inputs. The corresponding trial information is provided in **Table 3.17**.

Table 3.17. Summary of trial information for scrap melting by the electric arc.

Trial #	Scrap Type	Porosity	Amperage Set Point	Tap & Nominal Voltage
1	<i>Shredded (70 tons)</i>	0.86	53 kA	<i>Tap 18 with 856 V</i>
2	<i>Shredded (70 tons)</i>	0.86	55 kA	<i>Tap 22 with 1019 V</i>
3	<i>Shredded (70 tons)</i>	0.86	52 kA	<i>Tap 16 with 759 V</i>
4	<i>Busheling (50 tons)</i>	0.91	53 kA	<i>Tap 18 with 856 V</i>
5	<i>Busheling (50 tons)</i>	0.91	55 kA	<i>Tap 22 with 1019 V</i>

**Figure 3.68** shows the real-time data recorded in trial #1 and trial #4 as examples, including the electrode position and the mean current and voltage variation over time. For trial #1, the experimental data are analyzed as follows:

- 1) The electrode was firstly lowered by the operator to the position close to the scrap surface at a uniform speed. When the distance of the gap was less than a certain threshold, the arc was ignited, connecting the electrode and the scrap surface together, making the electric circuit detect the current. This moment was designated as the starting point (the 58th s).

- 2) After crossing the starting point, the electrode regulator took over the control of the electrode movement. The electrode gradually descended dependent on the scrap melting rate until the end of the electrode bore-down phase. During this period, the current gradually climbed to the amperage set point and remained steady. The voltage variation followed a similar pattern.
- 3) When the trial was near the end of the electrode bore-down phase (the 650th s), the operator manually lifted the electrode and extinguished the arc to end the melting process, which was shown as the liner rising of electrode position to the starting position and the sharp drop of current and voltage values to zero.
- 4) In the late of the electrode bore-down phase, the scrap pile may collapse due to the unstable bottom structure, which was reflected as the large fluctuations in the recorded data at the 498th second. To reduce the unnecessary factors in the validation, the data after the scrap collapse was not considered as the valid data for the validation, thus the valid data was taken from the 58th s to the 498th s for trial #1. For the trials without the scrap collapse, the valid data ended after the electrode lift-up.

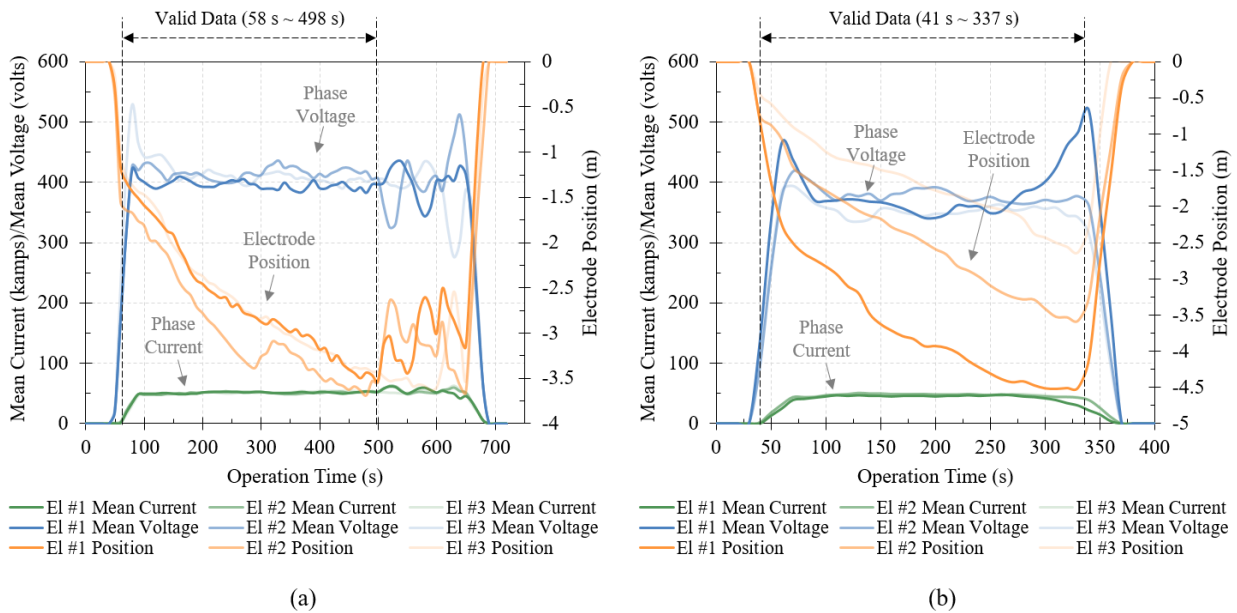


Figure 3.68. Experimental data – (a) trial #1 using shredded scrap;  
 (b) trial #4 using busheling scrap.

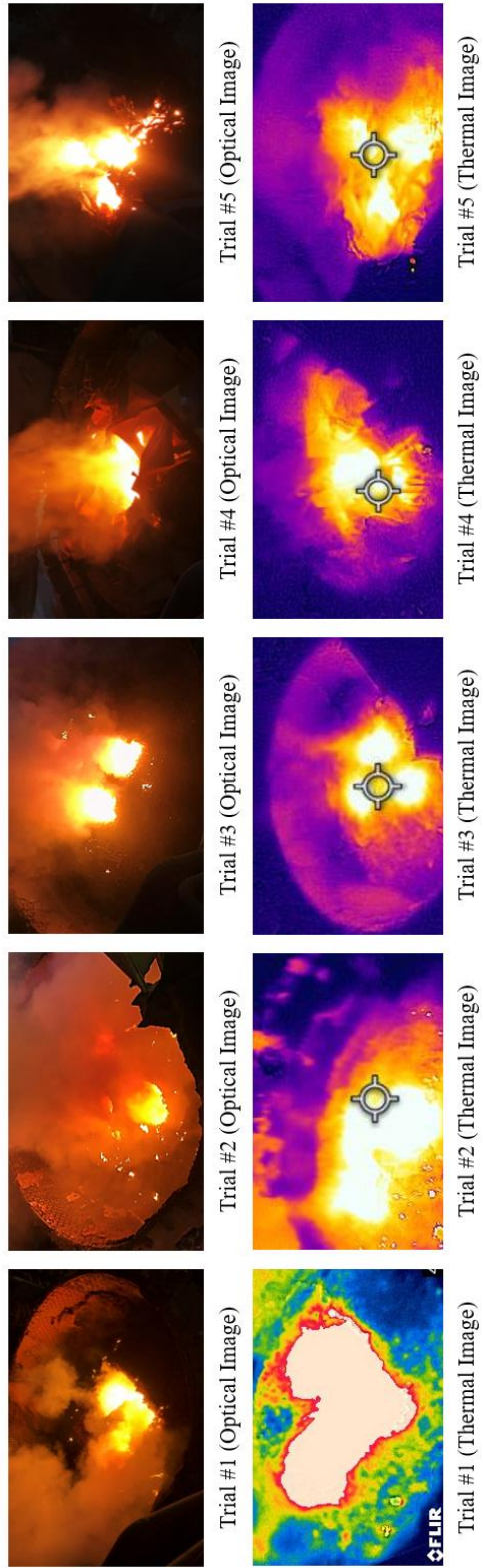


Figure 3.69. Observations of the final electrode pit size.

**Figure 3.69** presents the observation of the final electrode pit size by the optical images and the thermal images, among which the thermal images were captured with the FLIR TG297 portable industrial high-temperature thermal camera with an accuracy range of 100 to 1030 degrees Celsius. Since the gas inside the electrode pits is significantly heated during the bore-in, the pit region appears bright white in the thermal images. Aligning the measurement center of the thermal camera with the furnace center, the average temperature around the pit region is about 939 K (1230 F). It is noted that the position offset of the measurement center may cause a certain deviation in the measured value due to the long distance from the measured object. Outside the electrode pit region, the measured temperature is significantly reduced to the ambient temperature around the furnace wall. The comparison of CFD results and observations for the final electrode pit size is given in **Figure 3.70** with an average difference of about 9.18%.

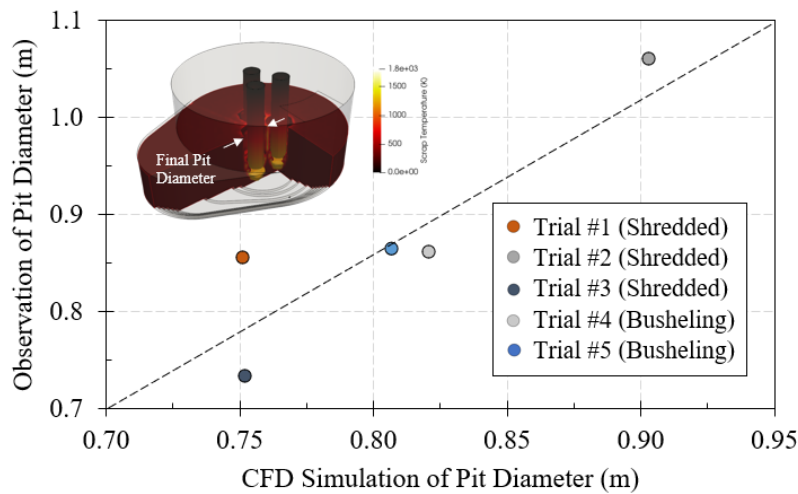


Figure 3.70. Comparison of CFD results and observations for final electrode pit size.

**Figure 3.71** shows the comparison of CFD results and experimental data for the real-time electrode position. The comparisons define the electrode position at the starting point of the valid data as 0. It can be seen that the electrode descending speed slowed down as the electrodes gradually bored into the scrap pile, which was caused by the repeated melting and solidification of liquid steel underneath the electrode tip. The re-solidified liquid steel fulfilled the pores in between scrap pieces leading to the reduction of the permeability and the increase of the scrap bulk density. In the comparison, the average difference is about 15.39%. The error is caused by a relatively large difference in the electrode position within the first 100 s. Considering that the newly-ignited arc is

unstable during this period, **Equation (3-57)** may need to be adjusted accordingly to take the arc instability into consideration, so that the relationship between the arc voltage and the arc length can be correctly estimated to improve the electrode position prediction at the beginning of the simulation.

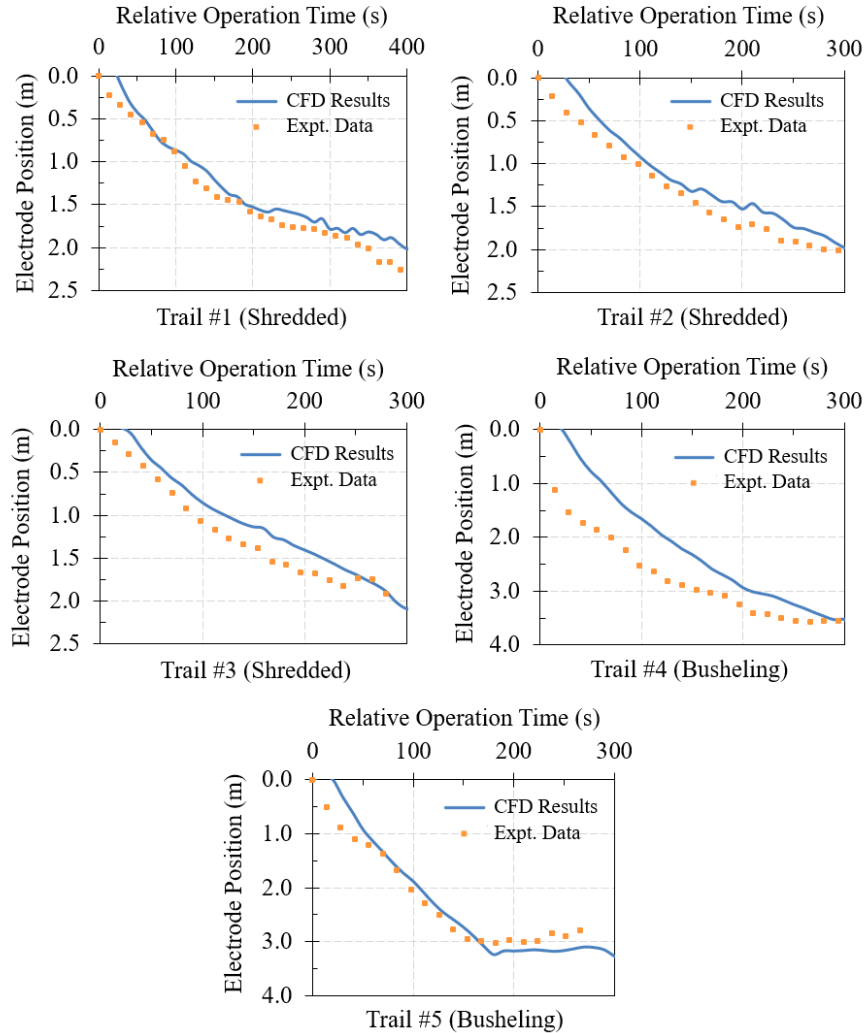


Figure 3.71. Comparison of CFD results and experimental data for real-time electrode position.

### 3.3.4.3 Scrap Melting Behavior

The results of a case study for the NLMK EAF scrap melting process under the typical run is illustrated in this section. The evaluations and discussions of the scrap melting behavior, the electric arc performance, and the burner performance are included.

**Figure 3.72** plots a series of results to show the overall scrap melting process. For the first bucket charge, the electrode bore-down phase takes about 300 s, which is in line with the observations in the plant. Under the effect of arc convection and radiation, only a small amount of scrap under or around the electrode melted in the first 300 s. The four burners heat and melt the scrap simultaneously from the surrounding cold spots by the combustion flame. The melted amount during this period only accounts for 7.7% of the total scrap charge. The electrode bore-down phase follows the main melting phase, which lasts 600 s (300 s to 900 s). During this phase, the central electrode pit and the surrounding burner melting cavities are further enlarged by arc radiation and flame convection. In the meantime, the arc continues to heat the bottom liquid bath so that the scrap pile is also melted by the hot liquid bath from the bottom, which results in insufficient support to the upper scrap, further causing the scrap to collapse. After 900 s, the second bucket of scrap is charged. Newly-charged scrap fills the central electrode pit and the melting process restarts from the electrode bore-down phase and follows the same inside-out, bottom-up melting pattern until the end (900 s to 2500 s).

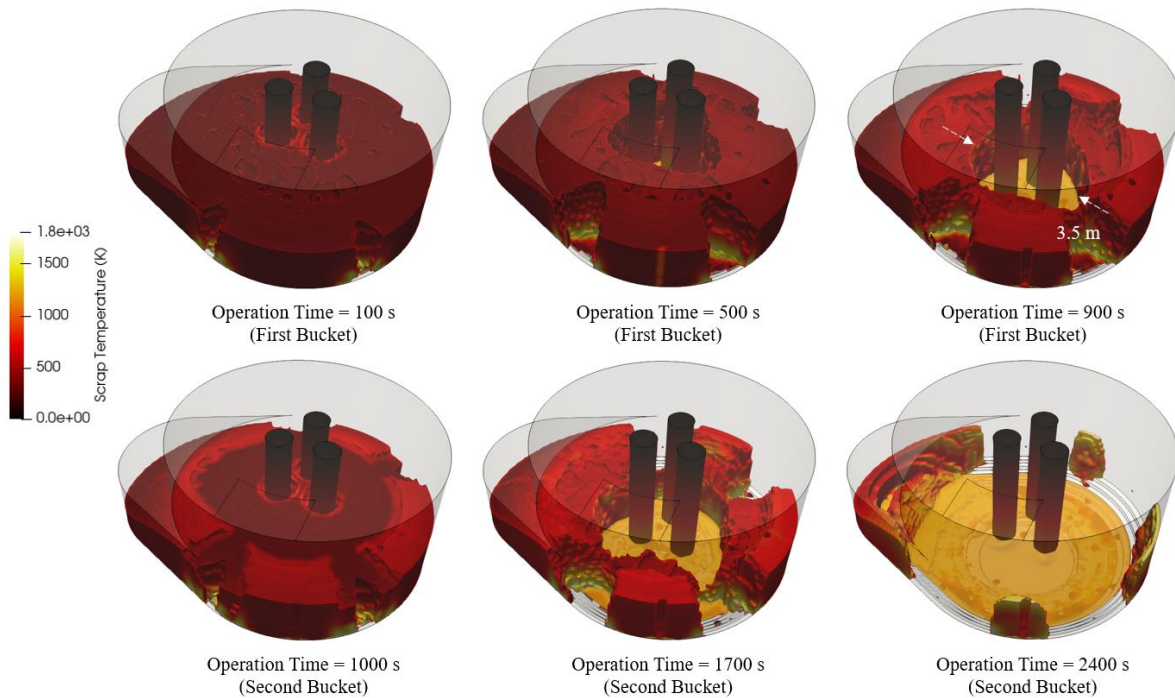


Figure 3.72. Simulated scrap melting process.

The above-described scrap melting process is quantitatively reflected in **Figure 3.73**, including the remaining scrap mass and the real-time electrode position. It can be seen that the melting rate of the main melting phase is much greater than that of the electrode bore-down phase. This is because most of the liquid steel formed beneath the electrode is in direct contact with the cold scrap and gas when dripping downwards, thereby causing its gradual re-solidification along the traveling path. Therefore, during the electrode bore-down phase, the liquid steel does not drop directly to the furnace bottom and merges with the liquid bath. After the electrode bore-down phase, a large amount of melted scrap starts to raise the bottom bath level, which is indicated by the corresponding electrode rising.

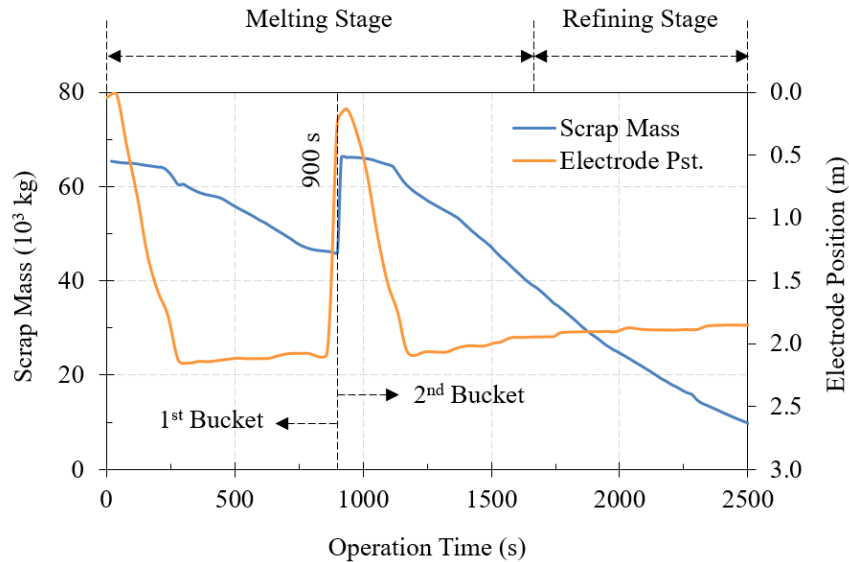


Figure 3.73. Variation of scrap mass and electrode position.

**Figure 3.74** shows the scrap melting profile (900 s) observation at the end of the first bucket melting but before the second bucket charge. There is still a large amount of un-melted scrap attached to the furnace wall and the melting profile is very irregular since the process is too dynamic. The diameter of the central electrode pit is estimated to be about 3.3 meters to 4.3 meters. Compared with the results at 900 s in **Figure 3.72**, the simulated scrap melting profile is relatively regular, with an average diameter of 3.5 m, and the difference is ranging from 6.1% to 18.6%.

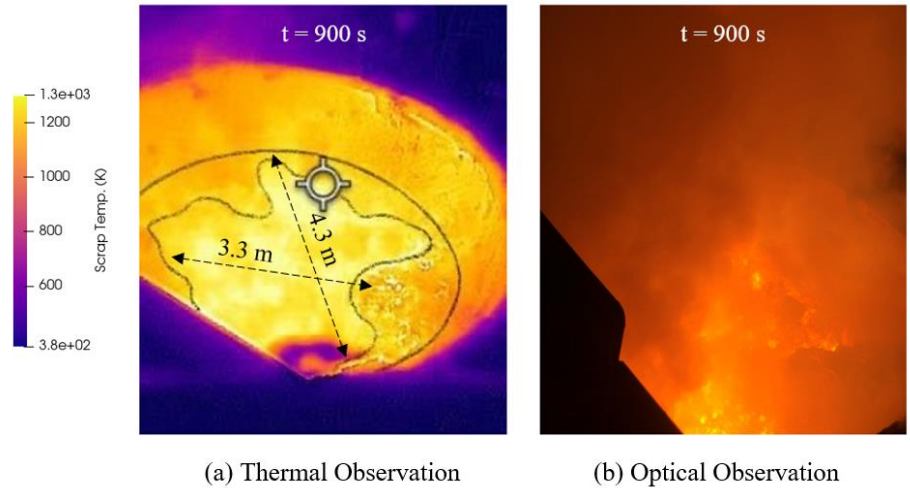


Figure 3.74. Observation of scrap melting profile at 900 s.

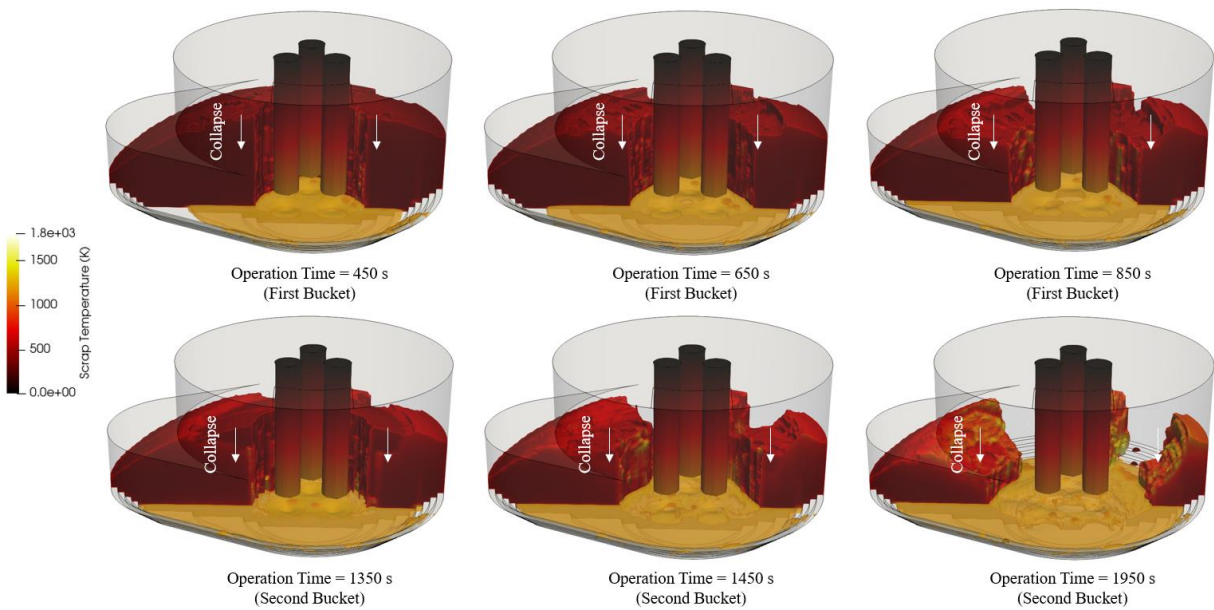


Figure 3.75. Simulated scrap collapse during melting.

**Figure 3.75** shows the simulated scrap collapse process. The scrap collapse is first detected at 450 s after charging, i.e., the 450th s for the first scrap bucket charge and the 1350th s for the second scrap bucket charge. In the initial stage of the collapse, it mainly occurs within a radius of about 1.7 meters from the center of the electrodes, after which it gradually extends to the entire scrap pile. The collapse around the three electrodes is mainly caused by the bottom diameter of the central electrode pit being larger than the upper diameter, while the overall vertical scrap collapse

is mainly caused by the in-bath melting of the scrap pile. As melting and collapse progress, the scrap melting profile at the vertical cross-section takes on a U-shape. It can also be seen from the results that the in-bath scrap melting in the refining stage is slower than expected. This is the main reason for 10 tons of un-melted scrap still remaining in the liquid bath at 2500 s.

Therefore, the stage-by-stage simulation methodology is recommended to capture the entire EAF steelmaking process, i.e., extracting the last-moment result of the melting stage as the initial conditions for the refining stage simulation. More details of the liquid steel refining simulation will be illustrated later.

### 3.3.4.4 Electric Arc Performance

**Figure 3.76** shows the variation of the arc radiation distribution overtime on the furnace roof and wall estimated by the Monte Carlo method described above, the quantitative representations of which are given in **Figure 3.77**.

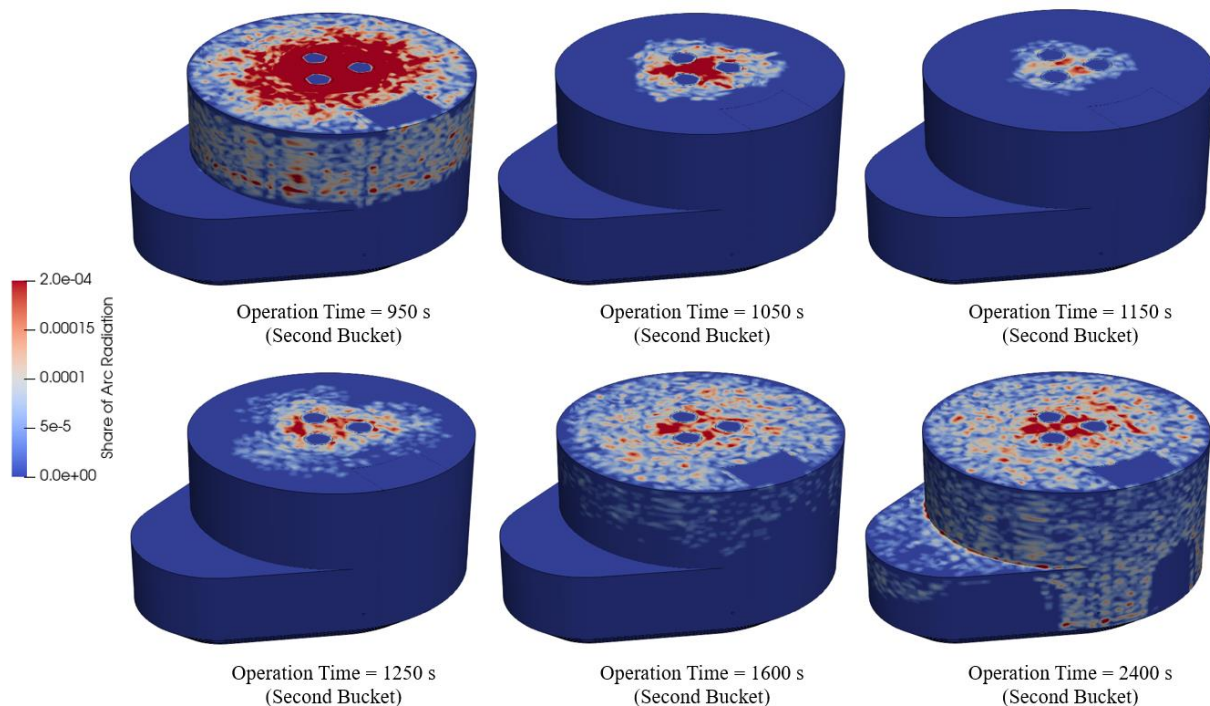


Figure 3.76. Simulated arc radiation distribution on furnace roof and wall.

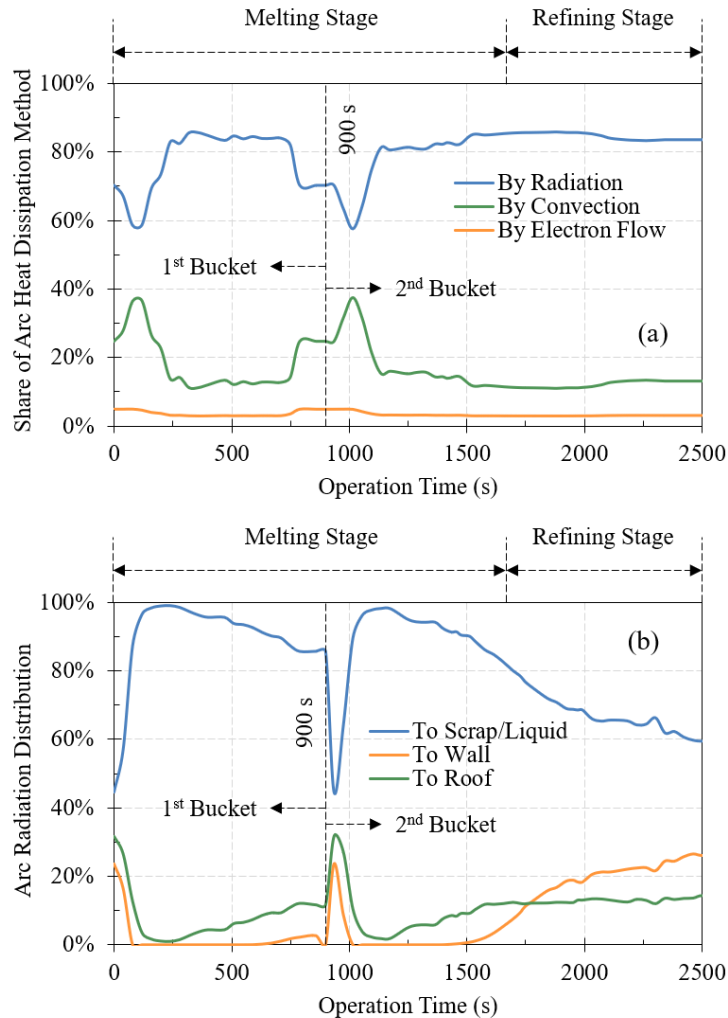


Figure 3.77. (a) variation of share of arc heat dissipation; (b) variation of arc radiation distribution.

Taking the second bucket charge as an example, in about 50 s (900 s to 950 s) after arc ignition, 30% to 40% of the arc heat can be dissipated through convection (25% to 35%) and electron flow (5%) to directly melt the scrap under the electrode tip, while 60% to 70% of the arc heat is radiated to the surroundings. During this period, the arc is completely exposed on the freeboard above the scrap pile leading to only 45% of the arc radiation being effectively absorbed by the scrap surface and the rest being lost to the furnace roof and wall. As the electrodes bore down into the scrap pile (950 s to 1150 s), the visibility of the arc to the furnace wall and roof gradually decreases, and most of the arc radiation is blocked by the scrap pile, causing its arc radiation absorption to increase significantly (45% to 98%). When there is no visibility between the arc and the furnace wall (1000

s), the share of arc radiation to the furnace wall is reduced to 0. At this time, only part of the furnace roof above the central electrode pit can receive arc radiation through the pit opening. When the electrode descends to the lowest position, the arc length and current reach the maximum values and remain relatively stable. Since then, about 80% to 85% of the arc heat can be transferred to the surrounding by radiation, and the rest of the arc heat directly heats the bath below the electrode tip. As the scrap collapses and the central electrode pit gradually expands, the share of arc radiation received by the furnace roof increases again (1150 s to 1500 s) and then remains stable at around 13%. From 1500 s onwards, the furnace wall becomes visible to the arc again, and the share of arc radiation it receives also begins to climb. The arc radiation received by the scrap surface gradually decreases in stead during this process.

Subsequent optimization of electrical energy utilization efficiency should focus on increasing the arc radiation to scrap surfaces while reducing arc radiation lost to the furnace roof and wall during melting. A feasible approach is to increase the electrode bore-down speed to reduce the arc heat loss in the initial stage of melting. In addition, the simulation results also show that the highest proportion of radiation to the furnace roof is at the beginning of the electrode bore-down phase, which can reach up to 30%, thus the arc reflection occurs frequently at this moment.

#### ***3.3.4.5 Burner Performance***

**Figure 3.78** shows the streamlines of the combustion gas produced by four coherent jet burners, colored by the gas temperature. The scrap pile in the furnace is adjusted to be grey-white for better readability. It can be seen that the combustion gas has the characteristics of high temperature and speed inside the burner melting cavities. Intense heat and momentum exchanges with the porous scrap pile occur when the combustion gas is pushed into it, causing the scrap temperature to increase fast while the gas temperature and velocity are significantly reduced. Due to its lower density, the combustion gas eventually meets in the freeboard region with the effect of buoyancy, and its remaining temperature further heats the freeboard region. As the melting progresses, the volume of the burner melting cavities is growing, and more high-temperature combustion gas directly enters the freeboard region through those big cavity openings without good heat exchange with the scrap pile. This results in a progressive drop in the burner efficiency, while the freeboard temperature rises instead.

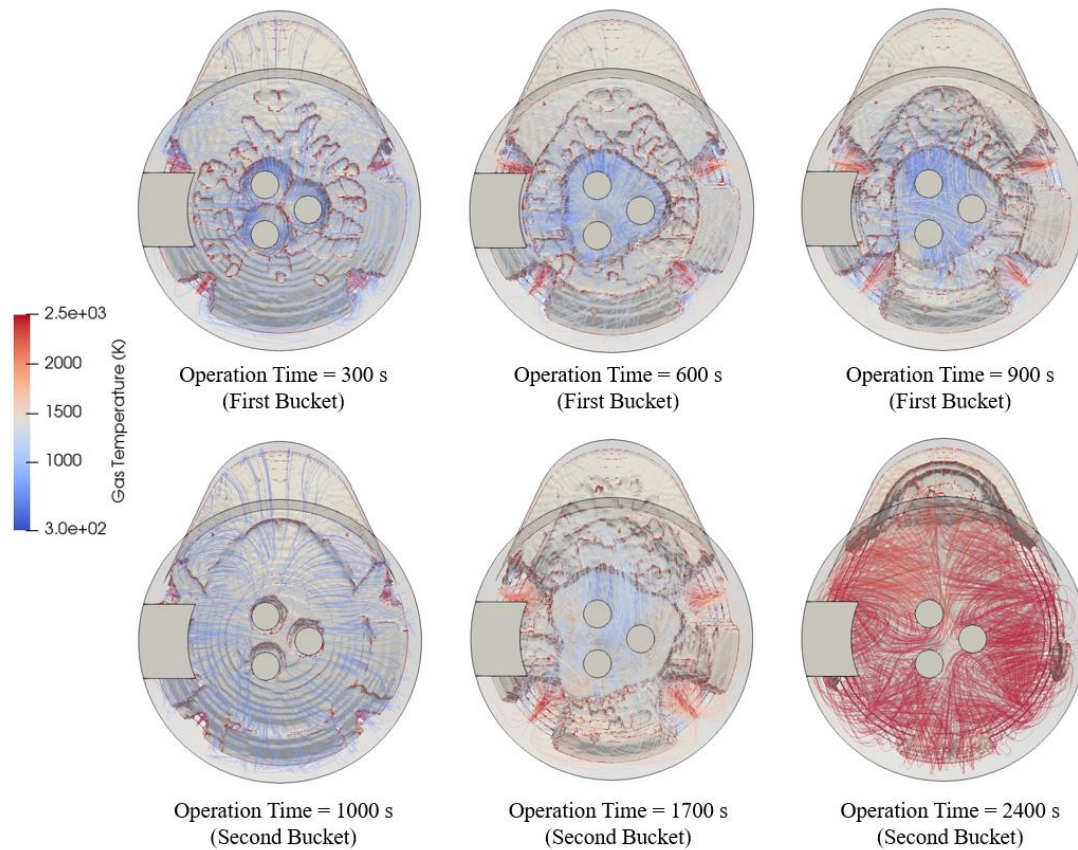


Figure 3.78. Streamlines from burners (colored by gas temperature).

The above process is quantitatively shown in **Figure 3.79**, including the variations of burner efficiency, gas temperature, and liquid temperature. For the first bucket charge, the burner efficiency decays from an initial 90% to 75% within 900 s. A second bucket charge then refills the melting cavities in front of the burners, enhancing the heat exchange between the combustion gas and the scrap pile, resulting in a short increase in burner efficiency. As melting progresses, the burner melting cavities gradually expand again, whereupon the burner efficiency also begins to decline. It is noted that the burner melting cavities merge with the central electrode pit at about 1700 s, from when the burner efficiency drops dramatically. This is because there is no more scrap in front of the burners to absorb the heat released by the combustion flame. Accordingly, a large amount of high-temperature combustion gas directly enters the freeboard region, causing the freeboard temperature to rise sharply, which can be seen in **Figure 3.79 (b)**.

Therefore, for the actual EAF operation, it is recommended to adjust the burner operation from the burner mode to the lance mode after 1700 s, because the lance mode only uses a small fuel flow rate (about 100 SCFM) to generate a flame envelope to protect the central supersonic oxygen jet, and the main function of the burner at this time is to deliver the oxygen to the bath instead of melting the scrap, which can improve the chemical energy utilization and also improve the in-bath scrap melting rate.

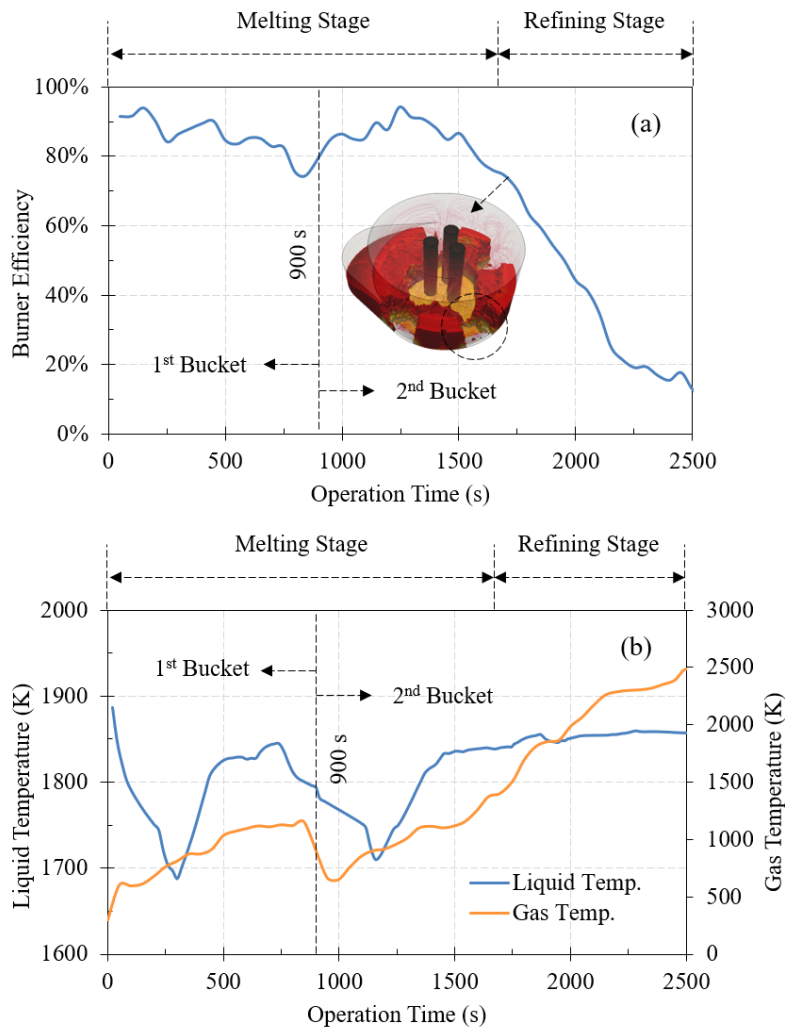


Figure 3.79. (a) variation of burner efficiency; (b) variation of gas/liquid temperature.

### 3.3.4.5 Summary

This section presents the results from the scrap melting simulator, which simulates the scrap melting stage, that is, the scrap melting by both AC electric arc and coherent jet burner in an

industry-scale EAF. The experimental validations of the scrap melting by arc were first time designed and implemented for the industry-scale NLMK 150-ton EAF, and a relatively good agreement was found by comparing the results with the experimental observations. The simulator was applied to investigate and reveal the physical principles in the scrap melting stage, and the major conclusions were made as follows:

- 1) The electrode bore-down phase takes about 300 s and only 7.7% of the total scrap charge is melted in this phase due to the re-solidification of the liquid steel during dripping.
- 2) The scrap melting in the main melting phase follows the inside-out, bottom-up melting pattern until the end. During this phase, the first scrap collapse normally happens at 450 s after charging. The collapse around the three electrodes is mainly caused by the bottom diameter of the central electrode pit being larger than the upper diameter, while the overall vertical scrap collapse is mainly caused by the in-bath melting of the scrap pile. The scrap melting profile normally takes on a U-shape at the vertical cross-section.
- 3) After arc ignition, 60% to 70% of the arc heat is radiated to the surrounding environment, of which only 45% of the arc radiation is effectively absorbed by the surface of the scrap steel, and the rest is lost to the furnace roof and furnace wall. The arc radiation absorbed by the scrap surface gradually climbs to 98% as the electrodes bore down into the scrap pile, then decrease and is stable at 80% to 85% as the scrap collapses and the central electrode pit gradually expands.
- 4) The burner efficiency decays from an initial 90% to 75% for the first bucket charge. A second bucket charge can make a short increase in burner efficiency, but as the burner melting cavities gradually expand again, the burner efficiency begins to decline again. At about 1700 s, the burner efficiency drops dramatically since there is no more scrap in front of the burners to absorb the heat released by the combustion flame. Therefore, a large amount of high-temperature combustion gas directly enters the freeboard region, resulting in a fast rising of the freeboard temperature.

### 3.3.5 In-bath Decarburization Simulator

This section presents the results from the in-bath decarburization simulator, which couples/integrates the scrap melting model, the coherent jet model, and the oxidation model to simulate the in-bath decarburization process in the liquid steel refining stage.

#### 3.3.5.1 Simulation Conditions

The baseline case of the in-bath decarburization simulator is performed in the liquid bath region of an industry-scale SDI AC EAF with four coherent jet burners and a door lance aiming to stir the bath and deliver the oxygen for refining. Four coherent jet burners are distributed 90 degrees apart on the four corners of the furnace and the door lance is inserted into the bath through the slag door located at the rear of the furnace to auxiliary the refining, thus five jet penetration cavities in total are generated on the bath surface as shown in **Figure 3.80**. The procedure of jet penetration cavity estimation has been detailly illustrated in the earlier sections. The slag layer is not included in the computational domain, that is, the top surface of the domain is the bottom surface of the slag layer. For a better mesh quality, complicated structures are simplified, and the total element number is 0.3 million after the mesh sensitivity study.

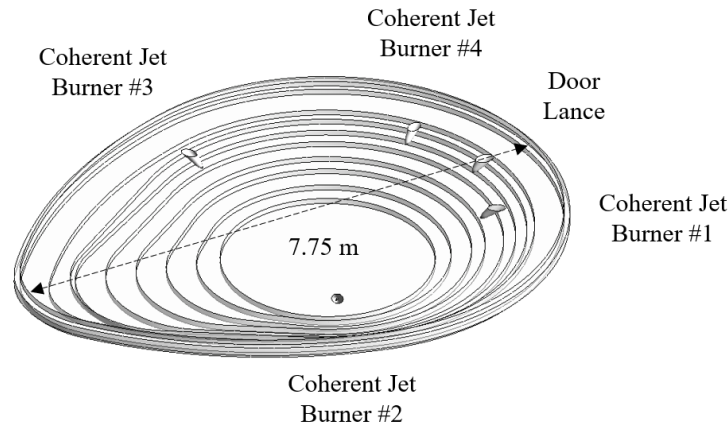


Figure 3.80. Computational domain for in-bath decarburization simulation.

All four coherent jet burners used in the refining stage are under the lance mode, whose the primary oxygen nozzle with a high flow rate (around 1200 SCFM) produces the supersonic oxygen jet, while the corresponding flow rates of the fuel nozzle and the secondary oxygen nozzle are

relatively low (around 80 SCFM), only to generate the shrouding combustion flame envelop to protect the central supersonic oxygen jet and slow the momentum decay in its traveling path. The initial liquid bath temperature is obtained from the previous scrap melting simulation, which is 1850 K in the present study. Other key parameters used in the simulation are given in **Table 3.18**.

Table 3.18. Key parameters in the model.

Name of Parameter	Value
<i>Slag layer density</i>	<i>4350 kg/m<sup>3</sup></i>
<i>Slag layer height</i>	<i>0.381 m</i>
<i>Angle of jet inclination</i>	<i>40° from horizontal</i>

### 3.3.5.1 Validations

#### 3.3.5.1.1 Jet Penetration Depth

The validation of the jet penetration cavity estimation was done by comparing the predicted jet penetration depth with the measurement data provided by the industry collaborator Linde.

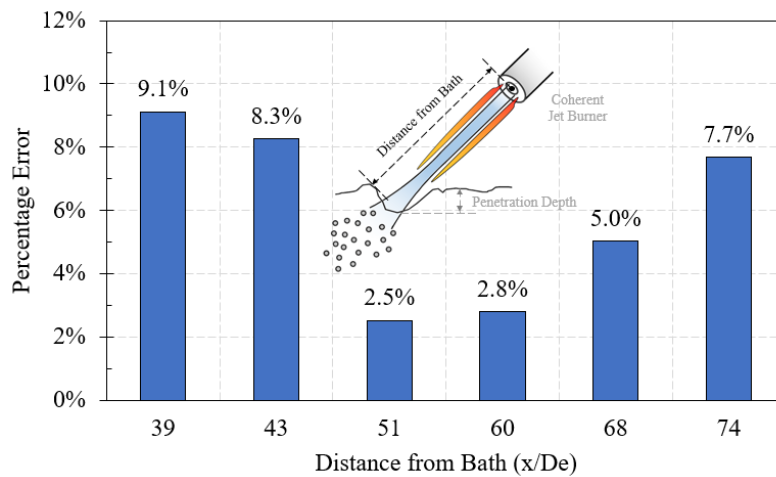


Figure 3.81. Validation for the estimated jet penetration depth.

With the fixed burner operating conditions, different jet penetration depths were first measured in the water model under the successive increasing distance between the jet nozzle exit and the liquid

steel bath surface, and then converted into the data for the real EAF operations. Six sets of available data were obtained for the present validation. It can be observed that when the nozzle-liquid surface distance is greater than the jet potential core length, the jet penetration depth can be significantly decreased due to the sharp-reduced jet momentum when reaching the liquid bath surface. Instead, if the nozzle-bath distance is less than the jet potential core length, the jet maintains the same axial velocity but the area of the jet mixing zone in the radial direction increases with the increase of the nozzle-bath distance. This results in a reduction of the jet maximum pressure gradient in the mixing zone, thereby reducing the jet penetration ability inside the liquid steel bath. The comparisons between the model predictions and the measured data for six sets are given in **Figure 3.81** with a percentage error of less than 10%.

### 3.3.5.1.2 Results at Tapping

The validation of the in-bath decarburization simulator was conducted by comparing the industrial data and the simulation results at tapping in an SDI typical run. The instant oxygen concentration and bath temperature were measured by the test rod inserted through the slag door once a time before and after the refining, in which the measured oxygen concentration was converted to the corresponding carbon content by the system automatically.

Table 3.19. Comparison of results at tapping (800 seconds).

	Total [%C] Reduction	Tapping Temperature
<i>Measurements (SDI)</i>	92.7% (0.41% → 0.03%)	1922 K
<i>Simulations (This Study)</i>	77.6% (0.41% → 0.092%)	1914 K
<i>% Difference</i>	16.3%	0.42%

The present study adopted the measured carbon content before the refining stage as the initial carbon content for the in-bath decarburization simulation and compared both the simulated final carbon content and the final tapping temperature at the end of the refining stage with measurement data to evaluate the model accuracy. The comparison results are given in **Table 3.19** with percentage differences of 16.3% and 0.42%, respectively. The error in the total carbon reduction prediction is mainly caused by different measurement locations. For the industrial data, the

measurement of carbon content is always taken from the region near the slag door, while the simulation data is based on volume-averaged. If taking the simulation data of carbon content near the slag door, the error can be reduced to 10.3%.

### ***3.3.5.2 Stirring Mechanism***

This section firstly performed the simulations without considering the in-bath chemical reactions (i.e. without oxidation model) to investigate the in-bath stirring mechanism under a cold flow field scenario. Generally, there are different stirring mechanisms that affect the flow characteristics of the molten bath, including the momentum stirring, the bubble stirring, and the electromagnetic stirring. Moreover, the buoyancy force arising from the bath temperature gradient and the bath concentration gradient also make contributions to stirring the bath. In the present study, the electromagnetic stirring is assumed to be neglected in this AC EAF due to the fact the induced electromagnetic field is limited to the small region around the arcs and has a minor effect on the molten bath flow [151-153]. The stirring caused by the buoyancy-driven flow was already involved in the model by applying the Boussinesq hypothesis for the liquid steel phase. The rest two stirring mechanisms, that is, the momentum stirring and the bubble stirring, are considered to be the main stirring power in the refining process, which are of great interest to be investigated in the present study.

For the coherent jet burner, the distance between the burner nozzle exit and the liquid steel bath surface is usually controlled to be within the jet potential core length to guarantee the coherent jet can maintain a relatively high kinetic energy when reaching the liquid steel bath. Under this condition, the coherent jet is able to push the liquid steel aside to form a cavity and transfer the momentum to the bath simultaneously. Generally, only a portion of the jet momentum can be transferred to a liquid steel bath for generating effective stirring. Sano et al. [137] reported that only 6% of the total jet momentum is transferable and this value has also been proved to be suitable in the current simulation under the given burner operating conditions. The stirring generated by this direct momentum transfer is called the momentum stirring. Another critical stirring mechanism during the refining process is the bubble stirring. The decarburization reaction will generate the CO bubbles that float upward together with oxygen bubbles quickly, creating a strong

stirring power inside the liquid steel bath due to the bubble-liquid drag force. The CO bubbles are eventually be absorbed by the slag layer to go through the subsequent chemical reactions there. It has been reported that the bubble stirring plays a key role in the homogenization of the flow field, therefore the following investigation is aimed to reveal the impact of those two stirring mechanisms on the flow development.

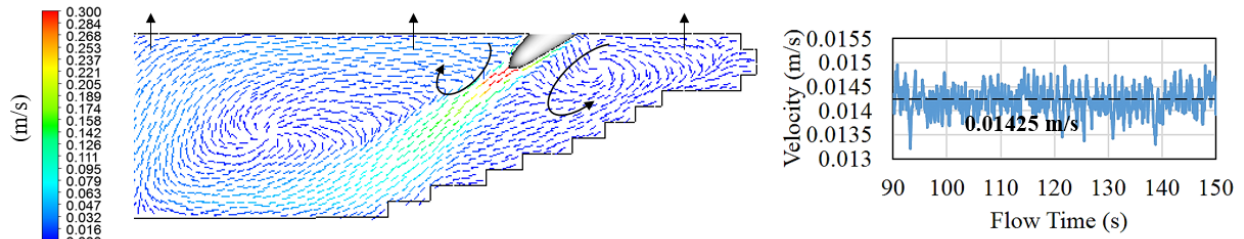


Figure 3.82. Momentum stirring without bubble stirring.

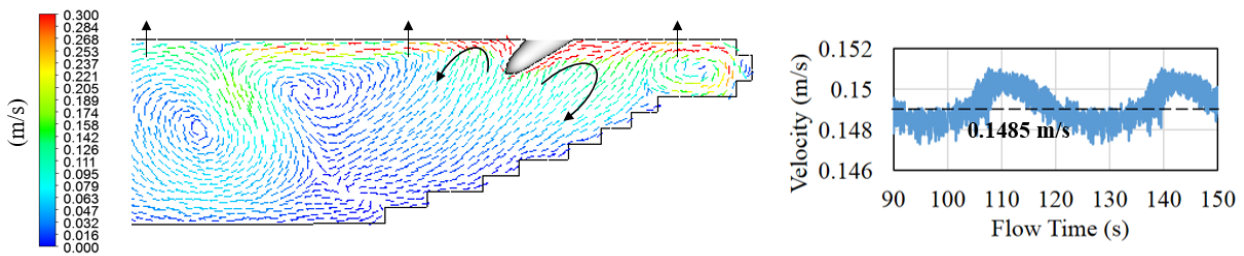


Figure 3.83. Momentum stirring with bubble stirring.

The comparison of the flow field with and without the bubble stirring is given in **Figure 3.82** and **Figure 3.83**. The high momentum transferred from the jet penetration cavity surface pushes the liquid steel flowing in the cavity axial direction, meanwhile generating vortices on both sides of the cavity. The volume-averaged liquid bath velocity fluctuates around a value of 0.01425 m/s. **Figure 3.83** shows the case considering both the momentum stirring and the bubble stirring. Compared with the case without the bubble stirring, the flow pattern is totally changed with the opposite vortices occurring near the jet cavity. This is mainly due to the intensive oxidation reactions generating the stronger bubble stirring, which dominates the flow and leads to better mixing. The volume-averaged velocity of the liquid steel bath is approximately 0.1485 m/s, which is about 10 times as much as the case only considering the momentum stirring. From this

comparison, it can be seen that bubble stirring greatly promotes the homogenization of the liquid steel bath and is one of the most important stirring mechanisms in the EAF refining stage.

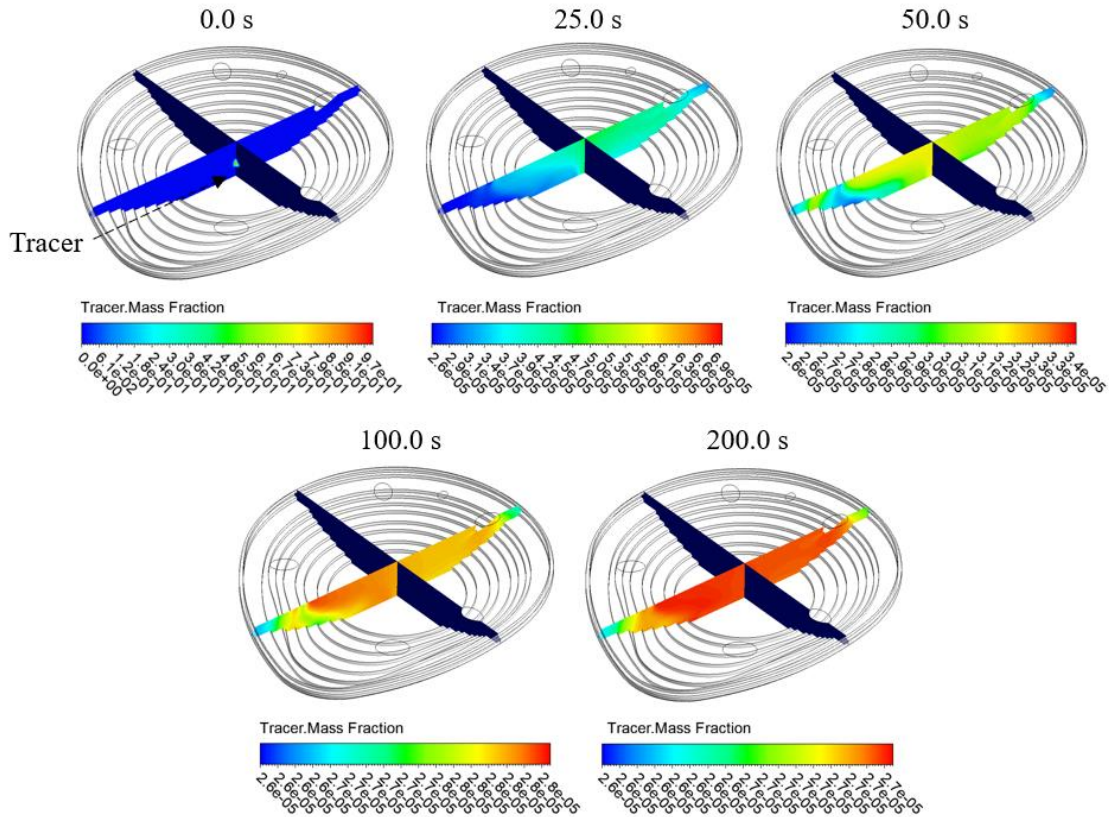


Figure 3.84. In-bath tracer mass fraction variation over time (with momentum transfer and bubble stirring).

The bath mixing efficiency evaluations for both cases were conducted with the results given in **Figure 3.84** and **Figure 3.85**. A tracer is introduced in the center of the liquid steel bath, and the area-averaged tracer concentration is monitored at three different horizontal planes in the bath to evaluate the mixing time. The vertical distance of those three horizontal planes from the furnace bottom is 0.07 m (plane monitor 1), 0.47 m (plane monitor 2), and 0.57 m (plane monitor 3), respectively. Plane monitor 1 is very close to the furnace bottom surface, which is aimed to monitor the dead zone and guarantee the full diffusion of the tracer in the domain. **Figure 3.84** plots the in-bath tracer mass fraction variation over time, and **Figure 3.85** shows the variation of the tracer molar concentration over time. When the fluctuation in the tracer molar concentration is negligible, the liquid steel bath reaches the fully-mixing status whose time is defined as the mixing time.

Without the bubble stirring, the mixing time is estimated to be 1665.3 s and is almost 9.5 times longer than the time needed for the case with the bubble stirring, which further proves the significance of the bubble stirring.

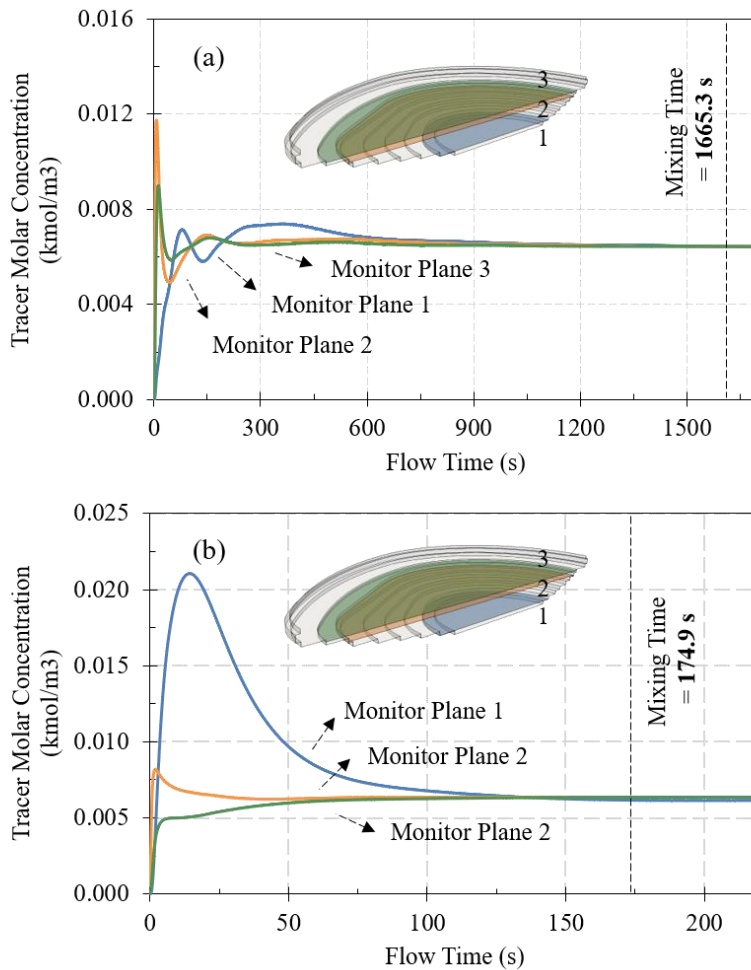


Figure 3.85. Mixing time of flow field – (a) without bubble stirring; (b) with bubble stirring.

### 3.3.5.3 Refining Efficiency

The in-bath decarburization simulator can be used to simulate the thermodynamic and kinetic coupled two-phase reacting flow to reveal the liquid steel refining efficiency. Generally, the carbon content and the bath temperature are two important indicators for the furnace operators to decide the time for tapping the liquid steel, thus the present study also uses them to evaluate the refining efficiency.

The variations of the volume-averaged bath temperature, carbon mass fraction, and manganese mass fraction from the simulations are plotted in **Figure 3.86**. After 800 seconds of refining (around 13 minutes), the simulated tapping temperature 1914 K, while the carbon content is decreased from 0.41% to 0.092% with a 0.318% reduction in total. The differences are respectively 16.3% and 0.42% compared with measurement data in SDI AC EAF. It is noted that the later bath temperature rising rate and decarburization rate become slower than that at the beginning of refining due to the smaller temperature/concentration difference, and the bath temperature is already close to the tapping temperature after 200 seconds. The oxides including CO, FeO, and MnO are generated within the bath and float upwards with the liquid flow until reaching the top surface of the domain, where they are eliminated to represent the absorption by the slag layer. The absorption amounts are used in the slag foaming model to estimate the slag forming height required by the freeboard post-combustion simulation.

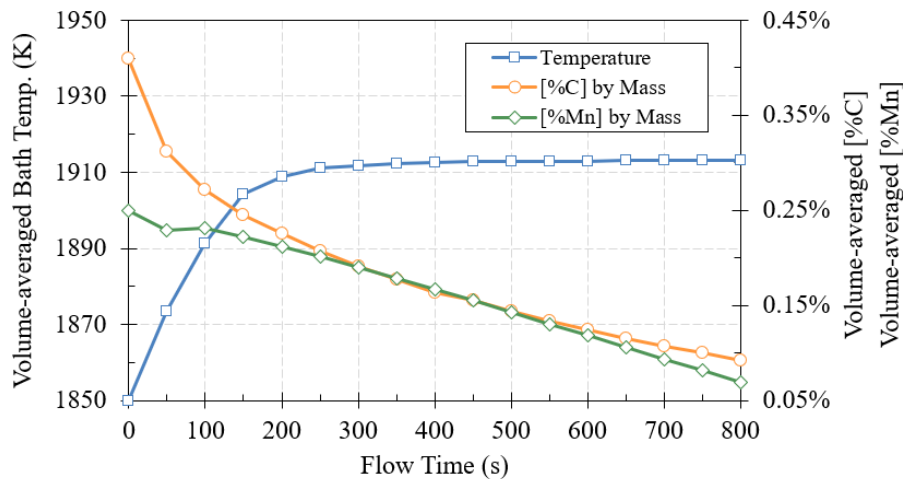


Figure 3.86. Variation of volume-averaged bath temperature, carbon content, and manganese content during refining.

The contours in **Figure 3.87** and **Figure 3.88** visualize the detailed distributions of in-bath carbon content and bath temperature, which are plotted on the cross-section plane through coherent jet burner #1.

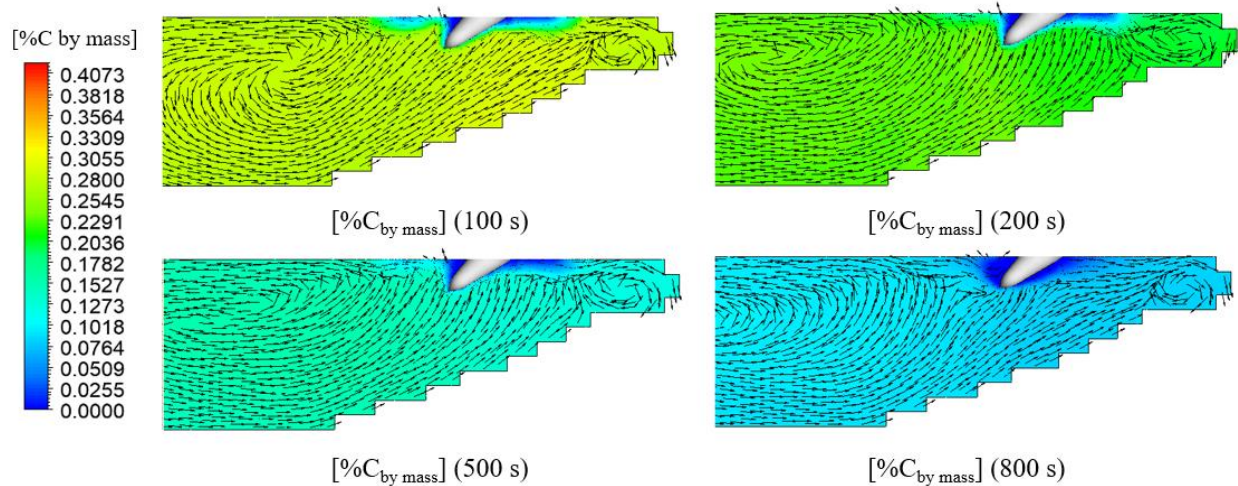


Figure 3.87. Variation of simulated in-bath carbon distribution near burner #1.

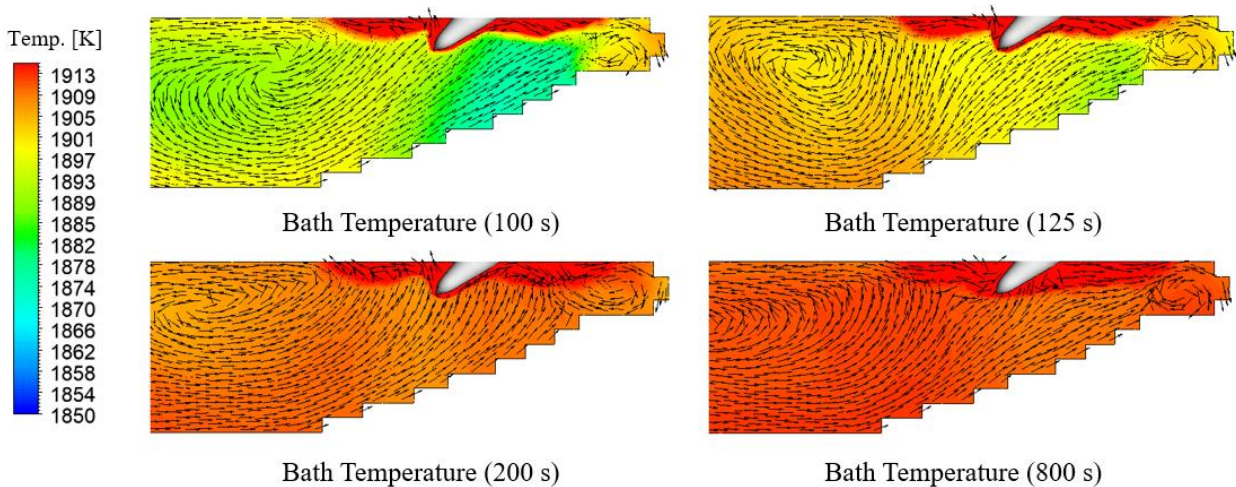


Figure 3.88. Variation of simulated bath temperature near burner #1.

It can be seen that the carbon content maintains relatively low near the jet penetration cavity due to a large amount of the oxygen bubbles injected through the cavity surface. The oxygen first oxidizes the reactive substances there and the excess oxygen either travels with the flow to the farther region or directly floats upward by the buoyancy and is absorbed by the slag layer bottom surface. Generally, due to the concentration difference and stirring effect, the carbon will continue to move to the vicinity of the jet penetration cavity and react with the remaining or newly injected oxygen to generate the CO bubbles. The CO bubbles cause the aforementioned bubble stirring, in turn, impacting the flow field. Moreover, since the oxygen reactions mainly occur around the jet

cavity, a large amount of chemical energy is released there heating up the liquid steel bath. Therefore, a red region representing high temperature can be observed around the jet penetration cavity in the contours. This thermal effect spreads to the entire liquid steel bath over time, resulting in a significant overall bath temperature rise.

### 3.3.5.4 In-bath Carbon Distribution

The current burner arrangement of the furnace is based on the arrangement commonly used in the industry, that is, the four coherent jet burners are pointed 45-degree downward to deliver oxygen to the bath and an immersed door lance through the slag door is also used to inject the oxygen. The variation of the simulated in-bath carbon distribution is plotted in **Figure 3.89**.

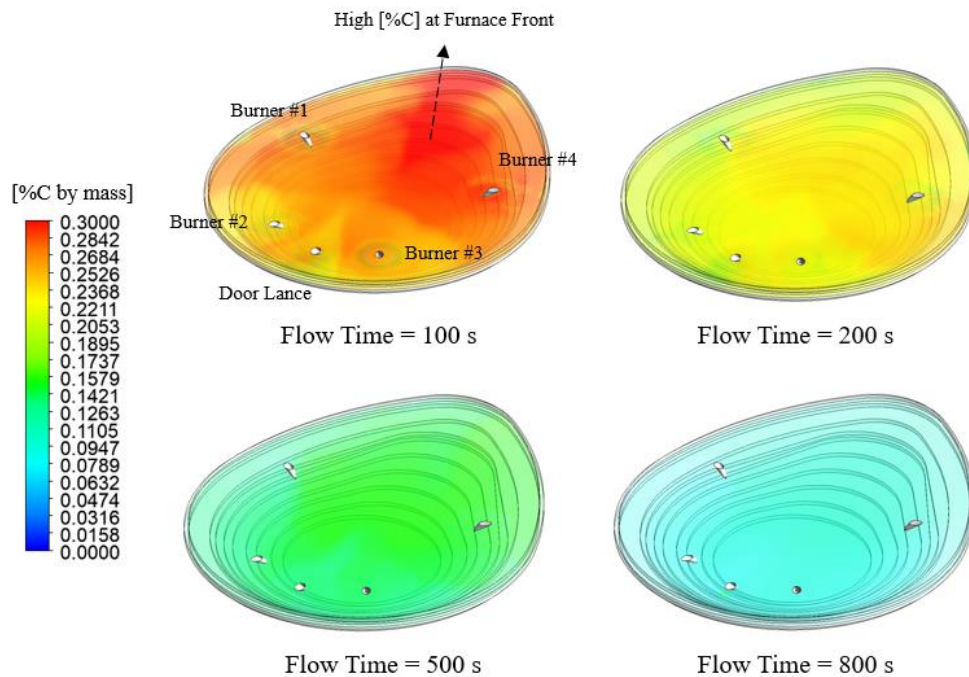


Figure 3.89. Variation of simulated in-bath carbon distribution.

It can be seen that the current burner arrangement results in an uneven carbon distribution in the liquid steel bath and the decarburization rate in the front part of the furnace is much slower than elsewhere. When the refining progresses and reaches around 200 seconds (about 3 minutes), the average carbon content in the front part of the furnace is about twice higher than that of other places. It is not difficult to tell from the burner arrangement that most of the burners are located in

the middle or rear of the furnace, which leads to issues including the weak stirring and less oxygen injection in front of the furnace. The decarburization in this front region mainly depends on the overall flow pattern in the bath, that is, the high carbon liquid steel flow travels from the front of the furnace to the middle or rear of the furnace so that the carbon content can be reacted with rich oxygen there. Obviously, such decarburization is very inefficient. If an inappropriate flow pattern occurs, the decarburization process may cause a serious production delay.

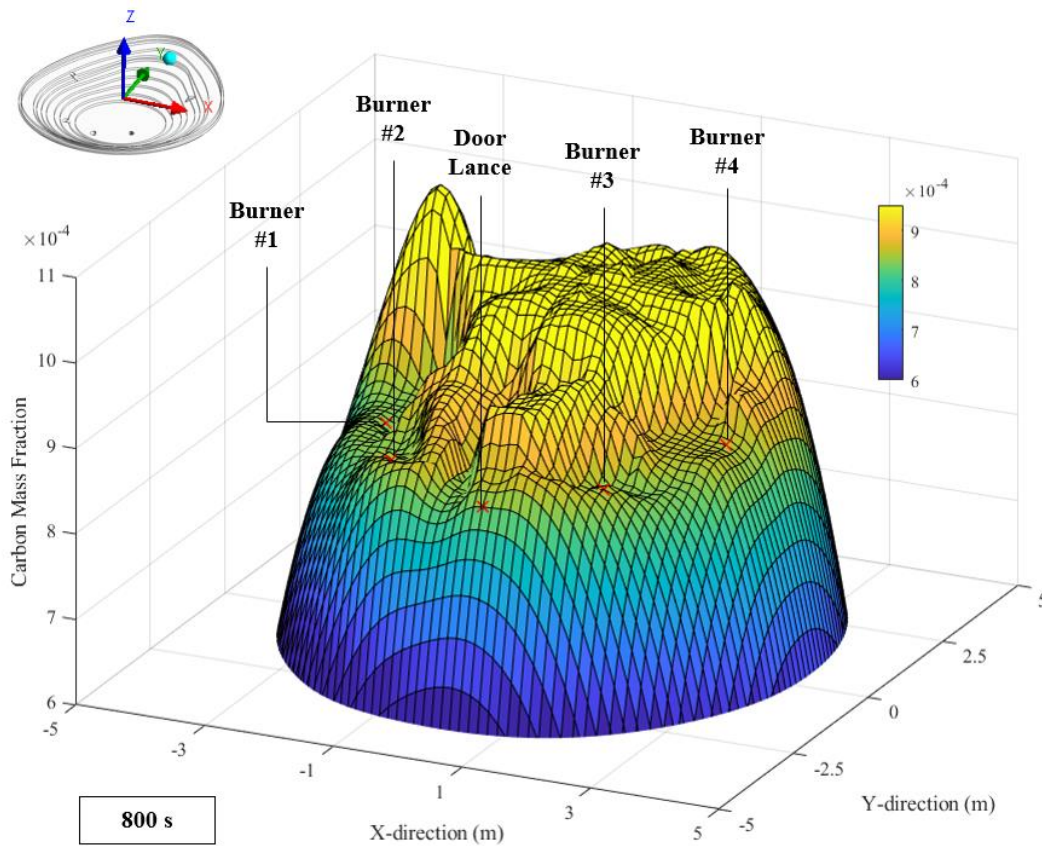


Figure 3.90. In-bath carbon mass fraction (0.5 m from furnace bottom) at tapping.

**Figure 3.90** further plots the detailed carbon mass fraction distribution on a plane (0.5 m from furnace bottom) at tapping. Obviously, the aforementioned uneven carbon distribution exists not only during the decarburization process but also at the end of the refining. Typically, the furnace operator inserts the test rod into the liquid steel bath through the slag door to measure the carbon content, whose value is used to represent the overall in-bath carbon content. Once both bath temperature and carbon content meet the requirement, the liquid steel can be tapped from the EAF.

Based on the simulation results, the carbon content near the slag door only reflects the status at the rear of the furnace since the bath is not well-stirred under the current burner arrangement. The simulated carbon content at the front of the furnace is 1.2 times higher than that at the rear of the furnace. Therefore, the direct tapping may result in the carbon content in the liquid steel exceeding the requirement.

### 3.3.5.4 Effect of Coherent Jet Burner #5 on Refining Efficiency

Based on the previous issue, SDI is interesting in replacing the original burner #5 to be a coherent jet burner for a better stirring and oxygen delivery in the front of the furnace, as shown in **Figure 3.91** and **Figure 3.92**.

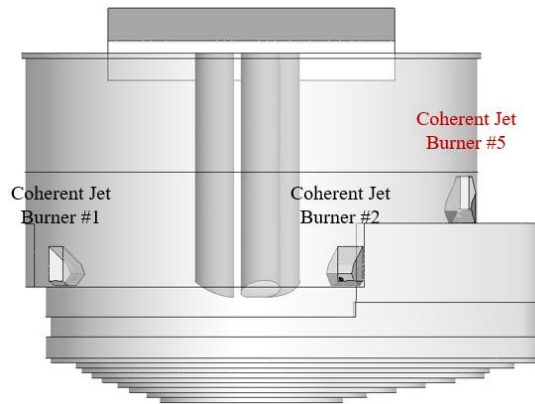


Figure 3.91. Coherent jet burner #5 in SDI EAF.

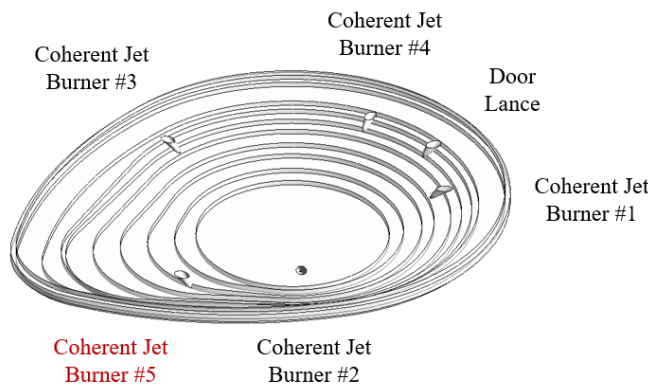


Figure 3.92. Computational domain with coherent jet burner #5.

The original burner #5 is a conventional burner, which normally does not involve in their EAF steelmaking process due to the undesired performance. The present study is aimed to reveal the impact of using coherent jet burner #5 on the refining efficiency and provide the guidance for potential furnace upgrade.

**Figure 3.93** shows the simulation results of the refining efficiency comparison with and without coherent jet burner #5. It can be seen that installing this burner brings an increase in tapping temperature from 1913 K to 1917 K and a reduction in tapping carbon content from 0.092% to 0.071%. Therefore, 2.5 minutes can be saved for each heat using the same tapping criteria as before, which leads to the fact that 2 more heats can be completed in the daily production producing considerable economic benefits throughout the year.

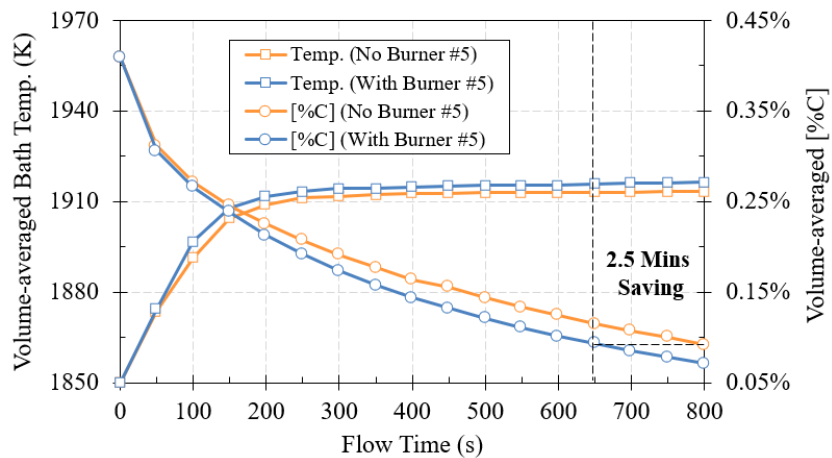


Figure 3.93. Refining efficiency comparison with and without coherent jet burner #5.

**Figure 3.94** plots the detailed carbon mass fraction distribution at tapping on the same plane as that in **Figure 3.90**. Under the consistent color range, the in-bath carbon content uniformity is largely improved by introducing the coherent jet burner #5. Meanwhile, the overall refining efficiency is further improved with the same amount of time, which can be reflected by the lower carbon mass fraction in the plot. Therefore, it is suggested to take the action for upgrading the original burner #5 to a coherent jet burner.

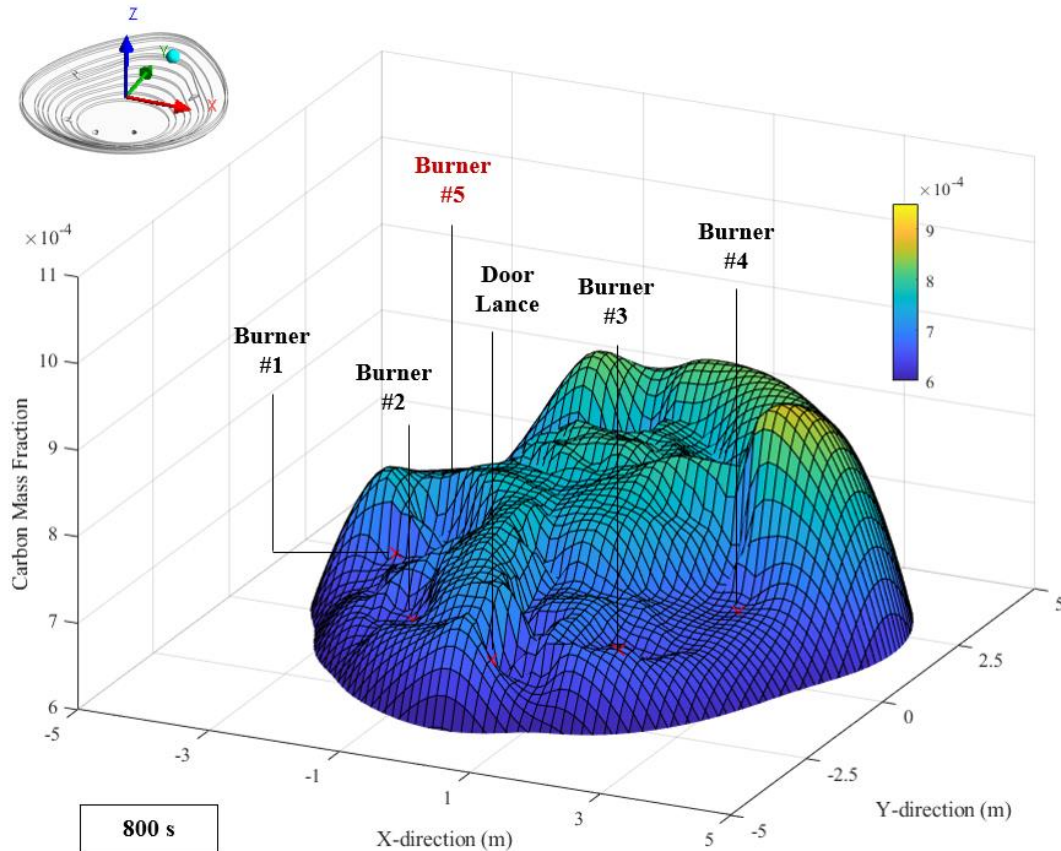


Figure 3.94. In-bath carbon mass fraction (0.5 m from furnace bottom) at tapping with burner #5.

### 3.3.5.5 Summary

This section presents the results from the in-bath decarburization simulator, which simulates the in-bath decarburization process in the liquid steel refining stage. The validations including the jet penetration depth and the tapping result were performed by comparing the results with the industrial measurement data, which shows relatively good accuracy of the simulator. The simulator predicts the liquid-gas two-phase reacting flow system for the analysis of the stirring mechanism, refining efficiency, and the in-bath carbon distribution. The main conclusions made by the present study are listed below:

- 1) The bubble stirring is proven to greatly promote the homogenization of the liquid steel bath and is one of the most important stirring mechanisms in the EAF refining stage. The bubble stirring needs to be considered as one of the fundamental stirring mechanisms for the future in-bath simulation.

- 2) A large amount of the oxygen bubbles injected from the cavity surface first oxidizes the reactive substances there releasing a large amount of the heat to the bath, while the excess oxygen either travels with the flow to the farther region or floats upward by the buoyancy and be absorbed by the slag layer. The carbon continues to move to the vicinity of the jet penetration cavity and react with the remaining or newly injected oxygen to generate the CO bubbles. The CO bubbles can float up with the flow causing the aforementioned in-bath bubble.
- 3) The current SDI burner arrangement results in an uneven carbon distribution in the liquid steel bath and the decarburization rate in the front part of the furnace is much slower than elsewhere. The burner arrangement that most of the burners are located in the middle or rear of the furnace, which leads to issues including the weak stirring and less oxygen injection in front of the furnace. Such decarburization is very inefficient. If an inappropriate flow pattern occurs, the decarburization process may cause a serious production delay
- 4) Introducing the coherent jet burner #5 to the original furnace can largely improve the in-bath carbon content uniformity and accelerate the refining process. 2.5 minutes can be saved for each heat using the same tapping criteria as before, which leads to the fact that 2 more heats can be completed in the daily production producing considerable economic benefits throughout the year.

### **3.3.6 Freeboard Post-Combustion Simulator**

This section presents the results from the freeboard post-combustion simulator, which couples/integrates the coherent jet model, the electric arc model, and the slag foaming model to simulate the freeboard post-combustion process in the liquid steel refining stage.

#### ***3.3.6.1 Simulation Conditions***

The freeboard post-combustion simulates the baseline case in an industry-scale SSAB 160-ton EAF, whose computational domain is given in **Figure 3.95**. The domain refers to the freeboard region above the slag layer with the bottom of the domain as the top slag surface allowing the CO from the bath to enter the freeboard for the post-combustion.

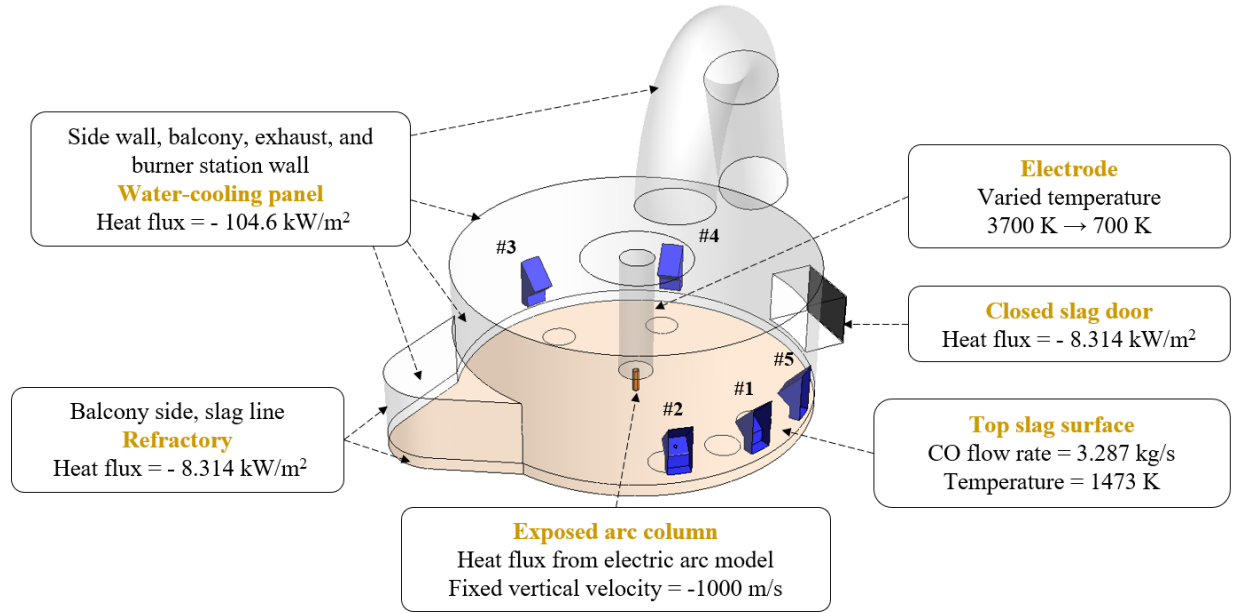


Figure 3.95. Computational domain for freeboard post-combustion simulation.

Table 3.20. Material thermal properties.

	Material	Specific Heat	Thermal Conductivity	Emissivity
<i>Water-cooling Panel</i>	<i>Steel</i>	<i>502 J/kg-K</i>	<i>75.83 W/m-K</i>	<i>0.8</i>
<i>Refractory</i>	<i>MgO</i>	<i>874 J/kg-K</i>	<i>4 W/m-K</i>	<i>0.31</i>
<i>Electrode</i>	<i>Graphite</i>	<i>710 J/kg-K</i>	<i>230 W/m-K</i>	<i>0.85</i>

It can be seen that five coherent jet burners are installed on both sides of the furnace wall to generate the supersonic oxygen jet shrouded by the combustion flame, which is simulated by the coherent jet model, and the coherent jets leave the domain through five outlets on the bottom of the domain. The furnace sidewall, balcony, exhaust, and burner station wall are all covered by the water-cooling panel to absorb the heat from the freeboard region due to the post-combustion, whose heat fluxes are calculated based on the industrial data provided by SSAB. The electric arc plasma generated by the electrode is treated as a small cylinder beneath the electrode tip in the computational domain. The slag foaming model is adopted to estimate the height for this column (i.e. exposed arc length), which has been detailed in the earlier sections. The boundary conditions for the exposed arc column are obtained from the arc heat transfer database and the arc momentum

transfer database determined by the electric arc simulator to consider the arc radiation effect and the plasma acceleration effect in the simulation. After the mesh sensitivity study, the total element number in the mesh is 4.8 million for the baseline simulation with some reasonable simplifications of the complicated furnace structure to guarantee the mesh quality. Key material thermal properties adopted in estimating the boundary conditions in **Figure 3.95** are listed in **Table 3.20**. The freeboard post-combustion simulator performs a steady-state simulation in the present study assuming the furnace operations remain unchanged during the entire liquid steel refining stage.

### 3.3.6.2 Validations

The freeboard post-combustion simulator was validated by the sidewall temperature prediction under two typical furnace operating conditions were selected including a no-overheating scenario and an overheating scenario as shown in **Figure 3.96**.

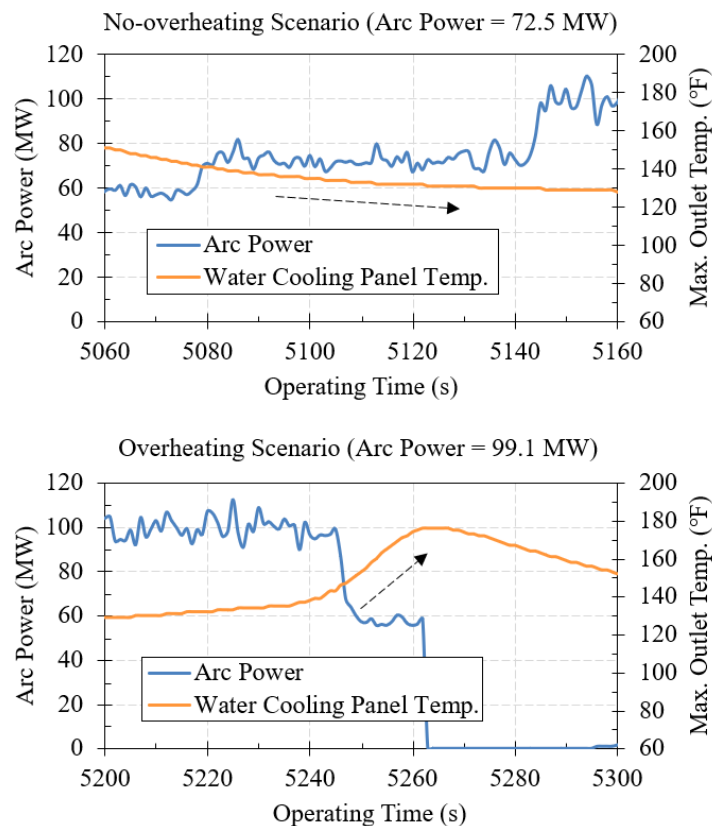


Figure 3.96. Analysis of water-cooling panel temperature.

If the SSAB EAF was operated at 72.5 MW arc power, the water-cooling panel temperature reported by the sensor remained relatively stable whose outlet water temperature was about 140 F. However, outlet water temperature increased significantly if elevating the arc power to 99.1 MW, which further triggered the warning alarm indicating the water-cooling panel overheating occurred inside the furnace. To protect the water-cooling panel, the system will reduce half of the arc power or even turn off the electric input, which impacts the production a lot.

The freeboard post-combustion simulator adopted the same operating conditions to reproduce the above two scenarios, whose results are given in **Figure 3.97**. It can be seen that the simulated maximum side wall temperature is about 1759 K lower than the warning temperature if the furnace is operated under 72.5 MW arc power, which indicates the overheating does not occur in the simulator results and is in line with the observation. If the arc power is further increased to 99.1 MW, the simulated maximum side wall temperature can reach up to 1809 K exceeding the warning temperature, which indicates there has been an overheating in the simulation and is consistent with the report.

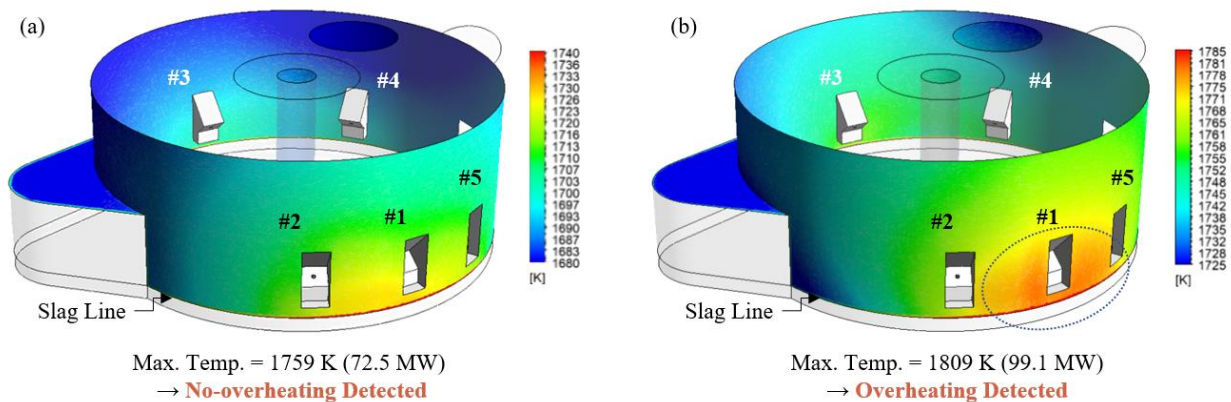


Figure 3.97. Simulation results for validations – (a) no-overheating; (b) overheating.

Considering that the no-overheating prediction and the overheating prediction are based on the correct simulation of the post-combustion in the freeboard region, the correct predictions for both scenarios prove that the freeboard post-combustion simulator has relatively good precision. Therefore, the potential causes of the water-cooling panel overheating can be investigated using this simulator.

### 3.3.6.3 Baseline Results

The key quantities distributions inside the furnace simulated from the baseline freeboard post-combustion simulator are given in **Figure 3.98** including the CO mass fraction distribution, the CO<sub>2</sub> mass fraction distribution, the gas temperature distribution, and the streamline colored by velocity.

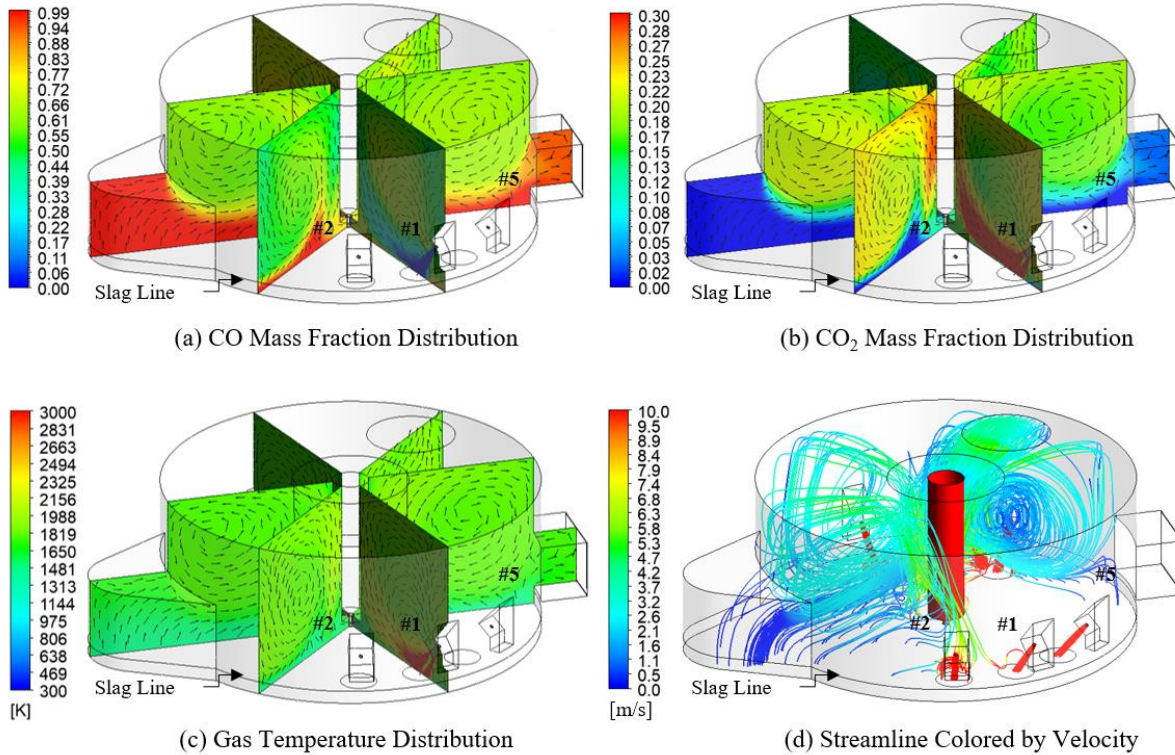


Figure 3.98. Baseline simulation results – (a) CO mass fraction distribution; (b) CO<sub>2</sub> mass fraction distribution; (c) gas temperature distribution; (d) streamline colored by velocity.

From the figures **Figure 3.98 (a)** and **Figure 3.98 (b)**, the CO entering the freeboard through the bottom of the domain undergoes sufficient post-combustion with oxygen provided by the coherent jet and produces CO<sub>2</sub>, thereby maintaining the areas near the burners with a relatively low CO mass fraction. For the regions away from the coherent jets, for example, the balcony, the oxygen-lean condition then results in insufficient post-combustion, which is reflected in the high CO concentration. Overall, the CO concentration decreases with the increase of the vertical height. On the other hand, intensive post-combustion tends to release more heat and cause heat accumulation. If the heat cannot be effectively discharged outside the furnace, a local high-temperature region

may be formed, as shown near the burner #1 in **Figure 3.98 (c)** and cause the local overheating inside the furnace. Normally, the region under the exhaust has more intensive vortexes which help to eliminate the local heat accumulation, as shown with the streamline in **Figure 3.98 (d)**.

### 3.3.6.4 Investigations of Water-cooling Panel Overheating

The freeboard post-combustion simulator was adopted to troubleshoot the SSAB water-cooling panel overheating from five perspectives, including the burner operation mode, the burner operating conditions, the bath level, the arc power, and the lime input.

#### 3.3.6.4.1 Effect of Burner Operation Mode

From SSAB data, both burner mode and lance mode were used for the liquid steel refining, whose operating conditions under different modes are given in **Table 3.21**.

Table 3.21. Burner operating conditions under different modes.

Nozzle Name	Burner #1	Burner #2	Burner #3	Burner #4	Burner #5
<i>Primary Oxygen</i>	<i>300 SCFM/1154 SCFM (Burner Mode/Lance Mode)</i>				<i>0</i>
<i>Secondary Oxygen</i>	<i>250 SCFM/70 SCFM (Burner Mode/Lance Mode)</i>			<i>520 SCFM</i>	
<i>Natural Gas</i>	<i>248 SCFM/68 SCFM (Burner Mode/Lance Mode)</i>			<i>230 SCFM/250 SCFM (Burner Mode/Lance Mode)</i>	

Under the lance mode, the primary oxygen nozzle with a high flow rate produces the supersonic oxygen jet, while the corresponding flow rates of the fuel nozzle and the secondary oxygen nozzle are relatively low, only to generate the shrouding combustion flame envelop to protect the central supersonic oxygen jet and slow the momentum decay in its traveling path. This mode aims to deliver more oxygen to the bath and creates stronger in-bath stirring. As for the burner mode, the flow rate of the primary oxygen nozzle is largely reduced instead so that the central oxygen jet is routinely to be in subsonic or sonic status. The corresponding flow rates through the fuel nozzles and the secondary oxygen nozzles are significantly elevated, which creates a larger flame and a higher burner power to achieve the purpose of scrap melting. These two different modes were

mixed used in the SSAB EAF refining stage, which may affect the post-combustion and gas flow of the freeboard, thus it is necessary to investigate the potential impact of burner operation mode on the overheating of the water-cooling panel.

In the present group study, the arc column is assumed to be covered by the slag layer meaning all arc power goes into the slag layer and the arc radiation does not directly impact the furnace wall temperature. The impact of arc exposure will be discussed in the later section. All five burners in the furnace are assumed to be operated in the same mode. The simulation results are given in **Figure 3.99**. The results show that the sidewall temperature distributions under different burner operation modes are similar to each other. The average sidewall temperature using the lance mode is slightly higher than that of using the burner mode due to the more intensive post-combustion above the bath. The maximum sidewall temperature can reach up to 1640 K under the lance mode but is lower than the warning temperature. The side with three burners for both cases experiences a much higher temperature compared with the other side, which indicates that the burner arrangement is inappropriate and the side with three burners is easier to have the potential local overheating issue. **Figure 3.100** shows the sidewall temperature distribution in four directions to further support the previous analysis. Overall, the inappropriate burner arrangement or different burner operation modes do not directly result in overheating in the present conditions, but the water-cooling panel has a high potential to be overheated near burner #1, burner #2, and burner #5. Trouble-shootings will focus on analyzing effects of the burner operating conditions, the bath level, the arc power, and the lime input in the next four sections.

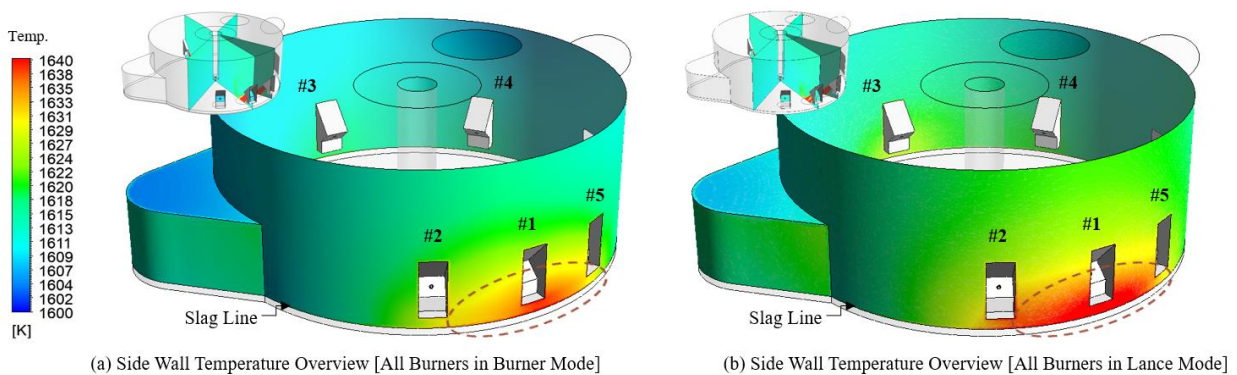


Figure 3.99. Effect of burner operation mode on sidewall temperature distribution.

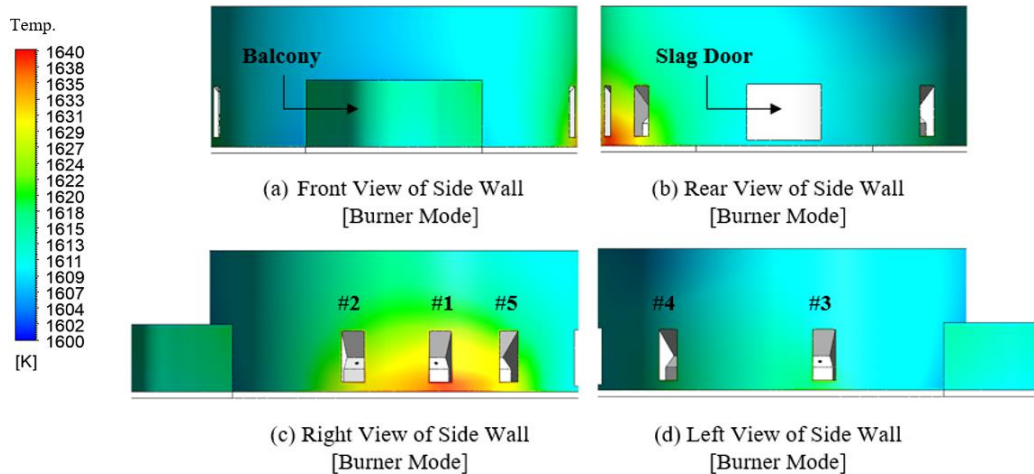


Figure 3.100. Sidewall temperature distribution in four viewing directions.

#### 3.3.6.4.2 Effect of Burner Operating Conditions

From **Table 3.21**, it is noted that burner #4 and burner #5 operated under the burner mode are without the primary oxygen, which is different from the rest burners and was also not in line with the normal burner operating conditions. All oxygen deliveries to the bath were directly coming from burners #1, burner #2, and burner #3. Such operations can be understood as reducing the liquid splashing to the slag door, but they may also result in inappropriate combustion and an unbalanced burner power input. Therefore, the impact of burner operating conditions on the sidewall temperature is explored in this group.

To evaluate the consequence of the inappropriate combustion, the total burner power input of 5 burners is averaged to ensure each burner has the same input power and each type of the nozzle has the same flow rates. This adjustment creates appropriate combustion but enlarges the high-temperature area on the sidewall, and the uniformity of the sidewall temperature gets worse, as shown in **Figure 3.101 (a) and (b)**. The average and maximum value of the sidewall temperature after the adjustment increases from 1613 K to 1614 K and from 1643 K to 1646 K, respectively. The standard deviation and the extreme wall temperature difference also indicate that the uniformity of the sidewall temperature distribution is reduced with the corresponding standard deviation changing from 6.37 K to 6.71 K and the extreme side wall temperature difference from 38.85 K to 41.35 K. Such conclusions can be explained by the separate coherent jet simulation

results given in **Figure 3.102**. The burner without the primary oxygen makes the hot gas be easier to mix with surrounding low-temperature gas reducing the impact on the sidewall temperature. With the primary oxygen, the combustion is reinforced leading to a higher wall temperature.

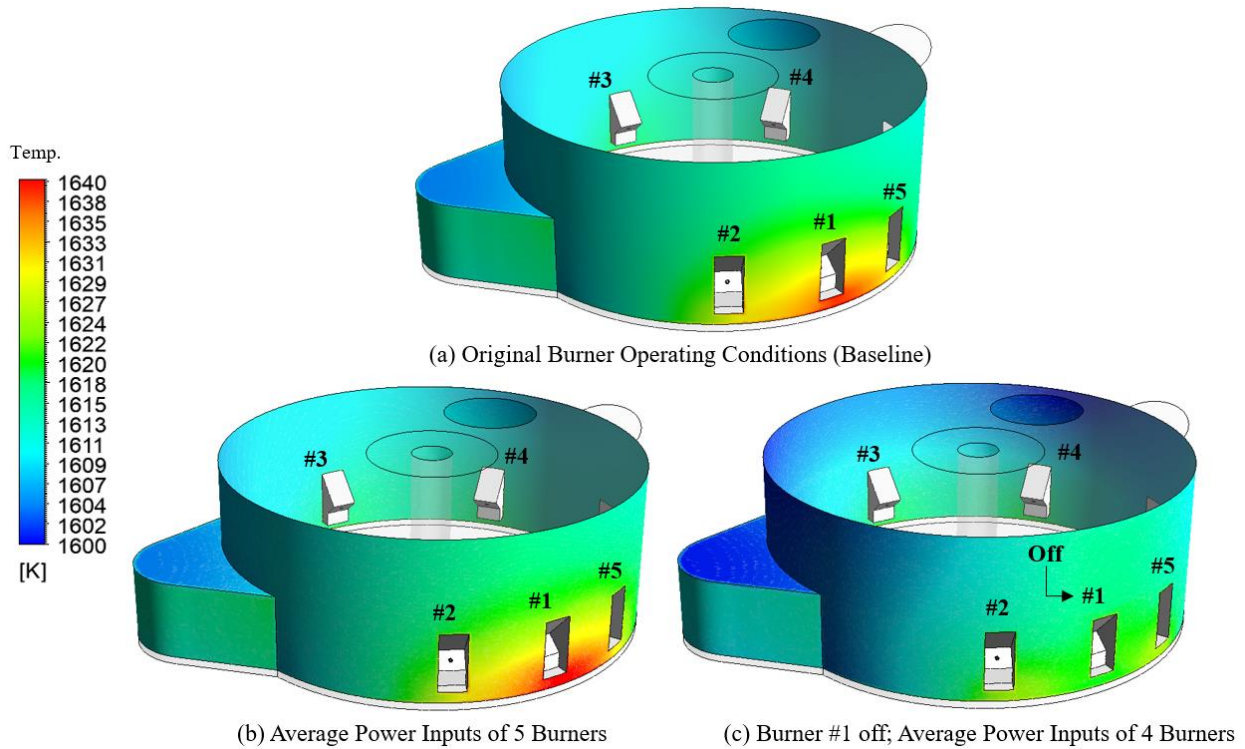


Figure 3.101. Effect of burner operating conditions on sidewall temperature distribution.

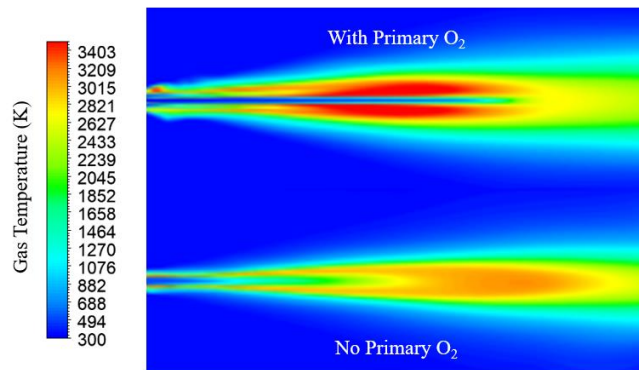


Figure 3.102. Coherent jet simulations with and without the primary oxygen.

To evaluate the consequence of the unbalanced burner power input, burner #1 is turned off to ensure the same number of burners on both sides, meanwhile averaging the operating conditions

among 4 burners to ensure the total burner power input is the same as the original. From **Figure 3.101 (c)**, the high-temperature region near burner #1, burner #2, and burner #5 is greatly reduced, and the corresponding average and maximum wall temperature can be reduced from 1613 K to 1610 K and from 1643 K to 1630 K, respectively. The standard deviation and the extreme wall temperature difference also reflect the increase in the side wall temperature uniformity: the standard deviation was reduced from 6.37 K to 5.54 K and the extreme side wall temperature difference is also reduced from 38.85 K to 29.8 K. Therefore, although the unbalanced burner arrangement does not directly result in overheating in the present conditions, it is the main cause to create the local high-temperature region near burner #1, burner #2, and burner #5. Overheating is easy to happen there if having other inappropriate furnace operations.

### 3.3.6.4.3 Effect of Bath Level

The amount of scrap charged in the furnace determines the bath level. Obviously, the larger the charge amount, the higher the bath level is, leading to more intensive post-combustion near the water-cooling panel on the sidewall. The present group is to quantitatively reveal the potential impact of the bath level on the sidewall temperature distribution.

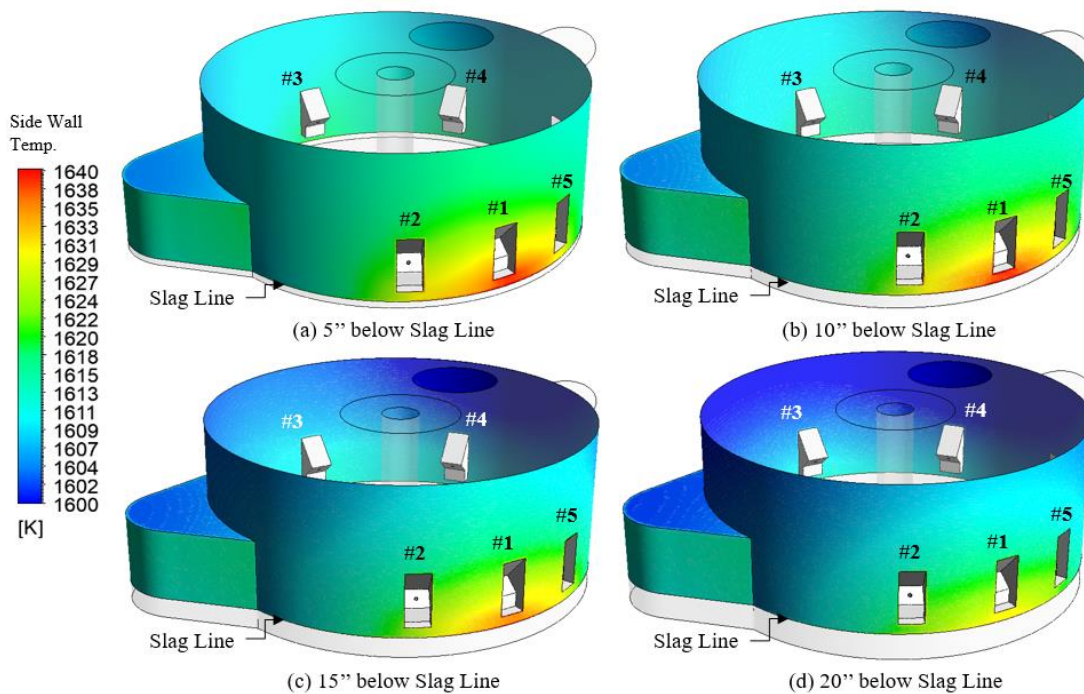


Figure 3.103. Effect of bath level on sidewall temperature distribution.

**Figure 3.103** demonstrates four different furnace sidewall temperature distributions with bath level 5'', 10'', 15'', and 20'' away from the slag line. It can be seen that decreasing the bath level can reduce the area of the local high-temperature region near burner #1, burner #2, and burner #5. The average sidewall temperature can be reduced from 1613 K to 1606 K, and the average sidewall temperature is decreased from 1643 K to 1635 K. Moreover, with the increase in the distance below the slag line, the standard deviation is increased from 38.85 K to 46.5 K, and the extreme wall temperature difference is increased from 6.37 K to 7.1 K.

In fact, decreasing the bath level does not eliminate the overheating issue directly, but moves the high-temperature region from the water-cooling panel to the refractory surface. From the perspective of avoiding the water-cooling panel overheating, charging less scrap can somehow help to reduce the possibility of having hot spots occurring there.

#### *3.3.6.4.4 Effect of Arc Power*

The present group aims to reveal the relation between arc power and arc exposure. From the electric arc simulator results, increasing the arc power gives a longer arc during the operation. If the slag layer is not well-foamed to cover the entire arc, the exposed arc directly emits a large amount of radiation to the freeboard region, which may promote the high-temperature region near burner #1, burner #2, and burner #5 to exceed the warning temperature and damage the water-cooling panel system. The present study covers the arc power ranging from 46 MW to 112.3 MW, and the corresponding results are given in **Figure 3.104** and **Figure 3.105**.

For the SSAB furnace, if the arc power is controlled within 59 MW, the electrode tip can be fully immersed into the slag layer and there is no arc exposure to the freeboard region. Under this condition, the arc heat is fully absorbed by the slag and maximizes the input electric energy utilization during the refining, and the maximum sidewall temperature is about 1617 K. If the arc power is further increased to the value between 59 MW to 99.1 MW, the partially exposed arc starts to heat up the entire furnace sidewall through radiation, and both average sidewall temperature and maximum sidewall temperature climb significantly. Once the arc power exceeds 99.1 MW, the maximum sidewall temperature reaches the warning temperature, and overheating can be detected. Therefore, the combined effect of inappropriate burner arrangement and the large

arc exposure is the main reason causing the overheating in the SSAB furnace. It is suggested to always control the arc power within 85.1 MW to avoid the overheating issue, or to further reduce the arc power below 59 MW to achieve the maximum input electric energy utilization.

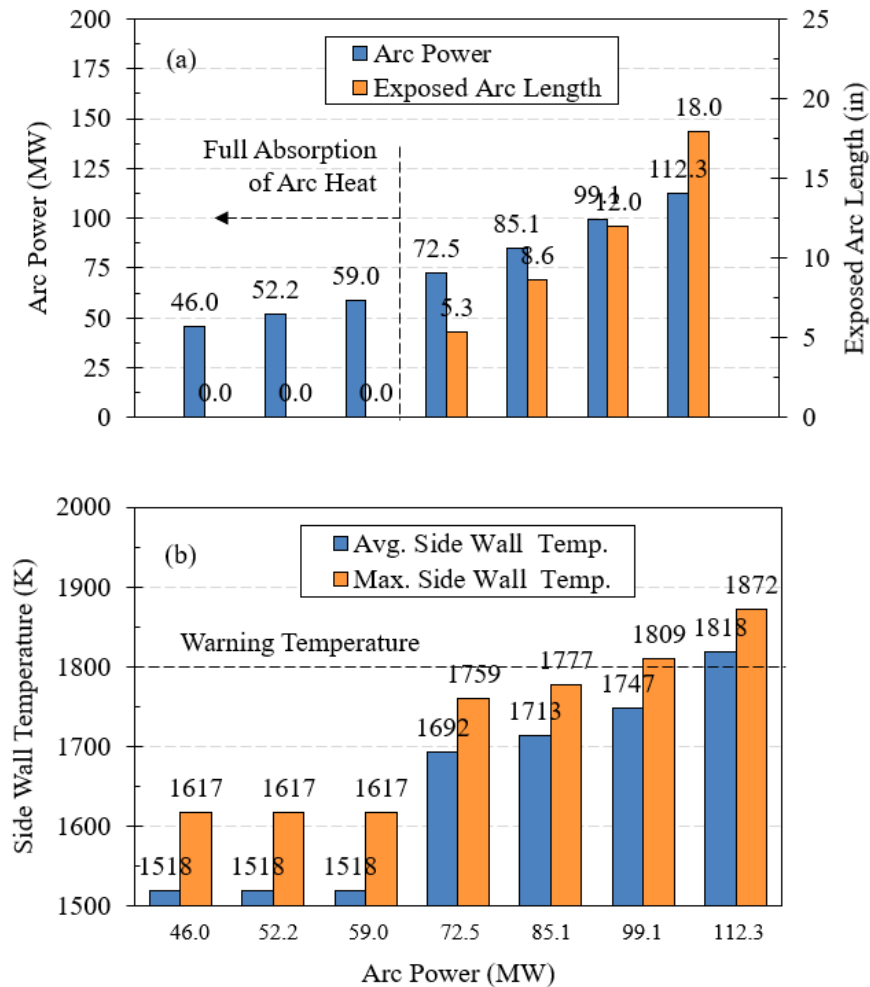


Figure 3.104. Effect of arc power on - (a) exposed arc length; (b) averaged and maximum sidewall temperature.

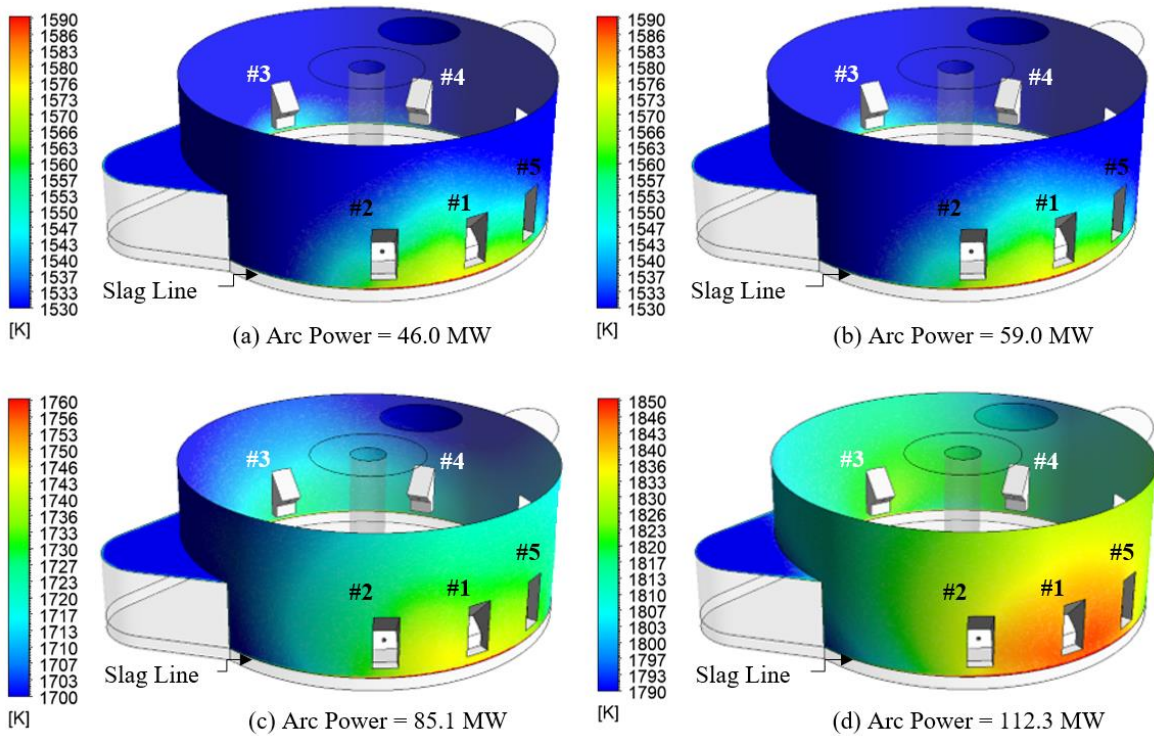


Figure 3.105. Effect of arc power on sidewall temperature distribution.

### 3.3.6.4.5 Effect of Lime Input

Normally, the lime can not only promote the slag foaming but also help to dephosphorize and desulphurize the scrap and protect the refractory. From the previous group, the slag foaming height is a key factor impacting the arc exposure and further determining the overheating, while the foaming process is highly related to the lime input during the liquid steel refining stage. Therefore, the present group investigates the effect of lime input on the sidewall temperature.

Based on the original lime input (95% CaO, 56.4% CaO, and 40.6% MgO), two cases with a proportional increase of 20% of total lime input and a proportional of 20% less total lime input are analyzed, whose results are shown in **Figure 3.106**. 20% reduction of the original lime input can lower the original slag foaming height from 12.08 inches to 11.08 inches leading the exposed arc length to increase from 8.62 inches to 9.62 inches, thus more arc radiation is received by the water-cooling panel causing the maximum sidewall temperature near burner #1, burner #2, and burner #5 to exceed the warning temperature and have the overheating. If the lime input is increased by 20% of the original lime input, although the slag foaming height is increased from 12.08 inches to

13.24 inches immersing the more arc column in the slag layer, the increased bath level also increases the sidewall temperature as analyzed in the earlier sections. Therefore, the combined effect makes its sidewall temperature distribution very similar to the case with original lime input. It is suggested to maintain the original lime input to achieve optimal economics for slag foaming.

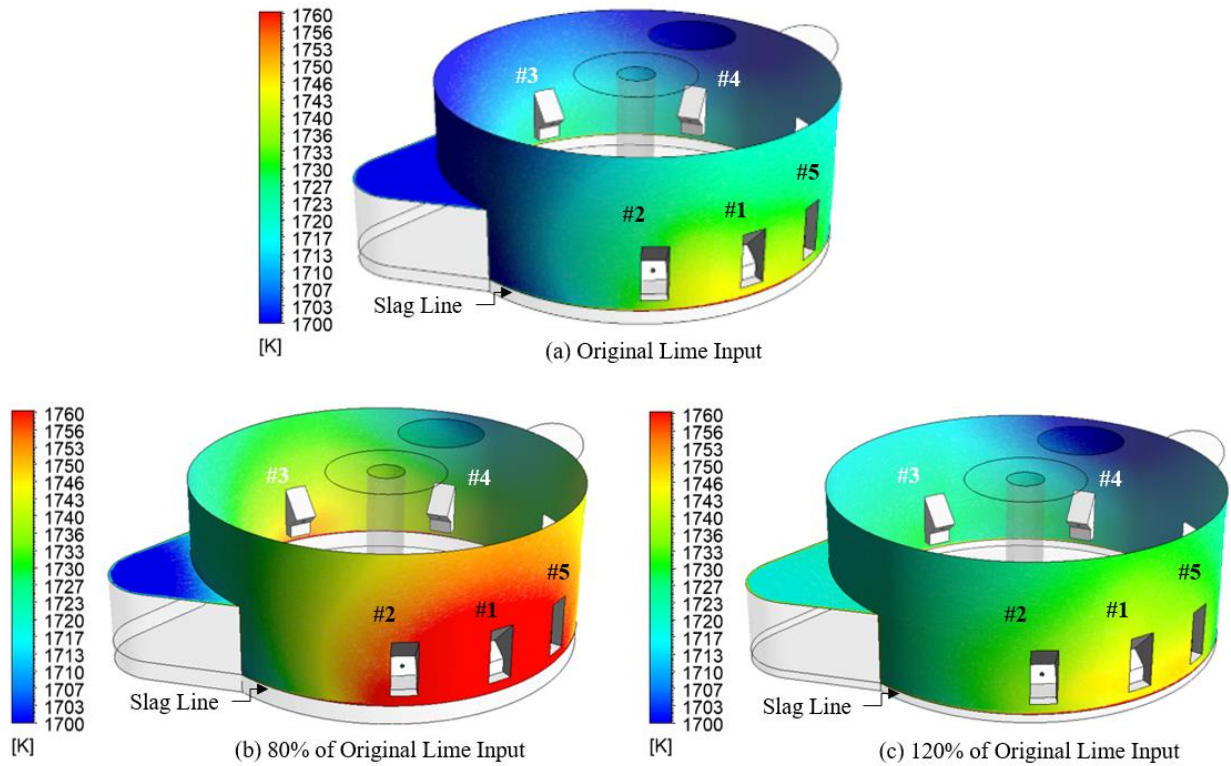


Figure 3.106. Effect of lime input on sidewall temperature distribution.

### 3.3.6.5 Web-based Online Calculator

Based on the freeboard post-combustion simulator, all results have been packaged and delivered as a web-based online calculator to SSAB, which can deliver instant results without running the CFD simulations in the simulator. The simulator is available in <https://steelconsortium.org/>.

The calculator can input the data including voltage, current, and slag composition to predict the exposed arc length, slag foaming height, total arc power delivery, share of different arc heat transfer mechanisms, sidewall temperature distribution, and the overheating warning. The online

calculator has also been integrated into the SSAB furnace operation system to assist the operator to have better control of their EAF.

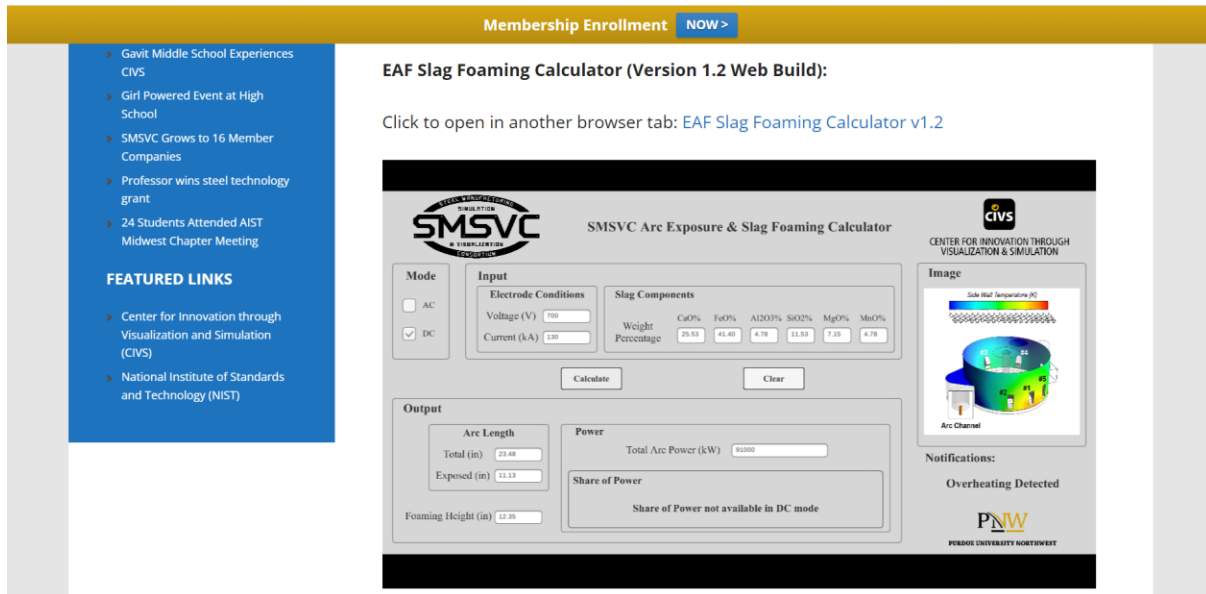


Figure 3.107. Real-Time online calculator launched in SMSVC official website.

### 3.3.6.6 Summary

This section presents the results from the freeboard post-combustion simulator, which simulates the freeboard post-combustion process in the liquid steel refining stage. The simulator was validated by the sidewall temperature prediction under two typical furnace operating conditions including a no-overheating scenario and an overheating scenario, which gave correct predictions consistent with the observations. The simulator was applied to troubleshoot the SSAB water-cooling panel overheating from five perspectives, including the burner operation mode, the burner operating conditions, the bath level, the arc power, and the lime input. A web-based online calculator was also delivered to SSAB to help better control the furnace based on the simulator results. The main research conclusions in the present section are given below:

- 1) The sidewall temperature distributions under different burner operation modes are similar to each other. The average sidewall temperature using the lance mode is slightly higher than that of using the burner mode, whose maximum sidewall temperature can reach up to 1640 K but is lower than the warning temperature. The side with three burners for both cases experiences a much higher temperature compared with the other

side, which indicates that the burner arrangement is inappropriate and the side with three burners is easier to have the potential local overheating issue.

- 2) The burner without the primary oxygen makes the hot gas be easier to mix with surrounding low-temperature gas reducing the impact on the sidewall temperature. With the primary oxygen, the combustion is reinforced leading to a higher wall temperature. Turning off burner #1 to ensure the same number of burners on both sides can greatly reduce the local high-temperature region near burner #1, burner #2, and burner #5, and make the sidewall temperature distribution more uniform.
- 3) The larger the charge amount, the higher the bath level is, leading to the local high-temperature region on the water-cooling panel near burner #1, burner #2, and burner #5. Decreasing the bath level does not eliminate the overheating issue directly, but moves the high-temperature region from the water-cooling panel to the refractory surface. From the perspective of avoiding the water-cooling panel overheating, charging less scrap can somehow help to reduce the possibility of having hot spots occurring there.
- 4) The combined effect of inappropriate burner arrangement and the large arc exposure is the main reason causing the overheating in the SSAB furnace. It is suggested to always control the arc power within 85.1 MW to avoid the overheating issue or to further reduce the arc power below 59 MW to achieve the maximum input electric energy utilization.
- 5) Reduction of the original lime input can cause the maximum sidewall temperature near burner #1, burner #2, and burner #5 to exceed the warning temperature and have the overheating. But charging more lime may not effectively reduce the overall sidewall temperature. It is suggested to maintain the original lime input to achieve optimal economics for foaming the slag.

## 4. CONCLUSIONS AND OUTLOOK

### 4.1 Conclusions

#### 4.1.1 Simulation Methodologies and CFD Models

Two state-of-the-art comprehensive EAF CFD models have been developed for simulating the lab-scale DC EAF and the industry-scale AC EAF:

- 1) For the lab-scale DC EAF, a direct-coupling methodology was developed for its comprehensive EAF CFD model which includes the solid steel melting model based on the enthalpy-porosity method and the electric arc model (for lab-scale DC arc) based on the Magneto Hydrodynamics (MHD) theory, so that the dynamic simulation of the steel ingot melting by DC arc in the lab-scale furnace can be achieved, which considered the continuous phase changing of solid steel, the ingot surface deformation, and the phase-to-phase interaction. Both stationary DC arc and the arc-solid steel interface heat transfer and force interaction were validated respectively against the experimental data in published literature. For the given lab-scale furnace, the DC arc behavioral characteristics with varying arc lengths generated by the moving electrode were analyzed, and the effects of both the initial arc length and the dynamic electrode movement on the steel ingot melting efficiency were revealed.
- 2) For the industry-scale AC EAF, an innovative integration methodology was proposed for its comprehensive EAF CFD model, which relies on the stage-by-stage approach to simulate the entire steelmaking process. Six simulators were developed for simulating sub-processes in the industry-scale AC EAF, and five models were developed for the above four simulators, including the scrap melting model, the electric arc model (for industry-scale AC arc), the coherent jet model, the oxidation model, and the slag foaming model, which can be partially integrated according to the mass, energy, and momentum balance. Specifically, the dual-cell approach and the stack approach were proposed for the scrap melting model to treat the scrap pile as the porous medium and simulate the scrap melting together with its dynamic collapse process. The statistical sampling method, the CFD-compatible Monte Carlo method, and the electrode regulation algorithm were proposed for the electric arc model to estimate the total AC arc power delivery, the arc

radiative heat dissipation, and the instantaneous electrode movement. The energetic approach was proposed to determine the penetration of the top-blown jet in the molten bath based on the results from the coherent jet model. The source term approach was proposed in the oxidation model to simulate the in-bath decarburization process, where the oxidation of carbon, iron, and manganese as well as the effect of those exothermic reactions on bath temperature rising was considered. Moreover, corresponding experiments were performed in the industry-scale EAF to validate the proposed simulators. The quantitative investigations and analyses were conducted afterward to explore and understand the coherent jet performance, the AC arc heat dissipation, the burner preheating characteristics, the scrap melting behavior, the in-bath decarburization efficiency, and the freeboard post-combustion status.

#### **4.1.2 Research Findings**

- 1) Increasing the arc length elevates the total arc power delivery since the longer arc increases the arc resistance, and increasing the RMS arc current also has a positive effect on the elevation of total arc power delivery. The faster growth of arc power delivery appears when having a higher arc current or longer arc length.
- 2) Longer arc length has a positive impact on increasing the arc radiation but a negative impact on increasing the arc convection and electron flow. Therefore, a short arc should be used initially when the electrode first bores down to minimize radiative heat dissipation to the roof and side walls from the exposed arc. A longer arc should be used after the electrode has bored down into the scrap to make the radiated power dissipate to the surrounding scrap more effectively.
- 3) The higher arc current reinforces the Lorentz force and Joule heating effect applied on the flow field leading to the arc plasma having stronger impingement on the cathode/anode surface and increasing the share of convection but reducing the share of radiation.
- 4) The turbulent viscosity and density of ambient gas are significantly reduced in the high ambient temperature environment, meanwhile, the heat transfer between the shrouding combustion flame and the environment is strengthened instead, leading to more effective protection of the center jet. Therefore, the relatively high freeboard ambient temperature

increases the jet potential core length and improve the jet performance during the refining stage, which can achieve a better oxygen delivery and jet kinetic energy to the bath.

- 5) Under the current high ambient temperature conditions, the fuel input plays an important role in determining the jet potential core length, and insufficient fuel input significantly reduces the coherent jet performance, leading to poor oxygen delivery and bath stirring intensity. For the given burner, the optimal fuel input can be achieved when the fuel/primary oxygen volumetric flow ratio exceeds 6.5%.
- 6) The burner efficiency decreases over time during the entire scrap preheating stage. For the baseline NLMK burner and scrap conditions, it is reduced from 84.02% to 77.96% within 10 minutes of operation.
- 7) Under different burner powers, higher burner power can accelerate the scrap heating and melting, but it is less economic if taking the burner efficiency into account.
- 8) Higher initial scrap temperature makes the scrap require less energy to be melted within the same amount of time, leading to a larger final melted percentage. However, the corresponding reduced gas-solid heat transfer rate results in a lower scrap heating rate and burner efficiency. Therefore, the higher initial scrap temperature benefits the faster melting rate, while the lower initial scrap temperature is good for improving the burner efficiency.
- 9) Using less dense scrap improves the void passage rate of the hot combustion gas and the gas residence time inside the scrap pile so that the gas-solid heat transfer rate is significantly increased. Therefore, no matter from the perspective of scrap melting efficiency or burner energy utilization, it is recommended to use high-porosity scrap for melting.
- 10) Adjusting the scrap porosity impacts the burner efficiency more than the burner power and the initial scrap temperature does. Burner power has absolute dominance in raising the scrap temperature and relatively the greatest impact on the melted percentage.
- 11) Although the scrap blockage does not impact the burner efficiency within a short time, it still needs to be avoided during the operation. The scrap blockage not only makes it difficult to heat the scrap pile deeper in the middle and back, which reduces scrap heating rate but also causes the flame blow-back, which leads to a serious ablation of the burner and surrounding refractories as well as the water-cooling panel overheat above the burner

- 12) For the comprehensive contribution rates of each factor on the scrap preheating stage, the burner power having the greatest impact at 57.3%, the scrap porosity contributing 32.9%, and the initial scrap temperature having a relatively minor impact at 9.8%.
- 13) For NLMK EAF, it is suggested to increase the burner power by 1.25 times, the initial scrap temperature by 2 times, and the scrap porosity by 1.06 times, which can improve overall scrap temperature rise and melted percentage by 29.29% and 63.42%, respectively.
- 14) The electrode bore-down phase takes about 300 s and only 7.7% of the total scrap charge is melted in this phase due to the re-solidification of the liquid steel during dripping.
- 15) The scrap melting in the main melting phase follows the inside-out, bottom-up melting pattern until the end. During this phase, the first scrap collapse normally happens at 450 s after charging. The collapse around the three electrodes is mainly caused by the bottom diameter of the central electrode pit being larger than the upper diameter, while the overall vertical scrap collapse is mainly caused by the in-bath melting of the scrap pile. The scrap melting profile normally takes on a U-shape at the vertical cross-section.
- 16) After arc ignition, 60% to 70% of the arc heat is radiated to the surrounding environment, of which only 45% of the arc radiation is effectively absorbed by the surface of the scrap steel, and the rest is lost to the furnace roof and furnace wall. The arc radiation absorbed by the scrap surface gradually climbs to 98% as the electrodes bore down into the scrap pile, then decrease and is stable at 80% to 85% as the scrap collapses and the central electrode pit gradually expands.
- 17) The burner efficiency decays from an initial 90% to 75% for the first bucket charge. A second bucket charge can make a short increase in burner efficiency, but as the burner melting cavities gradually expand again, the burner efficiency begins to decline again. At about 1700 s, the burner efficiency drops dramatically since there is no more scrap in front of the burners to absorb the heat released by the combustion flame. Therefore, a large amount of high-temperature combustion gas directly enters the freeboard region, resulting in a fast rising of the freeboard temperature.
- 18) The bubble stirring is proven to greatly promote the homogenization of the liquid steel bath and is one of the most important stirring mechanisms in the EAF refining stage. The

bubble stirring needs to be considered as one of the fundamental stirring mechanisms for the future in-bath simulation.

- 19) A large amount of the oxygen bubbles injected from the cavity surface first oxidizes the reactive substances there releasing a large amount of the heat to the bath, while the excess oxygen either travels with the flow to the farther region or floats upward by the buoyancy and be absorbed by the slag layer. The carbon continues to move to the vicinity of the jet penetration cavity and react with the remaining or newly injected oxygen to generate the CO bubbles. The CO bubbles can float up with the flow causing the aforementioned in-bath bubble.
- 20) The current SDI burner arrangement results in an uneven carbon distribution in the liquid steel bath and the decarburization rate in the front part of the furnace is much slower than elsewhere. The burner arrangement that most of the burners are located in the middle or rear of the furnace, which leads to issues including the weak stirring and less oxygen injection in front of the furnace. Such decarburization is very inefficient. If an inappropriate flow pattern occurs, the decarburization process may cause a serious production delay
- 21) Introducing the coherent jet burner #5 to the original furnace can largely improve the in-bath carbon content uniformity and accelerate the refining process. 2.5 minutes can be saved for each heat using the same tapping criteria as before, which leads to the fact that 2 more heats can be completed in the daily production producing considerable economic benefits throughout the year.
- 22) The sidewall temperature distributions under different burner operation modes are similar to each other. The average sidewall temperature using the lance mode is slightly higher than that of using the burner mode, whose maximum sidewall temperature can reach up to 1640 K but is lower than the warning temperature. The side with three burners for both cases experiences a much higher temperature compared with the other side, which indicates that the burner arrangement is inappropriate and the side with three burners is easier to have the potential local overheating issue.
- 23) The burner without the primary oxygen makes the hot gas be easier to mix with surrounding low-temperature gas reducing the impact on the sidewall temperature. With the primary oxygen, the combustion is reinforced leading to a higher wall temperature.

Turning off burner #1 to ensure the same number of burners on both sides can greatly reduce the local high-temperature region near burner #1, burner #2, and burner #5, and make the sidewall temperature distribution more uniform.

- 24) The larger the charge amount, the higher the bath level is, leading to the local high-temperature region on the water-cooling panel near burner #1, burner #2, and burner #5. Decreasing the bath level does not eliminate the overheating issue directly, but moves the high-temperature region from the water-cooling panel to the refractory surface. From the perspective of avoiding the water-cooling panel overheating, charging less scrap can somehow help to reduce the possibility of having hot spots occurring there.
- 25) The combined effect of inappropriate burner arrangement and the large arc exposure is the main reason causing the overheating in the SSAB furnace. It is suggested to always control the arc power within 85.1 MW to avoid the overheating issue or to further reduce the arc power below 59 MW to achieve the maximum input electric energy utilization.
- 26) Reduction of the original lime input can cause the maximum sidewall temperature near burner #1, burner #2, and burner #5 to exceed the warning temperature and have the overheating. But charging more lime may not effectively reduce the overall sidewall temperature. It is suggested to maintain the original lime input to achieve optimal economics for foaming the slag.

## 4.2 Outlook

Future efforts are suggested to be on enhancing the scrap melting simulator and the in-bath decarburization simulator and applying the developed comprehensive EAF CFD models to help the steel industry to solve more practical problems.

The scrap melting simulator can further consider the DRI/HBI melting and the gas-solid interphase reactions. The in-bath decarburization simulator can further consider the oxidations of Al and Si, electrode magnetic stirring, and the un-melted scrap in the bath. The comprehensive EAF CFD model for the lab-scale DC EAF can also be converted to the comprehensive EAF CFD model for the industry-scale DC EAF using the similar integration methodology developed for modeling the industry-scale AC EAF.

## REFERENCES

1. "What Is Steel and How Is Steel Made?" Eurofer. Accessed June 20, 2022. <https://www.eurofer.eu/about-steel/learn-about-steel/what-is-steel-and-how-is-steel-made/>.
2. "U.S. Energy Information Administration - EIA - Independent Statistics and Analysis." Manufacturing Energy Consumption Survey (MECS) - Data - U.S. Energy Information Administration (EIA). Accessed March 18, 2021.
3. "US Steel Sector Thrives as Mills Move up Quality Ladder." US steel sector thrives as mills move up quality ladder S&P Global Platts, May 9, 2019. <https://blogs.platts.com/2019/05/09/us-steel-mills-quality/>.
4. Association for Iron and Steel Technology (AIST), "2019 AIST Electric Arc Furnace Roundup," *Iron & Steel Technology*, pp. 128-151, 1 2019.
5. Schmitt, Robert J. "Introduction to electric arc furnace steelmaking." *CMP TechCommetary*, EPRI Center for Materials Production, OI 3 (1997): 4.
6. H. J. Odenthal, A. Kemminger, F. Krause, L. Sankowski, N. Uebber, N. Vogl, "Review on Modeling and Simulation of the Electric Arc Furnace (EAF)," *Steel Res. Int.*, vol. 89, No. 1 (2018), pp. 17-98.
7. Gerling, R., T. Louis, G. Schmeiduch, R. Sesselmann, A. Sieber, and J. Lubbe. "Improving AC-EAF operating process efficiency at Stahlwerk Bous with a hybrid model." *AISE Steel Technology(USA)* 78, no. 10 (2001): 41-45.
8. Wilson, Edward, Michael Kan, and Anjan Mirle. "Intelligent technologies for electric arc furnace optimization." In *ELECTRIC FURNACE CONFERENCE*, vol. 56, pp. 697-702. IRON AND STEEL SOCIETY OF AIME, 1998.
9. Evenson, E. J., and Michael J. Kempe. "Neural Network Modeling and Heuristic Control for Electric Arc Furnace Process Optimization." In *ELECTRIC FURNACE CONFERENCE*, vol. 56, pp. 675-688. IRON AND STEEL SOCIETY OF AIME, 1998.
10. Ameron, A.; Saxena, N.; Broome, K. "Optimizing EAF operations by dynamic process simulation." *Proceeding of the 56th Electric Furnace Conference*, 1998; pp 689–696.

11. Bekker, Johannes Gerhardt, Ian Keith Craig, and Petrus Christiaan Pistorius. "Modeling and simulation of an electric arc furnace process." *ISIJ international* 39, no. 1 (1999): 23-32.
12. Morales, R. D. "H. Rodríguez-Hernández, and AN Conejo." *ISIJ Int* 41 (2001): 426-35.
13. MacRosty, Richard DM, and Christopher LE Swartz. "Dynamic modeling of an industrial electric arc furnace." *Industrial & engineering chemistry research* 44, no. 21 (2005): 8067-8083.
14. Logar, Vito, Dejan Dovžan, and Igor Škrjanc. "Modeling and validation of an electric arc furnace: Part 1, heat and mass transfer." *ISIJ international* 52, no. 3 (2012): 402-412.
15. Opitz, Florian, and Peter Treffinger. "Physics-based modeling of electric operation, heat transfer, and scrap melting in an AC electric arc furnace." *Metallurgical and Materials Transactions B* 47, no. 2 (2016): 1489-1503.
16. Opitz, Florian, Peter Treffinger, and Jürgen Wöllenstein. "Modeling of Radiative Heat Transfer in an Electric Arc Furnace." *Metallurgical and Materials Transactions B* 48, no. 6 (2017): 3301-3315.
17. Hay, Thomas, Ville-Valtteri Visuri, Matti Aula, and Thomas Echterhof. "A Review of Mathematical Process Models for the Electric Arc Furnace Process." *steel research international* 92, no. 3 (2021): 2000395.
18. Mandal, Kamalesh. "Modeling of scrap heating by burners." PhD diss., 2010.
19. C. Giavani, E. Malfa, V. Battaglia. "The Evolution of Consteel® EAF." In *EEC 2012 – Electric Steelmaking Conference Proceedings*, 2012.
20. Voller, Vaughan R., and C. Prakash. "A fixed grid numerical modelling methodology for convection-diffusion mushy region phase-change problems." *International journal of heat and mass transfer* 30, no. 8 (1987): 1709-1719.
21. Brent, A. D., Vaughan R. Voller, and K. T. J. Reid. "Enthalpy-porosity technique for modeling convection-diffusion phase change: application to the melting of a pure metal." *Numerical Heat Transfer, Part A Applications* 13, no. 3 (1988): 297-318.
22. Li, Yan, Yanhui Feng, Xinxin Zhang, and Chuansong Wu. "Energy propagation in plasma arc welding with keyhole tracking." *Energy* 64 (2014): 1044-1056.

23. Li, T. Q., and C. S. Wu. "Numerical simulation of plasma arc welding with keyhole-dependent heat source and arc pressure distribution." *The International Journal of Advanced Manufacturing Technology* 78, no. 1-4 (2015): 593-602.
24. Yadav, Ankit, and Sushant Samir. "Experimental and numerical investigation of spatiotemporal characteristics of thermal energy storage system in a rectangular enclosure." *Journal of Energy Storage* 21 (2019): 405-417.
25. Saraswat, Amit, Ankit Verma, Sameer Khandekar, and Malay K. Das. "Latent Heat Thermal Energy Storage In A Heated Semi-Cylindrical Cavity: Experimental Results And Numerical Validation." *changes* 5 (2015): 7.
26. Karalis, K., N. Karkalos, G. S. E. Antipas, and A. Xenidis. "Pragmatic analysis of the electric submerged arc furnace continuum." *Royal Society open science* 4, no. 9 (2017): 170313.
27. Karalis, Konstantinos, Nikolaos Karalis, Nikolaos Karkalos, G. Antipas, and Antimos Xenidis. "Computational fluid dynamics analysis of a three-dimensional electric submerged arc furnace operation." *OSF Preprints* 20 (2020).
28. Carmona, Mauricio, and Cristóbal Cortés. "Numerical simulation of a secondary aluminum melting furnace heated by a plasma torch." *Journal of Materials Processing Technology* 214, no. 2 (2014): 334-346.
29. Arzpeyma, Niloofar, Ola Widlund, Mikael Ersson, and Pär Jönsson. "Mathematical modeling of scrap melting in an EAF using electromagnetic stirring." *ISIJ international* 53, no. 1 (2013): 48-55.
30. Xi, Xiaojun, Sai Chen, Shufeng Yang, Maolin Ye, and Jingshe Li. "Melting Characteristics of Multipiece Steel Scrap in Liquid Steel." *ISIJ International* (2020): ISIJINT-2020.
31. Xi, Xiaojun, Shufeng Yang, Jingshe Li, Xiaokang Chen, and Maolin Ye. "Thermal simulation experiments on scrap melting in liquid steel." *Ironmaking & Steelmaking* 47, no. 4 (2020): 442-448.
32. Li, Jianghua, Geoffery A. Brooks, and Nikolas Provatas. "Phase-field modeling of steel scrap melting in a liquid steel bath." In *AISTECH-CONFERENCE PROCEEDINGS-*, vol. 1, p. 833. ASSOCIATION FOR IRON & STEEL TECHNOLOGY, 2004.

33. Li, Jianghua, Nikolas Provatas, and Geoff Brooks. "Kinetics of scrap melting in liquid steel." *Metallurgical and materials transactions B* 36, no. 2 (2005): 293-302.
34. Li, Jianghua, and Nikolas Provatas. "Kinetics of scrap melting in liquid steel: multipiece scrap melting." *Metallurgical and Materials Transactions B* 39, no. 2 (2008): 268-279.
35. Li, Jianghua, and Mansoor Barati. "Kinetics and mechanism of decarburization and melting of direct-reduced iron pellets in slag." *Metallurgical and Materials Transactions B* 40, no. 1 (2009): 17-24.
36. Hsu, K. C., K. Etemadi, and E. Pfender. "Study of the free-burning high-intensity argon arc." *Journal of applied physics* 54, no. 3 (1983): 1293-1301.
37. Hsu, K. C., and E. Pfender. "Two-temperature modeling of the free-burning, high-intensity arc." *Journal of applied physics* 54, no. 8 (1983): 4359-4366.
38. McKelliget, J., and J. Szekely. "Heat transfer and fluid flow in the welding arc." *Metallurgical Transactions A* 17, no. 7 (1986): 1139-1148.
39. Tsai, M. C., and Sindo Kou. "Heat transfer and fluid flow in welding arcs produced by sharpened and flat electrodes." *International journal of heat and mass transfer* 33, no. 10 (1990): 2089-2098.
40. Lowke, J. J., P. Kovitya, and H. P. Schmidt. "Theory of free-burning arc columns including the influence of the cathode." *Journal of Physics D: Applied Physics* 25, no. 11 (1992): 1600.
41. Gonzalez, J. J., A. Gleizes, P. Proulx, and M. Boulos. "Mathematical modeling of a free-burning arc in the presence of metal vapor." *Journal of applied physics* 74, no. 5 (1993): 3065-3070.
42. Morrow, R., and J. J. Lowke. "A one-dimensional theory for the electrode sheaths of electric arcs." *Journal of physics D: Applied physics* 26, no. 4 (1993): 634.
43. Freton, P., J. J. Gonzalez, and A. Gleizes. "Comparison between a two-and a three-dimensional arc plasma configuration." *Journal of Physics D: Applied Physics* 33, no. 19 (2000): 2442.
44. Lago, F., J. J. Gonzalez, P. Freton, and A. Gleizes. "A numerical modelling of an electric arc and its interaction with the anode: Part I. The two-dimensional model." *Journal of Physics D: Applied Physics* 37, no. 6 (2004): 883.

45. Gonzalez, J. J., F. Lago, P. Freton, M. Masquere, and X. Franceries. "Numerical modelling of an electric arc and its interaction with the anode: part II. The three-dimensional model—influence of external forces on the arc column." *Journal of Physics D: Applied Physics* 38, no. 2 (2005): 306.
46. Alexis, Jonas, Marco Ramirez, Gerardo Trapaga, and Pär Jönsson. "Modeling of a DC electric arc furnace—heat transfer from the arc." *ISIJ international* 40, no. 11 (2000): 1089-1097.
47. Wang, F., Z. Jin, and Z. Zhu. "Numerical study of dc arc plasma and molten bath in dc electric arc furnace." *Ironmaking & steelmaking* 33, no. 1 (2006): 39-44.
48. Zhen, Wang, Wang Ninghui, Li Tie, and C. A. O. Yong. "3D numerical analysis of the arc plasma behavior in a submerged DC electric arc furnace for the production of fused MgO." *Plasma Science and Technology* 14, no. 4 (2012): 321.
49. Larsen, H. L., G. Liping, and J. A. Bakken. "A numerical model for the AC arc in the silicon metal furnace." In *Proc. INFACON*, pp. 517-527. 1995.
50. Bakken, J. A., Liping Gu, H. L. Larsen, and V. G. Sevastyanenko. "Numerical modeling of electric arcs." *Journal of engineering physics and thermophysics* 70, no. 4 (1997): 530-543.
51. Saevarsdottir, G. A., Hilde Loken Larsen, and Jon Arne Bakken. "Modelling of industrial ac-arcs." *High Temperature Material Processes: An International Quarterly of High-Technology Plasma Processes* 3, no. 1 (1999).
52. Moghadam, M. Mohebi, S. H. Seyedein, and M. Reza Aboutalebi. "Fluid flow and heat transfer modeling of AC arc in ferrosilicon submerged arc furnace." *Journal of iron and steel research, international* 17, no. 9 (2010): 14-18.
53. Daszkiewicz, Tomasz, and Witold Tarczyński. "Discharge channel displacement simulation in AC arc." *Archives of Electrical Engineering* 59, no. 1-2 (2010): 35-49.
54. Tarczyński, Witold, and Tomasz Daszkiewicz. "Switching arc simulation." *Przegląd Elektrotechniczny* 88, no. 7b (2012): 60-64.
55. Rehmet, Christophe, Frederic Fabry, Vandad Rohani, François Cauneau, and Laurent Fulcheri. "High speed video camera and electrical signal analyses of arcs behavior in a 3-Phase AC arc plasma torch." *Plasma Chemistry and Plasma processing* 33, no. 4 (2013): 779-796.

56. Rehmet, Christophe, Vandad Rohani, François Cauneau, and Laurent Fulcheri. "3D unsteady state MHD modeling of a 3-phase AC hot graphite electrodes plasma torch." *Plasma Chemistry and Plasma Processing* 33, no. 2 (2013): 491-515.
57. Rehmet, Christophe, Frédéric Fabry, Vandad Rohani, François Cauneau, and Laurent Fulcheri. "A comparison between MHD modeling and experimental results in a 3-phase AC arc plasma torch: influence of the electrode tip geometry." *Plasma Chemistry and Plasma Processing* 34, no. 4 (2014): 975-996.
58. Rehmet, Christophe, Frédéric Fabry, V. Rohani, François Cauneau, and Laurent Fulcheri. "Unsteady state analysis of free-burning arcs in a 3-Phase AC plasma torch: comparison between parallel and coplanar electrode configurations." *Plasma Sources Science and Technology* 23, no. 6 (2014): 065011.
59. Sanchez, J. L. G., M. A. Ramírez-Argaez, and A. N. Conejo. "Power delivery from the arc in AC electric arc furnaces with different gas atmospheres." *steel research international* 80, no. 2 (2009): 113-120.
60. Guo, D., and G. A. Irons. "Modeling of radiation intensity in an EAF." In *Third International Conference of CRD in the Minerals and process industry*, pp. 223-228. 2003.
61. Fathi, Amirhossein, Yadollah Saboohi, Igor Škrjanc, and Vito Logar. "Low computational-complexity model of EAF arc-heat distribution." *ISIJ international* 55, no. 7 (2015): 1353-1360.
62. Mathur, Pravin, and Charlie Messina. "Praxair CoJet™ Technology—Principles and Actual Results from Recent Installations." *AISE Steel Technology (USA)* 78, no. 5 (2001): 21-25.
63. Warty, S. K., and P. Mathur. "Praxair's CoJet® gas injection system: Delivering benefits and gaining useful knowledge for future enhancements." *Iron & steelmaker* 30, no. 3 (2003): 23-30.
64. Mathur, P. C. "Coherent jets in steelmaking: principles and learnings." *Praxair Metals Technologies, Indianapolis* (2004).
65. Anderson, J.E.; Farrenkopf, D.R. Coherent gas jet. U.S. Patent 5,823,762, 20 October 1998.
66. Ferri, M. B., F. Memoli, and E. Malfa. "Industrial application of supersonic lance-The KT system-numeric simulation, operating practice, results and perspectives." In

- AISTECH-CONFERENCE PROCEEDINGS-, vol. 1, p. 897. ASSOCIATION FOR IRON & STEEL TECHNOLOGY, 2004.
67. Candusso, Claudio. "Electric Arc Furnace sidewall fixed injectors developments and operational results." In AISTech 2006: Iron & Steel Technology Conference Proceedings(I & II). 2005.
  68. Jeong, Mi-seon, V. Kumar, H. D. Kim, T. Setoguchi, and S. Matsuo. "A computational characterization of the supersonic coherent jet." In 40th AIAA/ASME/SAE/ASEE Joint Propulsion Conference and Exhibit, p. 3525. 2004.
  69. Alam, Morshed, Jamal Naser, Geoffrey Brooks, and Andrea Fontana. "Computational fluid dynamics modeling of supersonic coherent jets for electric arc furnace steelmaking process." Metallurgical and Materials Transactions B 41, no. 6 (2010): 1354-1367.
  70. M. Alam, J. Naser, and G. Brooks, "Computational Fluid Dynamics Simulation of Supersonic Oxygen Jet Behavior at Steelmaking Temperature," Metall. Mater. Trans. B, vol. 41, no. 3, pp. 636–645, 2010.
  71. Wei, Guangsheng, Rong Zhu, Xuetao Wu, Lingzhi Yang, Kai Dong, Ting Cheng, and Tianping Tang. "Study on the fluid flow characteristics of coherent jets with CO<sub>2</sub> and O<sub>2</sub> mixed injection in electric arc furnace steelmaking processes." Metallurgical and Materials Transactions B 49, no. 3 (2018): 1405-1420.
  72. Wei, Guangsheng, Rong Zhu, Ting Cheng, Kai Dong, Lingzhi Yang, and Xuetao Wu. "Study on the impact characteristics of coherent supersonic jet and conventional supersonic jet in EAF steelmaking process." Metallurgical and Materials Transactions B 49, no. 1 (2018): 361-374.
  73. Wei, Guangsheng, Rong Zhu, Ting Cheng, Kai Dong, Lingzhi Yang, Tianping Tang, and Xuetao Wu. "Effect of main gas composition on flow field characteristics of supersonic coherent jets with CO<sub>2</sub> and O<sub>2</sub> mixed injection (COMI) at steelmaking temperature." ISIJ International 58, no. 5 (2018): 842-851.
  74. Liu, Fuhai, Rong Zhu, Kai Dong, and Shaoyan Hu. "Flow field characteristics of coherent jet with preheating oxygen under various ambient temperatures." ISIJ International (2016): ISIJINT-2015.

75. Liu, Fuhai, Rong Zhu, Kai Dong, and Shaoyan Hu. "Effect of ambient and oxygen temperature on flow field characteristics of coherent jet." *Metallurgical and Materials Transactions B* 47, no. 1 (2016): 228-243.
76. Tang, Guangwu, Yuchao Chen, Armin K. Silaen, Yury Krotov, Michael F. Riley, and Chenn Q. Zhou. "Effects of fuel input on coherent jet length at various ambient temperatures." *Applied Thermal Engineering* 153 (2019): 513-523.
77. Tang, Guangwu, Yuchao Chen, Armin K. Silaen, Yury Krotov, Michael F. Riley, and Chenn Q. Zhou. "Investigation on coherent jet potential core length in an electric arc furnace." *steel research international* 90, no. 4 (2019): 1800381.
78. Tang, Guangwu, Yuchao Chen, Armin K. Silaen, Tao Wang, and Chenn Q. Zhou. "Investigation of supersonic oxygen jet potential core length at various ambient temperatures." *JOM* 71, no. 2 (2019): 633-643.
79. Guo, D., and G. A. Irons. "Radiation Modeling in an EAF." In *AISTECH-CONFERENCE PROCEEDINGS-*, vol. 1, p. 991. ASSOCIATION FOR IRON & STEEL TECHNOLOGY, 2004.
80. Nakazono, Daisaku, Ken-ichi Abe, Michio Nishida, and Kouichi Kurita. "Supersonic O<sub>2</sub>-jet impingement on liquid iron with surface chemistry." *ISIJ international* 44, no. 1 (2004): 91-99.
81. Odenthal, Hans-Jürgen, Udo Falkenreck, and Jochen Schlüter. "CFD simulation of multiphase melt flows in steelmaking converters." (2006).
82. ERSSON, Mikael, Anders TILLIANDER, Lage JONSSON, and Par JONSSON. "3rd Int. Conf. on CFD in the Minerals and Process Industries, 2003 3rd Int. Conf. on CFD in the Minerals and Process Industries, 2003 71, 2003." *ISIJ international* 48, no. 4 (2008): 377-384.
83. Muñoz-Esparza, D., J-M. Buchlin, K. Myrillas, and R. Berger. "Numerical investigation of impinging gas jets onto deformable liquid layers." *Applied Mathematical Modelling* 36, no. 6 (2012): 2687-2700.
84. Alam, Morshed, Jamal Naser, Geoffrey Brooks, and Andrea Fontana. "A computational fluid dynamics model of shrouded supersonic jet impingement on a water surface." *ISIJ international* 52, no. 6 (2012): 1026-1035.

85. Wei, Guang-sheng, Rong Zhu, Ting Cheng, and Fei Zhao. "Numerical simulation of jet behavior and impingement characteristics of preheating shrouded supersonic jets." *Journal of Iron and Steel Research International* 23, no. 10 (2016): 997-1006.
86. Wei, Guangsheng, Rong Zhu, Xuetao Wu, Lingzhi Yang, Kai Dong, Ting Cheng, and Tianping Tang. "Study on the fluid flow characteristics of coherent jets with CO<sub>2</sub> and O<sub>2</sub> mixed injection in electric arc furnace steelmaking processes." *Metallurgical and Materials Transactions B* 49, no. 3 (2018): 1405-1420.
87. Wei, Guangsheng, Rong Zhu, Ting Cheng, Kai Dong, Lingzhi Yang, and Xuetao Wu. "Study on the impact characteristics of coherent supersonic jet and conventional supersonic jet in EAF steelmaking process." *Metallurgical and Materials Transactions B* 49, no. 1 (2018): 361-374.
88. Oltmann, Helmut, E. B. Pretorius, and L. W. B. Refractories. "Simulation of the Refining Stage of the EAF Process." In *AISE Conference*. 2002.
89. Matsuura, Hiroyuki, Christopher P. Manning, Raimundo AFO Fortes, and Richard J. Fruehan. "Development of a decarburization and slag formation model for the electric arc furnace." *ISIJ international* 48, no. 9 (2008): 1197-1205.
90. Memoli, Francesco, Carlo Mapelli, Pietro Ravanelli, and Marco Corbella. "Simulation of oxygen penetration and decarburisation in EAF using supersonic injection system." *ISIJ international* 44, no. 8 (2004): 1342-1349.
91. Li, Yun, and Richard J. Fruehan. "Computational fluid-dynamics simulation of postcombustion in the electric-arc furnace." *Metallurgical and Materials Transactions B* 34, no. 3 (2003): 333-343.
92. Chan, Elton, Matt Riley, Thomson MJ, and Evenson EJ. "Nitrogen oxides (NO<sub>x</sub>) formation and control in an electric arc furnace (EAF): Analysis with measurements and computational fluid dynamics (CFD) modeling." *ISIJ international* 44, no. 2 (2004): 429-438.
93. Al-Harbi, M.N.; Mishra, S.K.; Maity, M.; Al-Turky, S. "Computational Fluid- Dynamics Simulation of the Electrical Arc Furnace toward the Optimize the Service Life of Delta Refractory." In *Proc. of METEC InSteelCon 2011, Session 15*, pp. 1 – 9. METEC InSteelCon, 2011.

94. JLG, Sanchez, Conejo AN, and Ramirez-Argaez MA. "Effect of foamy slag height on hot spots formation inside the electric arc furnace based on a radiation model." *ISIJ international* 52, no. 5 (2012): 804-813.
95. Yigit, Cemil, Gokhan Coskun, Ekrem Buyukkaya, Ufuk Durmaz, and Hasan R. Güven. "CFD modeling of carbon combustion and electrode radiation in an electric arc furnace." *Applied Thermal Engineering* 90 (2015): 831-837.
96. Tanaka, Manabu, Masao Ushio, and John J. Lowke. "Numerical study of gas tungsten arc plasma with anode melting." *Vacuum* 73, no. 3-4 (2004): 381-389.
97. Li, Linmin, Baokuan Li, Lichao Liu, and Yuichi Motoyama. "Numerical Modeling of Fluid Flow, Heat Transfer and Arc–Melt Interaction in Tungsten Inert Gas Welding." *High Temperature Materials and Processes* 36, no. 4 (2017): 427-439.
98. Wu, C. S., Q. X. Hu, and J. Q. Gao. "An adaptive heat source model for finite-element analysis of keyhole plasma arc welding." *Computational Materials Science* 46, no. 1 (2009): 167-172.
99. Zhang, Tao, Chuan Song Wu, and Yanhui Feng. "Numerical analysis of heat transfer and fluid flow in keyhole plasma arc welding." *Numerical Heat Transfer, Part A: Applications* 60, no. 8 (2011): 685-698.
100. Jian, Xiaoxia, and Chuan Song Wu. "Numerical analysis of the coupled arc–weld pool–keyhole behaviors in stationary plasma arc welding." *International Journal of Heat and Mass Transfer* 84 (2015): 839-847.
101. Pan, Jiajing, Shengsun Hu, Lijun Yang, and Shujun Chen. "Numerical analysis of the heat transfer and material flow during keyhole plasma arc welding using a fully coupled tungsten–plasma–anode model." *Acta Materialia* 118 (2016): 221-229.
102. Lowke, J. J. "Simple theory of free-burning arcs." *Journal of physics D: Applied physics* 12, no. 11 (1979): 1873.
103. Boulos, Maher I., Pierre Fauchais, and Emil Pfender. *Thermal plasmas: fundamentals and applications*. Springer Science & Business Media, 2013.
104. Lowke, J. J., and M. Tanaka. "'LTE-diffusion approximation' for arc calculations." *Journal of Physics D: Applied Physics* 39, no. 16 (2006): 3634.

105. Tashiro, Shinichi, Minoru Miyata, and Manabu Tanaka. "Numerical analysis of AC tungsten inert gas welding of aluminum plate in consideration of oxide layer cleaning." *Thin Solid Films* 519, no. 20 (2011): 7025-7029.
106. Brackbill, Jeremiah U., Douglas B. Kothe, and Charles Zemach. "A continuum method for modeling surface tension." *Journal of computational physics* 100, no. 2 (1992): 335-354.
107. Fan, H. G., and R. Kovacevic. "Droplet formation, detachment, and impingement on the molten pool in gas metal arc welding." *Metallurgical and materials transactions B* 30, no. 4 (1999): 791-801.
108. Hu, J., and Hai-Lung Tsai. "Heat and mass transfer in gas metal arc welding. Part I: The arc." *International Journal of Heat and Mass Transfer* 50, no. 5-6 (2007): 833-846.
109. Fluent, A. N. S. Y. S. "Ansys fluent theory guide." ANSYS Inc., USA 15317 (2011): 724-746.
110. Cressault, Yann. "Propriétés des plasmas thermiques dans des mélanges argon-hydrogene-cuivre." PhD diss., 2001.
111. Chen, Yuchao, Qingxuan Luo, Armin K. Silaen, and Chenn Q. Zhou. "Multi-Physics Modeling of Steel Ingot Melting by Electric Arc Plasma and its Application to Electric Arc Furnace." *Frontiers in Materials* (2020): 336.
112. Mandal, Kamallesh, and Gordon A. Irons. "A Study of Scrap Heating By Burners. Part I: Experiments." *Metallurgical and Materials Transactions B* 44, no. 1 (2013): 184-195.
113. Mandal, Kamallesh, and Gordon A. Irons. "A Study of Scrap Heating by Burners: Part II—Numerical Modeling." *Metallurgical and Materials Transactions B* 44, no. 1 (2013): 196-209.
114. Guo, Diancai, and Gordon A. Irons. "Modeling of Gas Flow and Burner Heating in an Electric Arc Furnace." In *AISTech 2006: Iron & Steel Technology Conference Proceedings(I & II)*. 2005.
115. Kladias, N., and V. Prasad. "Experimental verification of Darcy-Brinkman-Forchheimer flow model for natural convection in porous media." *Journal of thermophysics and heat transfer* 5, no. 4 (1991): 560-576.
116. Patankar, Suhas. *Numerical heat transfer and fluid flow*. Taylor & Francis, 2018.

117. Kladias, N., and V. Prasad. "Experimental verification of Darcy-Brinkman-Forchheimer flow model for natural convection in porous media." *Journal of thermophysics and heat transfer* 5, no. 4 (1991): 560-576.
118. Ergun, Sabri. "Fluid flow through packed columns." *Chem. Eng. Prog.* 48 (1952): 89-94.
119. Schiller, Links. "A drag coefficient correlation." *Zeit. Ver. Deutsch. Ing.* 77 (1933): 318-320.
120. ZHANG, Xinghe, Reijiro TAKAHASHI, Hiroshi NOGAMI, and Jun-ichiro YAGI. "Numerical simulation of the moving bed furnace for reduction and melting of oxidized iron-scrap briquette containing coke breeze." *Tetsu-to-Hagané* 87, no. 5 (2001): 410-417.
121. Ranz, W. E., and W. R. Marshall. "Evaporation from droplets." *Chem. Eng. Prog* 48, no. 3 (1952): 141-146.
122. Lewis, R. W., and K. Ravindran. "Finite element simulation of metal casting." *International journal for numerical methods in engineering* 47, no. 1-3 (2000): 29-59.
123. Guo, Diancai, and Gordon A. Irons. "Modelling of steel scrap movement." *Applied mathematical modelling* 32, no. 10 (2008): 2041-2049.
124. Qian, F., B. Farouk, and R. Mutharasan. "Modeling of fluid flow and heat transfer in the plasma region of the dc electric arc furnace." *Metallurgical and materials transactions B* 26, no. 5 (1995): 1057-1067.
125. Chen, Yuchao, Qingxuan Luo, Armin K. Silaen, and Chenn Q. Zhou. "Multi-physics Modeling of Steel Ingot Melting by Electric Arc Plasma and its Application to EAF." *Frontiers in Materials* 7 (2020): 336.
126. Rehmet, C. "Theoretical and experimental study of a 3-phase AC plasma torch associated to a gasification process." PhD diss., PhD thesis dissertation defended on 23 September, 2013, MINES-ParisTech (196 pages), 2013.
127. Rehmet, Christophe, Frédéric Fabry, V. Rohani, François Cauneau, and Laurent Fulcheri. "Unsteady state analysis of free-burning arcs in a 3-Phase AC plasma torch: comparison between parallel and coplanar electrode configurations." *Plasma Sources Science and Technology* 23, no. 6 (2014): 065011.
128. Lee, Yongjoong, Henrik Nordborg, Yongsug Suh, and Peter Steimer. "Arc stability criteria in AC arc furnace and optimal converter topologies." In *APEC 07-Twenty-*

- Second Annual IEEE Applied Power Electronics Conference and Exposition, pp. 1280-1286. IEEE, 2007.
129. Bowman, Ben, and Klaus Krüger. Arc furnace physics. Düsseldorf: Verlag Stahleisen, 2009.
  130. Hay, Thomas, Jesus Hernandez, Suzanne Roberts, and Thomas Echterhof. "Calculation of view factors in electric arc furnace process modeling." *steel research international* 92, no. 2 (2021): 2000341.
  131. Billings, S. A., and H. Nicholson. "Modelling a three-phase electric arc furnace: a comparative study of control strategies." *Applied Mathematical Modelling* 1, no. 7 (1977): 355-361.
  132. Abdol-Hamid, Khaled S., S. Paul Pao, Steven J. Massey, and Alaa Elmiligui. "Temperature corrected turbulence model for high temperature jet flow." *J. Fluids Eng.* 126, no. 5 (2004): 844-850.
  133. Wakao, N., S. Kagaei, and T. Funazkri. "Effect of fluid dispersion coefficients on particle-to-fluid heat transfer coefficients in packed beds: correlation of Nusselt numbers." *Chemical engineering science* 34, no. 3 (1979): 325-336.
  134. C.C. Furnas: U.S. Bureau of Mines Bulletin, 1932, p. 261.
  135. Kitaev, Boris Ivanovich, Yu G. Yaroshenko, and V. D. Suchkov. Heat exchange in shaft furnaces. Elsevier, 2016.
  136. ISHIKAWA, Hidetake, Shozo MIZOGUCHI, and Kiyoshi SEGAWA. "A model study on jet penetration and slopping in the LD converter." *Tetsu-to-Hagané* 58, no. 1 (1972): 76-84.
  137. SANO, Masamichi, and Kazumi MORI. "Fluid flow and mixing characteristics in a gas-stirred molten metal bath." *Transactions of the Iron and Steel Institute of Japan* 23, no. 2 (1983): 169-175.
  138. Wei, Ji-He, and De-Ping Zhu. "Mathematical modeling of the argon-oxygen decarburization refining process of stainless steel: Part I. Mathematical model of the process." *Metallurgical and materials transactions B* 33, no. 1 (2002): 111-119.
  139. Shukla, Ajay Kumar, Brahma Deo, Stuart Millman, Bert Snoeijer, Aart Overbosch, and Abha Kapilashrami. "An insight into the mechanism and kinetics of reactions in BOF steelmaking: theory vs practice." *steel research international* 81, no. 11 (2010): 940-948.

140. Saint-Raymond, H., D. Huin, and F. Stouvenot. "Mechanisms and modeling of liquid steel decarburization below 10 ppm carbon." *Materials transactions, JIM* 41, no. 1 (2000): 17-21.
141. Chen, Jia-Xiang. "Handbook on Common Using Data, Graphs and Tables in Steelmaking." (1984): 383.
142. Ito, Kimihisa, and R. J. Fruehan. "Study on the foaming of CaO-SiO<sub>2</sub>-FeO slags: Part I. Foaming parameters and experimental results." *Metallurgical transactions B* 20, no. 4 (1989): 509-514.
143. Jiang, R., and R. J. Fruehan. "Slag foaming in bath smelting." *Metallurgical transactions B* 22, no. 4 (1991): 481-489.
144. Wu, Can, Qin Cheng, Kangbing Wu, Gang Wu, and Qing Li. "Graphene prepared by one-pot solvent exfoliation as a highly sensitive platform for electrochemical sensing." *Analytica Chimica Acta* 825 (2014): 26-33.
145. Xuan, Changji, Hiroyuki Shibata, Sohei Sukenaga, Pär Göran Jönsson, and Keiji Nakajima. "Wettability of Al<sub>2</sub>O<sub>3</sub>, MgO and Ti<sub>2</sub>O<sub>3</sub> by liquid iron and steel." *Isij International* 55, no. 9 (2015): 1882-1890.
146. Urbain, Georges. "Viscosity estimation of slags." *Steel research* 58, no. 3 (1987): 111-116.
147. Naghizadeh-Kashani, Yasman. "Calcul du transfert radiatif dans un plasma d'air." PhD diss., Toulouse, 1999.
148. Ramírez, Marco, Jonas Alexis, Gerardo Trapaga, Par Jönsson, and John Mckelliget. "Modeling of a DC electric arc furnace—mixing in the bath." *ISIJ international* 41, no. 10 (2001): 1146-1155.
149. Bowman, B. "Measurements of plasma velocity distributions in free-burning DC arcs up to 2160 A." *Journal of Physics D: Applied Physics* 5, no. 8 (1972): 1422.
150. Saravanan, Subramani, Govindan Nagarajan, and Santhanam Sampath. "Application of Taguchi's Orthogonal Array in Multi Response Optimization of NO<sub>x</sub> Emission of Crude Rice Bran Oil Methyl Ester Blend as a CI Engine Fuel." (2012).
151. David, F.; Tudorache, T.; Firteanu, V. Numerical evaluation of electromagnetic field effects in electric arc furnaces. In *The International Journal for Computation and Mathematics in Electrical and Electronic Engineering, COMPEL*, Melbourne, 2001.

152. OJP, G.; RamíRez-Argáez, M.A.; AN, C. Effect of arc length on fluid flow and mixing phenomena in AC electric arc furnaces. *ISIJ Int.* 2010, 50, 1–8.
153. Widlund, O.; Sand, U.; Hjortstam, O.; Zhang, X. Modelling of electric arc furnaces (EAF) with electromagnetic stirring. Västerås ABB 2012.
154. Pretorius, E.; Oltmann, H.; Jones, J. *EAF Fundamentals; LWB Refractories*: New York, NY, USA, 2010.

## PUBLICATIONS

### Journal Publications (13 Papers):

1. **Chen, Yuchao**, Steve Ryan, Armin K. Silaen, and Chenn Q. Zhou. "An investigation into EAF Burner Preheating and Melting Characteristics." *International Journal of Heat and Mass Transfer* (2022). [Under review]
2. **Chen, Yuchao**, Qingxuan Luo, Steve Ryan, Neel Busa, Armin K. Silaen, and Chenn Q. Zhou. "Effect of coherent jet burner on scrap melting in electric arc furnace." *Applied Thermal Engineering* 212 (2022): 118596.
3. **Chen, Yuchao**, Steve Ryan, Armin K. Silaen, and Chenn Q. Zhou. "Simulation of Scrap Melting Process in an AC Electric Arc Furnace: CFD Model Development and Experimental Validation." *Metallurgical and Materials Transactions B* (2022): 1-20.
4. **Chen, Yuchao**, Steve Ryan, Armin K. Silaen, and Chenn Q. Zhou. "Numerical investigation of AC electric arc plasma heat dissipation in EAF." *Ironmaking & Steelmaking* 49, no. 3 (2022): 255-267.
5. **Chen, Yuchao**, Yu Wang, Armin K. Silaen, and Chenn Q. Zhou. "Numerical Investigation of DC Electric Arc Behavior under the Consideration of Electrode Movement." *Iron & Steel Technology* (2021): 74-81.
6. **Chen, Yuchao**, Qingxuan Luo, Armin K. Silaen, and Chenn Q. Zhou. "Multi-physics modeling of steel ingot melting by electric arc plasma and its application to electric arc furnace." *Frontiers in Materials* (2020): 576831.
7. **Chen, Yuchao**, Armin K. Silaen, and Chenn Q. Zhou. "3D integrated modeling of supersonic coherent jet penetration and decarburization in EAF refining process." *Processes* 8, no. 6 (2020): 700.
8. **Chen, Yuchao**, Yu Wang, Guangwu Tang, Armin K. Silaen, Kyle Vanover, and Chenn Q. Zhou. "Numerical Investigation of Decarburization Reaction Characteristics in Electric Arc Furnace Steelmaking Process." *Iron & Steel Technology* (2020): 76-82.
9. Luo, Qingxuan, **Yuchao Chen**, Sunday Abraham, Yufeng Wang, Randy Petty, Armin K. Silaen, and Chenn Zhou. "Effects of EAF Operations on Water Cooling Panel Overheating." *Steel Research International* (2022): 2100844.

10. Tang, Guangwu, **Yuchao Chen**, Armin K. Silaen, Yury Krotov, Michael F. Riley, and Chenn Q. Zhou. "Effects of fuel input on coherent jet length at various ambient temperatures." *Applied Thermal Engineering* 153 (2019): 513-523.
11. Tang, Guangwu, **Yuchao Chen**, Armin K. Silaen, Yury Krotov, Michael F. Riley, and Chenn Q. Zhou. "Investigation on coherent jet potential core length in an electric arc furnace." *Steel Research International* 90, no. 4 (2019): 1800381.
12. Tang, Guangwu, **Yuchao Chen**, Armin K. Silaen, Tao Wang, and Chenn Q. Zhou. "Investigation of supersonic oxygen jet potential core length at various ambient temperatures." *JOM* 71, no. 2 (2019): 633-643.
13. Tang, Guangwu, **Yuchao Chen**, Armin K. Silaen, Andrew Spencer, Yury Krotov, and Chenn Q. Zhou. "Modeling of Scrap Pre-Heating by Oxy-Fuel Combustion in an Electric Arc Furnace." *Iron & Steel Technology* (2019): 34-41.

**Conference Publications (10 Papers):**

1. **Chen, Yuchao**, Qingxuan Luo, Armin K. Silaen, and Chenn Q. Zhou. "Numerical Investigation of EAF Arc Exposure and Water-panel Overheating." In *AISTech 2022- Proceedings of the Iron & Steel Technology Conference*. Pittsburgh, Pennsylvania, USA. May 16 – May 19, 2022.
2. **Chen, Yuchao**, Steve Ryan, Armin K. Silaen, and Chenn Q. Zhou. "CFD Modeling and Experimental Investigation of Scrap Melting and Heat Transfer in AC Electric Arc Furnace." In *Proceedings of the 9th International Conference on Modeling and Simulation of Metallurgical Processes in Steelmaking*. Virtual. October 4-7, 2021.
3. **Chen, Yuchao**, Yu Wang, Armin K. Silaen, and Chenn Q. Zhou. "Numerical Investigation of DC Electric Arc Behavior under the Consideration of Electrode Movement." In *AISTech 2021- Proceedings of the Iron & Steel Technology Conference*. Nashville, Tennessee, USA. June 29 – July 1, 2021.
4. **Chen, Yuchao**, Steve Ryan, Armin K. Silaen, and Chenn Q. Zhou. "Experimental Study and CFD Modelling of Scrap Melting Behaviour in AC EAF." In *Proceedings of the 4th European Academic Symposium on EAF Steelmaking*. Virtual. June 16 - June 18, 2021
5. **Chen, Yuchao**, Yu Wang, Guangwu Tang, Armin K. Silaen, Kyle Vanover, and Chenn Q. Zhou. "Numerical Investigation of Decarburization Reaction Characteristics in Electric

- Arc Furnace Steelmaking Process.” In AISTech 2019-Proceedings of the Iron & Steel Technology Conference, pp. 789-796. Pittsburgh, Pennsylvania, USA. May 6–9, 2019.
6. **Chen, Yuchao**, Armin K. Silaen, Kyle Vanover, and Chenn Q. Zhou. “Numerical Simulation of Fluid Flow During the Steel Refining Process in an Electric Arc Furnace.” In Proceedings of the Materials Science & Technology 2018, p. 348. Columbus, Ohio, USA. October 14-18, 2018.
  7. **Chen, Yuchao**, Armin K. Silaen, Nicholas Walla, Kurt Johnson, and Chenn Q. Zhou. "Optimization of Heat Transfer Process in a Walking Beam Reheat Furnace Using Computational Fluid Dynamics." In Proceedings of the ASME 2018 International Mechanical Engineering Congress and Exposition. Volume 8A: Heat Transfer and Thermal Engineering. Pittsburgh, Pennsylvania, USA. November 9–15, 2018.
  8. **Chen, Yuchao**, Xiang Liu, Armin K. Silaen, Kurt Johnson, and Chenn Q. Zhou. "Investigation of combustion and heat transfer in an industrial reheating furnace using CFD." In TMS Annual Meeting & Exhibition, pp. 187-198. Springer, Cham, 2018.
  9. Tang, Guangwu, **Yuchao Chen**, Yu Wang, Armin K. Silaen, Kyle Vanover, and Chenn Q. Zhou. “Numerical Simulation of Oxy-Natural Gas Combustion in an Electric Arc Furnace.” In Proceedings of the 8th International Conference on Modeling and Simulation of Metallurgical Processes in Steelmaking, pp. 270-280. Toronto, Ont., Canada. August 13-15, 2019.
  10. Tang, Guangwu, **Yuchao Chen**, Armin K. Silaen, Yury Krotov, and Chenn Q. Zhou. "Effects of steel scrap oxidation on scrap preheating process in an electric arc furnace." In 10th International Symposium on High-Temperature Metallurgical Processing, pp. 453-465. Springer, Cham, 2019.